8-2023

Volatile Cycling and Metasomatism in Flat-Slab Subduction Zones of the Central Andes

Coleman Hiett
Utah State University

VOLATILE CYCLING AND METASOMATISM IN FLAT-SLAB SUBDUCTION ZONES OF THE CENTRAL ANDES

by

Coleman Hiett

A dissertation submitted in partial fulfillment
of the requirements for the degree

of

DOCTOR OF PHILOSOPHY

in Geosciences

Approved:

Dennis L. Newell, Ph.D. Major Professor	Alexis K. Ault, Ph.D. Committee Member
John W. Shervais, Ph.D. Committee Member	Anthony R. Lowry, Ph.D. Committee Member
Micah J. Jessup, Ph.D. Committee Member	D. Richard Cutler, Ph.D. Vice Provost for Graduate Studies

UTAH STATE UNIVERSITY
Logan, Utah

2023

ABSTRACT

Volatile Cycling and Metasomatism in Flat-Slab Subduction Zones of the Central Andes

by

Coleman D. Hiett, Doctor of Philosophy,

Utah State University, 2023

Major Professor: Dr. Dennis L. Newell
Department: Geosciences

Flat-slab subduction represents a confounding gap in our understanding of chemical cycling and continental evolution in the global tectonic system. This research leverages the juxtaposition of active and ancient flat-slab systems in the Central Andes and novel applications of geochemical methods to gain new insight into these processes. I combine stable isotope geochemistry with various other geochemical and petrologic tools to interrogate volatile cycling and metasomatism in Andean lithosphere of Southern Peru, employing observations from geothermal springs above the modern Peruvian flat slab and xenolith-hosting volcanic rocks from the region overlying the Oligocene Altiplano flat slab.

A geochemical survey of geothermal systems across the Peruvian Andes reveals mantle and crustal degassing in response to active flat slab-fluid transfer and continental hydration. Helium isotope ratios ranging from 0.26 to 2.40 R_C/R_A (air-corrected $^3He/^4He$ ratio relative to the air ratio) demonstrate a regionally extensive mantle helium flux that

demands persistent slab-to-lithosphere fluid transfer and implicates permeable pathways through metasomatized lithosphere. Corresponding C and N isotope systematics coupled with relative gas abundances and aqueous geochemistry demonstrate mantle and crustal contributions of CO_2 and N_2 sampled by geothermal systems. Variability in mantle volatile signatures reflect mantle-to-surface transit times and mixing between deep volatile sources that are locally modulated by tectonism in the subducting slab and continental crust. Xenoliths recovered from Quaternary lava flows in the northern Altiplano Plateau include a suite of phlogopite-rich alkaline igneous lithologies that yield phlogopite δD values of -74 to -38 ‰ VSMOW and bulk-rock incompatible trace element enrichments (e.g., Rb, Ba $>10^2$ × primitive mantle) indicating derivation from a metasomatized mantle source enriched by subduction derived fluids or melts. A second suite of calcite- and phlogopite-rich ultramafic xenoliths sample the metasomatized mantle itself. Calcite $\delta^{13}C$ and $\delta^{18}O$ values of -2.49 to +0.77 ‰ VPDB and +15.8 to +16.4 ‰ VSMOW, bulk-rock incompatible element enrichments (e.g., Cs, Rb, Pb > 10^2 × primitive mantle), and observations from xenolith hosting alkaline lava flows elicit a model in which mantle metasomatism was facilitated by melting of subducted sediments accreted to the base of the lithosphere during Oligocene shallow subduction. The collective results of this dissertation highlight novel insight into chemical cycling and metasomatism in flat-slab systems, including lithosphere-scale volatile transfer and the role of underplated slab material in mantle metasomatism. More broadly, this work represents profound advances in our understanding of the coupled tectonic and chemical evolution of the Andean lithosphere and Cordilleran regions globally.

(290 pages)

PUBLIC ABSTRACT

Volatile Cycling and Metasomatism in Flat-Slab Subduction Zones of the Central Andes

Coleman D. Hiett

Flat-slab subduction, where an oceanic plate subducts horizontally below a continental margin for hundreds of kilometers, is an enigmatic but prevalent tectonic configuration in which chemical cycling and alteration of the continental plate is poorly constrained. Geochemical investigations in regions of modern and ancient flat-slab subduction in the Central Andes afford an opportunity to study this process. Certain elements naturally occur with varying number of neutrons in their nuclei (isotopes), and measurements of isotope ratios within geologic materials inform on chemical sources and geologic processes. This research leverages stable isotope analyses and other geochemical tools to investigate volatiles and other material transferred from a flat slab to the overlying continental plate and how this chemically modifies the roots of continental mountain belts. I employ geochemical investigation of gasses emitted from thermal springs above a modern flat-slab subduction zone in central Peru, as well as investigations of volcanic rocks that entrained fragments of the crust and mantle during ascent to the surface (xenoliths) in a region affected by shallow subduction > 25 million years ago.

Geochemical analyses of thermal springs across the Peruvian Andes, including helium, carbon, and nitrogen stable isotope ratios, relative gas abundances, and aqueous geochemistry, reveal mantle and crustal degassing in response to active flat slab-fluid

transfer and continental hydration. Mantle volatile fluxes require continuous fluid transfer and permeable pathways through chemically modified continental crust and mantle. Variability in deep volatile signatures reflect mantle-to-surface transit times and mixing between mantle and crustal volatile sources that are locally influenced by tectonic processes in the oceanic and continental plates.

Xenoliths recovered from Quaternary lava flows in the northern Altiplano Plateau include a suite of mica-rich alkaline igneous lithologies that yield hydrogen isotope ratios and trace element characteristics indicating formation by melting of a chemically modified mantle source enriched by fluids or melts during flat-slab subduction. A second suite of carbonate- and mica-rich mantle xenoliths are samples of the modified mantle. Carbon and oxygen isotope ratios of calcite and trace element characteristics of these xenoliths, coupled with observations from xenolith hosting alkaline lava flows, reveal that chemical modification of the mantle was facilitated by melts of subducted sediments accreted to the base of the continental plate during flat-slab subduction. The collective results of this dissertation highlight novel insight into chemical cycling and modification of the continental mantle in flat-slab systems, including plate-scale volatile transport and the role of subducted sediments in mantle alteration. More broadly, this work represents profound advances in our understanding of the coupled tectonic and chemical evolution of the Andean Cordillera and continental margins globally.

(290 pages)

ACKNOWLEDGMENTS

First and foremost, I thank my advisor Dennis Newell, whose support, encouragement, and dedicated mentorship over the last five years has been invaluable to my growth as a scientist, a teacher, and a colleague. I would also like to thank my committee members, Alexis Ault, John Shervais, Tony Lowry, and Micah Jessup, for their engagement in my work and our many inspiring discussions that helped to move my research forward. Additionally, I want to thank Lon Abbott, whose mentorship and passion for teaching inspired me to pursue a PhD in geosciences.

Many colleagues and friends were instrumental in the research presented in this dissertation. The first two chapters of this dissertation were made possible through prior research led by Dennis Newell, Brandt Scott, and Heather Upin, and with assistance in the field by Micah Jessup, Tyler Grambling, and Natalie Tanski. I had the pleasure of working with two undergraduate researchers, Alyssa Schiwal and Jacob Ladner, whose research played an important role in this work. I also am indebted to Professor Jose Cardenas Roque of the Univesidad National de San Antonio del Cusco and to Alberto Cafferata of Caraz, Peru for providing crucial logistical support for accomplishing field work. I appreciate the help with laboratory analyses and insightful conversations provided by Andrew Lonero (USU), Andy Hunt (USGS), Tobias Fischer (UNM), Aaron Bell (CU), and Emily Verplank (CU), and FenAnn Shen (USU).

The faculty, staff, and students of the USU Geosciences department have been a valuable source of support throughout my education and research. I particularly appreciate office mates Rob, Harriet, Ema, and Jordan for keeping me sane throughout

long days at work. I also want to thank Hollie Richards for her guidance through the financial and administrative mazes of academia, and for making sure students had what they needed to succeed, including ample snacks. I have been especially lucky to have the support and encouragement of my partner and colleague Natalie Tanski.

This research was made possible through funding from The National Science Foundation (including a Graduate Research Fellowship and grant NSF-EAR-1623034), a USU Presidential Doctoral Research Fellowship, a student research grant from the Geological Society of America, and support from the USU Department of Geosciences.

Coleman D. Hiett

DEDICATION

For my dad, who my siblings and I mocked for always talking about rocks, but who instilled in me a passion for geology and continues to contemplate provocative questions in continental tectonics in his spare time. And to Natalie, who shares my love for mountains and canyons and the processes that sculpt them, and who has provided endless support since we met in GEOL-2001.

CONTENTS

Page

LIST OF TABLES

Page

CHAPTER 4

APPENDIX A

APPENDIX B

APPENDIX C

LIST OF FIGURES

Page

CHAPTER 1

CHAPTER 2

CHAPTER 3

CHAPTER 4

CHAPTER 5

APPENDIX A

APPENDIX B

APPENDIX C

CHAPTER 1

INTRODUCTION

OVERVIEW

The dynamic processes of subduction, mantle wedge convection, and arc magmatism exert broad control over the evolution of Earth's mantle, crustal, and surface chemical reservoirs. Often viewed in terms of a "subduction factory", these complex geologic systems take inputs in the form of altered oceanic lithosphere and generate outputs that include metamorphosed slab material, which is ultimately incorporated into the convecting mantle, and slab-derived fluids, melts, or sediments that interact with and modify the mantle wedge and overlying lithosphere. This latter output, the recycling of slab material into the overlying lithosphere, is the primary focus of this dissertation. Along ~90% of the global subduction system, much of the mass transfer to overlying lithosphere is filtered through an asthenospheric wedge, where elevated temperatures and hydrous conditions result in partial melting and subsequent arc magmatism. Magmatism transports slab- and mantle-derived components into and through the overlying crust, and the recycling efficiency and mechanisms of mass transfer can be scrutinized through geochemical investigation of volcanic arc materials.

Approximately 10% of the modern global subduction system exhibits a shallow or flat-slab subduction (Gutscher et al., 2000), creating a unique geodynamic environment for chemical cycling that is challenging to investigate due to the lack of obvious outputs at the Earth's surface. In this endmember geometry, a shallow subduction angle

essentially closes the asthenospheric wedge, placing the subducting plate in contact with the overlying lithosphere for several hundreds of kilometers inboard of the trench. Slab-derived volatiles are released directly into the continental lithosphere, rather than an asthenospheric wedge, resulting in the characteristic volcanic gap associated with flat slabs.

Research in the last two decades suggests that flat-slab subduction leads to pervasive hydration and metasomatism of the overlying continental lithosphere, with drastic implications for the mechanical and chemical evolution of the convergent margin. For example, this process is invoked in the geologic evolution of both the western U.S. Cordillera and the Altiplano-Puna Plateau of South America, both of which experienced episodes of flat-slab subduction followed by some combination of explosive ignimbrite activity, surface uplift, changes in the style and/or location of continental deformation, and delamination of the lower lithosphere (Kay and Kay, 1993; Humphreys et al., 2003; Hoke and Lamb, 2007; Jones et al., 2015). Theoretical models for fluid transfer and continental hydration are compelling (e.g., Humphreys et al., 2003; Currie and Beaumont, 2011), yet evidence for this process is limited to xenolith and volcanic rock studies (e.g., Jones et al., 2015; Butcher et al., 2017b; Marshall et al., 2017; Farmer et al., 2020) and geophysical surveys (e.g., Humphreys et al., 2003; Porter et al., 2012; Dougherty and Clayton, 2015). Direct observation of present-day flat-slab-to-lithosphere fluid transfer has remained elusive, with open questions regarding mechanisms for volatile transport at depth and volatile cycling in these settings. Furthermore, the fossil record of hydration and metasomatism afforded by xenoliths and alkaline basalts in

regions previously affected by flat-slab subduction is limited, so chemical evolution of the continental lithosphere in these settings is still poorly constrained.

This dissertation seeks to address these outstanding questions by applying an innovative combination of low-temperature geochemistry of geothermal systems and high-temperature geochemistry of continental basalts and xenoliths. The following studies are focused in the central Andean Cordillera, where the juxtaposition of the modern Peruvian flat slab and ancient Altiplano-Puna flat slabs (Fig. 1) affords a holistic investigation of flat-slab volatile cycling and continental lithosphere evolution that traverses both space and time. The first two chapters detail insights from a geochemical investigation of Peruvian hot springs in a region of modern flat-slab subduction, with geothermal systems providing a window into active fluid-rock interaction in the crust and mantle and informing of metasomatic and metamorphic processes that are otherwise unobservable from the Earth's surface. I utilize stable isotope, noble gas, and aqueous geochemistry of hot spring gases to characterize deep volatile sources, contextualizing these observations into tectonic and geodynamic frameworks through consideration of geophysical and geologic information. The latter two chapters are geochemical studies of xenoliths and continental volcanism located in the northern Altiplano Plateau, which together provide a means for directly sampling the deep lithosphere and identifying fossil evidence for metasomatism in a region affected by Oligocene shallow subduction. For this my primary tools are stable isotope, major and trace element geochemistry, and in-situ chemical/microtextural observations.

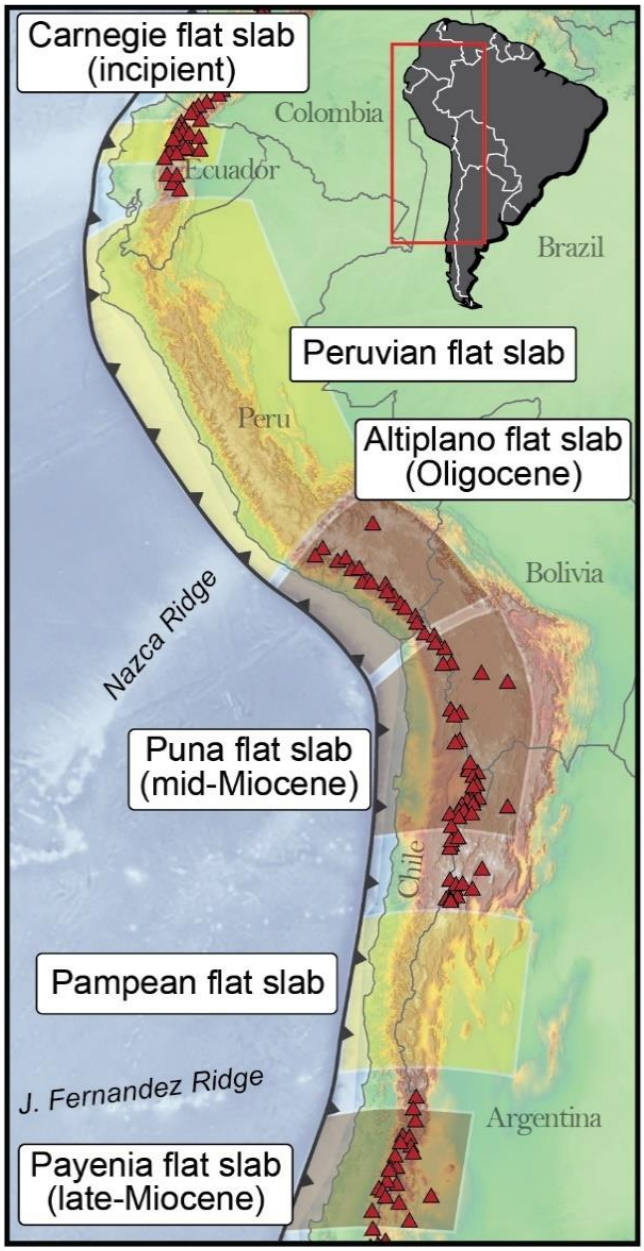

Figure 1. Map of western margin of South America highlighting regions of modern and ancient flat-slab subduction (after Ramos and Folguera, 2009)**.**

THERMAL SPRINGS AS A PROBE FOR DEEP FLUID-LITHOSPHERE INTERACTION

Volatile geochemistry is key to assessing the contributions of crustal and mantle fluids in geothermal systems and can inform on critical processes such as melting, metamorphism, and fluid-rock interaction in the deep lithosphere. Furthermore, deeply sourced volatile fluxes elicit implications regarding permeability and fluid pressures in the deep lithosphere, which can provide valuable insight into earthquake mechanics and the geometry and scale of large fault systems (e.g., Kennedy et al., 1997; Newell et al., 2023). Volatile geochemistry also aids in understanding the sources, concentration, or storage of valuable resources such as hydrocarbons, critical minerals, or captured carbon dioxide (e.g., Ballentine et al., 2001; Gilfillan et al., 2008). In the following chapters, the primary utility of this research is identifying contributions of volatiles from the deep lithosphere, interpreting the tectonic processes driving degassing, and constraining the processes that are modulating volatile production and transit to the surface.

Volatile geochemistry, which encompasses stable isotope ratios of volatile species, noble gas concentrations, and relative gas abundances, together with aqueous geochemistry of geothermal systems, affords scrutiny of both volatile sources and chemical modification processes such as fluid-rock interaction, mineral precipitation, and fluid degassing in spring systems. For example, deviations from the standard gas concentrations of air-saturated water can be used to assess reservoir-scale gas-water equilibration, fluid migration, groundwater recharge conditions, or the addition of crustal and/or mantle volatiles (Ballentine and Burnard, 2002; Ballentine et al., 2002; Graham, 2002). Noble gas isotope ratios are central to these studies as certain isotopes are

continuously produced within the crust by radioactive decay of U and Th (^{4}He), K (^{40}Ar), or by nucleogenic reactions (e.g. ^{21}Ne; Ballentine and Burnard, 2002), while other isotopes are primarily sourced from the mantle (^{3}He, ^{20}Ne). This work relies heavily on helium isotope ratios (^{3}He/^{4}He), which are uniquely suited to identify mantle volatile contributions due to the large difference in isotopic ratios between the upper mantle (8 ± 1 R_A, where R_A is the atmospheric ^{3}He/^{4}He of 1.39×10^{-6}) and crustal reservoirs (~0.02 – 0.1 R_A), and the low concentration of atmospherically-derived helium (1 R_A) in meteoric waters (O'Nions and Oxburgh, 1988). In combination with carbon isotope ratios (δ^{13}C values) of CO_2 and dissolved inorganic carbon (DIC), these analyses also provide information on carbon sources and potential modification processes such as phase separation or mineral precipitation (e.g., Sano and Marty, 1995; Van Soest et al., 1998; Shaw et al., 2003; Ray et al., 2009; Karolytė et al., 2019). These methods leverage the different δ^{13}C values (reported relative to Vienna Pee Dee Belemnite; VPDB) of upper mantle (-6.2 ± 2.5 ‰), organic carbon sources (< -20 ‰) and marine carbonate (~0 ‰) carbon sources (Sano and Marty, 1995) and the distinct $CO_2/^{3}$He ratio of the upper mantle (~2×10^{9} for MORB) compared to the crust (> 10^{12}; O'Nions and Oxburgh, 1988). Similarly, δ^{15}N values (reported relative to atmospheric N_2) provide information on potential nitrogen sources including slab sediments (+7 ± 4 ‰) and the upper mantle (-5 ± 2 ‰; Sano et al., 1998). Additionally, the relative abundances of dissolved gas species (e.g. CO_2, N_2, Ar, He, Ne) are diagnostic of tectonic setting and provide additional information on fluid sources and mixing (Giggenbach et al., 1993).

These techniques have been regularly applied to understand volatile sources, mixing, and modification across volcanic arcs (e.g., Ray et al., 2009), hot-spots (e.g.,

Graham, 2002), regional-scale continental settings (e.g., Newell et al., 2005), and basin-scale natural-gas reservoirs (e.g., Karolytė et al., 2019). In arc systems, such studies are critical to evaluating the recycling efficiency of volatiles carried into subduction systems and partitioned into arc magmas, metasomatized forearc lithosphere, or incorporated into the deep mantle (e.g., Hilton et al., 1993, 2002; Sano and Marty, 1995; Fischer et al., 2015; Barry et al., 2019). These studies often target fumaroles that provide relatively undiluted samples of volcanic gases. Further from active volcanism, or in amagmatic regions, volatiles fluxes can be evaluated through study of deeply circulating geothermal systems, where care must be taken to account for greater dilution with air saturated meteoric water and potential modification through water-rock-gas interactions. Mantle volatile fluxes in geothermal systems far from volcanism were traditionally taken as evidence for blind magmatism or remnant magmatic fluids preserved within the crust (e.g., O'Nions and Oxburgh, 1988). However, research in the last few decades has shown examples of amagmatic mantle volatile fluxes through transform faults (e.g., Kennedy et al., 1997; Klemperer et al., 2013), extensional basins (e.g., Dodson et al., 1998; Kennedy and Van Soest, 2007), and Cordilleran regions (e.g., Newell et al., 2005; Karlstrom et al., 2013). In these settings, mantle gasses consisting primarily of CO_2 escape from the upper mantle and exploit lithospheric structures to transit the continental lithosphere, for example utilizing strike-slip faults with high shear strain rates (Kennedy and Van Soest, 2007). This recognition of amagmatic mantle degassing inspires questions regarding deep mantle processes that mobilize volatiles and the mechanisms that facilitate volatile advection in the presumably impermeable deep lithosphere.

Application of these methods in Peru was motivated by a study of thermal springs along the Cordillera Blanca detachment (CBD) fault that found evidence for mantle-derived fluids transiting the lithosphere above the modern Peruvian flat slab (Newell et al., 2015). Helium isotope ratios indicate up to ~35% mantle helium in thermal springs issuing along the CBD fault, which is an active orogen-perpendicular extensional system. Hypotheses for mantle helium in CBD fault springs included volatiles mobilized from the subcontinental lithospheric mantle (SCLM) by slab-derived fluids or degassing of mobile asthenosphere related to a potential tear in the subducting Nazca Plate (Antonijevic et al., 2015, 2016; Scire et al., 2016; Bishop et al., 2017).

This work leverages the existing dataset of Newell et al. (2015) and dramatically expands its scope, providing insight into the nature of mantle volatiles in thermal springs along the length of the Peruvian Andes and resolving their connection to fluid-lithosphere interaction above the Peruvian flat slab. Geochemical analyses of this thermal spring transect ultimately provide evidence for widespread degassing of mantle and crustal volatiles, including He, CO_2, and N_2. Together with considerations of the current geodynamic framework in Peru, I conclude that mantle degassing is driven by flat slab-to-lithosphere fluid transfer and metasomatism in the lithospheric mantle. Springs in the active backarc to the south of the modern flat slab, in an area previously affected by Oligocene shallow subduction, show that the effects of hydration and metasomatism persist for >25 Ma after the cessation of shallow subduction in the form of dehydration and/or melting that mobilizes mantle volatiles. Regional variations in degassing signatures are linked to tectonism and slab morphology, showing that deformation in both the subducting and overriding lithospheres modulate volatile fluxes. Furthermore,

calculations of CO_2 fluxes from Peruvian springs reveal a considerable and previously unrecognized carbon flux from the region that is equivalent to ~0.2% of the total flux from subaerial volcanism, suggesting that mantle and crustal degassing from flat-slab volcanic gaps is a critical missing piece of global volatile cycling models.

XENOLITHS AND POTASSIC BASALTS AS A WINDOW INTO DEEP LITHOSPHERE METASOMATISM

Potassic basalts make up a small fraction of observed volcanism across the Earth's surface, but their petrogenesis through melting of altered upper mantle lithologies make them valuable resources that can inform on the nature of mantle alteration. Furthermore, these lavas commonly entrain mantle and lower crustal xenoliths which afford direct scrutiny of lithospheric structure and metasomatized lithologies at depth. In intercontinental settings, potassic basalts (*sensu lato*; including, but not limited to, lamproites, lamprophyres, leucitites, tephrites, trachybasalts, and shoshonites) are often located in post-subduction and/or post-collisional settings, and geochemical signatures akin to arc magmas support their derivation from a mantle metasomatized by recycled subducted material. Geochemical analyses of both xenoliths and their volcanic host rocks provide key information on the processes and materials responsible for the metasomatism that precedes basaltic volcanism. Such metasomatism is an important yet poorly constrained biproduct of the subduction factory, which together with materials transferred to the deeper mantle, balance the inputs of subducted lithosphere and the outputs of arc magmatism.

Metasomatism of the continental lithosphere can occur through various mineralogical changes, but generally involves replacement of anhydrous and dense phases with hydrous lower density mineral assemblages. For example, at temperatures < 700 °C, the addition of water to mantle lithologies can convert assemblages of olivine, pyroxene, and magnetite to secondary assemblages of serpentine, talc, brucite, and antigorite (Hyndman and Peacock, 2003; Facer et al., 2009; Smith, 2010). At higher temperatures above the stability field of these minerals (~700 – 1000 °C), silica-rich hydrous fluids or melts can convert olivine to orthopyroxene (McInnes et al., 2001; Facer et al., 2009), and fluids with elevated potassium concentrations can also generate phlogopite (Tatsumi and Eggins, 1995; Mallik et al., 2015). The greater compositional variability of crustal rocks enables a wider variety of metasomatic reactions to occur. For example, mafic granulites composed of garnet, pyroxene, and feldspar may experience alteration and growth of secondary assemblages that include chlorite, micas, zoisite, antigorite, albite, calcite, and monazite (Jones et al., 2015; Butcher et al., 2017). Examples of these metasomatic reactions are observed in mantle and crustal xenoliths in various continental settings including the western U.S. (Selverstone et al., 1999; Facer et al., 2009; Smith, 2010; Jones et al., 2015; Butcher et al., 2017), western and central Europe (Zinngrebe and Foley, 1995; Downes, 2001), or northeastern China (Zhang et al., 2007). Mantle wedge metasomatism is also recorded in mantle xenoliths recovered from arc lavas (McInnes et al., 2001; Ionov, 2010) and exhumed peridotite massifs in the Italian Alps (Zanetti et al., 1999; Sharp et al., 2010; Cannaò et al., 2022). Studies have also highlighted the geophysical signatures of altered mantle and lower crustal domains

and inferred similar mineral assemblages based on their seismic velocity properties (e.g., Wagner et al., 2005, 2008; Porter et al., 2012; Jones et al., 2015).

Evidence for mantle metasomatism is also apparent from the geochemistry of potassic rocks from many of the same regions (e.g., western North America, Kempton et al., 1991; eastern China, Zhang et al., 1995) and elsewhere (e.g., Tibet, Miller et al., 1999; Italy, Peccerillo, 1999). In these cases, evidence for metasomatism comes from major element compositions characteristic of enriched mantle sources (e.g., the potassic bulk compositions of these lavas are generally taken to indicate modal enrichments of phlogopite or potassic amphiboles in their mantle source) and trace element compositions and/or radiogenic isotope ratios indicative of fluid or melt enrichment.

The metasomatism highlighted by these studies can impact the rheology of the lithosphere in a number of ways, including a reduction in the ductile flow strength of silicate minerals (Rutter and Brodie, 1995; Rybacki et al., 2006), mineralogical changes (Williams et al., 2014; Jones et al., 2015), the promotion of partial melting (Humphreys et al., 2003), and advective heat transfer (Yardley, 2009; Berry et al., 2022). Rheological weakening may then play in important role in strain localization and the patterns of deformation along convergent margins (e.g., Lowry and Pérez-Gussinyé, 2011; Horton, 2018) or facilitate delamination of the lower portion of the lithosphere (Levander et al., 2011). Other notable consequences of extensive hydration and metasomatism include widespread explosive (ignimbrite) volcanism (Farmer et al., 2008) and increased lithospheric buoyancy imparted by thermal effects and mineralogical changes (Humphreys et al., 2003; Jones et al., 2015; Berry et al., 2022). In the western U.S., subduction-derived fluid transfer has been widely recognized as an important factor in

regional lithospheric evolution. In the central Andes, compositional and thermal changes that likely accompanied shallow subduction have not been thoroughly investigated as a source of buoyancy or rheological weakening, which may help to explain the debated history of Cenozoic deformation and surface uplift (e.g., Garzione et al., 2017; Saylor et al., 2023).

In the northern Altiplano Plateau, geochemical characteristics of Cenozoic alkaline magmatism demonstrate the presence of metasomatized mantle underlying the region (Sandeman et al., 1995; Carlier et al., 2005), yet the nature of metasomatism and its influence on the tectonomagmatic history of the margin is unresolved. Research in this dissertation details geochemical analyses of xenoliths collected from the Quaternary Rumicolca Formation in southern Peru, which comprises a series of small monogenetic lava flows or domal structures along the Cusco Vilconata fault system (CVFS). Rumicolca Formation lavas fall into two compositional groups. One group includes seven occurrences of lamproite, lamprophyre and shoshonite lavas described by Carlier et al. (2005) and Carlier & Lorand (2008, 1997). A second group constituting a larger proportion of Rumicolca Formation lavas (>30 flows) exhibit intermediate silica contents and are marginal between alkaline (latites) and calc-alkaline compositions (andesites and dacites). The petrogenesis of these lavas has received less attention due to their apparently more evolved chemistry. Interestingly though, it is this group that includes lavas with abundant lower crustal and mantle xenoliths.

Two suites of xenoliths collected from Rumicolca lavas are investigated to constrain the history of mantle metasomatism in this region. One suite comprises phlogopite and clinopyroxene-rich, coarse-grained, mafic igneous lithologies best

described as phaneritic kersantites, which display major and trace element compositions and hydrogen isotope ratios that indicate subduction-derived metasomatism in their lithospheric mantle melt source. A second group of phlogopite- and calcite-bearing ultramafic xenoliths serve as samples of metasomatized lithospheric mantle underlying the Altiplano region which, in agreement with the first suite, show evidence of enrichment by hydrous melts with a subducted sediment affinity. Combining these results with geochemical analyses of Rumicolca Formation lavas, I propose a provocative model coupling compositional variability in Rumicolca lavas to the metasomatism observed in the ultramafic xenoliths. In this model, intermediate lavas formed by melting of subducted sediments/mélange accreted to the base of the Andean lithosphere during shallow subduction and potassic basalts result from metasomatic reactions between silicic melts and mantle peridotite, leaving a residual assemblage of phlogopite- and orthopyroxene- enriched peridotite. This research provides an unprecedented window into deep mantle metasomatism in the lithospheric root of the northern Altiplano Plateau, offering novel insight into its geodynamic evolution.

DISSERTATION STRUCTURE AND PUBLICATION

This dissertation comprises four chapters. Chapters 2 and 3 report observations and interpretations from the geochemical survey of thermal springs throughout the Peruvian Andes. Chapter 2 was published in *Earth and Planetary Science Letters* in 2021 and focuses on helium isotope and noble gas systematics across the spring transect and discusses evidence for fluid transfer and continental hydration in a modern flat-slab subduction system. Chapter 3 leverages the key findings from the preceding chapter and

expands the investigation into more abundant volatiles (CO_2, N_2) associated with slab-to-lithosphere fluid transfer and the resulting mantle/crustal degassing. This chapter was published in a 2022 volume of *Chemical Geology*.

The ensuing two chapters report results from geochemical analyses of xenoliths and alkaline volcanic rocks collected from southern Peru. Chapter 4 details an investigation of kersantite xenoliths, focusing on hydrogen isotope analyses of phlogopite and bulk-rock trace element analyses that evidence derivation from a metasomatized mantle source enriched by fluids or melts during Oligocene shallow subduction. This chapter is in preparation for submission to the journal *Geochemistry, Geophysics, and Geosystems*. Chapter 5 reports geochemical analyses and interpretations based on a suite of metasomatized ultramafic xenoliths that display evidence for metasomatism by volatile-rich melts of subducted sedimentary material. This chapter also includes petrologic analyses of Rumicolca Formation lavas which are ultimately used to develop a new model linking accretion of subducted sediments during shallow subduction to subsequent magmatism and mantle metasomatism in this region. This chapter is in preparation for submission to the Journal *AGU Advances*. In all four chapters, I played a primary role in conducting the research and manuscript preparation.

REFERENCES

Antonijevic, S., Wagner, L.S., Beck, S.L., Long, M.D., Zandt, G., and Tavera, H., 2016, Effects of change in slab geometry on the mantle flow and slab fabric in Southern Peru: Journal of Geophysical Research: Solid Earth, v. 121, p. 7252–7270, doi:10.1002/2016JB013064.

Antonijevic, S.K., Wagner, L.S., Kumar, A., Beck, S.L., Long, M.D., Zandt, G., Tavera, H., and Condori, C., 2015, The role of ridges in the formation and longevity of flat slabs: Nature, v. 524, p. 212–215, doi:10.1038/nature14648.

Ballentine, C.J., Burgess, R., and Marty, B., 2002, Tracing fluid origin, transport and interaction in the crust: Reviews in Mineralogy and Geochemistry, v. 47, doi:10.2138/rmg.2002.47.13.

Ballentine, C.J., and Burnard, P.G., 2002, Production, Release and Transport of Noble Gases in the Continental Crust: Reviews in Mineralogy and Geochemistry, v. 47, p. 481–538, doi:10.2138/rmg.2002.47.12.

Ballentine, C.J., Schoell, M., Coleman, D., and Cain, B.A., 2001, 300-Myr-old magmatic CO2 in natural gas reservoirs of the west Texas Permian basin: Nature, v. 409, p. 327–331, doi:10.1038/35053046.

Barry, P.H. et al., 2019, Forearc carbon sink reduces long-term volatile recycling into the mantle: Nature, v. 568, p. 487–492, doi:10.1038/s41586-019-1131-5.

Behn, M.D., Kelemen, P.B., Hirth, G., Hacker, B.R., and Massonne, H.J., 2011, Diapirs as the source of the sediment signature in arc lavas: Nature Geoscience 2011 4:9, v. 4, p. 641–646, doi:10.1038/ngeo1214.

Berry, M.A., Lowry, A.R., Ma, X., Kanda, R.V.S., and Schutt, D.L., 2022, Wet roots of high elevation in the western United States: Earth and Planetary Science Letters, v. 584, doi:10.1016/j.epsl.2022.117483.

Bishop, B.T., Beck, S.L., Zandt, G., Wagner, L., Long, M., Antonijevic, S.K., Kumar, A., and Tavera, H., 2017, Causes and consequences of flat-slab subduction in southern Peru: Geosphere, v. 13, p. 1392–1407, doi:10.1130/GES01440.1.

Butcher, L.A., Mahan, K.H., and Allaz, J.M., 2017a, Late Cretaceous crustal hydration in the Colorado Plateau , USA , from xenolith petrology and monazite geochronology: Lithosphere, p. 561–578, doi:10.1130/L583.1.

Butcher, L.A., Mahan, K.H., and Allaz, J.M., 2017b, Late Cretaceous crustal hydration in the Colorado Plateau, USA, from xenolith petrology and monazite geochronology: Lithosphere, v. 9, doi:10.1130/L583.1.

Cannaò, E., Tiepolo, M., Fumagalli, P., Grieco, G., and Agostini, S., 2022, Metasomatism in the Finero Phlogopite Peridotite: New insights from C and N concentrations and δ13C - δ11B signatures: Chemical Geology, v. 614, p. 121181, doi:10.1016/J.CHEMGEO.2022.121181.

Carlier, G., and Lorand, J.-P., 1997, First occurrence of diopside sanidine phlogopite lamproite in the Andean Cordillera: the Huacancha and Morojarja dikes, southern Peru: Canadian Journal of Earth Sciences, v. 34, p. 1118–1127, doi:10.1139/e17-090.

Carlier, G., and Lorand, J.P., 2008, Zr-rich accessory minerals (titanite, perrierite, zirconolite, baddeleyite) record strong oxidation associated with magma mixing in the south Peruvian potassic province: Lithos, v. 104, p. 54–70, doi:10.1016/j.lithos.2007.11.008.

Carlier, G., Lorand, J.P., Liégeois, J.P., Fornari, M., Soler, P., Carlotto, V., and Cárdenas, J., 2005, Potassic-ultrapotassic mafic rocks delineate two lithospheric mantle blocks beneath the southern Peruvian Altiplano: Geology, v. 33, p. 601–604, doi:10.1130/G21643.1.

Codillo, E.A., Le Roux, V., and Marschall, H.R., 2018, Arc-like magmas generated by mélange-peridotite interaction in the mantle wedge: Nature Communications 2018 9:1, v. 9, p. 1–11, doi:10.1038/s41467-018-05313-2.

Currie, C.A., and Beaumont, C., 2011, Are diamond-bearing Cretaceous kimberlites related to low-angle subduction beneath western North America? Earth and Planetary Science Letters, v. 303, p. 59–70, doi:10.1016/j.epsl.2010.12.036.

Currie, C.A., Beaumont, C., and Huismans, R.S., 2007, The fate of subducted sediments: A case for backarc intrusion and underplating: Geology, v. 35, doi:10.1130/G24098A.1.

Dodson, A., DePaolo, D.J., and Kennedy, B.M., 1998, Helium isotopes in lithospheric mantle: Evidence from Tertiary basalts of the western USA: Geochimica et Cosmochimica Acta, v. 62, p. 3775–3787, doi:10.1016/S0016-7037(98)00267-1.

Dougherty, S.L., and Clayton, R.W., 2015, Seismic structure in southern Peru: Evidence for a smooth contortion between flat and normal subduction of the Nazca Plate: Geophysical Journal International, v. 200, p. 534–555, doi:10.1093/gji/ggu415.

Downes, H., 2001, Formation and modification of the shallow sub-continental lithospheric mantle: A review of geochemical evidence from ultramatic xenolith suites and tectonically emplaced ultramafic massifs of Western and Central Europe: Journal of Petrology, v. 42, doi:10.1093/petrology/42.1.233.

Facer, J., Downes, H., and Beard, A., 2009, In situ serpentinization and hydrous fluid metasomatism in spinel dunite xenoliths from the Bearpaw Mountains, Montana, USA: Journal of Petrology, v. 50, p. 1443–1475, doi:10.1093/petrology/egp037.

Farmer, G.L., Bailley, T., and Elkins-Tanton, L.T., 2008, Mantle source volumes and the origin of the mid-Tertiary ignimbrite flare-up in the southern Rocky Mountains, western U.S.: Lithos, v. 102, p. 279–294, doi:10.1016/j.lithos.2007.08.014.

Farmer, G.L., Fritz, D.E., and Glazner, A.F., 2020, Identifying Metasomatized Continental Lithospheric Mantle Involvement in Cenozoic Magmatism From Ta/Th Values, Southwestern North America: Geochemistry, Geophysics, Geosystems, v. 21, doi:10.1029/2019gc008499.

Fischer, T.P. et al., 2015, Temporal variations in fumarole gas chemistry at Poás volcano, Costa Rica: Journal of Volcanology and Geothermal Research, v. 294, p. 56–70, doi:10.1016/j.jvolgeores.2015.02.002.

Garzione, C.N. et al., 2017, Tectonic Evolution of the Central Andean Plateau and Implications for the Growth of Plateaus: Annual Review of Earth and Planetary Sciences, v. 45, p. 529–559, doi:10.1146/annurev-earth-063016-020612.

Giggenbach, W.F., Sano, Y., and Wakita, H., 1993, Isotopic composition of helium, and CO2 and CH4 contents in gases produced along the New Zealand part of a convergent plate boundary: Geochimica et Cosmochimica Acta, v. 57, p. 3427–3455, doi:10.1016/0016-7037(93)90549-C.

Gilfillan, S.M.V., Ballentine, C.J., Holland, G., Blagburn, D., Lollar, B.S., Stevens, S., Schoell, M., and Cassidy, M., 2008, The noble gas geochemistry of natural CO2 gas reservoirs from the Colorado Plateau and Rocky Mountain provinces, USA: Geochimica et Cosmochimica Acta, v. 72, p. 1174–1198, doi:10.1016/j.gca.2007.10.009.

Graham, D.W., 2002, Noble Gas Isotope Geochemistry of Mid-Ocean Ridge and Ocean Island Basalts: Characterization of Mantle Source Reservoirs: Reviews in Mineralogy and Geochemistry, v. 47, p. 247–317, doi:10.2138/rmg.2002.47.8.

Gutscher, M.A., Spakman, W., Bijwaard, H., and Engdahl, E.R., 2000, Geodynamics of flat subduction: Seismicity and tomographic constraints from the Andean margin: Tectonics, v. 19, p. 814–833, doi:10.1029/1999TC001152.

Hilton, D.R., Fischer, T.P., and Marry, B., 2002, Noble gases and volatile recycling at subduction zones: Reviews in Mineralogy and Geochemistry, v. 47, p. 319–370, doi:10.2138/rmg.2002.47.9.

Hilton, D.R., Hammerschmidt, K., Teufel, S., and Friedrichsen, H., 1993, Helium isotope characteristics of Andean geothermal fluids and lavas: Earth and Planetary Science Letters, v. 120, p. 265–282, doi:10.1016/0012-821X(93)90244-4.

Hoke, L., and Lamb, S., 2007, Cenozoic behind-arc volcanism in the Bolivian Andes, South America: implications for mantle melt generation and lithospheric structure: Journal of the Geological Society, v. 164, p. 795–814, doi:10.1144/0016-76492006-092.

Horton, B.K., 2018, Tectonic Regimes of the Central and Southern Andes: Responses to Variations in Plate Coupling During Subduction: Tectonics, v. 37, doi:10.1002/2017TC004624.

Humphreys, E., Hessler, E., Dueker, K., Farmer, G.L., Erslev, E., and Atwater, T., 2003, How Laramide-Age Hydration of North American Lithosphere by the Farallon Slab Controlled Subsequent Activity in the Western United States: International Geology Review, v. 45, p. 575–595, doi:10.2747/0020-6814.45.7.575.

Hyndman, R.D., and Peacock, S.M., 2003, Serpentinization of the forearc mantle: Earth and Planetary Science Letters, v. 212, p. 417–432, doi:10.1016/S0012-821X(03)00263-2.

Ionov, D.A., 2010, Petrology of mantle wedge lithosphere: New data on supra-subduction zone peridotite xenoliths from the andesitic Avacha volcano, Kamchatka: Journal of Petrology, v. 51, doi:10.1093/petrology/egp090.

Jones, C.H., Mahan, K.H., Butcher, L.A., Levandowski, W.B., and Farmer, G.L., 2015, Continental uplift through crustal hydration: Geology, v. 43, p. 355–358, doi:10.1130/G36509.1.

Karlstrom, K.E., Crossey, L.J., Hilton, D.R., and Barry, P.H., 2013, Mantle 3He and CO2 degassing in carbonic and geothermal springs of Colorado and implications for neotectonics of the Rocky Mountains: Geology, v. 41, doi:10.1130/G34007.1.

Karolytė, R., Johnson, G., Györe, D., Serno, S., Flude, S., Stuart, F.M., Chivas, A.R., Boyce, A., and Gilfillan, S.M.V., 2019, Tracing the migration of mantle CO2 in gas fields and mineral

water springs in south-east Australia using noble gas and stable isotopes: Geochimica et Cosmochimica Acta, v. 259, p. 109–128, doi:10.1016/j.gca.2019.06.002.

Kay, R.W., and Kay, M.S., 1993, Delamination and delamination magmatism: Tectonophysics, v. 219, p. 177–189, doi:10.1016/0040-1951(93)90295-U.

Kempton, P.D., Fitton, J.G., Hawkesworth, C.J., and Ormerod, D.S., 1991, Isotopic and trace element constraints on the composition and evolution of the lithosphere beneath the southwestern United States: Journal of Geophysical Research, v. 96, doi:10.1029/91jb00373.

Kennedy, B.M., Kharaka, Y.K., Evans, W.C., Ellwood, A., DePaolo, D.J., Thordsen, J., Ambats, G., and Mariner, R.H., 1997, Mantle fluids in the San Andreas fault system, California: Science, v. 278, p. 1278–1281, doi:10.1126/science.278.5341.1278.

Kennedy, B.M., and Van Soest, M.C., 2007, Flow of mantle fluids through the ductile lower crust: Helium isotope trends: Science, v. 318, p. 1433–1436, doi:10.1126/science.1147537.

Klemperer, S.L., Kennedy, B.M., Sastry, S.R., Makovsky, Y., Harinarayana, T., and Leech, M.L., 2013, Mantle fluids in the Karakoram fault: Helium isotope evidence: Earth and Planetary Science Letters, v. 366, p. 59–70, doi:10.1016/j.epsl.2013.01.013.

Levander, A., Schmandt, B., Miller, M.S., Liu, K., Karlstrom, K.E., Crow, R.S., Lee, C.T.A., and Humphreys, E.D., 2011, Continuing Colorado plateau uplift by delamination-style convective lithospheric downwelling: Nature, v. 472, p. 461–465, doi:10.1038/nature10001.

Lowry, A.R., and Pérez-Gussinyé, M., 2011a, The role of crustal quartz in controlling Cordilleran deformation: Nature, v. 471, p. 353–359, doi:10.1038/nature09912.

Mallik, A., Nelson, J., and Dasgupta, R., 2015, Partial melting of fertile peridotite fluxed by hydrous rhyolitic melt at 2–3 GPa: implications for mantle wedge hybridization by sediment melt and generation of ultrapotassic magmas in convergent margins: Contributions to Mineralogy and Petrology, v. 169, doi:10.1007/s00410-015-1139-2.

Marshall, E.W., Barnes, J.D., and Lassiter, J.C., 2017, The role of serpentinite-derived fluids in metasomatism of the Colorado Plateau (USA) lithospheric mantle: Geology, v. 45, p. 1103–1106, doi:10.1130/G39444.1.

McInnes, B.I.A., Gregoire, M., Binns, R.A., Herzig, P.M., and Hannington, M.D., 2001, Hydrous metasomatism of oceanic sub-arc mantle, Lihir, Papua New Guinea: Petrology and geochemistry of fluid-metasomatised mantle wedge xenoliths: Earth and Planetary Science Letters, v. 188, doi:10.1016/S0012-821X(01)00306-5.

Miller, C., Schuster, R., Klötzli, U., Frank, W., and Purtscheller, F., 1999, Post-collisional potassic and ultrapotassic magmatism in SW Tibet: Geochemical and Sr-Nd-Pb-O isotopic constraints for mantle source characteristics and petrogenesis: Journal of Petrology, v. 40, p. 1399–1424, doi:10.1093/PETROJ/40.9.1399.

Newell, D.L., Crossey, L.J., Karlstrom, K.E., Fischer, T.P., and Hilton, D.R., 2005, Continental-scale links between the mantle and groundwater systems of the western United States:

Evidence from travertine springs and regional He isotope data: GSA Today, v. 15, p. 4–10, doi:10.1130/1052-5173(2005)015[4:CSLBTM]2.0.CO;2.

Newell, D.L., Jessup, M.J., Hilton, D.R., Shaw, C.A., and Hughes, C.A., 2015, Mantle-derived helium in hot springs of the Cordillera Blanca , Peru : Implications for mantle-to-crust fl uid transfer in a fl at-slab subduction setting: Chemical Geology, v. 417, p. 200–209, doi:10.1016/j.chemgeo.2015.10.003.

Newell, D.L., Benowitz, J.A., Regan, S.P., and Hiett, C.D., 2023, Roadblocks and speed limits: Mantle-to-surface volatile flux through the lithospheric-scale Denali fault, Alaska: Geology, v. 51, p. 576–580, doi:10.1130/G51068.1.

O'Nions, R.K., and Oxburgh, E.R., 1988, Helium, volatile fluxes and the development of continental crust: Earth and Planetary Science Letters, v. 90, p. 331–347, doi:10.1016/0012-821X(88)90134-3.

Peccerillo, A., 1999, Multiple mantle metasomatism in central-southern Italy: Geochemical effects, timing and geodynamic implications: Geology, v. 27, doi:10.1130/0091-7613(1999)027<0315:MMMICS>2.3.CO;2.

Porter, R., Gilbert, H., Zandt, G., Beck, S., Warren, L., Calkins, J., Alvarado, P., and Anderson, M., 2012, Shear wave velocities in the Pampean flat-slab region from Rayleigh wave tomography: Implications for slab and upper mantle hydration: Journal of Geophysical Research B: Solid Earth, v. 117, p. 1–21, doi:10.1029/2012JB009350.

Ramos, V.A., and Folguera, A., 2009, Andean flat-slab subduction through time: Geological Society, London, Special Publications, v. 327, p. 31–54, doi:10.1144/SP327.3.

Ray, M.C., Hilton, D.R., Muñoz, J., Fischer, T.P., and Shaw, A.M., 2009, The effects of volatile recycling , degassing and crustal contamination on the helium and carbon geochemistry of hydrothermal fl uids from the Southern Volcanic Zone of Chile: Chemical Geology, v. 266, p. 38–49, doi:10.1016/j.chemgeo.2008.12.026.

Rutter, E.H., and Brodie, K.H., 1995, Mechanistic interactions between deformation and metamorphism: Geological Journal, v. 30, p. 227–240, doi:10.1002/gj.3350300304.

Rybacki, E., Gottschalk, M., Wirth, R., and Dresen, G., 2006, Influence of water fugacity and activation volume on the flow properties of fine-grained anorthite aggregates: Journal of Geophysical Research: Solid Earth, v. 111, doi:10.1029/2005JB003663.

Sandeman, H.A., Clark, A.H., and Farrar, E., 1995, An Integrated Tectono-Magmatic Model for the Evolution of the Southern Peruvian Andes (13–20°S) since 55 Ma: International Geology Review, v. 37, p. 1039–1073, doi:10.1080/00206819509465439.

Sano, Y., and Marty, B., 1995, Origin of carbon in fumarolic gas from island arcs: Chemical Geology, v. 199, p. 265–274.

Sano, Y., Takahata, N., Nishio, Y., and Marty, B., 1998, Nitrogen recycling in subduction zones: Geophysical Research Letters, v. 25, p. 2289–2292, doi:10.1029/98GL01687.

Saylor, J. E., Sundell, K. E., Perez, N. D., Hensley, J. B., McCain, P., Runyon, B., Alvarez, P., Cárdenas, J., Usnayo, W. P., & Valer, C. S., 2023, Basin formation, magmatism, and exhumation document southward migrating flat-slab subduction in the central Andes: Earth and Planetary Science Letters, v, 606, p. 118050, https://doi.org/10.1016/J.EPSL.2023.118050

Scire, A., Zandt, G., Beck, S., Long, M., Wagner, L., Minaya, E., and Tavera, H., 2016, Imaging the transition from flat to normal subduction: Variations in the structure of the Nazca slab and upper mantle under southern Peru and northwestern Bolivia: Geophysical Journal International, v. 204, p. 457–479, doi:10.1093/gji/ggv452.

Selverstone, J., Aurora, P., and Condie, K.C., 1999, Xenolithic evidence for Proterozoic crustal evolution beneath the Colorado Plateau: Bulletin of the Geological Society of America, v. 111, p. 590–606, doi:10.1130/0016-7606(1999)111<0590:XEFPCE>2.3.CO;2.

Sharp, Z., Selverstone, J., Halick, M., and Barnes, J., 2010, A Chlorine and Hydrogen Isotope Study of Metasomatized Peridotites from the Finero Body, Ivrea Zone, Italy: Geophysical Research Abstracts, v. 12, p. 2010–12683.

Shaw, A.M., Hilton, D.R., Fischer, T.P., Walker, J.A., and Alvarado, G.E., 2003, Contrasting He-C relationships in Nicaragua and Costa Rica: Insights into C cycling through subduction zones: Earth and Planetary Science Letters, v. 214, p. 499–513, doi:10.1016/S0012-821X(03)00401-1.

Smith, D., 2010, Antigorite peridotite, metaserpentinite, and other inclusions within diatremes on the Colorado plateau, SW USA: Implications for the mantle wedge during low-angle subduction: Journal of Petrology, v. 51, doi:10.1093/petrology/egq022.

Van Soest, M.C., Hilton, D.R., and Kreulen, R., 1998, Tracing crustal and slab contributions to arc magmatism in the Lesser Antilles island arc using helium and carbon relationships in geothermal fluids: Geochimica et Cosmochimica Acta, v. 62, p. 3323–3335, doi:10.1016/S0016-7037(98)00241-5.

Tatsumi, Y., and Eggins, S., 1995, Subduction zone magmatism: Subduction zone magmatism,.

Wagner, L.S., Anderson, M.L., Jackson, J.M., Beck, S.L., and Zandt, G., 2008, Seismic evidence for orthopyroxene enrichment in the continental lithosphere: Geology, v. 36, doi:10.1130/G25108A.1.

Wagner, L.S., Beck, S., and Zandt, G., 2005, Upper mantle structure in the south central Chilean subduction zone (30° to 36°S): Journal of Geophysical Research: Solid Earth, v. 110, p. 1–20, doi:10.1029/2004JB003238.

Williams, M.L., Dumond, G., Mahan, K., Regan, S., and Holland, M., 2014, Garnet-forming reactions in felsic orthogneiss: Implications for densification and strengthening of the lower continental crust: Earth and Planetary Science Letters, v. 405, p. 207–219, doi:10.1016/j.epsl.2014.08.030.

Yardley, B.W.D., 2009, The role of water in the evolution of the continental crust: Journal of the Geological Society, v. 166, doi:10.1144/0016-76492008-101.

Zanetti, A., Mazzucchelli, M., Rivalenti, G., Vannucci, R., Zanetti, A., Vannucci, R., Mazzucchelli, M., and Rivalenti, G., 1999, The Finero phlogopite-peridotite massif: an example of subduction-related metasomatism: Contrib Mineral Petrol, v. 134.

Zhang, M., Hu, P., Niu, Y., and Su, S., 2007, Chemical and stable isotopic constraints on the nature and origin of volatiles in the sub-continental lithospheric mantle beneath eastern China: Lithos, v. 96, p. 55–66, doi:10.1016/j.lithos.2006.10.006.

Zhang, M., Suddaby, P., Thompson, R.N., Thirlwall, M.F., and Menzies, M.A., 1995, Potassic Volcanic Rocks in NE China: Geochemical Constraints on Mantle Source and Magma Genesis: Journal of Petrology, v. 36, p. 1275–1303, doi:10.1093/PETROLOGY/36.5.1275.

Zinngrebe, E., and Foley, S.F., 1995, Metasomatism in mantle xenoliths from Gees, West Eifel, Germany: Evidence for the genesis of calc-alkaline glasses and metasomatic Ca-enrichment: Contributions to Mineralogy and Petrology, v. 122, doi:10.1007/s004100050114.

CHAPTER 2

^{3}HE EVIDENCE FOR FLUID TRANSFER AND CONTINENTAL HYDRATION ABOVE A FLAT SLAB[1]

ABSTRACT

The transfer of large volumes of fluid to the overriding lithosphere during flat-slab subduction should drastically alter the physical and chemical properties of continental margins. However, this process is poorly understood and without active magmatism, direct evidence for fluid transfer has remained elusive in modern systems. New helium isotope ratios (^{3}He/^{4}He) and gas species abundances in thermal springs above the Peruvian flat slab in South America demonstrate widespread transit of mantle-derived volatiles through thick (>45 km) continental crust. An unambiguous mantle signature is present in all 52 springs investigated over a 200,000 km^2 region, with ^{3}He/^{4}He ratios ranging from 0.26 to 2.40 R_C/R_A (^{3}He/^{4}He ratio relative to the air ratio, R_A, of 1.39×10^{-6}, corrected for air-derived helium). In the absence of recent magmatism, the observed ^{3}He/^{4}He ratios are best explained by slab-derived fluids mobilizing helium from the subcontinental lithospheric mantle (SCLM). As slab- and mantle-derived volatiles migrate through the continental crust, ^{3}He/^{4}He ratios are reduced from SCLM values (6.1 ± 2.1 R_A) by ingrowth of radiogenic ^{4}He and mixing with crustal fluids. The highest ^{3}He/^{4}He ratios in the flat slab region are observed above a probable tear in the

[1] Paper published in *Earth and Planetary Science Letters* (February 2021) with author list:
C.D. Hiett[a], D.L. Newell[a], M.J. Jessup[b]
[a]Utah State University, [b]University of Tennessee

Nazca Plate and along the Cordillera Blanca Detachment fault, implying that these features promote faster fluid transport through the crust. Our observations require a persistent flux of slab-derived fluids to move lithospheric-mantle-derived volatiles into and through the continental crust, providing evidence for active continental hydration in a modern flat-slab subduction system. Similar results from springs located in the backarc region to the south of the flat slab indicate that the mantle lithosphere below the northern Altiplano is experiencing dehydration and/or partial melting resulting from a mid-Cenozoic episode of flat-slab subduction.

1. INTRODUCTION

Fluids released during the subduction of oceanic lithosphere lead to hydration and metasomatism in the overlying mantle wedge (e.g. Hyndman and Peacock, 2003), but the inboard extent of major alteration is typically not expected to extend beyond the active volcanic arc. Along the Mariana forearc, for example, seamounts extrude serpentinized mantle wedge material with isotopic and elemental enrichments characteristic of slab-derived fluids (e.g. Savov et al., 2007). For most subduction geometries, fluid transfer and alteration continue down-dip along the subduction interface until elevated temperatures lead to partial melting of the mantle, resulting in arc volcanism. Slab- and mantle-derived fluids are partitioned into the melt and carried back towards the surface, where they manifest as volcanic gases emitted from fumaroles, hot springs, or volcanic eruptions. Along ~10 % of the global subduction system, however, the subduction angle is shallow enough to eliminate asthenosphere above the dehydrating slab and depress temperatures such that arc volcanism is inhibited (Gutscher et al., 2000). Here slab fluids

are carried further from the trench, effectively enlarging the area over which fluids can infiltrate and alter the overriding lithosphere.

In regions with histories of ancient flat-slab subduction, such as the western U.S. cordillera and Altiplano-Puna Plateau in South America, extensive continental hydration is invoked in explanations for reduced lithospheric strength, mantle delamination, volcanic (ignimbrite) flare-ups, and increased lithospheric buoyancy (e.g. James and Sacks, 1999; Humphreys et al., 2003; Levander et al., 2011; Jones et al., 2015). Theoretical models for fluid transfer and continental hydration are compelling, yet evidence for this process is limited to xenolith and volcanic rock studies (e.g. Lee, 2005; Jones et al., 2015; Farmer et al., 2020) and geophysical surveys (e.g. Humphreys et al., 2003; Porter et al., 2012). Direct observation of present-day flat-slab fluid transfer to the lithosphere has remained elusive, with open questions regarding mechanisms for fluid transport at depth, volatile cycling in these settings, and interactions with the continental lithosphere.

Gas species isotopes and abundances are commonly analyzed to constrain volatile sources and mixing processes in regions with active magmatism, providing a means to detect the migration of slab- and mantle-derived volatiles through the crust. Helium isotope ratios ($^3He/^4He$) are diagnostic for tracing mantle volatile contributions due to the large difference in isotopic ratios between the upper mantle as sampled by mid-ocean ridge basalts (MORB; 8 ± 1 R_A, where R_A is the $^3He/^4He$ of air, 1.39×10^{-6}) and crustal reservoirs (~0.02 – 0.1 R_A), and the low concentration of atmospherically-derived helium (1 R_A) in meteoric waters (O'Nions and Oxburgh, 1988). Helium isotope ratios are coupled with CO_2 abundances to trace carbon provenance because the upper mantle has a

distinct $CO_2/^3He$ ratio (~2×10^9 for MORB; Marty and Jambon, 1987) compared to the crust (> 10^{12}; O'Nions and Oxburgh, 1988). The relative abundances of dissolved gas species (e.g. CO_2, N_2, Ar, He, Ne) are diagnostic of tectonic setting and provide additional information on fluid sources and mixing (Giggenbach et al., 1993).

Researchers commonly use these methods to understand volatile cycling along active volcanic arcs by sampling gases from fumaroles, fluid and melt inclusions, and thermal springs. For example, measured $^3He/^4He$ ratios along active segments of the Andean arc commonly fall between 1 and 7 R_C/R_A (R_A value corrected for air-derived helium; e.g. Hilton et al., 1993; Ray et al., 2009), with higher values reflecting rapid magmatic ascent through the crust (e.g. 8.84 R_C/R_A at Galeras volcano; Sano et al., 1997) and lower values due to greater contamination of crustal radiogenic ^4He. Due to the inherent lack of volcanism, similar studies above flat slabs have been notably absent. Prior to this study, a single thermal spring has been analyzed for $^3He/^4He$ from above the Pampean flat slab in central Chile, yielding an enigmatic value of 1.45 R_C/R_A that was interpreted to reflect remnant magmatic helium or melting in an extremely thin mantle wedge (Hilton et al., 1993).

Here we present helium isotope ratios and gas species abundances in thermal springs along the 1,500 km long volcanic gap above the Peruvian flat slab. Seven hot springs included in this study where initially presented in Newell et al. (2015). These springs emanate from the Cordillera Blanca Detachment (CBD) fault, an active extensional system in central Peruvian Andes, and yield $^3He/^4He$ ratios as high as 1.95 R_C/R_A, which were interpreted to reflect mantle helium being mobilized from the SCLM by slab-derived fluids. However, it was unclear whether this mantle-volatile signature

extended away from the CBD fault or if mantle volatiles were related to a potential slab tear to the south of the Cordillera Blanca that was imaged with geophysical methods (Antonijevic et al., 2015). In order to constrain the nature of mantle volatiles in Peruvian springs, we expand this initial dataset to include 52 thermal springs that cover the flat-slab region from the Cordillera Blanca into the backarc behind the modern volcanic front in southern Peru (Fig. 1). $^{3}He/^{4}He$ ratios, $CO_2/^{3}He$ ratios, and gas abundances provide information on the sources of spring gases and chemical modification in the geothermal systems. Our dataset covers a broad area of the Peruvian margin, allowing us to assess any influence that slab morphology or crustal structures may exert on the sources and transport of deeply sourced volatiles.

2. GEOLOGICAL SETTING

Between 3° and 15° S, the Nazca Plate descends at approximately 30° to ~100 km depth where it shallows to nearly horizontal until ~600 km inboard from the trench (Fig. 1; Scire et al., 2016; Bishop et al., 2017). Arc volcanism has been absent north of 13° S since ca. 4 Ma following the subduction of the Nazca Ridge at ca. 12 Ma (Rosenbaum et al., 2005). Asthenospheric mantle is evidently absent above the flat slab, with separation between the oceanic Moho and continental Moho ranging from <20 km above the Nazca Ridge to <45 km further north (Bishop et al., 2017). One exception may be at a potential tear in the Nazca Plate described along the northern edge of the Nazca Ridge (Fig. 1; Antonijevic et al., 2015, 2016; Scire et al., 2016; Bishop et al., 2017), with geophysical evidence for asthenosphere locally flowing through the tear (Antonijevic et al., 2016). Despite regional tectonic shortening since the Eocene, active, arc-perpendicular extension

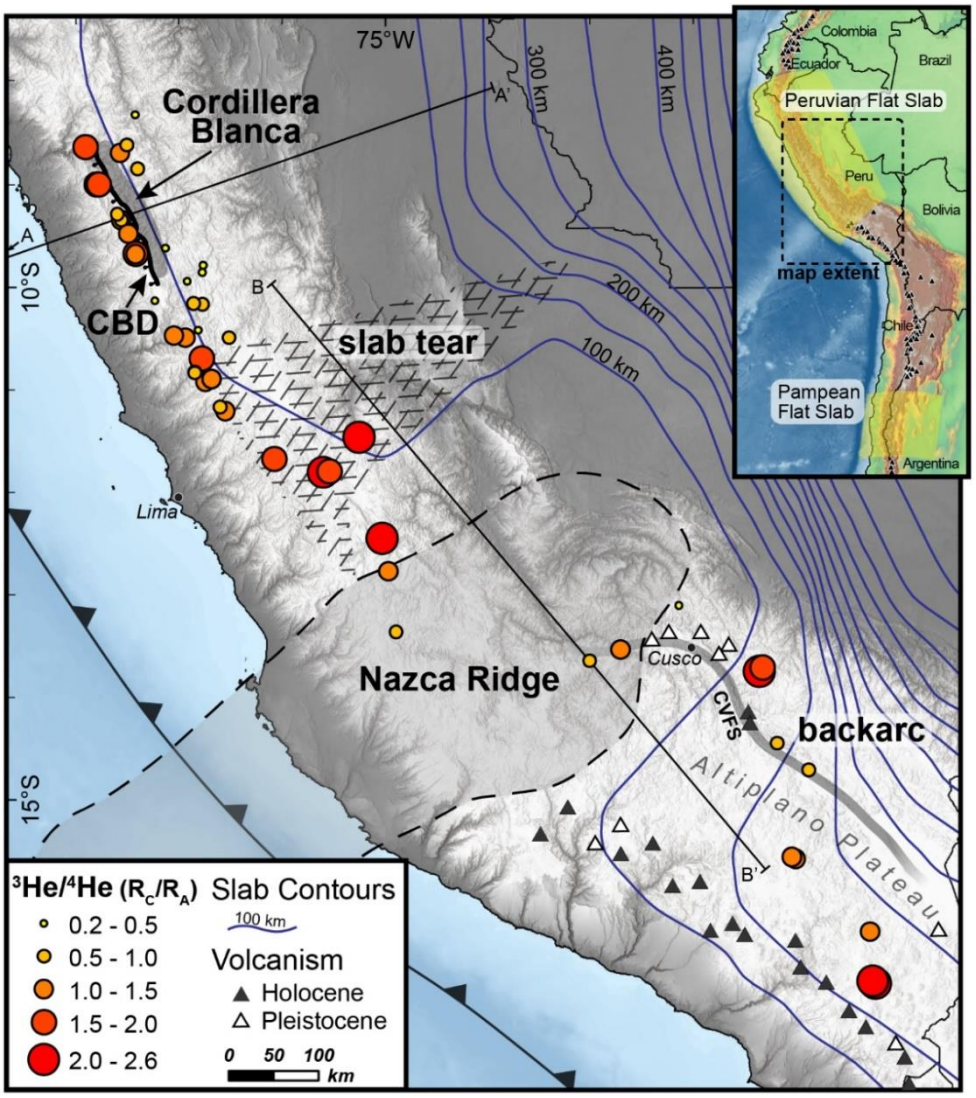

Figure 1. ^{3}He/^{4}He ratios (reported as R_C/R_A) from thermal springs in southern Peru. Higher values (larger circles) indicate greater contribution of mantle helium. All springs yield ^{3}He/^{4}He ratios >0.1 R_C/R_A, indicating unambiguous mantle helium addition. Blue contours indicate depth of the Nazca slab (after Scire et al., 2016). Locations of the CBD fault and Nazca Ridge (after Bishop et al., 2017), and the backarc region are highlighted. The hatched pattern depicts the region overlying the slab tear and combines interpretations from Antonijevic et al. (2015) and Scire et al. (2016). Quaternary volcanism is shown by white (Pleistocene) and black (Holocene) triangles. Quaternary backarc volcanism closely follows the trace of the Cusco-Vilcanota fault system (CVFS). Lines A-A' and B-B' correspond to schematic cross sections shown in Figure 4. Inset map of western South America shows map extent, Quaternary arc volcanism, and location of the Peruvian and Pampean flat slabs. (Digital terrain model courtesy of Esri, Airbus, USGS, NGA, NASA, CGIAR)

since ca. 5.4 Ma is observed along the CBD fault in the central Peruvian Andes, where footwall exhumation of the ca. 14 - 5 Ma Cordillera Blanca Batholith has produced the second highest topography in the Andes (Giovanni et al., 2010). South of the Nazca Ridge and east of the active volcanic arc, Quaternary volcanism is restricted to small-volume mafic to intermediate lava flows that have erupted along the Cusco-Vilcanota fault zone (Fig. 1). Potassic and ultra-potassic compositions reflect a metasomatically enriched mantle source (Carlier et al., 2005) that is likely related to a mid-Cenozoic episode of shallow subduction below what is now the Altiplano Plateau.

Throughout the Peruvian Andes, thermal springs emanate near valley bottoms along the numerous fault networks associated with the Marañón fold and thrust belt and more recent extensional structures such as the CBD fault. Geothermal circulation is driven by large hydraulic gradients provided by the dramatic relief throughout the cordillera. Hot spring waters are commonly salty (≤19,000 ppm TDS) and contain high dissolved gas loads. Reservoir temperature estimates (RTE) of 200 – 275 °C for springs along the CBD fault suggest maximum fluid circulation to depths of 9-11 km (Newell et al., 2015; Scott et al., 2020). In the same region but distal to the CBD fault, RTE of 40 – 98 °C suggest more modest circulation depths to <4 km (Scott et al., 2020).

3. METHODS

3.1. Sample collection

Spring sampling in Peru was conducted over the course of five field campaigns, with geochemical analyses previously reported from springs sampled in 2013 (Newell et al., 2015) and 2017 (Scott et al., 2020). Springs were chosen for sampling and analyses

based on a combination of high temperature, high salinity, location, and accessibility. Spring waters and gases were sampled as close to their source as possible to avoid the effects of degassing and atmospheric exchange. Temperature, pH, and conductivity where measured in the field using an Oakton pH/conductivity/temperature portable meter. Springs were sampled for major and trace element chemistry using standard groundwater sampling techniques (USGS, 2006). Water or gas samples for analysis of gas species isotopes and abundances were collected in 12 in. × 3/8 in. OD (~30 cm × 0.95 cm) copper tubes sealed with refrigeration clamps after purging with spring waters/gases following standard noble gas sampling protocols (Hilton et al., 2002). Gas samples were collected at springs that were actively degassing (bubbling); water samples (dissolved gases) were collected at springs that were not actively degassing.

3.2. Analytical techniques

Major and trace element concentrations in spring water were determined at the Utah State University Water Research Laboratory using a Dionex Ion Chromatograph (anions) and an Agilent Inductively Coupled Plasma-Mass Spectrometer (cations). Total alkalinity was measured by manual colorimetric titration. The geochemical modelling software PHREEQC (Parkhurst and Appelo, 2013) was used to calculate ion balances and total dissolved inorganic carbonate (TDIC).

For samples taken from springs along the CBD fault described in Newell et al. (2015), noble gas isotopes and concentrations were measured at the Fluids and Volatiles Laboratory at Scripps Institute of Oceanography using gas extraction, purification, and analytical procedures described in Shaw et al. (2003). For all other samples, noble gas

isotopes and concentrations were measured at the USGS Noble Gas Laboratory in Lakewood, Colorado using gas extraction, purification, and analytical procedures described in Hunt (2015). Measured $^{3}He/^{4}He$ ratios and helium concentrations ($[He]_M$) are corrected for air contamination as appropriate following Hilton (1996) as shown in footnotes of Supplementary Table A.1.

Because our sample suite contains both free and dissolved gas samples, we "re-dissolve" our free-gas helium and neon concentrations so that water and gas samples can be accurately compared; therefore, reported [He], He/Ne and $CO_2/^{3}He$ values are all in terms of dissolved gases. These methods rely on the assumption that the free gases collected from bubbling springs represent the gases that have evolved from spring waters in the near surface and that this phase change occurred as an equilibrium process. The similarity between our re-dissolved values and measurements from dissolved gas samples demonstrates that this approach is reliable. The measured partial pressure of any gas species *x* (p_x; in atm) can be related to the concentration of dissolved gas ($[x]_{dissolved}$; in $cm^3STP\ gH_2O^{-1}$) in equilibrium with the gas phase by:

$$[x]_{dissolved} = H^{CP} \times p_x \times R \times T_{STP} / (1000 \times P_{STP}) \quad (1)$$

where R is the ideal gas constant (in cm^3 atm mol^{-1} K^{-1}), T_{STP} is 273.15 K, P_{STP} is 1 atm, and H^{CP} is the Henry's law constant corrected for spring temperature and salinity (Smith and Kennedy, 1983; Sander, 2015). Raw gas concentrations and conversion factors are given in Supplementary Table A.2.

For samples taken from the CBD fault springs described in Newell et al. (2015), CO_2 concentrations used to calculate $CO_2/^{3}He$ ratios were measured manometrically after

acidifying samples to release all dissolved CO_2 in conjunction with noble gas measurements. For all other samples, $CO_2/^3He$ ratios were derived using the TDIC modelled from aqueous chemical analysis in PHREEQC and the dissolved $[He]_C$ values multiplied by R_C/R_A.

Relative dry gas abundances (CO_2, N_2, O_2, Ar, He, H_2, CO, CH_4) were measured for a subset of our samples (n=34) at the University of New Mexico Volatiles Laboratory using a GOW-MAC Gas Chromatograph (GC) and Pfeiffer Quadrupole MS (QMS) following methods described in Fischer et al. (2015). Low gas yields for several samples resulted in unreliable QMS data, and in these cases only GC data is reported.

4. RESULTS

Measured $^3He/^4He$ ratios of springs above the flat slab (n = 43), after correction for air contribution, range from 0.26 to 2.40 R_C/R_A (Fig. 1, Supplementary Table A.1). All analyzed springs have values >0.1 R_C/R_A indicating the unambiguous addition of mantle volatiles (O'Nions and Oxburgh, 1988). The highest $^3He/^4He$ ratios above the flat slab are along the CBD fault and above the slab tear region (Fig. 1). Springs within the backarc region to the south (n = 9) yield overall higher values (0.90 to 2.52 R_C/R_A), but are similar to the highest values observed above the flat slab. Measured $CO_2/^3He$ ratios span 7 orders of magnitude, from 7.9×10^9 to 8.2×10^{16}. There is no relationship between $CO_2/^3He$ and $^3He/^4He$ ratios (Fig. 3b), but $CO_2/^3He$ ratios are strongly inversely correlated to helium concentrations (Fig. 3a). He/Ne ratios, which help distinguish between crustal/mantle (He/Ne >1000) and meteoric fluids (He/Ne ≈ 0.32), range from 0.28 to 2190, with higher values corresponding with higher $^3He/^4He$ ratios (Fig. 4).

N_2-Ar-He systematics are similar to magmatic gases seen in intercontinental and MOR settings, and suggest mixing between deeply-derived fluids (with high He/Ar ratios) and meteoric waters (Fig. 2a; Supplementary Table A.3; Giggenbach et al., 1993). Interestingly, relative gas abundances do not correlate to $^3He/^4He$ ratios (Fig. 2b). Backarc springs have consistently higher N_2/Ar ratios compared to springs above the flat slab.

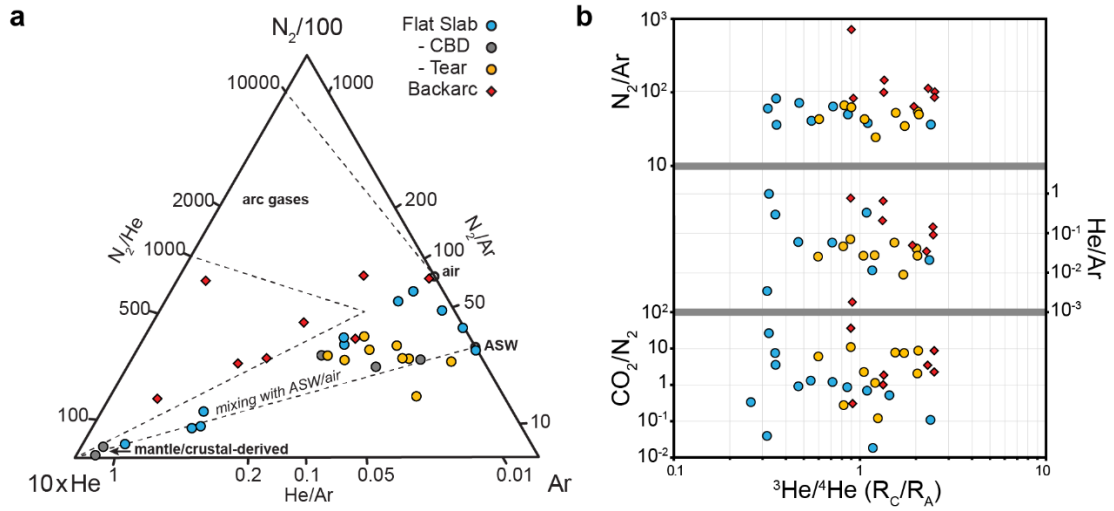

Figure 2. Geochemical trends of thermal spring gases. a, Ternary diagram showing relationship between N_2-Ar-He abundances (after Giggenbach et al., 1993). Mantle/crustal gases are dominated by helium, and arc gases include a larger nitrogen component from subducted slab sediments. Air and ASW are distinguished by high argon and negligible helium. Peruvian thermal spring gases plot in the field expected for mixing between mantle/crust-derived gases and air/ASW, with backarc springs exhibiting consistently higher nitrogen abundances. **b,** Gas abundance ratios (CO_2/N_2, He/Ar, and N_2/Ar) plotted against $^3He/^4He$ ratios (R_C/R_A). Note the lack of correlation between gas abundance and helium isotope ratios, suggesting that relative gas abundances are not controlled simply by mixing between mantle-derived fluids and meteoric waters.

5. DISCUSSION

5.1. Interpretation of mantle-helium source in the flat slab region

Assuming binary mixing with an asthenospheric (MORB) source (8 R_A), $^3He/^4He$ ratios imply that 3 – 30 % of the helium in springs above the flat slab is mantle derived. Alternatively, if helium originates from the subcontinental lithospheric mantle (SCLM; 6.1 ± 2.1 R_A; Day et al., 2015), this increases to 4 – 39 % mantle-derived helium. Elevated $^3He/^4He$ ratios in continental settings are commonly associated with active volcanism or extensional tectonism (O'Nions and Oxburgh, 1988), but are also observed along major strike-slip faults (e.g. Kennedy et al., 1997; de Leeuw et al., 2010) and within orogenic belts and plateaus (e.g. Hoke et al., 2000; Newell et al., 2005). Away from active volcanism, elevated $^3He/^4He$ ratios are explained by deeply penetrating faults/shear zones that accommodate CO_2 degassing from mobile and perhaps partially molten asthenosphere, with the highest ratios occurring along vertically oriented shear zones with high strain rates (Kennedy and van Soest, 2007). Given the geometry of the Peruvian flat slab, the mantle material sandwiched between the continental and oceanic crust is expected to be relatively cold and isolated from the convecting asthenosphere and is therefore best described as SCLM. Modelled pressure and temperature conditions for the Pampean flat slab of central Chile, which has a similar geometry to the Peruvian flat slab, predict temperatures of <700 °C in the mantle above the flat slab (Marot et al., 2014). Geophysical investigations give no indication of partial melt, consistent with arguments that temperatures are too low to induce melting in a flat-slab setting (Gutscher et al., 2000). The SCLM is not expected to actively degas like the asthenosphere, leading to the characteristically low $^3He/^4He$ ratios (0.02 to 0.1 R_A) observed in deeply-sourced

fluids across stable cratons (e.g. O'Nions and Oxburgh, 1988). Therefore, an alternative mechanism is needed to explain mantle helium mobility above the flat slab.

5.1.1. SCLM volatiles mobilized by slab-derived fluids

We suggest that a continuous flux of slab-derived fluids into the overriding plate is mobilizing helium from sub-crustal depths. The slab itself is an unlikely helium source, as collective data from volcanic arcs suggests that a slab's helium budget is lost during the early stages of subduction (Sano and Fischer, 2013). We propose that slab-derived fluids are mobilizing helium from the SCLM. Helium in the SCLM is hosted primarily within CO_2-rich mineral fluid inclusions (Dunai and Porcelli, 2002; Gautheron and Moreira, 2002; Day et al., 2015), and would be liberated during fluid-induced phase transformations. As slab fluids migrate through the mantle and into the crust, fluid chemistry and transport mechanisms are moderated by metamorphic and metasomatic reactions, with helium and other volatiles strongly partitioning into the evolving fluid phase. Aqueous fluids in the deep crust are rapidly consumed through hydration reactions (Yardley et al., 2010). Diffusion is not a viable transport mechanism for helium over crustal scales (Ballentine and Burnard, 2002), so persistent replenishment of fluids is required to sustain these reactions and to move helium with other volatiles from the SCLM and through the crust. Therefore, the flux of slab fluids must be relatively continuous, and the widespread presence of mantle helium in hot springs implies that extensively hydrated conduits exist to promote sustained deep fluid transport through the crust.

The observed relationship between $CO_2/^3He$ and helium concentrations suggests that much of the CO_2 degassing from thermal springs may also be from a similar mantle source (i.e., from the SCLM). The observed inverse correlation can be explained by phase separation and fractionation during fluid degassing, which can be modelled as an open system (Rayleigh) fractionation process where helium and CO_2 are removed in different proportions based on their solubilities (Fig. 3a; following de Leeuw et al., 2010; Newell et al., 2015). Residual dissolved gas ratios after degassing [$(CO_2/^3He)_{final}$] are calculated by:

$$(CO_2/^3He)_{final} = (CO_2/^3He)_{initial} \times f^{(\alpha-1)} \quad (2)$$

where f is the fraction of helium remaining (i.e. reflecting the extent of degassing from any initial concentration) and α is the ratio of the solubilities of helium and CO_2 in water [$\alpha = S_{He}/S_{CO2} = 1.18\times10^{-2}$ (30 °C), 7.66×10^{-2} (200 °C); Weiss, 1971, 1974]. These calculations assume that the solubility of ^3He and ^4He are equivalent at these conditions (e.g. Weiss, 1970). The relatively close accordance of the data to a single trend suggests that most spring waters start with similar mantle-like $CO_2/^3He$ ratios before degassing, which implies that much of the CO_2 also has a SCLM origin and may be acting as a carrier fluid for helium. Along the CBD fault, carbon stable isotope ratios of CO_2 are consistent with a mantle source (Newell et al., 2015), but interpretations are complicated by modification and mixing within the geothermal system and are beyond the scope of this paper. Additionally, that the re-dissolved gas samples fall consistently along this trend suggests that widespread open-system fractionation of He and CO_2 is occurring at significant depths during fluid transport and is not representative of accumulated gases that have exsolved from individual spring systems. The highest dissolved $CO_2/^3He$ ratios

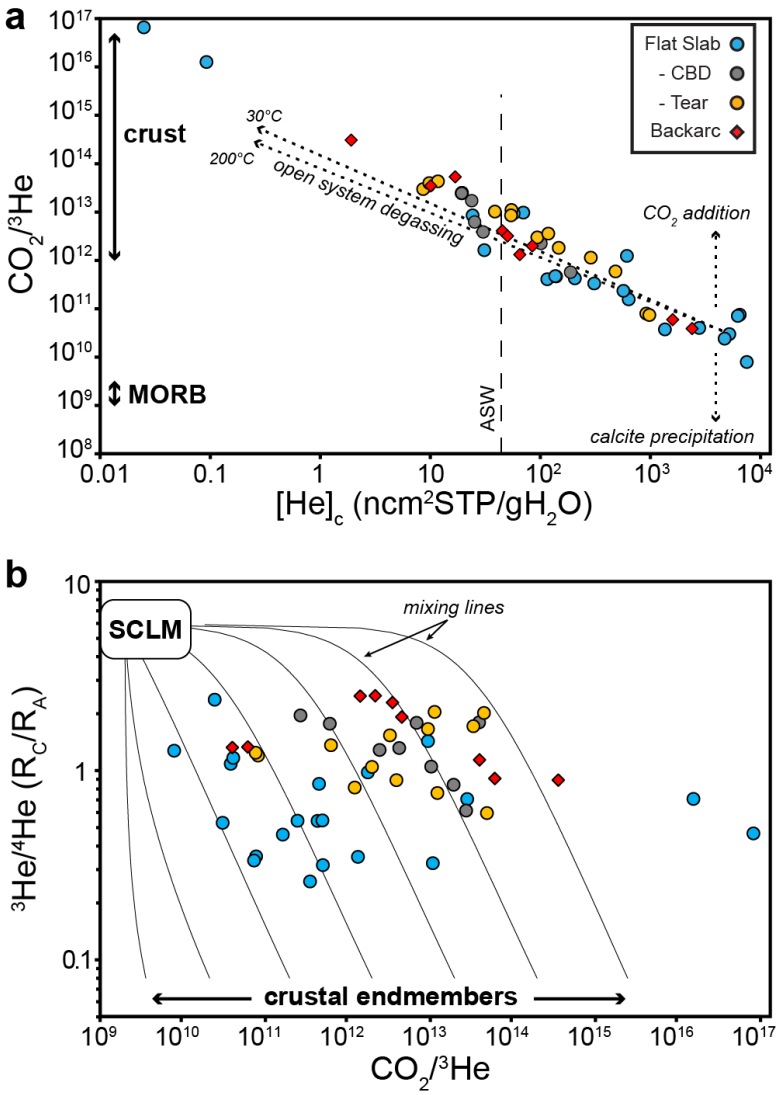

Figure 3. Relationships between $CO_2/^3He$ ratios, dissolved helium concentrations, and $^3He/^4He$ ratios. a, Inverse relationship between $CO_2/^3He$ ratios (dissolved) and dissolved helium concentrations. Data shows close accordance to the trend expected for open system (Rayleigh) fractionation during degassing, shown as two diagonal dotted lines corresponding to degassing at 30 and 200 °C. Vertical dotted lines represent trends expected for CO_2 addition or carbonate precipitation. $CO_2/^3He$ ranges for mantle and crustal endmembers are shown for reference. Vertical dashed line represents helium concentration of air saturated water (ASW) at sea level. **b**, $^3He/^4He$ (R_C/R_A) vs. $CO_2/^3He$ relationships between hot spring samples and binary mixing curves between a SCLM endmember and various crustal reservoirs (after O'Nions and Oxburgh, 1988). Note that the data is not consistent with simple binary mixing between a mantle and narrow range of crustal endmembers, and degassing strongly impacting the $CO_2/^3He$ ratios can explain the variability.

(1.54×10^{16} and 8.24×10^{16}), although exceeding published observations from crustal fluids, are consistent with extensive gas stripping and CO_2/He fractionation. The second order variability along the inverse trend may be attributed to local crustal CO_2 addition or calcite precipitation (Fig. 3a). Binary mixing between crustal and mantle fluid end members cannot explain this trend because mixing alone would require crustal $CO_2/^3He$ end members that vary by nearly 7 orders of magnitude, which is unreasonable (Fig. 3b).

5.1.2. Remnant magmatic fluids

An alternative interpretation is that our results reflect "fossil" magmatic fluids preserved in the crust from earlier arc magmatism. In this scenario, asthenospheric-derived mantle helium may be preserved in residual magmatic fluids or within the igneous rock itself, but helium isotope ratios will rapidly drop as radiogenic ^4He is produced in the crust (e.g. Kennedy and van Soest, 2006; Newell et al., 2015). We estimate the residual $^3He/^4He$ ratio of the magmatic fluid ($^3He/^4He_t$) using:

$$^3He/^4He_t = {}^3He_0 / ({}^4He_{rad} \times t + {}^4He_0) \quad (3)$$

where $^3He_0$ and $^4He_0$ are initial concentrations in the fluid (mol gH_2O^{-1}), and t is in years. $^4He_{rad}$ is the accumulation rate of radiogenic helium in the fluid (mol gH_2O^{-1} $year^{-1}$), which is calculated by:

$$^4He_{rad} = {}^4He_{prod} \times (1-\varphi) / \varphi \quad (4)$$

where $^4He_{prod}$ is the crustal production rate (mol g^{-1} $year^{-1}$) and φ is porosity. We use a generous porosity of 10% to represent the middle to upper crust. Although higher porosities are found in the upper-most crust, regional unroofing in Peru requires that

preserved magmatic fluids would have resided at depths of at least several kilometers, and higher porosities would not be expected for a magmatic fluid to remain isolated and immobile. A value of 2.63×10^{-17} mol g^{-1} $year^{-1}$ was used for $^4He_{prod}$ in the upper crust (Ballentine and Burnard, 2002). An initial helium concentration ($^4He_0$) of 5.3×10^{-11} (mol g^{-1}) is based on the average mantle values observed along the southern volcanic zone in Chile (Ray et al., 2009; Newell et al., 2015). Initial helium concentrations can also be calculated using the measured $^3He/^4He$ ratio and ^4He concentration from samples with the most reliable helium concentrations (least degassed), assuming that all ^3He came from a mantle endmember with a known $^3He/^4He$ ratio. Using the six samples with highest helium concentrations (4.72×10^{-6} to 7.72×10^{-6} cm^3STP gH_2O^{-1}), and assuming a MORB source (8 R_A), the average initial ^4He concentration of our fluid is 7.34×10^{-7} cm^3STP g^{-1} (3.00×10^{-11} mol g^{-1}), similar but slightly lower than observations from the southern volcanic zone. Because our least degassed samples could still have experienced some degassing, we chose to use the higher value of 5.3×10^{-11} mol g^{-1} as a more conservative option in this calculation. In this model, our choice of a high porosity and a MORB helium source with a high initial ^4He concentration provides the most ideal conditions for a magmatic fluid emplaced in the upper crust to retain high $^3He/^4He$ ratios.

Under these optimal conditions for preserving the fossil magmatic helium signature, a magmatic fluid (8 R_A) emplaced in the upper crust at 4 Ma would have a present-day value of ~0.4 R_A (Fig. 4). This estimate does not consider magmatic crustal assimilation or mixing between the primary magmatic fluids and crustal fluids, which will occur (e.g. Taylor, 1977; Hilton et al., 1993; Hu et al., 1998) and further reduce the residual $^3He/^4He$ ratio. Furthermore, the most recent arc magmatism for much of our

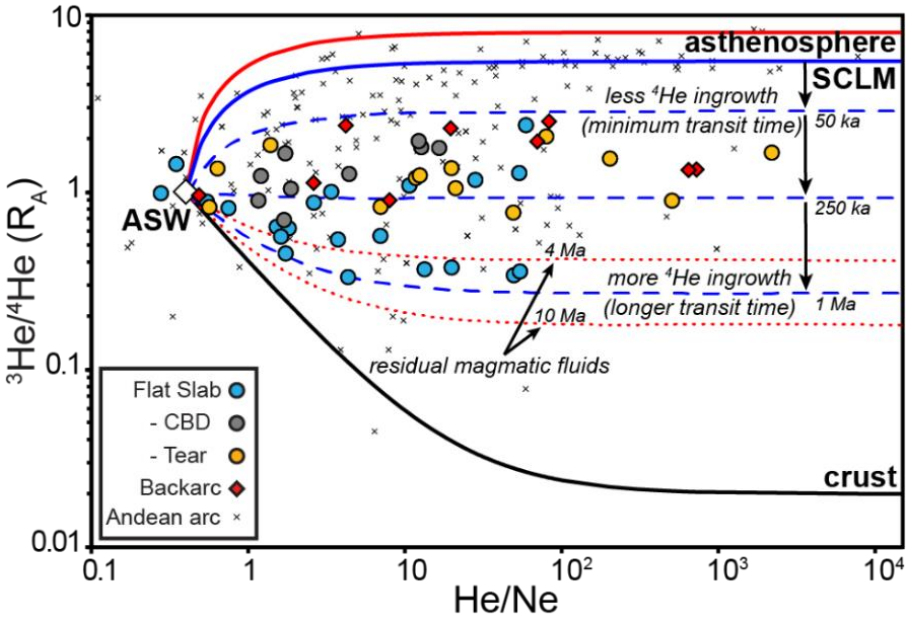

Figure 4. ^{3}He/^{4}He ratios (R_A, uncorrected for air contamination) vs. He/Ne ratios demonstrating the effect of radiogenic ^{4}He ingrowth during fluid transit through the crust. Solid lines represent two-component mixing between air saturated water (ASW; 1 R_A; He/Ne = 0.32) and SCLM fluids (blue; 6.1 R_A, He/Ne >1000), asthenosphere fluids (red; 8 R_A, He/Ne >1000), or crustal fluids (black; 0.02 R_A, He/Ne >1000). Blue dashed lines illustrate the expected reduction of ^{3}He/^{4}He ratios as a function of crustal transit time for fluids carrying helium mobilized from the SCLM. Red dotted lines show the reduction of ^{3}He/^{4}He ratios for residual magmatic fluids emplaced in the upper crust by prior magmatism, which cannot explain the observed ^{3}He/^{4}He ratios given the absence of recent volcanism in central Peru (see text for detailed calculations). In both scenarios, time dependent ^{3}He/^{4}He ratios are considered maximum estimates, as much lower porosities are expected and in combination with mixing with crustal fluids would result in lower ^{3}He/^{4}He ratios. Data reported from the active Andean arc is also shown (Newell et al., 2015, and references therein), demonstrating a trend towards asthenospheric values at high He/Ne ratios.

study area is significantly older than 4 Ma (Rosenbaum et al., 2005) and we observe no relationship between ^{3}He/^{4}He ratios and the age of local igneous rocks. Because the observed ^{3}He/^{4}He ratios observed in this study exceed those predicted for this

mechanism, we dismiss this explanation. Instead, we favor a model where a present-day flux of slab-derived fluids is mobilizing helium from the SCLM.

5.2. Implications of regional $^{3}He/^{4}He$ variability for crustal fluid transit times

Ultramafic xenoliths and phenocrysts in alkali basalts from the SCLM yield $^{3}He/^{4}He$ ratios that are slightly lower (more radiogenic) than the asthenosphere, with a mean of 6.1 ± 2.1 R_A (Day et al., 2015). If the SCLM were relatively young, as would be the case if it were remnant asthenospheric wedge material that cooled after slab shallowing, then $^{3}He/^{4}He$ ratios may be closer to the MORB endmember of 8 ± 1 R_A. However, the Peruvian flat slab is thought to have displaced a significant amount of upper-plate material along the southward migrating Nazca Ridge (Bishop et al., 2017). Thus it is more likely that the existing SCLM formed during crustal formation and contains $^{3}He/^{4}He$ ratios closer to the estimated global mean for SCLM. Lower $^{3}He/^{4}He$ ratios observed in Peruvian thermal springs must be a result of further radiogenic ^{4}He ingrowth and mixing with ^{4}He-rich crustal fluids. Springs with aqueous chemistries characteristic of deep geothermal circulation (CBD fault springs) yield higher $^{3}He/^{4}He$ ratios than springs associated with more shallow, and likely much younger, groundwater circulation (Newell et al., 2015; Scott et al., 2020), suggesting that the magnitude of crustal fluid input (^{4}He ingrowth) is not a function of groundwater residence time in the upper crust. The variability among observed $^{3}He/^{4}He$ ratios, as well as the discrepancy between maximum $^{3}He/^{4}He$ ratios and the inferred SCLM helium source, likely reflects fluid transit time through the continental crust (Fig. 4).

Equations (3) and (4) can also be used to calculate crustal residence times (transit times) for helium mobilized from the SCLM. In the earlier calculation (Section 5.1.2), we chose inputs to represent fluid emplaced into the upper crust during arc magmatism and to give that fluid the best-case scenario for preserving high $^{3}He/^{4}He$ ratios over time. Here different inputs are chosen to match the observed helium isotope ratios and concentrations and to align with our interpretation of the SCLM as a mantle-helium source. The starting fluid is assumed to have an initial $^{3}He/^{4}He$ ratio of the SCLM (6.1 R_A) and an initial ^{4}He concentration calculated from our six least degassed samples as discussed above (3.9×10^{-11} mol gH_2O^{-1}). Because fluid transit through the ductile crust is presumably much slower than transit through the upper crust, we use an average ^{4}He production rate for the lower and middle crust (8.71×10^{-17} mol g^{-1} $year^{-1}$; Ballentine and Burnard, 2002). In this calculation a porosity of 1 % is used as an extreme upper-limit for the porosity expected in the deep crust. The observed $^{3}He/^{4}He$ ratios correspond to transit times ranging from 648 ka to 1.03 Ma. A crustal thickness of 50 km requires vertical continuous flow rates of 49 – 771 mm/year, up to five times higher than flow rates calculated for mantle fluids transiting major strike-slip fault systems (Kennedy et al., 1997; Kulongoski et al., 2013). Lower porosities are likely, as well as mixing with ^{4}He rich crustal fluids, so our calculated flow rates are considered minimum estimates. We emphasize that these calculations are not intended as a mechanistic model for fluid migration through the crust. Rather, they provide a means for estimating fluid flow rates using the time dependent dilution of the helium isotope system by crustal ^{4}He production and serve as a basis for comparison to similar calculations in other tectonic settings.

Higher $^{3}He/^{4}He$ ratios measured along the CBD fault and above the probable slab tear imply a more rapid transit through the crust compared to elsewhere above the flat slab. Crustal thickness across the spring sampling transect varies from ~30 to ~70 km, although the majority of locations overlie 50 – 60 km thick crust. We do not observe a relationship between crustal thickness and $^{3}He/^{4}He$ ratios (Supplementary Fig. A.1), so other explanations are required for the apparent disparities in fluid transit times. As for the elevated values along the CBD fault, the moderately dipping fault zone allows for more rapid fluid ascent through the upper crust, but its inferred listric geometry does not provide a structurally-controlled fluid pathway below ~10 km (Giovanni et al., 2010). Instead, we propose that localized extension and exhumation along the CBD promotes retrograde metamorphism and accelerated hydration reactions at depth, creating a fluid pressure gradient that focuses a persistent fluid flux into and up through the crust below the CBD (Fig. 5).

To the south, elevated $^{3}He/^{4}He$ ratios observed above the slab tear region could be related to asthenosphere entering the tear, as is suggested by recent measurements of seismic anisotropy (Antonijevic et al., 2016). Higher temperatures would accelerate slab devolatilization and decrease the water absorbing capacity of the continental lithosphere, increasing fluid flow rates through the crust (Fig. 5). Asthenosphere upwelling through the tear could also trigger partial melting of hydrated SCLM or decompression melting in the asthenosphere, which would increase fluid production or release volatiles with higher endmember $^{3}He/^{4}He$ ratios, respectively. In either case, our data corroborates with geophysical evidence that suggest the Nazca Plate is tearing north of the Nazca Ridge.

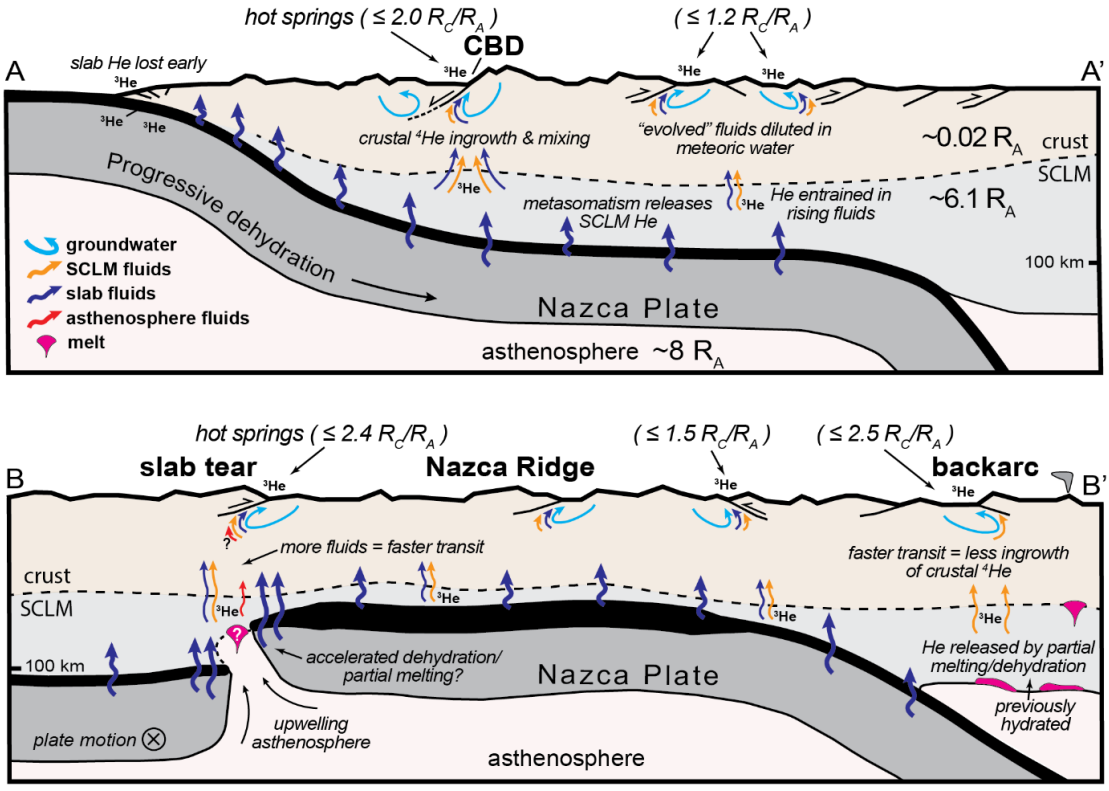

Figure 5. Schematic cross sections illustrating slab-derived fluids mobilizing helium from the SCLM and the effects of the slab tear, crustal detachment faulting (CBD fault) and partial mantle melting and/or dehydration in the backarc. General cross section locations are shown as lines A-A' and B-B' in Figure 1. Arrow colors correspond to the various endmember fluid sources as shown in the upper cross section. The observed ^{3}He/^{4}He ratios in Peruvian thermal springs are best explained by a contribution of helium mobilized from the SCLM. In the flat-slab region, slab fluids sustain metasomatism and metamorphic reactions that release mantle volatiles. In the backarc, fluids are released from the SCLM as a result of partial melting or dehydration of previously hydrated mantle material. Initial ^{3}He/^{4}He ratios of ~6.1 R_A in SCLM fluids are lowered by the time dependent ingrowth of radiogenic ^{4}He and mixing with ^{4}He rich crustal fluids. Higher ^{3}He/^{4}He ratios in surface springs of the CBD, slab tear, and backarc regions indicate faster fluid transit times.

5.3. Interpretation of mantle-helium source in the backarc region

The similarity between $^3He/^4He$ ratios from the backarc region and above the flat slab is unexpected, as alkaline mafic magmatism should quickly transport mantle volatiles with minimal crustal contamination. This suggests that the mantle helium signature in backarc springs is decoupled from the scattered Quaternary volcanism and is instead controlled by fluid processes similar to those operating above the flat slab. We propose that the mantle helium in backarc springs is a result of aqueous fluid production in the SCLM and/or lower crust, and that the ubiquitous maximum $^3He/^4He$ ratio of ~2.5 R_C/R_A is a manifestation of the minimum transit time required for fluids to traverse the thick Andean crust. Comparable values in the backarc region of the Bolivian Altiplano are attributed to a broad region of partial melting in the SCLM and basalt emplacement in the lower crust (Hoke et al., 1994). In both regions, aqueous fluids with mantle-derived volatiles could be released during crystallization of partial melts at depth or simply during dehydration reactions in the SCLM and lower crust. Both processes are expected consequences of hydrated lithosphere re-equilibrating with asthenosphere after episodes of flat-slab subduction at ~36 – 23 Ma and 18 – 12 Ma (Ramos and Folguera, 2009). Consistently higher N_2 abundances in backarc springs (Fig. 2b) may indicate that the hotter thermal regime associated with the backarc region allows for the remobilization of N_2 that was previously transferred to the continental lithosphere; however, isotopic evidence will ultimately be needed to constrain nitrogen sources. These interpretations provide insight into the state of the continental lithosphere below the Altiplano Plateau and suggests that volatiles transferred to the continental lithosphere during flat-slab subduction may persist for at least tens of millions of years after removal of the flat slab.

5.4. Relative gas abundances

The lack of correlation between relative gas abundances (e.g. C/N, He/Ar and N_2/He ratios) and $^3He/^4He$ ratios (Fig. 2b) suggests that the volatile load in these Peruvian thermal springs is not controlled simply by mixing between mantle-derived fluids and meteoric waters. Instead, they appear to represent mixing between meteoric waters and deeply-derived fluids in general. In other words, relative gas abundances provide insight into the shallow (i.e. crustal-meteoric) fluid history, with $^3He/^4He$ ratios providing a definitive indicator of a mantle volatile contribution. Analysis of carbon and nitrogen isotope ratios are needed to identify additional contributions of mantle-derived volatiles and to further constrain the balance of meteoric, crustal, and mantle fluids in these springs.

6. CONCLUSION

Our findings demonstrate ongoing fluid transfer and continental hydration in an active flat-slab setting. Furthermore, we show that tectonic heterogeneities in both the upper and lower plates can influence the rate of fluid transfer from slab to surface, and that the subsequent effects of fluid transfer, such as dehydration and partial melting, may persist long after the resumption of steep subduction. More work is needed to quantify fluid fluxes into the lithosphere and constrain their distribution, which are key to developing models for the geodynamic evolution of convergent margins. Accurate estimates of fluid fluxes require better regional constraints on helium isotope ratios and concentrations in the SCLM and a more quantitative understanding of fluid transport mechanisms through the deep crust. However, our current results corroborate arguments

that fluid transfer during flat-slab subduction leads to significant chemical alteration of the SCLM and continental crust. If the Andean margin is the type example for continental arcs, then its long history of transient flat-slab subduction (Ramos and Folguera, 2009) attests to the prevalence of these processes throughout the formation and evolution of Earth's continental lithosphere.

REFERENCES

Antonijevic, S.K., Wagner, L.S., Beck, S.L., Long, M.D., Zandt, G., and Tavera, H., 2016, Effects of change in slab geometry on the mantle flow and slab fabric in Southern Peru: Journal of Geophysical Research: Solid Earth, v. 121, p. 7252–7270, doi:10.1002/2016JB013064.

Antonijevic, S.K., Wagner, L.S., Kumar, A., Beck, S.L., Long, M.D., Zandt, G., Tavera, H., and Condori, C., 2015, The role of ridges in the formation and longevity of flat slabs: Nature, v. 524, p. 212–215, doi:10.1038/nature14648.

Ballentine, C.J., and Burnard, P.G., 2002, Production, release and transport of noble gases in the continental crust: Reviews in Mineralogy and Geochemistry, v. 47, doi:10.2138/rmg.2002.47.12.

Bishop, B.T., Beck, S.L., Zandt, G., Wagner, L., Long, M., Antonijevic, S.K., Kumar, A., and Tavera, H., 2017, Causes and consequences of flat-slab subduction in southern Peru: Geosphere, v. 13, p. 1392–1407, doi:10.1130/GES01440.1.

Carlier, G., Lorand, J.P., Liégeois, J.P., Fornari, M., Soler, P., Carlotto, V., and Cárdenas, J., 2005, Potassic-ultrapotassic mafic rocks delineate two lithospheric mantle blocks beneath the southern Peruvian Altiplano: Geology, v. 33, p. 601–604, doi:10.1130/G21643.1.

Day, J.M.D., Barry, P.H., Hilton, D.R., Burgess, R., Pearson, D.G., and Taylor, L.A., 2015, The helium flux from the continents and ubiquity of low-3He/4He recycled crust and lithosphere: Geochimica et Cosmochimica Acta, v. 153, p. 116–133, doi:10.1016/j.gca.2015.01.008.

Dunai, T.J., and Porcelli, D., 2002, Storage and transport of noble gases in the subcontinental lithosphere: Reviews in Mineralogy and Geochemistry, v. 47, doi:10.2138/rmg.2002.47.10.

Farmer, G.L., Fritz, D.E., and Glazner, A.F., 2020, Identifying Metasomatized Continental Lithospheric Mantle Involvement in Cenozoic Magmatism From Ta/Th Values, Southwestern North America: Geochemistry, Geophysics, Geosystems, v. 21, doi:10.1029/2019gc008499.

Fischer, T.P. et al., 2015, Temporal variations in fumarole gas chemistry at Poás volcano, Costa Rica: Journal of Volcanology and Geothermal Research, v. 294, p. 56–70, doi:10.1016/j.jvolgeores.2015.02.002.

Gautheron, C., and Moreira, M., 2002, Helium signature of the subcontinental lithospheric mantle: Earth and Planetary Science Letters, v. 199, p. 39–47, doi:10.1016/S0012-821X(02)00563-0.

Giggenbach, W.., Sano, Y., and Wakita, H., 1993, Isotopic composition of helium, and CO2 and CH4 contents in gases produced along the New Zealand part of a convergent plate boundary: Geochimica et Cosmochimica Acta, v. 57, p. 3427–3455, doi:10.1016/0016-7037(93)90549-C.

Giovanni, M.K., Horton, B.K., Garzione, C.N., McNulty, B., and Grove, M., 2010, Extensional basin evolution in the Cordillera Blanca, Peru: Stratigraphic and isotopic records of detachment faulting and orogenic collapse in the Andean hinterland: Tectonics, v. 29, doi:10.1029/2010TC002666.

Gutscher, M.A., Maury, F., Eissen, J.P., and Bourdon, E., 2000, Can slab melting be caused by flat subduction? Geology, v. 28, p. 535–538, doi:10.1130/0091-7613(2000)28<535:csmbcb>2.0.co;2.

Hilton, D.R., 1996, The helium and carbon isotope systematics of a continental geothermal system: Results from monitoring studies at Long Valley caldera (California, U.S.A.): Chemical Geology, v. 127, p. 269–295, doi:10.1016/0009-2541(95)00134-4.

Hilton, D.R., Fischer, T.P., and Marry, B., 2002, Noble gases and volatile recycling at subduction zones: Reviews in Mineralogy and Geochemistry, v. 47, doi:10.2138/rmg.2002.47.9.

Hilton, D.R., Hammerschmidt, K., Teufel, S., and Friedrichsen, H., 1993, Helium isotope characteristics of Andean geothermal fluids and lavas: Earth and Planetary Science Letters, v. 120, p. 265–282, doi:10.1016/0012-821X(93)90244-4.

Hoke, L., Hilton, D.R., Lamb, S.H., Hammerschmidt, K., and Friedrichsen, H., 1994, 3He evidence for a wide zone of active mantle melting beneath the Central Andes: Earth and Planetary Science Letters, v. 128, p. 341–355, doi:10.1016/0012-821X(94)90155-4.

Hoke, L., Lamb, S., Hilton, D.R., and Poreda, R.J., 2000, Southern limit of mantle-derived geothermal helium emissions in Tibet: Implications for lithospheric structure: Earth and Planetary Science Letters, v. 180, p. 297–308, doi:10.1016/S0012-821X(00)00174-6.

Hu, R., Burnard, P.G., Turner, G., and Bi, X., 1998, Helium and Argon isotope systematics in fluid inclusions of Machangqing copper deposit in west Yunnan Province, China: Chemical Geology, v. 146, p. 55–63, doi:10.1016/S0009-2541(98)00003-5.

Humphreys, E., Hessler, E., Dueker, K., Farmer, G.L., Erslev, E., and Atwater, T., 2003, How Laramide-Age Hydration of North American Lithosphere by the Farallon Slab Controlled Subsequent Activity in the Western United States: International Geology Review, v. 45, p. 575–595, doi:10.2747/0020-6814.45.7.575.

Hunt, A.G., 2015, U.S. Geological Survey Noble Gas Laboratory's standard operating procedures for the measurement of dissolved gas in water samples:, doi:10.3133/tm5a11.

Hyndman, R.D., and Peacock, S.M., 2003, Serpentinization of the forearc mantle: Earth and Planetary Science Letters, v. 212, p. 417–432, doi:10.1016/S0012-821X(03)00263-2.

James, D., and Sacks, I., 1999, Cenozoic formation of central Andes: a geophysical perspective, *in* Geology and Ore Deposits of the Central Andes, p. 1–25.

Jones, C.H., Mahan, K.H., Butcher, L.A., Levandowski, W.B., and Farmer, G.L., 2015, Continental uplift through crustal hydration: Geology, v. 43, p. 355–358, doi:10.1130/G36509.1.

Kennedy, B.M., Kharaka, Y.K., Evans, W.C., Ellwood, A., DePaolo, D.J., Thordsen, J., Ambats, G., and Mariner, R.H., 1997, Mantle fluids in the San Andreas fault system, California: Science, v. 278, p. 1278–1281, doi:10.1126/science.278.5341.1278.

Kennedy, B.M., and van Soest, M.C., 2006, A helium isotope perspective on the Dixie Valley, Nevada, hydrothermal system: Geothermics, v. 35, p. 26–43, doi:10.1016/j.geothermics.2005.09.004.

Kennedy, B.M., and van Soest, M.C., 2007, Flow of mantle fluids through the ductile lower crust: Helium isotope trends: Science, v. 318, p. 1433–1436, doi:10.1126/science.1147537.

Kulongoski, J.T., Hilton, D.R., Barry, P.H., Esser, B.K., Hillegonds, D., and Belitz, K., 2013, Volatile fluxes through the Big Bend section of the San Andreas Fault, California: Helium and carbon-dioxide systematics: Chemical Geology, v. 339, p.

92–102, doi:10.1016/j.chemgeo.2012.09.007.

Lee, C.A., 2005, Trace Element Evidence for Hydrous Metasomatism at the Base of the North American Lithosphere and Possible Association with Laramide Low-Angle Subduction: The Journal of Geology, v. 113, p. 673–685, doi:10.1086/449327.

de Leeuw, G.A.M., Hilton, D.R., Güleç, N., and Mutlu, H., 2010, Regional and temporal variations in CO2/3He, 3He/4He and δ13C along the North Anatolian Fault Zone, Turkey: Applied Geochemistry, v. 25, p. 524–539, doi:10.1016/j.apgeochem.2010.01.010.

Levander, A., Schmandt, B., Miller, M.S., Liu, K., Karlstrom, K.E., Crow, R.S., Lee, C.T.A., and Humphreys, E.D., 2011, Continuing Colorado plateau uplift by delamination-style convective lithospheric downwelling: Nature, v. 472, p. 461–465, doi:10.1038/nature10001.

Marot, M., Monfret, T., Gerbault, M., Nolet, G., Ranalli, G., and Pardo, M., 2014, Flat versus normal subduction zones: A comparison based on 3-D regional traveltime tomography and petrological modelling of central Chile and western Argentina (29°-35°S): Geophysical Journal International, v. 199, p. 1633–1654, doi:10.1093/gji/ggu355.

Marty, B., and Jambon, A., 1987, C/^{3}He in volatile fluxes from the solid Earth: implications for carbon geodynamics: Earth and Planetary Science Letters, v. 83, p. 16–26, doi:10.1016/0012-821X(87)90047-1.

Newell, D.L., Crossey, L.J., Karlstrom, K.E., Fischer, T.P., and Hilton, D.R., 2005, Continental-scale links between the mantle and groundwater systems of the western United States: Evidence from travertine springs and regional He isotope data: GSA Today, v. 15, p. 4–10, doi:10.1130/1052-5173(2005)015[4:CSLBTM]2.0.CO;2.

Newell, D.L., Jessup, M.J., Hilton, D.R., Shaw, C.A., and Hughes, C.A., 2015, Mantle-derived helium in hot springs of the Cordillera Blanca , Peru : Implications for mantle-to-crust fl uid transfer in a fl at-slab subduction setting: Chemical Geology, v. 417, p. 200–209, doi:10.1016/j.chemgeo.2015.10.003.

O'Nions, R.K., and Oxburgh, E.R., 1988, Helium, volatile fluxes and the development of continental crust: Earth and Planetary Science Letters, v. 90, p. 331–347, doi:10.1016/0012-821X(88)90134-3.

Parkhurst, D.L., and Appelo, C.A.J., 2013, Description of Input and Examples for PHREEQC Version 3 — A Computer Program for Speciation , Batch-Reaction , One-Dimensional Transport , and Inverse Geochemical Calculations.: U.S. Geological Survey Techniques and Methods, book 6, chapter A43,

doi:10.1016/0029-6554(94)90020-5.

Porter, R., Gilbert, H., Zandt, G., Beck, S., Warren, L., Calkins, J., Alvarado, P., and Anderson, M., 2012, Shear wave velocities in the Pampean flat-slab region from Rayleigh wave tomography: Implications for slab and upper mantle hydration: Journal of Geophysical Research B: Solid Earth, v. 117, p. 1–21, doi:10.1029/2012JB009350.

Ramos, V.A., and Folguera, A., 2009, Andean flat-slab subduction through time: Geological Society, London, Special Publications, v. 327, p. 31–54, doi:10.1144/SP327.3.

Ray, M.C., Hilton, D.R., Muñoz, J., Fischer, T.P., and Shaw, A.M., 2009, The effects of volatile recycling, degassing and crustal contamination on the helium and carbon geochemistry of hydrothermal fl uids from the Southern Volcanic Zone of Chile: Chemical Geology, v. 266, p. 38–49, doi:10.1016/j.chemgeo.2008.12.026.

Rosenbaum, G., Giles, D., Saxon, M., Betts, P.G., Weinberg, R.F., and Duboz, C., 2005, Subduction of the Nazca Ridge and the Inca Plateau: Insights into the formation of ore deposits in Peru: Earth and Planetary Science Letters, v. 239, p. 18–32, doi:10.1016/j.epsl.2005.08.003.

Sander, R., 2015, Compilation of Henry's law constants (version 4.0) for water as solvent: Atmospheric Chemistry and Physics, v. 15, p. 4399–4981, doi:10.5194/acp-15-4399-2015.

Sano, Y., and Fischer, T.P., 2013, The analysis and interpretation of noble gases in modern hydrothermal systems, *in* Advances in Isotope Geochemistry, doi:10.1007/978-3-642-28836-4_10.

Sano, Y., Gamo, T., and Williams, S.N., 1997, Secular variations of helium and carbon isotopes at Galeras volcano, Colombia: Journal of Volcanology and Geothermal Research, v. 77, p. 255–265, doi:10.1016/S0377-0273(96)00098-4.

Savov, I.P., Ryan, J.G., D'Antonio, M., and Fryer, P., 2007, Shallow slab fluid release across and along the Mariana arc-basin system: Insights from geochemistry of serpentinized peridotites from the Mariana fore arc: Journal of Geophysical Research: Solid Earth, v. 112, doi:10.1029/2006JB004749.

Scire, A., Zandt, G., Beck, S., Long, M., Wagner, L., Minaya, E., and Tavera, H., 2016, Imaging the transition from flat to normal subduction: Variations in the structure of the Nazca slab and upper mantle under southern Peru and northwestern Bolivia: Geophysical Journal International, v. 204, p. 457–479, doi:10.1093/gji/ggv452.

Scott, B.E., Newell, D.L., Jessup, M.J., Grambling, T., and Shaw, C.A., 2020, Structural

controls on crustal fluid circulation and hot spring geochemistry above a flat-slab subduction zone, Peru: Geochemistry, Geophysics, Geosystems, v. 21, doi:10.1029/2020gc008919.

Shaw, A.M., Hilton, D.R., Fischer, T.P., Walker, J.A., and Alvarado, G.E., 2003, Contrasting He-C relationships in Nicaragua and Costa Rica: Insights into C cycling through subduction zones: Earth and Planetary Science Letters, v. 214, p. 499–513, doi:10.1016/S0012-821X(03)00401-1.

Smith, S.P., and Kennedy, B.M., 1983, The solubility of noble gases in water and in NaCl brine: Geochimica et Cosmochimica Acta, v. 47, p. 503–515, doi:10.1016/0016-7037(83)90273-9.

Taylor, H.P., 1977, Water/rock interactions and the origin of H2O in granitic batholiths: Journal of the Geological Society, v. 133, p. 509–558, doi:10.1144/gsjgs.133.6.0509.

U.S. Geological Survey, 2006, Collection of Water Samples (ver. 2.0): U.S. Geological Survey Techniques of Water-Resources Investigations, book 9, chapter A4, doi:10.3133/twri09A4.

Weiss, R.F., 1970, Helium isotope effect in solution in water and seawater: Science, v. 168, p. 247–248, doi:10.1126/science.168.3928.247.

Weiss, R.F., 1971, Solubility of Helium and Neon in Water and Seawater: Journal of Chemical and Engineering Data, v. 16, p. 235–241, doi:10.1021/je60049a019.

Weiss, R.F., 1974, Carbon dioxide in water and seawater: the solubility of a non-ideal gas: Marine Chemistry, v. 2, p. 203–215, doi:10.1016/0304-4203(74)90015-2.

Yardley, B.W.D., Harlov, D.E., and Heinrich, W., 2010, Rates of retrograde metamorphism and their implications for crustal rheology: Geofluids, v. 10, p. 234–240, doi:10.1111/j.1468-8123.2010.00286.x.

CHAPTER 3

DEEP CO_2 AND N_2 EMISSIONS FROM PERUVIAN HOT SPRINGS: STABLE ISOTOPIC CONSTRAINTS ON VOLATILE CYCLING IN A FLAT-SLAB SUBDUCTION ZONE[1]

ABSTRACT

Gas-rich hot springs throughout the Peruvian Andes contain a surprising contribution of mantle and crustal volatiles (CO_2 and N_2) despite being located along a volcanic gap associated with modern flat-slab subduction. Similar mantle and crustal volatile degassing is observed in springs from the backarc region of the northern Altiplano Plateau which experienced flat-slab subduction in the Oligocene. We constrain the sources of deeply-derived volatiles using C, N, O and H stable isotope analyses alongside previously reported helium isotope ($^3He/^4He$) and gas abundance data. $\delta^{18}O$ and δ^2H values of spring waters are consistent with regional meteoric water, with deviations towards higher values due to fluid mixing and high-temperature fluid-rock interaction. $\delta^{15}N$ values of N_2 gas range from -0.5 to +4.4 ‰ (vs AIR), indicating contributions of mantle and crustal (sedimentary) nitrogen. $\delta^{13}C$ values of dissolved inorganic carbon (DIC) and CO_2 gas from bubbling springs are used to model initial $\delta^{13}C$ values before degassing, with resulting values ranging from -13.6 to -0.3 ‰ (vs VPDB) and an average value of -6.9 ‰. DIC concentrations range from 1 to 57 mmol/kg, of

[1] Paper published in *Chemical Geology* (April 2022) with author list:
C.D. Hiett[a], D.L. Newell[a], M.J. Jessup[b], T.A. Grambling[b], B.E. Scott[a], H.E. Upin[a]
[a]Utah State University, [b]University of Tennessee

which carbonate dissolution accounts for only a small fraction (average of 15%). The remaining carbon (1 to 44 mmol/kg) is derived from a mixture of deep CO_2 sources with endmember $\delta^{13}C$ values of -7 ‰ and -14 ‰ which, in light of relationships with $^{3}He/^{4}He$ ratios, are interpreted to be the subcontinental lithospheric mantle (SCLM) and metamorphic crustal carbon, respectively. These results are consistent with previous interpretations that slab-to-lithosphere fluid transfer is mobilizing volatiles from the SCLM to the continental crust above the flat slab and confirms that mantle CO_2 is migrating with mantle helium. Metamorphic CO_2 and N_2 are mobilized from the continental crust and entrained by mantle fluids on their way to the surface. In the backarc region, similar geochemical patterns suggest that volatiles are released by dehydration and/or partial melting of previously hydrated lithosphere. We estimate a CO_2 flux of ~ $3x10^{8}$ mol yr^{-1} (34 t d^{-1}) from 45 springs with available discharge values. If scaled to all reported thermal springs in Peru, then the total CO_2 emissions from Peruvian thermal springs may approach $2x10^{9}$ mol yr^{-1} (203 t d^{-1}), or ~0.2 % of global emissions from subaerial volcanism. Regional CO_2 emissions may be 10 to 100 times greater when considering CO_2 diffusely lost along fault zones or temporarily dissolved near-surface aquifers. These results demonstrate that flat-slab subduction leads to an efficient and unexpected transfer of mantle and crustal volatiles to Earth's surface, and more generally, that deep volatile fluxes in subduction zones are not limited to active volcanism.

1. INTRODUCTION

Constraining long-term sources and sinks of volatiles such as CO_2, H_2O, and N_2 is critical for understanding climate feedbacks and the chemical evolution of the Earth

system, with few processes exerting more control on volatile cycling than subduction. An important question is what proportion of volatiles carried into subduction systems are either delivered to the deep mantle, incorporated in the overlying lithosphere, or ultimately returned to the surface. Orogenesis along convergent margins is similarly important for volatile cycling and can act as a source of CO_2 via metamorphic fluid production, and as a sink for CO_2 via silicate weathering. A large body of research has focused on constraining these volatile fluxes (e.g., Sano and Williams, 1996; Sano et al., 2001; Hilton et al., 2002; Fischer et al., 2002; Shaw et al., 2008) but variability across subduction systems leaves many questions unanswered. Much of this work has focused on subaerial volcanism, but recently there has been more attention given to volatile fluxes in amagmatic regions of convergent margins (Chiodini et al., 2000; Mörner and Etiope, 2002; Barry et al., 2019; Hiett et al., 2021).

In a typical subduction zone, water released from the dehydrating slab leads to melting in the asthenospheric wedge and arc volcanism. Slab-derived volatiles and incompatible elements are then transferred to the continental lithosphere as components of the melt phase, with a portion of these volatiles delivered to the surface via volcanism (see review by Bebout, 2013). In a flat-slab subduction setting, the shallow dip of the subducting oceanic lithosphere essentially closes off the mantle wedge for hundreds of kilometers inboard of the trench and fluids are transferred directly into the overlying continental lithosphere. Without magmatism as an efficient transport mechanism, fluids are expected to lead to widespread hydration and metasomatism in the base of the continental lithosphere, inducing compositional changes that can have profound impacts on the geologic evolution of a convergent margin (e.g., Humphreys et al., 2003).

Hydration and metasomatism of the subcontinental lithospheric mantle (SCLM) and lower crust may lead to weaker rheologies, lower densities, decreased solidus temperatures, and chemical heterogeneities. These changes may then manifest as regional surface uplift, enhanced crustal shortening, explosive volcanism, and mantle instabilities (James and Sacks, 1999; Farmer et al., 2008; Levander et al., 2011; Lowry and Pérez-Gussinyé, 2011; Jones et al., 2015). Despite these implications, our understanding of this process is limited. Remaining questions include the spatial extent of fluid transfer, how fluids migrate through the SCLM and deep crust, and the extent of alteration in the lithosphere.

Evidence for this process has been observed in xenoliths and volcanic rocks from regions of ancient shallow subduction (e.g., Jones et al., 2015; Butcher et al., 2017; Farmer et al., 2020), as well as geophysical surveys from regions of both ancient and modern flat slabs (e.g. Humphreys et al., 2003; Porter et al., 2012). More recently, Newell et al. (2015) and Hiett et al. (2021) have shown that mantle helium is present in gas-rich thermal springs above the modern Peruvian flat slab, which in the absence of recent magmatism is interpreted to reflect slab-derived fluids mobilizing volatiles from the SCLM and into the overlying continental crust via upward migrating fronts of hydration reactions. Helium isotopes provide a relatively straightforward means for detecting mantle-derived helium (e.g., Ozima and Podosek, 2001), but helium is present in only trace amounts and other more abundant volatiles are involved in this fluid-transfer process, whether from the subducting slab, mantle wedge, or continental crust. CO_2 in particular is commonly invoked as a carrier gas for mantle helium in amagmatic settings (Kennedy et al., 1997; Kulongoski et al., 2005; Newell et al., 2005; de Leeuw et al.,

2010), and is the primary phase present in helium-bearing mantle fluid inclusions (Andersen and Neumann, 2001; Dunai and Porcelli, 2002; Gautheron and Moreira, 2002). Similarly, N_2 present in arc volcanic volatiles traces mantle, meteoric, and sedimentary sources (e.g., Fischer et al., 2002; Mitchell et al., 2010), but can also be enigmatically abundant more distal to magmatism with less constrained origins (e.g., Newell et al., 2008; de Moor et al., 2013). Unlike helium, tracing the origin of CO_2 and other volatiles (e.g., N_2) is more challenging due to the overlapping isotopic values of mantle and crustal sources, uncertainties in the isotopic composition of the deep crust, and the possibility of isotopic fractionation during processes such as metamorphic and hydrothermal degassing, mineral precipitation, or near-surface microbiological metabolism.

In this contribution we investigate the sources of CO_2 and N_2 in hot springs of the Peruvian Andes in the active flat-slab subduction setting and the adjacent backarc of the northern Altiplano. We present new C, N, O, and H stable isotope measurements of gases and waters from thermal springs with the goals of determining volatile sources and possible associations with slab-to-lithosphere fluid transfer processes. We combine this new isotopic data with previously published noble gas and stable isotopic compositions and gas abundances reported for these springs (Newell et al., 2015; Scott et al., 2020; Hiett et al., 2021). We show that much of the carbon emitted from Peruvian hot springs is deeply derived, with variable sources including the SCLM and continental crust. Nitrogen is largely atmospheric in origin but includes important components of mantle and crustal sedimentary nitrogen.

2. GEOLOGIC BACKGROUND

2.1. Subduction style along the Peruvian margin

The dynamic nature of oceanic-continental subduction is well demonstrated along the Andean margin, with both shallow and steeply dipping subduction angles as well as ancient episodes of low-angle subduction apparent from rock record (Ramos and Folguera, 2009). The Peruvian margin alone encompasses this range in subduction behavior and is therefore well suited for investigating the linkages between variations in subduction style and volatile cycling.

The Peruvian flat slab is one of three recognized modern flat-slab segments along the Andean margin and, at ~1500 km wide, is by far the largest. Arc volcanism began waning at ca. 12 Ma and was extinguished across most of the flat-slab region by ca. 4 Ma (Rosenbaum et al., 2005), suggesting that a flat-slab geometry was established by that time. For much of this region, arc volcanism appears to have been scarce or entirely absent for much longer (Rosenbaum et al., 2005). The Nazca Ridge, a marine aseismic ridge formed by the interaction of the Easter-Salas Hotspot and the East Pacific Rise, forms the southern boundary of the modern flat-slab subduction segment (Fig. 1). Along the ridge and to the north, the Nazca plate descends to a depth of ~100 km then becomes roughly horizontal until ~600 km inboard from the trench where it resumes a steep dive into the mantle (Gutscher et al., 2000b; Scire et al., 2016; Bishop et al., 2017). The northern end of the flat slab, near the Peru-Ecuador border, is hypothesized to coincide with the fully subducted Inca Plateau based on its conjugate bathymetric feature on the Pacific Plate, the Marquesas Plateau (Gutscher et al., 1999). A broad sag in the Nazca Plate exists between the Nazca Ridge and Inca Plateau, potentially due to buoyant

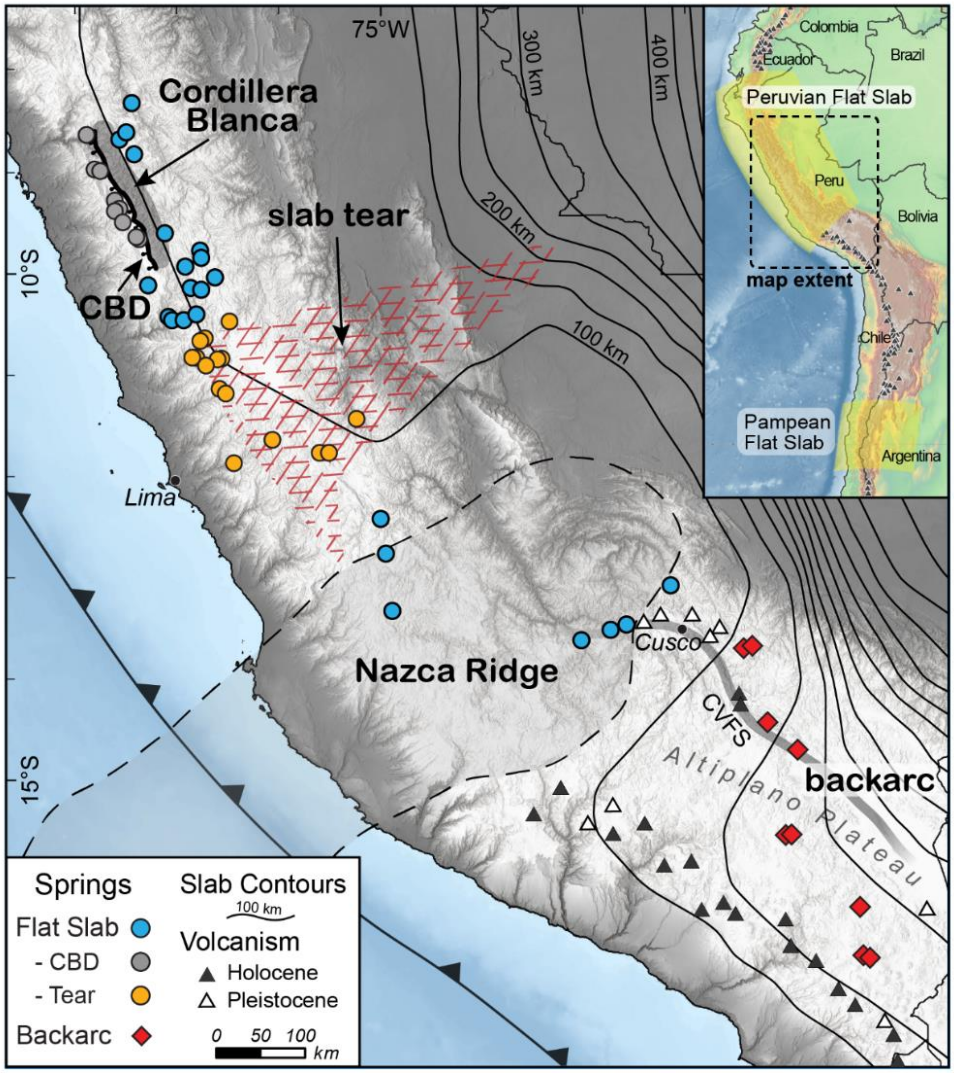

Figure 1. Map showing the location of hot springs discussed in this study and other key geologic features along the Peruvian margin. Springs from the modern flat-slab region are shown as circles with colors denoting their spring groups discussed in section 2.2. Springs from the backarc region are shown as red diamonds. Contours indicate the depth of the Nazca slab (after Scire et al., 2016). Locations of the CBD fault, Nazca Ridge (after Bishop et al., 2017), and backarc region are highlighted. The region overlying the slab-tear is shown by the red hatched pattern and combines interpretations from Antonijevic et al. (2015) and Scire et al. (2016). Quaternary volcanism is shown by the white (Holocene) and black (Pleistocene) triangles. Quaternary backarc volcanism follows the trace of the Cusco-Vilcanota fault system (CVFS). Inset map of western South America shows the locations of the Peruvian and Pampean flat slabs and Quaternary arc volcanism. (Digital terrain model courtesy of Esri, Airbus, USGS, NGA, NASA, CGIAR)

support from these features. Recent geophysical surveys have described a tear in the Nazca slab at the southern end of this sag (Fig. 1; Antonijevic et al., 2015, 2016; Scire et al., 2016; Bishop et al., 2017), although the extent and geometry of the tear is still unclear. Interactions between the tearing slab and the asthenosphere are supported by helium isotope data, with higher helium isotope ratios suggesting enhanced fluid transfer and faster volatile transit through the continental crust in the region above the tear (Hiett et al., 2021). Locally along the trace of the Nazca Ridge, the relatively small separation between the Moho of the subducting slab and the Moho of the overriding plate suggests that much, if not all, of the SCLM has been tectonically eroded by ridge subduction (Bishop et al., 2017). Our data is scarce in this area, but analyzed springs exhibit between 12 and 21% mantle helium (Hiett et al., 2021), suggesting that some thickness of the lithospheric mantle must be present above the Nazca Ridge. Interestingly, Axen et al. (2008) interprets similar processes during the Laramide orogeny in western North America where flat-slab subduction removed much, but not all of the SCLM.

South of the Nazca Ridge the subduction angle changes to a more typical ~30°, coincident with the reemergence of an active volcanic arc (Scire et al., 2016). Here the cordillera widens from 200 - 300 km in the north to more than 400 km wide to the south, forming the northern portion of the Altiplano Plateau. Arc volcanism in this region has shifted dramatically through the Cenozoic (Mamani et al., 2010), and along with patterns of crustal deformation, points to an Oligocene episode of shallow to flat-slab subduction in southern Peru (Isacks, 1988; Sandeman et al., 1995; James and Sacks, 1999; Ramos and Folguera, 2009). Scattered backarc volcanism has been relatively continuous since the end of the Oligocene, including small-volume mafic volcanism and large ignimbrite

eruptions (Carlier et al., 2005; Hoke and Lamb, 2007; Mamani et al., 2010). Quaternary volcanism is restricted to small-volume alkaline lava flows that erupted along the Cusco-Vilcanota fault zone (Fig. 1). Potassic and ultra-potassic compositions reflect a metasomatically enriched mantle source (Carlier et al., 2005) that is potentially related to the mid-Cenozoic episode of shallow subduction below the Altiplano.

2.2. Geothermal springs

Hot springs are common throughout the Peruvian Andes, with dramatic relief and variable heat flow providing the hydraulic gradients that promote deep groundwater circulation. Hot springs are commonly associated with, but are not restricted to, major fault systems or neotectonic structures and occur in various structural and lithological settings throughout the cordillera. We group springs in this study into those that occur in the modern flat-slab region and those from the active backarc of southern Peru (Fig. 1). Two subsets of springs within the flat-slab region are recognized, including springs in the region above the proposed tear in the Nazca slab and springs associated with the Cordillera Blanca Detachment (CBD) fault (includes springs issuing near the CBD fault trace and in the adjacent hanging wall). The ~200 km long WSW-dipping CBD fault has accommodated synconvergent orogen-perpendicular extension since ca. 5.4 Ma, with footwall exhumation of the ca. 14–5 Ma Cordillera Blanca Batholith producing the second highest topography in the Andes (Giovanni et al., 2010; Margirier et al., 2016), including Peru's highest peak, Huascarán (6,655 m). Thermal springs along the CBD fault and the slab-tear region exhibit higher $^{3}He/^{4}He$ ratios than springs from elsewhere

above the flat slab, suggesting that these tectonic features influence the slab-to-lithosphere fluid transfer process (Hiett et al., 2021).

Aqueous chemistries of spring waters are considerably variable, reflecting the diversity in local lithologies and structural settings across our study area (e.g., Scott et al., 2020). Regardless, springs are commonly salty (≤19,000 ppm TDS) and contain high dissolved gas loads, with many of the sampled springs actively effervescing (bubbling). Small bubble trails are most common in bubbling springs, but many springs exhibit vigorous degassing (noted in the field as "Jacuzzi jets"; Fig. 2a). Spring waters have temperatures ranging from 17 to 90 °C and are slightly acidic to slightly alkaline (pH = 5.0 – 8.0). Most springs exhibit active or relatively recent carbonate precipitation at the surface, and several have developed especially large travertine deposits. For example, most of the town of Huancavelica (spring sample DN19CP-31) is built on a travertine deposit with an aerial extent of ~2.3 km^2 (Morche et al., 2003), and the travertine spring mound complex at Aguas Calientes (spring sample DN19CP-30) extends for ~150 vertical meters down the hillside (Fig. 2b). Reservoir temperature estimates (RTE) of 200 – 275 °C for springs along the CBD fault suggest maximum fluid circulation to depths of 9 or 11 km depending on choice of geothermal gradient (Newell et al., 2015; Scott et al., 2020). In the same region but distal to the CBD fault, RTE of 40 – 98 °C suggest more modest circulation depths to <4 km (Scott et al., 2020).

Dissolved inorganic carbon concentrations (DIC) and gas abundances are reported in Hiett et al. (2021) and are briefly summarized here. DIC concentrations (includes aqueous CO_2, H_2CO_3, HCO_3^- and CO_3^{2-}) ranges from 1.3 to 57 mmol/kg (average of 20 mmol/kg), with log P_{CO2} from -2.96 to 0.46 atm. Springs within the flat-slab region, but

Figure 2. Photos showing examples of vigorously degassing hot springs and large travertine spring deposits in Peru. a) Gas discharges at Acaya hot spring (sample DN19CP-26), part of the slab-tear group, noted in the field as resembling "Jacuzzi jets". b) Large (~150 m tall) travertine spring mound at Aguas Calientes (sample DN19CP-30). The telephone pole on the right side of the photo (noted by white arrow) is ~15 m tall.

unassociated with the CBD fault or slab tear region, generally have the lower concentrations of DIC. Spring gases are generally dominated by CO_2 and N_2, with C/N ratios ranging from 0.02 to 38.9 (average of 5.4). N_2-Ar-He relationships are similar to magmatic and crustal gases in intercontinental and mid-ocean ridge settings, suggesting mixing between He-rich deeply derived fluids and meteoric waters. Backarc springs show consistently higher N_2/Ar ratios compared to springs above the flat slab. Helium isotope ratios ($^3He/^4He$) fall between 0.26 and 2.52 R_C/R_A (where R_C is the air corrected ratio in the sample, normalized to the air ratio, R_A, of 1.39×10^{-6}; O'Nions and Oxburgh, 1988), and show no clear correlation to gas abundances. $CO_2/^3He$ ratios span a uniquely wide range from mantle-like values of 7.9×10^9 towards crustal values as high as 8.2×10^{16} and show a strong inverse correlation with helium concentrations, interpreted to reflect solubility-based fractionation during open-system phase separation in the geothermal systems (Weiss, 1971, 1974; de Leeuw et al., 2010).

3. METHODS

3.1. Sample collection

Spring sampling in Peru was conducted over the course of five field campaigns between 2013 and 2019. In total, 56 springs were analyzed for carbon stable isotope ratios ($\delta^{13}C$ of CO_2 and DIC), 24 for nitrogen stable isotope ratios ($\delta^{15}N$ of N_2), 70 for water oxygen and hydrogen stable isotope ratios ($\delta^{18}O$ and δ^2H), 52 for noble gas isotopes and concentrations, and 37 for relative gas abundances. Aqueous geochemistry and stable isotope analyses ($\delta^{13}C$, $\delta^{18}O$ and δ^2H) for springs along the CBD fault are reported in Newell et al. (2015). Aqueous geochemistry and stable isotope analyses ($\delta^{13}C$,

$\delta^{18}O$, and $\delta^{2}H$) of springs from the adjacent region, including the Cordillera Huayhuash and footwall of the CBD fault are reported in Scott et al. (2020). Helium isotope ratios ($^{3}He/^{4}He$) and gas abundances for the entire spring transect are reported in Hiett et al. (2021).

Springs were targeted based on a combination of high temperature, high salinity, and accessibility. Samples were collected as close to the spring source as possible to avoid the effects of degassing and atmospheric exchange. Temperature, pH, and conductivity were measured in the field using an Oakton portable multimeter. Springs were sampled for major and trace element chemistry using standard groundwater sampling techniques (U.S. Geological Survey, 2006). At each spring, water was collected in amber glass vials with no headspace for carbon stable isotope analysis of dissolved inorganic carbon ($\delta^{13}C_{DIC}$), and water $\delta^{18}O$ and $\delta^{2}H$. At springs that were actively bubbling, additional samples for stable isotope analysis of CO_2 gas ($\delta^{13}C_{CO2}$) and N_2 gas ($\delta^{15}N$) were collected in 12 ml Exetainer® vials by filling vials with spring water and inverting them underwater to allow gas to replace the water (after Newell et al., 2008). For most springs sampled in 2019, splits of dry gas were collected in 12 mL evacuated Exetainer® vials during gas abundance analysis at the University of New Mexico Volatiles Laboratory for analysis of $\delta^{15}N$ of N_2 from non-bubbling springs. 19 water samples were collected from rivers and cold springs throughout spring sampling in order to establish $\delta^{18}O$ and $\delta^{2}H$ values for local meteoric waters. Sampling protocols for noble gas isotopes and concentrations and relative gas abundances are described in Hiett et al. (2021).

3.2. Chemical and isotopic analysis

Major and trace element concentrations in hot spring water were measured at the Utah State University (USU) Water Research Laboratory using a Dionex Ion Chromatograph (anions) and an Agilent Inductively Coupled Plasma-Mass Spectrometer (cations). The minimum reporting limits for major ions and trace elements are reported in Supplementary Tables B.4 and B.5. The uncertainty on major cations and anions is ±2 mg/L and for trace elements is ±1.8 µg/L. Total alkalinity was measured by manual colorimetric titration. The geochemical modeling software PHREEQC (Parkhurst and Appelo, 2013) was used to model equilibrium aqueous chemistries for each spring, including total DIC concentrations, ion speciation, P_{CO2}, and mineral solubility indices.

For hot springs sampled along the CBD fault and adjacent hanging wall, carbon isotope measurements were performed at the Scripps Institution of Oceanography using a Thermo Finnigan Delta Plus isotope ratio mass spectrometer (IRMS) using dual-inlet methods. Results for these samples are reported in Newell et al. (2015) and included herein. For all other spring samples, $\delta^{13}C$, $\delta^{15}N$, $\delta^{18}O$ and $\delta^{2}H$ values were determined at the USU Department of Geosciences Stable Isotope Laboratory via continuous flow (CF-IRMS) methods using a Thermo Scientific Delta V Advantage IRMS with Thermo Scientific TC/EA and GasBench II interfaces. Isotopic measurements are reported using delta notation in per mil (‰). Carbon isotope compositions of CO_2 gas ($\delta^{13}C_{CO2}$) and DIC ($\delta^{13}C_{DIC}$) were measured using the Gasbench II and are calibrated to the Vienna Pee Dee Belemnite (VPDB) scale using NBS-19 and USGS-44 with an uncertainty of ± 0.1 ‰ based on repeat analyses of in-house calcite standards. The $\delta^{13}C_{DIC}$ measurements

followed a modified phosphoric acid method (Salata et al., 2000) as described in Scott et al. (2020).

Nitrogen stable isotope compositions ($\delta^{15}N$ values) of spring gases were determined using the Gasbench II and were calibrated to AIR (0.0 ‰) using methods modified from Newell et al. (2008) and de Moor et al. (2013). To prevent back-streaming of atmosphere into the sample line during $\delta^{15}N$ analysis with the Gasbench II interface, sample vials were brought to ambient pressure by injecting with ultra-pure helium using a two-hole Gasbench needle with low helium flow rate. The length of the outflow capillary was extended to ~3 m and the end submersed in vacuum pump oil. Helium was injected into the vial until bubbling occurred through the outflow capillary. Reported $\delta^{15}N$ values have an uncertainty of ± 0.2 ‰ based on repeat analyses of air standards.

High-temperature conversion elemental analysis (TC/EA) and CO_2 equilibration (Gasbench II) were used to determine oxygen and hydrogen isotopic compositions, respectively. $\delta^{18}O$ and $\delta^{2}H$ values are reported relative to Vienna Standard Mean Ocean Water (VSMOW), calibrated using VSMOW and Standard Light Antarctic Precipitation (SLAP) standards (Nelson, 2000). Based on replicate analyses of in-house standards, analytical precision for $\delta^{18}O$ and $\delta^{2}H$ values was 0.06 ‰ and 2.0 ‰, respectively.

Analytical approaches for determining $^{3}He/^{4}He$ ratios, $CO_2/^{3}He$, absolute and relative gas compositions are discussed in Hiett et al. (2021). It is important to note that measured noble gas concentrations of free gas samples were used to calculate dissolved concentrations to allow for equal comparison of helium concentrations, $CO_2/^{3}He$, and He/Ne ratios between water and gas samples.

3.3. Carbon isotope modeling

In bubbling springs, equilibrium isotopic fractionation between CO_2 gas and DIC leads to a relative depletion in $^{13}CO_2$ in the exsolving gas phase, leading to lower $\delta^{13}C$ values of CO_2 gas compared to the remaining DIC (Deines et al., 1974). We use the measured $\delta^{13}C_{CO2}$ and $\delta^{13}C_{DIC}$ to model the initial $\delta^{13}C$ value ($\delta^{13}C_i$) of spring water before degassing, allowing for accurate comparison of $\delta^{13}C$ values for all springs, whether actively degassing or not. This process is modeled as an open-system (Rayleigh) fractionation process under equilibrium conditions using (e.g., Sharp, 2017):

$$\delta^{13}C_{DIC} = \delta^{13}C_i + (1000 + \delta^{13}C_i)\,[f^{(\alpha-1)}-1] \quad (1)$$

$$\delta^{13}C_{CO2} = [1000 + \delta^{13}C_i - (1000 + \delta^{13}C_i)\,(f)^{\alpha} - 1000f]/f \quad (2)$$

where $\delta^{13}C_{CO2}$ is the integrated isotopic value of the exsolved CO_2 gas, f is the fraction of DIC remaining (from 1 to 0), and α is the temperature dependent fractionation factor between CO_2 and DIC species ($\alpha_{CO2\text{-}DIC}$). The fractionation factor is calculated from the individual temperature dependent fractionations between CO_2 and H_2CO_3 or HCO_3^- ($\alpha_{CO2\text{-}H2CO3}$, $\alpha_{CO2\text{-}HCO3\text{-}}$) weighted by the relative proportions of H_2CO_3 and HCO_3^- determined using PHREEQ (Deines et al., 1974; Supplementery Table B.2). CO_3^{2-} concentrations are negligible at the observed pH range (5.0 to 8.0) and are not considered.

4. RESULTS AND DISCUSSION

4.1. Oxygen and Hydrogen

New $\delta^{18}O$ and $\delta^{2}H$ values for 40 hot springs are reported along with previously published $\delta^{18}O$ and $\delta^{2}H$ values from Newell et al. (2015) and Scott et al (2020) in Supplementary Table B.1. By spring group, $\delta^{18}O$ and $\delta^{2}H$ values range from -16.8 to -12.8 ‰ and -130 to -95 ‰ (flat slab), -14.7 to -4.9 ‰ and -113 to -74 ‰ (CBD), -16.4 to -9.4 ‰ and -123 to -69 ‰ (slab tear), and -17.9 to -9.4 ‰ and -141 to -121 ‰ (backarc) (Fig. 3). We also report new $\delta^{18}O$ and $\delta^{2}H$ values for 15 surface waters sources in the flat-slab and backarc region (Supplementary Table B.3), which along with previously reported meteoric water values from Scott et al. (2020) define a local meteoric water line (LMWL) with a slope of 6.9 (r^2= 0.80), slightly lower than the global meteoric water line (GMWL; slope = 8; Craig, 1961). Two meteoric water samples exhibit $\delta^{18}O$ and $\delta^{2}H$ values that fall significantly to the right of the GMWL and are excluded from the LMWL regression. One of these samples is from Lake Titicaca, of which evaporation accounts for an estimated 91 % of water loss (Roche et al., 1992), and the other is a small pond with no outlet near the town of Quiches (Scott et al., 2020). Evaporation from isolated bodies of water can lead to isotopic evolution with a slope less than the GMWL (Craig and Gordon, 1965).

The majority of springs, including all springs from the flat slab and tear groups, fall near both the LMWL and GMWL (Fig. 3). CBD fault springs generally fall higher along the meteoric water lines (higher $\delta^{18}O$ and $\delta^{2}H$ values), while backarc springs fall lower along meteoric water lines (lower $\delta^{18}O$ and $\delta^{2}H$ values). A number of springs from the CBD and backarc suites form separate positive trends away from the meteoric water

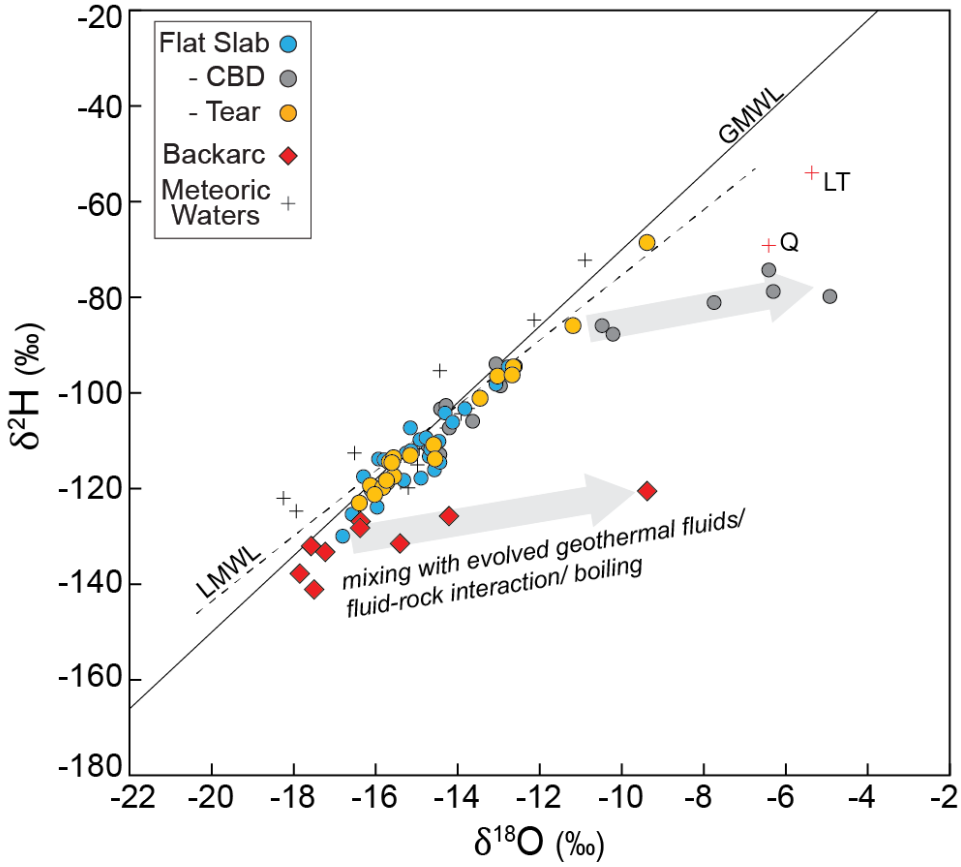

Figure 3. $\delta^{18}O$ versus $\delta^{2}H$ values (vs VSMOW) for hot springs and local meteoric water samples from across the Peruvian margin. Meteoric waters define a local meteoric water lines (LMWL) with slightly lower slope than the global meteoric water line (GMWL; Craig, 1961). Most hot springs plot near the LMWL and GMWL, demonstrating the meteoric origin of spring waters. Springs from the backarc and springs associated with the CBD fault form linear trends with slopes less than the meteoric water lines which are attributed to mixing with deep saline hydrothermal fluids and high-temperature fluid-rock interactions. Two meteoric samples are not included in the LMWL regression (red crosses) due to anomalously high $\delta^{18}O$ values associated with evaporation in isolated bodies of water (LT = Lake Titicaca, Q = Quiches). Analytical errors associated with $\delta^{18}O$ versus $\delta^{2}H$ measurements are smaller than symbol size.

lines, with some springs falling near meteoric water values and others trending towards higher $\delta^{18}O$ and $\delta^{2}H$ values. As individual datasets, $\delta^{18}O$ and $\delta^{2}H$ values from CBD springs and backarc springs form positive linear correlations with slopes of 3.4 (r^2 = 0.9) and 1.9 (r^2 = 0.6), respectively.

The close accordance between the majority of the springs and the meteoric water lines demonstrates the overwhelmingly meteoric origin for water in the geothermal systems. Positive correlations to higher $\delta^{18}O$ and $\delta^{2}H$ values than the meteoric water lines seen in CBD and backarc springs may be explained by kinetic isotope fractionation associated with evaporation or steam separation during boiling, by mixing with deeply-circulated hydrothermal fluids, and/or water isotopic exchange with bedrock at elevated temperatures. Interaction between geothermal fluids and silicate bedrock will increase the $\delta^{18}O$ values of geothermal waters due to isotopic exchange with silicates, but the $\delta^{2}H$ values are only minimally affected leading to near-horizontal trends from the GMWL to higher delta values (Taylor, 1977). For CBD springs, Newell et al. (2015) and Scott et al. (2020) identified a positive correlation between $\delta^{18}O$ values, and Cl^- and HCO_3^- concentrations, suggesting that mixing between infiltrating meteoric waters and a deep saline hydrothermal brine exerts control over water chemistry. These correlations are not present in the backarc springs. Instead, we note statistically significant positive correlations between $\delta^{18}O$ and dissolved K (r^2 = 0.7, p = 0.005) and As (r^2 = 0.7, p = 0.004), which suggests that high-temperature fluid interaction with silicates and other minerals is likely responsible for increased K and As concentrations as well as higher $\delta^{18}O$ values (Supplementary Fig. B.1). However, similar correlations with other dissolved ions are not observed. We also note a modest positive correlation between $\delta^{18}O$ values

and $^{3}He/^{4}He$ for backarc springs (r^2 = 0.45, p = 0.05) that is not observed in other spring groups. This correlation suggests that thermal fluids that preserve evidence of high-temperature oxygen isotope exchange with bedrock are also associated with higher fluxes of mantle-derived helium.

4.2. Nitrogen

Nitrogen stable isotope values are reported in Supplementary Table B.1 for 24 springs from the flat-slab region (including the slab-tear region) and backarc. By spring group, $\delta^{15}N$ values range from +0.4 to +2.0 ‰ (flat slab), -0.5 to +4.4 ‰ (tear), and +0.3 to +3.7 ‰ (backarc). N_2/He, N_2/Ar, and C/N_2 ratios reported in Hiett et al. (2021) range from 39 to $4.1x10^4$ (average of $3.6x10^3$) and 23 to 750 (average of 89), and 0.02 to 39 (average of 5.4), respectively. $\delta^{15}N$ values do not show any clear correlation with gas abundance ratios or other stable isotope measurements and span a similar range for springs from the flat-slab region and backarc.

Possible nitrogen sources included air (0 ‰), crustal/sedimentary nitrogen (+7 ± 4 ‰), and mantle-derived nitrogen (-5 ± 2 ‰ for MORB-mantle; Sano et al., 2001). In contrast to the MORB-mantle, the isotopic signature of the SCLM is poorly constrained and likely quite variable depending on the history of metasomatism, melt depletion, and sediment underplating (e.g., Yokochi et al., 2009; Barry and Broadley, 2021). However, estimated $\delta^{15}N$ values for mantle wedge fluids (~-15‰; Yamamoto et al., 2020), metasomatized Siberian SCLM (-7 ± 1‰; Barry and Broadley, 2021), and pristine European SCLM (-4.5 ± 1 ‰; Bräuer et al., 2004) are distinctly low compared to atmospheric and sedimentary nitrogen.

Because $\delta^{15}N$ values result from mixing between atmospheric (meteoric), mantle, and sedimentary nitrogen, $\delta^{15}N$ values are commonly combined with N_2/He ratios which help to distinguish mantle or crustal gasses from air (e.g., Fischer et al., 2002) (Fig. 4). Together, $\delta^{15}N$ values and N_2/He ratios can be used to determine the mixing ratios (*f*) of nitrogen from air (N_2/He = $1.489x10^5$), sediment (N_2/He = $1.05x10^4$), and mantle (N_2/He = 150 for MORB) for each sample using the following equations (following Sano et al., 2001; Fischer et al., 2002):

$$(\delta^{15}N)_{obs} = f_M(\delta^{15}N)_M + f_A(\delta^{15}N)_A + f_S(\delta^{15}N)_S \quad (3)$$

$$1/(N_2/He)_{obs} = f_M/(N_2/He)_M + f_A/(N_2/He)_A + f_S/(N_2/He)_S \quad (4)$$

$$f_M + f_S + f_A = 1 \quad (5)$$

where the subscripts A, S, M, and obs refer to the $\delta^{15}N$ and N_2/He values for the air, sediment, mantle, and observed values, respectively. Calculated mixing ratios are given in Supplementary Table B.1. We choose MORB as the mantle endmember due to the uncertainty in values for the SCLM. Most Peruvian hot springs (excluding two) can be explained by mixing between atmospheric nitrogen and a deep nitrogen endmember composed of 47 to 88 % sedimentary nitrogen (%S) and 53 to 12 % mantle-derived nitrogen (where %S = 100 x f_S / (f_S + f_M); Fig. 4). This approach assumes that nitrogen and helium are not fractionated during transport from mantle or crustal sources, or modified within shallow thermal systems (e.g., via microbial metabolism impacting N_2 concentrations).

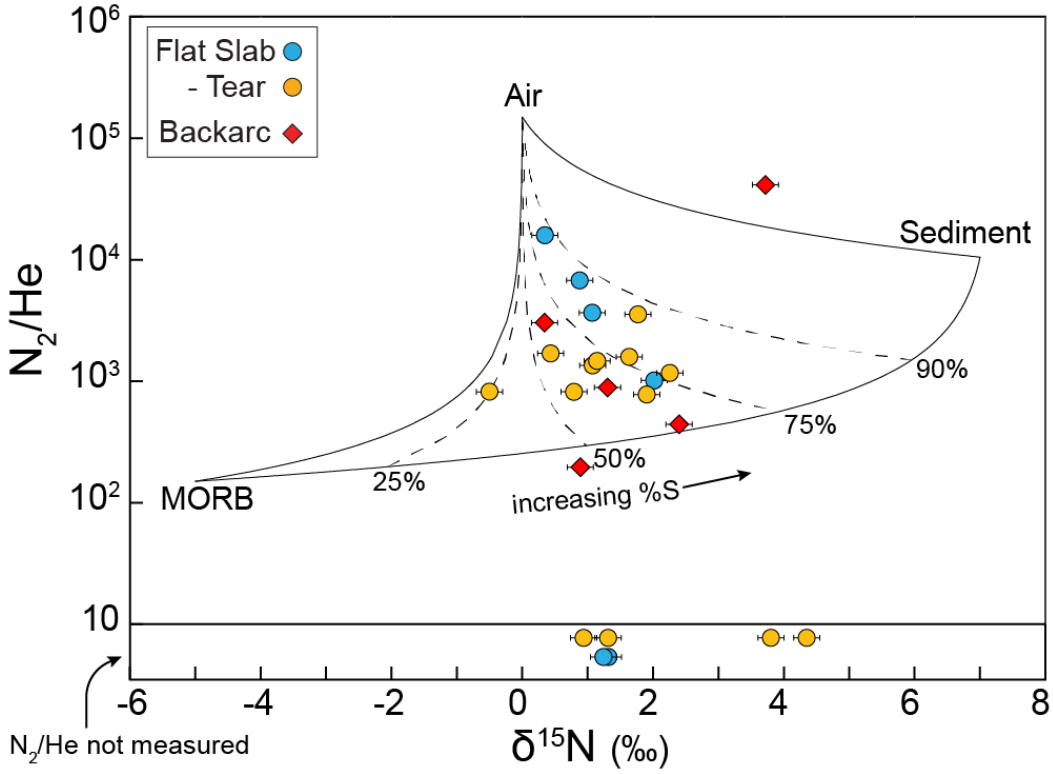

Figure 4. Plot of $\delta^{15}N$ versus N_2/He for a subset of springs and endmember N_2 sources including air (0 ‰, 1.489×10^5), sediments (+7 ‰, $1.05x10^4$), and MORB mantle (-5 ‰, 1.5×10^2). We also show $\delta^{15}N$ values for springs without measured N_2/He ratios at the bottom of the plot. Endmember $\delta^{15}N$ and N_2/He values are from Sano et al. (2001) and Fischer et al. (2002). Solid lines represent binary mixing between endmember N_2 sources. Dashed lines represent air addition to a mixture of sedimentary and mantle nitrogen, denoted by the percent of sedimentary nitrogen (%S). Most Peruvian hot springs (excluding 2) can be explained by mixing between atmospheric nitrogen and a deep nitrogen endmember composed of 47 to 88 %S. Error bars are ± 0.2 ‰.

Hiett et al. (2021) noted that backarc springs yielded higher N_2/Ar and N_2/He ratios on average when compared to other springs from the flat-slab region. Nitrogen isotopes do not offer any indication for different nitrogen sources between springs in the backarc or flat-slab region. In any case, isotopic and abundance data indicate that there is

a component of deeply sourced nitrogen in Peruvian springs, likely of crustal sedimentary origin with modest contributions of mantle nitrogen.

4.3. Carbon

New $\delta^{13}C$ values (includes measured $\delta^{13}C_{DIC}$ and modeled $\delta^{13}C_i$ for non-bubbling and bubbling springs, respectively) are reported along with previously published $\delta^{13}C$ values from Newell et al. (2015) and Scott et al (2020) in Supplementary Table B.1. From bubbling springs, the measured $\delta^{13}C_{DIC}$ and $\delta^{13}C_{CO2}$ values and other parameters used to model $\delta^{13}C_i$ are shown in Supplementary Table B.2. $\delta^{13}C$ values of all springs range from --13.6 to -0.3 ‰, with an average value of -6.9 ‰. Springs from each spring group exhibit similar ranges of $\delta^{13}C$ values and do not cluster towards specific values. One exception to this are springs from the CBD fault and adjacent hanging wall which all yield values in the lower half of the data range (-13.6 to -6.3 ‰). There is no correlation between $\delta^{13}C$ values and He/Ar, N_2/Ar, or C/N_2 ratios. Instead, $\delta^{13}C$ values exhibit only modest variability across a wide range of volatile abundance ratios (e.g. C/N_2; Fig. 5).

4.3.1. Distinguishing external carbon

The high DIC and P_{CO2} in the investigated springs (section 2.2) are distinct from natural ground waters in the absence of an external CO_2 source, and the wide range in $\delta^{13}C$ values implies that carbon is derived from multiple sources. Infiltrating meteoric waters have low initial DIC (~0.03 mmol/kg) and $\delta^{13}C$ values near -4.5 ‰ (VPDB), reflecting equilibrium with atmospheric CO_2 ($\delta^{13}C$ = -8 ‰; Chiodini et al., 2000). As groundwater infiltrates through soils, CO_2 from microbial respiration dissolves into

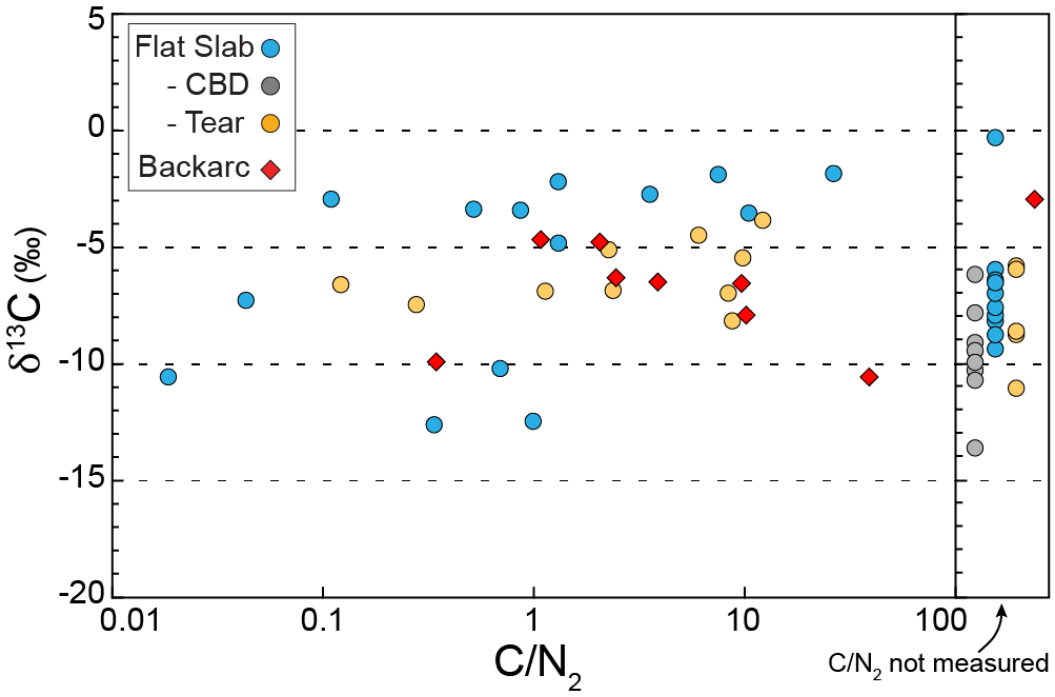

Figure 5. Plot of $\delta^{13}C$ vs C/N_2 ratios showing the range in $\delta^{13}C$ values (includes measured $\delta^{13}C_{DIC}$ and modeled $\delta^{13}C_i$ for non-bubbling and bubbling springs, respectively) for each spring group. $\delta^{13}C$ values for springs with unknown C/N_2 ratios are shown on the right. Error associated with $\delta^{13}C$ measurements is roughly the size of the symbols.

groundwater, increasing DIC while lowering $\delta^{13}C$ values (~ -18 to -28 ‰ depending on ecological conditions; e.g., Deines et al., 1974; Chiodini et al., 2000). Dissolved CO_2 lowers the pH of groundwaters via the production of carbonic acid, and in turn leads to the dissolution of carbonate minerals and bedrock (~0 ‰; Craig, 1953) and increase in $\delta^{13}C$ values. Dissolution of carbonate consumes H^+ and acts to increases the pH of groundwaters and naturally limits the amount of carbonate dissolution that can occur. Modeling of this stepwise process of soil CO_2 addition and subsequent carbonate dissolution results in infiltrating waters with $\delta^{13}C$ values between -10 and -17 ‰ and low to moderate DIC concentrations (<10 mmol/kg; Chiodini et al., 2000), in agreement with

observations of natural ground waters in cratonic regions (e.g., Deines et al., 1974; Zhao et al., 2015). Thus, DIC up to 57 mmol/kg and variable $\delta^{13}C$ values observed in Peruvian hot springs require significant additional inputs of CO_2 from carbonates.

A simple geochemical model uses the aqueous chemistry of spring waters to estimate the amount of DIC derived from dissolution of carbonate bedrock within the geothermal system, allowing us to more accurately define the amount and isotopic character of carbon derived from either organic or deeper sources (i.e., crustal or mantle fluids). Because the dissolution of carbonate bedrock results in equal molar concentrations of carbon and $Ca^{2+} + Mg^{2+}$, and because SO_4^{2-} concentrations are approximately equal to the amount of Ca^{2+} derived from the dissolution of gypsum and anhydrite, we calculate the concentration of DIC from carbonate bedrock (C_{carb}, in mmol/kg; following Chiodini et al., 2000) as:

$$C_{carb} = Ca^{2+} + Mg^{2+} - SO_4^{2-} \quad (6)$$

with the remaining carbon from organic or deep sources, referred to as external carbon (C_{ext}), calculated as:

$$C_{ext} = DIC - C_{carb} \quad (7)$$

This approach is valid under the assumptions that fluid interaction with silicate bedrock is not a primary control on Ca^{2+} and Mg^{2+} concentrations, and that SO_4^{2-} is derived primarily from dissolution of gypsum or anhydrite. Control of aqueous chemistry by equilibrium with marine carbonates and evaporites is consistent with local bedrock geology in this region. Although chemical exchange between geothermal fluids and silicate minerals is likely (section 4.1), this process is expected to be of second-order

importance for Ca^{2+} and Mg^{2+} concentrations (e.g., Chiodini et al., 2000; Crossey et al., 2009). Another factor that could impact the calculation of C_{carb}, in this geologic setting is the dissolution of carbonates in the subducting slab or deep continental lithosphere by aqueous fluids contributing dissolved Ca^{2+}, Mg^{2+}, and CO_2 to migrating fluids (e.g., Ague and Nicolescu, 2014). Not properly accounting for these cations would lead to an overestimation of C_{carb} and underestimation of C_{ext}. However, we suggest that Ca^{2+} or Mg^{2+} liberated to fluids in these deep settings would not be as mobile as CO_2 and most likely be reprecipitated in silicate minerals before contributing to the chemistry of shallow geothermal fluids.

Using this model, C_{carb} accounts for 0 to 41 % of the total DIC, with an average of 15 %. The remaining DIC (C_{ext}) is derived from either shallow organic sources, including soil CO_2 or oxidation of organic matter in sediments, or from deep sources, which encompasses carbon from crustal fluids, mantle fluids, or potentially the subducting slab. Because the isotopic composition of C_{carb} can be estimated at ~ 0 ‰ (Craig, 1953), the $\delta^{13}C$ value of C_{ext} ($\delta^{13}C_{ext}$) can be calculated by mass balance (following Chiodini et al., 2000) using:

$$C_{ext} \times \delta^{13}C_{ext} = (DIC \times \delta^{13}C) - (C_{carb} \times \delta^{13}C_{carb}) \quad (8)$$

Figure 6 shows the relationship between $\delta^{13}C_{ext}$ values and C_{ext} for each spring. Previous authors employing this method have observed trends explained by binary mixing between a low C_{ext} endmember with low $\delta^{13}C_{ext}$ (< 4 mmol/kg and -28 ‰), reflecting small contributions of near-surface-derived carbon from organic sources, with a high C_{ext} endmember with $\delta^{13}C_{ext}$ values of -6 or -3 ‰, interpreted as a generalized deep

carbon source (inset, Fig. 6; Chiodini et al., 2000; Crossey et al., 2009). Peruvian springs do not conform to a similar single binary mixing trend and instead show evidence for multiple sources of external inorganic carbon, leading to high C_{ext} with variable $\delta^{13}C_{ext}$ values. Hot springs with high C_{ext} (> 20 mmol/kg) form two distinct trends, one towards a $\delta^{13}C_{ext}$ value of -7 ‰ and another towards -14 ‰. Only one spring exhibits low $\delta^{13}C_{ext}$ values and low C_{ext} concentrations that are commonly attributed to DIC dominated by soil CO_2, and one spring has high C_{ext} with a uniquely low C_{ext} value of -18.9 ‰. Deep carbon sources with $\delta^{13}C_{ext}$ values of -7 and -14 ‰ therefore appear to dominate the DIC budget of Peruvian hot springs.

A few samples with moderate C_{ext} concentrations trend towards higher $\delta^{13}C_{ext}$ values (~0 ‰). The majority of springs forming this trend are from the flat-slab region but unassociated with the slab tear or CBD fault (Fig. 1). One possible explanation is that carbonate bedrock is a source of C_{ext} in these springs. Dissolved carbonate sources are accounted for and removed from these calculated C_{ext} and $\delta^{13}C_{ext}$ values using equations (6) – (8); however, carbonates may still contribute CO_2 to crustal fluids via thermal decomposition (decarbonation), or potentially from deep carbonate dissolution from the slab, mantle or lower crust (e.g., Ague and Nicolescu, 2014). An alternative explanation for some of the data is that isotopic fractionation during open-system degassing in the geothermal systems has led to higher $\delta^{13}C$ values in these springs. On the basis of $CO_2/^3He$ ratios and their relationship to He concentrations, Hiett et al. (2021) concluded that open-system degassing within the geothermal systems is likely responsible for elevated $CO_2/^3He$ in many of these springs, due to the much lower solubility of He compared to CO_2. At low temperatures (<110 °C) this process can lead to isotopic

fractionation, with $^{13}CO_2$ depleted in the vapor phase compared to $^{12}CO_2$, increasing the $\delta^{13}C$ of the residual fluid (Vogel et al., 1970). Flat-slab springs, which are on average cooler than other groups, show a general trend towards higher $\delta^{13}C$ values with increasing $CO_2/^3He$ (section 4.3.3; figure 8), suggesting that degassing processes in concert with CO_2 additions from deep carbonate sources are responsible for data patterns.

Carbonate precipitation at depth can similarly modify $\delta^{13}C$ values as CO_2 rich fluids migrate through the crust. At low to moderately high fluid temperatures, ^{13}C is favored in the precipitating carbonate driving the remaining fluid towards progressively lower $\delta^{13}C$ values (Bottinga, 1968). This process has been invoked in the cold forearc region of Costa Rica to explain patterns of lower $\delta^{13}C$ values in springs with lower DIC that appear to follow Rayleigh fractionation trends (Barry et al., 2019). This pattern of progressively lower $\delta^{13}C_{ext}$ values with decreasing C_{ext} is not evident in most of our dataset, with possible the exception of some springs from the flat slab region. Additionally, most springs have relatively high carbonate alkalinity and Ca concentrations, are slightly acidic, and have high P_{CO2}, which are not consistent with geothermal waters that have lost large portions of their carbon to carbonate minerals before reaching the surface. Although this process cannot be completely ruled out, we suggest it is not a significant process in our study area.

4.3.2. Potential deep carbon sources

Potential sources of deep CO_2 may include mantle-derived fluids, metamorphic fluids from the continental crust, or fluids released from the devolatilizing Nazca Plate during subduction. Mantle-derived CO_2 is commonly observed in regions of active

volcanism, where it is advected through the crust as a component of the melt and exsolved with decreasing pressure and temperature. Fluxes of mantle carbon unassociated with magmatism are also observed along large transverse fault systems such as the San Andreas and Anatolian faults, as well as in some orogenic belts and plateaus (Kennedy et al., 1997; Newell et al., 2005; de Leeuw et al., 2010; Karlstrom et al., 2013; Kulongoski et al., 2013). These observations are generally interpreted to reflect passive degassing of active, and perhaps partially molten asthenosphere, with the highest fluxes through steeply dipping crustal shear zones with high strain rates (Kennedy and Van Soest, 2007). Asthenospheric carbon is characterized by a relatively narrow range of $\delta^{13}C$ values (-6.5 ± 2.5‰) and $CO_2/^3He$ ratios (~$2x10^9$; e.g., Marty and Jambon, 1987; Sano and Marty, 1995). The chemical and isotopic signature of the SCLM is generally similar to the asthenosphere but more variable, reflecting the potential for open system chemical evolution such as metasomatic enrichment and melt depletion in subduction systems. Reported $\delta^{13}C$ values for the SCLM range from -2 to -8 ‰ (Cartigny, 2005; Hahm et al., 2008; Lee et al., 2016; Bräuer et al., 2016), with $CO_2/^3He$ ratios ranging up to 10^{13} (Dunai and Porcelli, 2002) but commonly < $8x10^9$ (Hahm et al., 2008; Fischer et al., 2009; Lee et al., 2016; Bräuer et al., 2016).

There is no evidence for active magmatism in the flat-slab region over the last ca. 4 Ma, consistent with previous suggestions that thermal conditions in a flat-slab setting are insufficient for melting to occur (Gutscher et al., 2000a). The mantle material sandwiched between the subducting Nazca Plate and continental crust is expected to be relatively cold and isolated from convective asthenosphere and is therefore best described as SCLM. Mantle-derived helium in Peruvian thermal springs is interpreted to be sourced

from the SCLM, where it is mobilized by infiltrating slab-derived fluids (Newell et al., 2015; Hiett et al., 2021). Fluid transfer leads to hydration and metasomatism in the SCLM, and mantle volatiles stored primarily in fluid inclusions are released into the migrating volatile phase. Xenolith studies show that CO_2-rich fluids commonly occupy mantle fluid inclusions (Andersen and Neumann, 2001; Dunai and Porcelli, 2002; Gautheron and Moreira, 2002), and therefore represent a possible source for deep CO_2 associated with mantle helium.

Metamorphism and metasomatism within the continental crust may also be a significant source of CO_2. Carbonate minerals and organic carbon in metasediments will both react to produce CO_2 at high temperatures, which can be facilitated by the presence of free water (Kerrick et al., 1995; Kerrick, 2001). Isotopic fractionation during decarbonation will lead to CO_2 enriched in ^{13}C relative to carbonate bedrock by up to ~+4 ‰ (Chacko et al., 1991). The isotopic composition of CO_2 produced through pyrolysis of organic sediments is highly dependent on the redox conditions in the fluid environment, but is likely to be relatively depleted in $^{13}CO_2$ (Giggenbach, 1997; Evans et al., 2008). The crust may also sequester mantle-derived carbon via magmatism or the infiltration of mantle fluids. Thus, the $\delta^{13}C$ value of metamorphic fluids will depend on the lithologies present at depth and the tectono-magmatic history of the crust. Fluid inclusions in quartz veins from the Himalayan basement were interpreted to sample metamorphic fluids and had CO_2 with $\delta^{13}C$ values ranging from -15 to +2.3‰, reflecting this variability (Evans et al., 2008). Bulk crustal carbon has been previously suggested to have $\delta^{13}C$ values between -5 to -7‰ (Javoy et al., 1986; Sherwood Lollar et al., 1997; Nelson et al., 2009), reflecting the addition of carbon from carbonates, organic carbon, and mantle fluids, and

agreeing with the average value observed in fluid inclusions from the Himalayan crust of -5.0 ‰ (Evans et al., 2008).

Devolatilization of the subducting slab is not only a source of aqueous fluids, but also a potential CO_2 source. Carbon is carried into the subduction zone in sediments (organic matter and limestone) and as carbonates deposited within the altered oceanic crust (AOC) and potentially the uppermost oceanic mantle. Decarbonation of slab sediments and AOC is strongly dependent on the thermal regime in the subduction zone (Kerrick and Connolly, 1998, 2001a,b; Fischer et al., 2002; Mitchell et al., 2010), as well as interactions with aqueous fluids (Gorman et al., 2006). Thus, the isotopic character of slab-derived CO_2 will be dependent on the proportions of organic carbon and carbonates experiencing devolatilization at a given point along the subduction path (Sano and Marty, 1995). Therefore the $\delta^{13}C$ values of carbon from the subducting slab may vary from carbonate-like values (~0 ‰) to much lower values with increasing organic matter contributions. Based on a global compilation of carbon isotopes of volcanic arc gas emissions, an average of 85% of the carbon released from a slab at sub arc depths is derived from carbonates and 15% from organic sediments (Sano and Williams, 1996), which would yield a mean $\delta^{13}C$ value of -4.5 ‰ (assuming $\delta^{13}C$ value of -30 ‰ for organic matter).

The external carbon source with low $\delta^{13}C$ (~-14 ‰) suggested by trends between C_{ext} and $\delta^{13}C_{ext}$ (Fig. 6) must include some contribution of organic carbon and is consistent with the lowest $\delta^{13}C$ values of metamorphic CO_2 observed by Evans et al. (2008) ($\delta^{13}C$ = -15 ‰). This $\delta^{13}C$ value is also within the possible range of slab-derived carbon. Most springs associated with the CBD fault appear to fall on a trend towards this

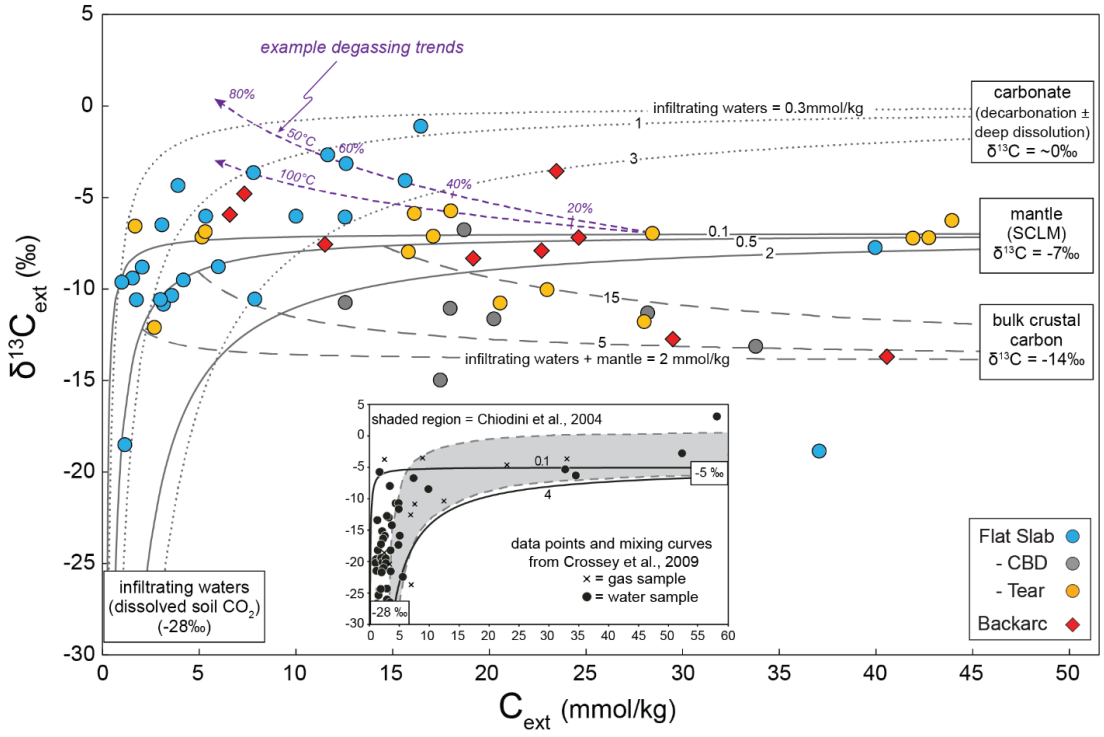

Figure 6. $\delta^{13}C_{ext}$ plotted against C_{ext} demonstrating the concentrations and isotopic values of CO_2 after subtracting carbon derived from dissolution of carbonate bedrock. Remaining external carbon (C_{ext}) is derived from near-surface organic sources (e.g., soil CO_2) or from deeper CO_2 sources. Peruvian hot springs with high C_{ext} (> 20 mmol/kg) form two separate trends towards $\delta^{13}C_{ext}$ values of -7 ‰ and -14 ‰ with increasing C_{ext}, reflecting springs with increasing additions of CO_2 from two isotopically distinct endmembers. Based on relationships with helium isotopes, we interpret these deep CO_2 endmembers to be the SCLM (-7 ‰) and continental crust (-14 ‰). Some springs with moderate C_{ext} concentrations trend towards higher $\delta^{13}C_{ext}$ values (~0 ‰), indicating addition of CO_2 from carbonate bedrock and/or isotopic fractionation from degassing. Calculated mixing curves are shown, demonstrating that data patterns can be explained by mixing between infiltrating waters characterized by variable amounts of organic carbon (concentrations shown along curve; $\delta^{13}C_{ext}$ = -28 ‰) and empirically determined endmembers [SCLM (solid black lines), bulk crust (dashed lines), carbonate bedrock (dotted lines)]. Mixing curves for the bulk crustal endmember originate from the organic-SCLM mixing curve following our interpretation that mantle fluids are mobilizing crustal volatiles. Dashed purple lines are representative examples showing the potential effects of open-system fractionation during degassing for spring waters with temperatures of 50 and 100 °C; percentages indicate the amount of CO_2 lost to degassing. Inset highlights results using similar methods for springs from the Colorado Plateau and Arizona Transition Zone (Crossey et al., 2009) and from central Italy (Chiodini et al., 2004).

endmember, as well as a few from the backarc and slab-tear region. Because slab-derived carbon is unlikely to be a significant CO_2 source once in the backarc region, we rule out the Nazca slab for this CO_2 endmember in the backarc hot springs. If the carbon source for this endmember is similar in the flat-slab and backarc regions, it suggests that a slab-derived component is also unlikely in the flat-slab springs.

The external carbon source with $\delta^{13}C_{ext}$ near -7 ‰ is consistent with values for carbon from the MORB-mantle (-6.5 ± 2.5 ‰) and SCLM (-2 to -8 ‰) and falls near the previously cited range for bulk crustal carbon (-5 to -7 ‰). Slab-derived carbon could also have a similar isotopic signature. Four flat-slab hot springs that are dominated by this endmember carbon isotope signature, including three from the slab-tear region, also exhibit some of the highest concentrations of C_{ext} (≥ 40 mmol/kg) in this study. A few backarc springs appear to fall on this same mixing trend as well, and following the argument in the prior paragraph, a slab-derived source of CO_2 seems unlikely to be responsible for the -7 ‰ endmember, but cannot be completely eliminated.

4.3.3. Mantle vs Crustal Carbon – He-C relationships

Thus far we have shown evidence for significant contributions of deeply sourced CO_2 in these springs, but carbon isotopes alone are unable to distinguish between crustal and mantle carbon sources. Helium isotope ratios, however, are ideal for distinguishing mantle and crustal fluids. High $^3He/^4He$ ratios act to fingerprint mantle volatiles because the mantle holds a high proportion of primordial ^3He acquired during planetary formation (e.g., MORB mantle $^3He/^4He = 8 \pm 1\ R_C/R_A$; Ozima and Podosek, 2001). Due to the concentration of radioactive U and Th in the crust, crustal fluids are dominated by

radiogenic ^{4}He and low ^{3}He/^{4}He ratios (~0.02 – 0.1 R_C/R_A; O'Nions and Oxburgh, 1988). Mantle-helium is present in all of the springs in this study, with the observed variability in ^{3}He/^{4}He ratios (0.26 to 2.52 R_C/R_A) likely due to variable amounts of crustal contamination as mantle-derived volatiles migrate through the continental crust (Hiett et al., 2021). Higher ^{3}He/^{4}He ratios imply faster transit through the crust, likely facilitated by larger volumes of slab- and mantle-derived fluids that act as a carrier fluid for mantle helium.

Springs with the highest ^{3}He/^{4}He ratios (up to 2.52 R_C/R_A) exhibit $\delta^{13}C_{ext}$ values clustering towards a relatively constant value of -7 ‰ (Fig. 7), consistent with a mantle CO_2 source. Springs with lower ^{3}He/^{4}He ratios, and hence more dilution with crustal volatiles (and lower flux of mantle helium), yield more variable $\delta^{13}C_{ext}$ values ranging from -18.9 to -1.1 ‰. These springs are largely from the flat-slab region but unassociated with the slab-tear region or CBD fault, and also have generally lower DIC and C_{ext} (Fig. 7). However, a number of springs with lower $\delta^{13}C_{ext}$ values and moderate ^{3}He/^{4}He ratios have moderate to high C_{ext} concentrations. Most of these springs fall on the trend towards $\delta^{13}C_{ext}$ values of ~-14 ‰ (Fig. 6). Two springs from the flat-slab group exhibit low ^{3}He/^{4}He ratios and the lowest $\delta^{13}C_{ext}$ values (~-19 ‰) in this study, consistent with organic sources, including one with high C_{ext} and one with low C_{ext}.

We suggest that springs with the highest ^{3}He/^{4}He ratios are associated with higher concentrations of mantle-derived carbon, leading to consistent $\delta^{13}C_{ext}$ values near -7 ‰. The deep carbon source with a $\delta^{13}C$ value of -7 ‰ is interpreted to be the SCLM. The apparent affinity for mantle-like $\delta^{13}C$ values at high ^{3}He/^{4}He ratios suggests a common source for CO_2 and mantle helium, which further implies that CO_2 is acting as a carrier

fluid for mantle helium. We note that Hiett et al. (2021) attributed the SCLM as the source of mantle helium in these springs. The much wider range in $\delta^{13}C_{ext}$ values (higher and lower than -7 ‰) for springs with lower $^{3}He/^{4}He$ ratios imply a greater proportion of crustal carbon mixing with mantle fluids. For example, springs from the flat slab region that display lower $\delta^{13}C_{ext}$ and C_{ext} values (Fig. 6) also contain significant contributions of mantle-derived helium and conform to the trend towards mantle-like $\delta^{13}C_{ext}$ values for springs with higher $^{3}He/^{4}He$ ratios (Fig. 7). Additionally, a population of springs predominantly from the flat-slab region have higher $\delta^{13}C_{ext}$ values that do not conform to the mixing trend with the -7 ‰ endmember (Fig. 6). As described earlier, these springs fall on trends consistent with additions of isotopically heavier crustal carbon from deep carbonate sources, but these values could also be partially explained by isotopic fractionation due to open-system degassing from geothermal fluids (Fig. 6).

The springs that form the trend towards lower $\delta^{13}C_{ext}$ values of -14 ‰ (Fig. 6) appear to have a wider range of $^{3}He/^{4}He$ ratios, which implies that deep CO_2 and helium in these springs are not necessarily genetically linked. For example, the two backarc springs with lower $^{3}He/^{4}He$ ratios and low $\delta^{13}C_{ext}$ values likely are carrying CO_2 and helium dominated by crustal sources. In contrast, CBD springs with high $^{3}He/^{4}He$ ratios and low $\delta^{13}C_{ext}$ values near -14 ‰ may have modest amounts (~30 %) of mantle helium but mostly crustal CO_2. In other words, isotopically lighter CO_2 appears to be more prevalent in these springs regardless of the mantle helium contribution. If this CO_2 endmember is slab derived, then we might expect consistently higher $^{3}He/^{4}He$ ratios because these fluids would have to transit through the SCLM (and mobilize helium) before entering the continental crust. Although we cannot rule out the slab, we suggest

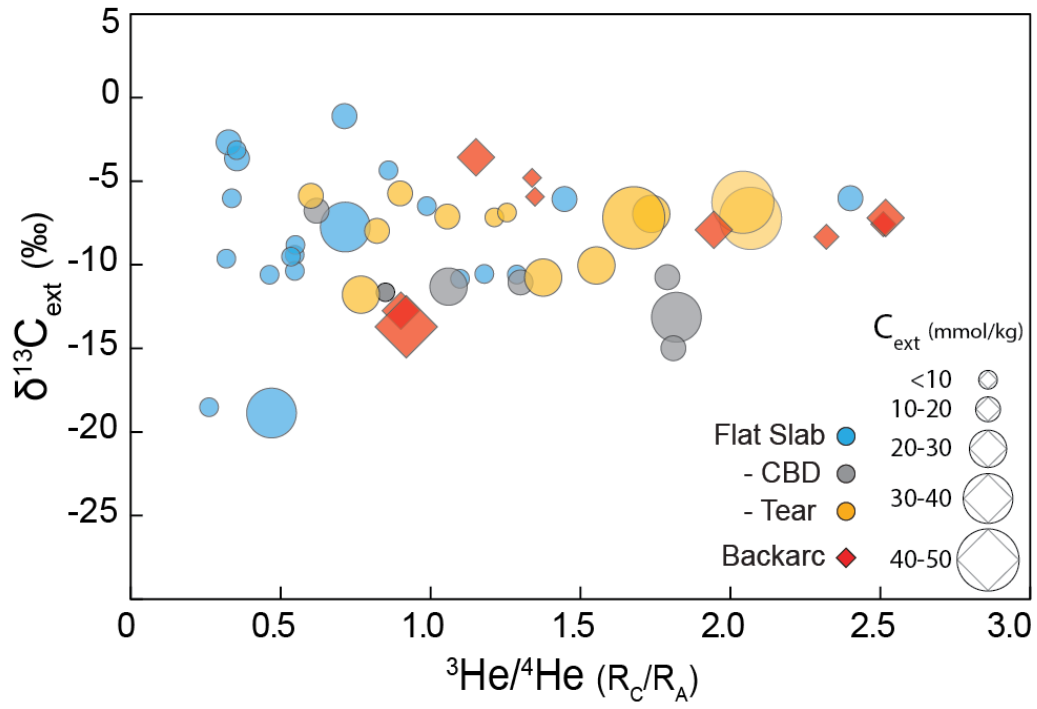

Figure 7. Peruvian spring $\delta^{13}C_{ext}$ versus $^{3}He/^{4}He$ ratios, with symbols sized according to C_{ext} concentrations. Hot springs with the highest $^{3}He/^{4}He$ ratios cluster near a $\delta^{13}C_{ext}$ value of -7 ‰, demonstrating that springs with higher proportions of mantle helium also have CO_2 dominated by the interpreted SCLM endmember. Springs with lower $^{3}He/^{4}He$ ratios exhibit a wider range of $\delta^{13}C_{ext}$ values, interpreted to reflect larger additions of crustal CO_2. Springs with high C_{ext} and low $\delta^{13}C_{ext}$ values (dominated by the interpreted crustal CO_2 endmember) exhibit variable $^{3}He/^{4}He$ ratios, demonstrating that crustal CO_2 contributions can be independent of mantle fluid contributions.

that metamorphic fluids from the continental crust are a more likely carbon source for this endmember.

$CO_2/^{3}He$ ratios provide another useful metric for assessing mixing between mantle and crustal fluids because MORB mantle has a relatively constant ratio of ~2×10^{9} (Marty and Jambon, 1987) in contrast to crustal fluids which have more variable, and generally much higher, $CO_2/^{3}He$ ratios (commonly 1×10^{11} to 1×10^{13} ; e.g., O'Nions and

Oxburgh, 1988). $CO_2/^3He$ ratios are commonly combined with $\delta^{13}C$ values to quantitatively evaluate mixing proportions between mantle and crustal sources (after Sano and Marty, 1995). However, this approach requires that CO_2 and He are not fractionated, which appears to be the case for these hot springs leading to $CO_2/^3He$ ratios as high as ~10^{16} (Hiett et al., 2021). Regardless, combined $\delta^{13}C_{ext}$ values and $C_{ext}/^3He$ ratios of Peruvian spring gases are consistent with mixing between an SCLM endmember (-7 ‰ and 2 – 7x10^9, respectively), a "bulk crustal" endmember (-14 ‰ and >10^{11}), and a carbonate endmember (~0 ‰ and >10^{11}) (Fig. 8). To model the simultaneous impact of open-system degassing on $\delta^{13}C$ values and $CO_2/^3He$ ratios we first calculate the evolution of $CO_2/^3He$ ratios during degassing using the Rayleigh fractionation equation (following de Leeuw et al., 2010; Hiett et al., 2021):

$$CO_2/^3He_{\,final} = CO_2/^3He_{\,initial} \times f_{He}^{(\alpha-1)} \quad (9)$$

where f_{He} is the fraction of helium remaining (i.e., reflecting the extent of degassing from any initial concentration) and α is the temperature-dependent ratio of the solubilities of helium and CO_2 in water [$\alpha = S_{He}/S_{CO2} = 1.83\times10^{-2}$ (50 °C), 3.93×10^{-2} (100 °C); Weiss, 1971, 1974]. We assume that helium isotopes are not fractionated significantly during degassing (Weiss, 1970), and that the fraction of ^3He remaining is the same as ^4He, which is effectively the total helium. To calculate the isotopic fractionation of carbon due to progressive degassing, we first relate the fraction of CO_2 remaining (f_{CO2}) for any f_{He} via:

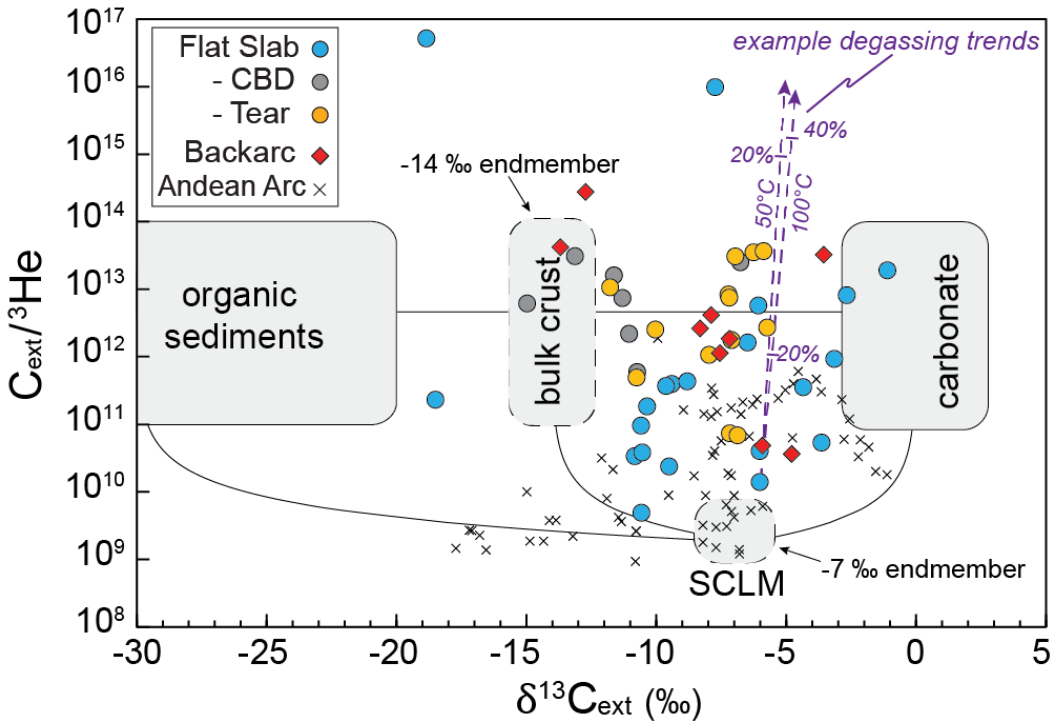

Figure 8. $C_{ext}/^3He$ vs $\delta^{13}C_{ext}$ mixing diagram showing endmember CO_2 sources (after Sano and Marty, 1995), with interpreted endmembers shown as dashed boxes. Peruvian hot springs fall within a region defined by mixing of CO_2 sourced from the SCLM ($\delta^{13}C$ = -7 ‰, $CO_2/^3He$ = 2 to 8 x10^9), an interpreted bulk crustal endmember ($\delta^{13}C$ = -14 ‰, $CO_2/^3He > 10^{11}$), and carbonate bedrock ($\delta^{13}C$ = 0 ‰, $CO_2/^3He > 10^{11}$). Open-system degassing trajectories show the evolution of $CO_2/^3He$ and $\delta^{13}C$ in the residual fluid during phase separation at temperatures of 50 and 100 °C; percentages indicate amount of CO_2 degassed. Reported measurements from the Andean arc are also shown and are compiled in Newell et al. (2015). Carbonate precipitation trajectories are not depicted on this diagram but would result in trends toward lower $CO_2/^3He$ and $\delta^{13}C$ values that are not observed.

$$f_{CO2} = f_{He} \times f_{He}^{(\alpha-1)} \quad (10)$$

We then use equation (1) to calculate the isotopic evolution as a function of f_{CO2} [note that equation (1) uses a different α than equations (9) and (10)]. The degassing

trajectories shown in figure 8 show that relatively low amounts of degassing (~10 % CO_2 loss) can shift $CO_2/^3He$ ratios from mantle to crustal values with minimal impact on $\delta^{13}C$ values. This suggests that addition of carbon from decarbonation may be responsible for higher $\delta^{13}C$ values approaching 0 ‰ observed in a number of flat slab and backarc springs. Addition of CO_2 from this process will also contribute to higher $CO_2/^3He$ ratios, in combination with degassing fractionation (e.g., Hiett et al., 2021).

4.3.4. CO_2 flux estimate

Through degassing of DIC and active bubbling at spring sources, these springs represent a measurable source of atmospheric CO_2 that has thus far been unrecorded. We estimate the total carbon flux from this suite of springs by multiplying C_{ext} by previously published discharge measurements made by the Peruvian geologic survey INGEMMET (Supplementary Table B.6; Steinmüller and Huamaní Huaccán, 1999; Huamaní Huaccán, 2000; Huamaní Huaccán and Valenzuala Ortiz, 2001), which are qualitatively similar to our field observations. For bubbling springs, we estimate the fraction of C_{ext} that has exsolved as CO_2 gas based on our modeling of $\delta^{13}C_i$ from $\delta^{13}C_{DIC}$ and $\delta^{13}C_{CO2}$ (see Section 3.3 and Supplemental Table B.2). By combining CO_2 discharged as DIC and CO_2 gas, we calculate a CO_2 release rate from deep sources to the surface of ~ 3×10^8 mol yr^{-1} from the 45 springs with available discharge estimates, equivalent to 34 t d^{-1}. Estimated CO_2 gas releases from actively bubbling springs makes up 65 % of this total discharge. These springs represent only a small fraction of the 269 thermal springs and vapor emissions reported from Peru (Steinmüller and Núñez Juárez, 1998; Steinmüller and Huamaní Huaccán, 1999; Huamaní Huaccán, 2000; Huamaní Huaccán and Valenzuala

Ortiz, 2001, 2003). If we assume that these features have similar average CO_2 discharge rates, then the total deeply-sourced CO_2 emissions from Peruvian thermal springs may approach 2×10^9 mol yr^{-1}, or 203 t d^{-1}, which is ~0.2 % of global emissions from subaerial volcanism (~10^{12} mol yr^{-1}; Williams et al., 1992). However, these calculations assume only point discharges from spring emanations. It is likely that this significantly underestimates the CO_2 flux to the surface that may be diffusively lost along fault zones or temporarily dissolved into near-surface aquifers. For example, the CO_2 discharge from individual springs in the Himalaya were used to estimate the regional CO_2-flux (Becker et al., 2008; Newell et al., 2008). These two studies assumed diffuse discharges along fault zones from different regions to scale-up to the entire Himalaya-Tibet orogen, and although quite uncertain, yielded similar estimates (~10^{11} mol/yr^{-1}) consistent with other theoretical predictions (e.g., Kerrick and Caldeira, 1999). We do not attempt similar scaling calculations here, but it is reasonable to expect that the actual CO_2 discharge from the flat-slab subduction and backarc regions of Peru to be a factor of 10 – 100 higher.

4.4. Regional variability and implications

Deeply sourced CO_2 and N_2 are consistent observations for the springs in this study, yet some spring groups exhibit unique volatile chemistries, particularly regarding concentrations and sources of deep CO_2. For example, flat-slab hot springs (excluding those associated with the CBD fault or slab tear) generally have lower C_{ext} and DIC compared to other spring groups. Along with lower average $^3He/^4He$ ratios, this suggests overall lower fluxes of mantle and crustal volatiles to the surface. Flat-slab springs may therefore be representative of the background volatile flux associated with this

subduction zone segment, while crustal extension and the tearing slab act to locally enhance volatile transfer into the continental crust (Hiett et al., 2021).

Hot springs associated with crustal extension along the CBD fault exhibit consistently lower $\delta^{13}C_{ext}$ values that trend towards the assumed bulk crustal endmember (Fig. 6). A higher proportion of metamorphic crustal carbon (i.e., mixed organic and carbonate sources) may be related to the burial and thermal breakdown of Mesozoic sediments present within the hanging-wall of the CBD fault (e.g., Giovanni et al., 2010). Triassic-Jurassic Pucará Group sediments that are buried in the hanging wall contain abundant carbonates and organic-rich shales (Szekely and Trowbridge Grose, 1972) and are likely sources of metamorphic CO_2.

A surprising outcome of this study is the lack of variability observed between different regions of the Peruvian margin, particularly between the flat-slab springs (including the CBD fault and slab tear region) and the active backarc. Hiett et al. (2021) noted that similar $^3He/^4He$ ratios for these springs suggests similar processes are responsible for moving mantle volatiles through the continental crust. In the flat-slab region, fluids migrating from the dehydrating Nazca Plate mobilize volatiles from the SCLM (through metasomatic and hydration reactions), which subsequently migrate through the continental crust. In the backarc, volatiles are mobilized from the SCLM during dehydration and/or partial melting of previously hydrated lithosphere and similarly migrate through the continental crust. We suggest that these same processes are responsible for the mantle-derived CO_2 and N_2 observed in these springs (with characteristic $\delta^{13}C$ of -7 ‰ and $\delta^{15}N$ of -5 ‰, respectively) and that mantle volatiles are mobilizing and mixing with crustal CO_2 and N_2 during transit through the continental

crust. Crustal CO_2 appears to be dominated by a mixture of organic and carbonate sources (i.e., bulk crustal carbon with $\delta^{13}C$ = ~-14 ‰), although a carbonate endmember is also prevalent in some springs (~0 ‰). In the flat-slab region, we cannot rule out that a fraction of this carbon is derived from the devolatilizing Nazca slab, but we feel that this is an unlikely contributor in the backarc.

Given the dynamic nature of subduction zones as exemplified along the Andean arc, this process is likely more prevalent along continental margins than previously realized. For example, dehydration of previously hydrated lithosphere may be responsible for amagmatic fluxes of mantle CO_2 observed in other regions with histories of low-angle subduction such as the Bolivian Altiplano (Hoke et al., 1994), the Colorado Plateau and Arizona Transition Zone (Crossey et al., 2009), and the southern Rocky Mountains (Karlstrom et al., 2013). Flat-slab subduction occurs along ~10% of the global subduction system today (Gutscher et al., 2000b), and along with backarc regions, may constitute a significant and unaccounted source of CO_2.

5. SUMMARY AND CONCLUSIONS

Stable isotope and volatile geochemistry of Peruvian hot springs provides remarkable evidence for amagmatic fluxes of mantle and crustal volatiles in regions of modern and ancient flat-slab subduction. We measured $\delta^{13}C$ and $\delta^{15}N$ values of spring gases and $\delta^{18}O$ and $\delta^{2}H$ values of spring waters from a suite of hot springs that span from the Peruvian flat slab (including a region of active syn-convergent extension and the region above a tear forming in the Nazca Plate) into the active backarc of southern Peru. Consistent with most hot spring systems, $\delta^{18}O$ and $\delta^{2}H$ values confirm the dominantly

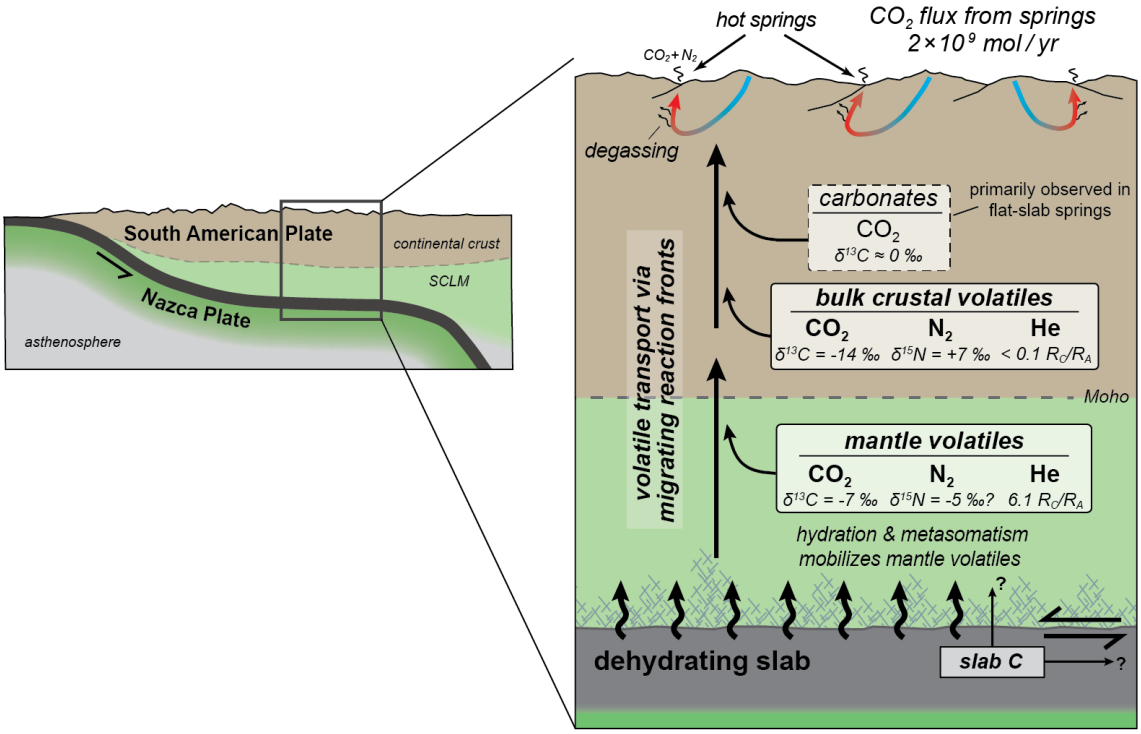

Figure 9. Generalized schematic cross section through the continental lithosphere and oceanic crust in the flat-slab region showing the interpreted sources of mantle and crustal volatiles in Peruvian hot springs. Similar volatile sources are interpreted for the backarc region, although here mantle volatiles are mobilized via dehydration and/or melting in the SCLM (see text for discussion).

meteoric origin of geothermal waters; however, the isotopic composition of dissolved volatiles in these springs provides a critical window to deeply derived contributions. Based on $\delta^{15}N$ values, N_2 gas is dominated by an atmospheric source with modest contributions of crustal (sedimentary) and mantle N_2. Carbon emitted from springs in the form of CO_2 gas and DIC yield $\delta^{13}C$ values that demonstrate mixing between mantle and crustal sources. We employ a simple geochemical model to account for the carbon derived through carbonate dissolution. Remaining concentrations of external carbon are

as high as 44 mmol/kg (median = 14 mmol/kg), which is comparable to observations in springs from the volcanic region of central Italy (Chiodini et al., 2004) and generally higher than springs in the extensional region of the southwestern Colorado Plateau and Arizona Transition Zone (Crossey et al., 2009). This external CO_2 is derived from multiple deep CO_2 sources with distinct endmember $\delta^{13}C$ values of -7 ‰ and -14 ‰, which we interpret to be the SCLM and metamorphic crustal fluids. The occurrence of slab-derived carbon is unlikely in the backarc, and although not favored as a major source in the flat-slab springs, cannot be completely ruled out. We suggest that the colder thermal regimes associated with low-angle subduction may delay and reduce the amount of slab decarbonation.

We estimate a deep CO_2 flux of $3x10^8$ mol yr^{-1} from 45 springs with available discharge measurements. If scaled to all reported thermal springs in Peru, then the total CO_2 emissions from Peruvian thermal springs may approach $2x10^9$ mol yr^{-1}, or ~0.2 % of global emissions from subaerial volcanism. This estimate does not consider diffuse degassing through fault zones and shallow aquifer systems and is likely to be considerably underestimated. Quantitative models for global CO_2 cycling often note large uncertainties regarding diffuse CO_2 degassing through amagmatic portions of volcanic arcs (Williams et al., 1992; Kerrick, 2001; Mörner and Etiope, 2002; Kelemen and Manning, 2015) despite the longstanding observation that such amagmatic fluxes may constitute a significant yet difficult to constrain flux of CO_2 (Irwin and Barnes, 1980; Kerrick et al., 1995; Barry et al., 2019). Thus, this study represents one of many case studies needed to improve models of global CO_2 degassing. Additionally, although isotopic constraints on N_2 sources are few outside of active magmatic systems, our results

suggest that in addition to unrecognized CO_2 emissions, the volcanic gaps along subduction zones may be active regions of nitrogen degassing.

REFERENCES

Ague, J.J., and Nicolescu, S., 2014, Carbon dioxide released from subduction zones by fluid-mediated reactions: Nature Geoscience 2014 7:5, v. 7, p. 355–360, doi:10.1038/ngeo2143.

Andersen, T., and Neumann, E.R., 2001, Fluid inclusions in mantle xenoliths: Lithos, v. 55, p. 301–320, doi:10.1016/S0024-4937(00)00049-9.

Antonijevic, S., Wagner, L.S., Beck, S.L., Long, M.D., Zandt, G., and Tavera, H., 2016, Effects of change in slab geometry on the mantle flow and slab fabric in Southern Peru: Journal of Geophysical Research: Solid Earth, v. 121, p. 7252–7270, doi:10.1002/2016JB013064.

Antonijevic, S.K., Wagner, L.S., Kumar, A., Beck, S.L., Long, M.D., Zandt, G., Tavera, H., and Condori, C., 2015, The role of ridges in the formation and longevity of flat slabs: Nature, v. 524, p. 212–215, doi:10.1038/nature14648.

Axen, G.J., van Wijk, J.W., and Currie, C.A., 2018, Basal continental mantle lithosphere displaced by flat-slab subduction: Nature Geoscience 2018 11:12, v. 11, p. 961–964, doi:10.1038/s41561-018-0263-9.

Barry, P.H. et al., 2019, Forearc carbon sink reduces long-term volatile recycling into the mantle: Nature, v. 568, p. 487–492, doi:10.1038/s41586-019-1131-5.

Barry, P.H., and Broadley, M.W., 2021, Nitrogen and noble gases reveal a complex history of metasomatism in the Siberian lithospheric mantle: Earth and Planetary Science Letters, v. 556, p. 116707, doi:10.1016/j.epsl.2020.116707.

Bebout, G.E., 2013, Chemical and Isotopic Cycling in Subduction Zones, *in* Treatise on Geochemistry: Second Edition, Elsevier Inc., v. 4, p. 703–747, doi:10.1016/B978-0-08-095975-7.00322-3.

Becker, J.A., Bickle, M.J., Galy, A., and Holland, T.J.B., 2008, Himalayan metamorphic CO2 fluxes: Quantitative constraints from hydrothermal springs: Earth and Planetary Science Letters, v. 265, p. 616–629, doi:10.1016/j.epsl.2007.10.046.

Bishop, B.T., Beck, S.L., Zandt, G., Wagner, L., Long, M., Antonijevic, S.K., Kumar, A., and Tavera, H., 2017, Causes and consequences of flat-slab subduction in southern Peru: Geosphere, v. 13, p. 1392–1407, doi:10.1130/GES01440.1.

Bottinga, Y., 1968, Calculation of fractionation factors for carbon and oxygen isotopic exchange in the system calcite-carbon dioxide-water: Journal of Physical Chemistry, v. 72, p. 800–808, doi:10.1021/J100849A008.

Bräuer, K., Geissler, W.H., Kämpf, H., Niedermannn, S., and Rman, N., 2016, Helium and carbon isotope signatures of gas exhalations in the westernmost part of the Pannonian Basin (SE Austria/NE Slovenia): Evidence for active lithospheric mantle degassing: Chemical Geology, v. 422, p. 60–70, doi:10.1016/j.chemgeo.2015.12.016.

Bräuer, K., Kämpf, H., Niedermann, S., Strauch, G., and Weise, S.M., 2004, Evidence for a nitrogen flux directly derived from the European subcontinental mantle in the Western Eger Rift, Central Europe: Geochimica et Cosmochimica Acta, v. 68, p. 4935–4947, doi:10.1016/j.gca.2004.05.032.

Butcher, L.A., Mahan, K.H., and Allaz, J.M., 2017, Late Cretaceous crustal hydration in the Colorado Plateau , USA , from xenolith petrology and monazite geochronology: Lithosphere, p. 561–578, doi:10.1130/L583.1.

Carlier, G., Lorand, J.P., Liégeois, J.P., Fornari, M., Soler, P., Carlotto, V., and Cárdenas, J., 2005, Potassic-ultrapotassic mafic rocks delineate two lithospheric mantle blocks beneath the southern Peruvian Altiplano: Geology, v. 33, p. 601–604, doi:10.1130/G21643.1.

Cartigny, P., 2005, Stable Isotopes and the Origin of Diamond: Elements, v. 1, p. 79–84, doi:10.2113/gselements.1.2.79.

Chiodini, G., Cardellini, C., Amato, A., Boschi, E., Caliro, S., Frondini, F., and Ventura, G., 2004, Carbon dioxide Earth degassing and seismogenesis in central and southern Italy: Geophysical Research Letters, v. 31, doi:10.1029/2004GL019480.

Chiodini, G., Frondini, F., Cardellini, C., Parello, F., and Peruzzi, L., 2000, Rate of diffuse carbon dioxide Earth degassing estimated from carbon balance of regional aquifers: The case of central Apennine, Italy: Journal of Geophysical Research: Solid Earth, v. 105, p. 8423–8434, doi:10.1029/1999JB900355.

Craig, H., 1961, Isotopic variations in meteoric waters: Science, v. 133, p. 1702–1703, doi:10.1126/science.133.3465.1702.

Craig, H., 1953, The geochemistry of the stable carbon isotopes: Geochimica et Cosmochimica Acta, v. 3, p. 53–92, doi:10.1016/0016-7037(53)90001-5.

Craig, H., and Gordon, L., 1965, Deuterium and oxygen 18 variations in the ocean and marine atmosphere, *in* Stable Isotopes in Oceanographic Studies, Pisa, Spoleto, Italy, Consiglio Nazional delle Richerche, p. 122- undefined.

Crossey, L.J. et al., 2009, Degassing of mantle-derived CO 2 and He from springs in the southern Colorado Plateau region — Neotectonic connections and implications for groundwater systems:, doi:10.1130/B26394.1.

Deines, P., Langmuir, D., and Harmon, R.S., 1974, Stable carbon isotope ratios and the existence of a gas phase in the evolution of carbonate ground waters: Geochimica et Cosmochimica Acta, v. 38, p. 1147–1164, doi:10.1016/0016-7037(74)90010-6.

Dunai, T.J., and Porcelli, D., 2002, Storage and transport of noble gases in the subcontinental lithosphere: Reviews in Mineralogy and Geochemistry, v. 47, doi:10.2138/rmg.2002.47.10.

Evans, M.J., Derry, L.A., and France-Lanord, C., 2008, Degassing of metamorphic carbon dioxide from the Nepal Himalaya: Geochemistry, Geophysics, Geosystems, v. 9, p. n/a-n/a, doi:10.1029/2007GC001796.

Farmer, G.L., Bailley, T., and Elkins-Tanton, L.T., 2008, Mantle source volumes and the origin of the mid-Tertiary ignimbrite flare-up in the southern Rocky Mountains, western U.S.: Lithos, v. 102, p. 279–294, doi:10.1016/j.lithos.2007.08.014.

Farmer, G.L., Fritz, D.E., and Glazner, A.F., 2020, Identifying Metasomatized Continental Lithospheric Mantle Involvement in Cenozoic Magmatism From Ta/Th Values, Southwestern North America: Geochemistry, Geophysics, Geosystems, v. 21, doi:10.1029/2019gc008499.

Fischer, T.P., Burnard, P., Marty, B., Hilton, D.R., Füri, E., Palhol, F., Sharp, Z.D., and Mangasini, F., 2009, Upper-mantle volatile chemistry at Oldoinyo Lengai volcano and the origin of carbonatites: Nature, v. 459, p. 77–80, doi:10.1038/nature07977.

Fischer, T.P., Hitton, D.R., Zimmer, M.M., Shaw, A.M., Sharp, Z.D., and Walker, J.A., 2002, Subduction and recycling of nitrogen along the Central American margin: Science, v. 297, p. 1154–1157, doi:10.1126/science.1073995.

Gautheron, C., and Moreira, M., 2002, Helium signature of the subcontinental lithospheric mantle: Earth and Planetary Science Letters, v. 199, p. 39–47, doi:10.1016/S0012-821X(02)00563-0.

Giggenbach, W.F., 1997, Relative importance of thermodynamic and kinetic processes in governing the chemical and isotopic composition of carbon gases in high-heatflow sedimentary basins: Geochimica et Cosmochimica Acta, v. 61, p. 3763–3785, doi:10.1016/S0016-7037(97)00171-3.

Giovanni, M.K., Horton, B.K., Garzione, C.N., McNulty, B., and Grove, M., 2010, Extensional basin evolution in the Cordillera Blanca, Peru: Stratigraphic and isotopic records of detachment faulting and orogenic collapse in the Andean

hinterland: Tectonics, v. 29, doi:10.1029/2010TC002666.

Gorman, P.J., Kerrick, D.M., and Connolly, J.A.D., 2006, Modeling open system metamorphic decarbonation of subducting slabs: Geochemistry, Geophysics, Geosystems, v. 7, doi:10.1029/2005GC001125.

Gutscher, M.A., Maury, F., Eissen, J.P., and Bourdon, E., 2000a, Can slab melting be caused by flat subduction? Geology, v. 28, p. 535–538, doi:10.1130/0091-7613(2000)28<535:csmbcb>2.0.co;2.

Gutscher, M.A., Olivet, J.L., Aslanian, D., Eissen, J.P., and Maury, R., 1999, The “lost Inca Plateau”: Cause of flat subduction beneath Peru? Earth and Planetary Science Letters, v. 171, p. 335–341, doi:10.1016/S0012-821X(99)00153-3.

Gutscher, M.A., Spakman, W., Bijwaard, H., and Engdahl, E.R., 2000b, Geodynamics of flat subduction: Seismicity and tomographic constraints from the Andean margin: Tectonics, v. 19, p. 814–833, doi:10.1029/1999TC001152.

Hahm, D., Hilton, D.R., Cho, M., Wei, H., and Kim, K.-R., 2008, Geothermal He and CO_2 variations at Changbaishan intra-plate volcano (NE China) and the nature of the sub-continental lithospheric mantle: Geophysical Research Letters, v. 35, p. L22304, doi:10.1029/2008GL035955.

Hiett, C.D., Newell, D.L., and Jessup, M.J., 2021, ^{3}He evidence for fluid transfer and continental hydration above a flat slab: Earth and Planetary Science Letters, v. 556, p. 116722, doi:10.1016/j.epsl.2020.116722.

Hilton, D.R., Fischer, T.P., and Marry, B., 2002, Noble gases and volatile recycling at subduction zones: Reviews in Mineralogy and Geochemistry, v. 47, p. 319–370, doi:10.2138/rmg.2002.47.9.

Hoke, L., Hilton, D.R., Lamb, S.H., Hammerschmidt, K., and Friedrichsen, H., 1994, 3He evidence for a wide zone of active mantle melting beneath the Central Andes: Earth and Planetary Science Letters, v. 128, p. 341–355, doi:10.1016/0012-821X(94)90155-4.

Hoke, L., and Lamb, S., 2007, Cenozoic behind-arc volcanism in the Bolivian Andes, South America: implications for mantle melt generation and lithospheric structure: Journal of the Geological Society, v. 164, p. 795–814, doi:10.1144/0016-76492006-092.

Huamaní Huaccán, A., 2000, Aguas Termales y Minerales en el Norte del Perú: INGEMMET Boletin, Serie D: Estudio Regionales,.

Huamaní Huaccán, A., and Valenzuala Ortiz, G., 2003, Aguas Termales y Minerales en

el Oriente Central del Peru: INGEMMET Boletin, Serie D: Estudio Regionales, v. 25.

Huamaní Huaccán, A., and Valenzuala Ortiz, G., 2001, Aguas Termales y Minerales en el Suroriente del Peru: INGEMMET Boletin, Serie D: Estudio Regionales, p. 124.

Humphreys, E., Hessler, E., Dueker, K., Farmer, G.L., Erslev, E., and Atwater, T., 2003, How Laramide-Age Hydration of North American Lithosphere by the Farallon Slab Controlled Subsequent Activity in the Western United States: International Geology Review, v. 45, p. 575–595, doi:10.2747/0020-6814.45.7.575.

Irwin, W.P., and Barnes, I., 1980, Tectonic relations of carbon dioxide discharges and earthquakes.: Journal of Geophysical Research, v. 85, p. 3115–3121, doi:10.1029/JB085iB06p03115.

Isacks, B.L., 1988, Uplift of the central Andean Plateau and bending of the Bolivian Orocline.: Journal of Geophysical Research, v. 93, p. 3211–3231, doi:10.1029/JB093iB04p03211.

James, D., and Sacks, I., 1999, Cenozoic formation of central Andes: a geophysical perspective, *in* Geology and Ore Deposits of the Central Andes, p. 1–25.

Javoy, M., Pineau, F., and Delorme, H., 1986, Carbon and nitrogen isotopes in the mantle: Chemical Geology, v. 57, p. 41–62, doi:10.1016/0009-2541(86)90093-8.

Jones, C.H., Mahan, K.H., Butcher, L.A., Levandowski, W.B., and Farmer, G.L., 2015, Continental uplift through crustal hydration: Geology, v. 43, p. 355–358, doi:10.1130/G36509.1.

Karlstrom, K.E., Crossey, L.J., Hilton, D.R., and Barry, P.H., 2013, Mantle 3He and CO2 degassing in carbonic and geothermal springs of Colorado and implications for neotectonics of the Rocky Mountains: Geology, v. 41, doi:10.1130/G34007.1.

Kelemen, P.B., and Manning, C.E., 2015, Reevaluating carbon fluxes in subduction zones, what goes down, mostly comes up: Proceedings of the National Academy of Sciences of the United States of America, v. 112, p. E3997–E4006, doi:10.1073/pnas.1507889112.

Kennedy, B.M., Kharaka, Y.K., Evans, W.C., Ellwood, A., DePaolo, D.J., Thordsen, J., Ambats, G., and Mariner, R.H., 1997, Mantle fluids in the San Andreas fault system, California: Science, v. 278, p. 1278–1281, doi:10.1126/science.278.5341.1278.

Kennedy, B.M., and Van Soest, M.C., 2007, Flow of mantle fluids through the ductile lower crust: Helium isotope trends: Science, v. 318, p. 1433–1436, doi:10.1126/science.1147537.

Kerrick, D.M., 2001, Present and past nonanthropogenic CO_2 degassing from the solid earth: Reviews of Geophysics, v. 39, p. 565–585, doi:10.1029/2001RG000105.

Kerrick, D.M., and Caldeira, K., 1999, Was the Himalayan orogen a climatically significant coupled source and sink for atmospheric CO2 during the Cenozoic? Earth and Planetary Science Letters, v. 173, p. 195–203, doi:10.1016/S0012-821X(99)00229-0.

Kerrick, D.M., and Connelly, J.A.D., 2001, Metamorphic devolatilization of subducted marine sediments and the transport of volatiles into the Earth's mantle: Nature, v. 411, p. 293–296, doi:10.1038/35077056.

Kerrick, D.M., and Connolly, J.A.D., 2001, Metamorphic devolatilization of subducted oceanic metabasalts: Implications for seismicity, arc magmatism and volatile recycling: Earth and Planetary Science Letters, v. 189, p. 19–29, doi:10.1016/S0012-821X(01)00347-8.

Kerrick, D.M., and Connolly, J.A.D., 1998, Subduction of ophicarbonates and recycling of CO2 and H2O: Geology, v. 26, p. 375–378, doi:10.1130/0091-7613(1998)026<0375:SOOARO>2.3.CO;2.

Kerrick, D.M., McKibben, M.A., Seward, T.M., and Caldeira, K., 1995, Convective hydrothermal C02 emission from high heat flow regions: Chemical Geology, v. 121, p. 285–293, doi:10.1016/0009-2541(94)00148-2.

Kulongoski, J.T., Hilton, D.R., Barry, P.H., Esser, B.K., Hillegonds, D., and Belitz, K., 2013, Volatile fluxes through the Big Bend section of the San Andreas Fault, California: Helium and carbon-dioxide systematics: Chemical Geology, v. 339, p. 92–102, doi:10.1016/j.chemgeo.2012.09.007.

Kulongoski, J.T., Hilton, D.R., and Izbicki, J.A., 2005, Source and movement of helium in the eastern Morongo groundwater Basin: The influence of regional tectonics on crustal and mantle helium fluxes: Geochimica et Cosmochimica Acta, doi:10.1016/j.gca.2005.03.001.

Lee, H., Muirhead, J.D., Fischer, T.P., Ebinger, C.J., Kattenhorn, S.A., Sharp, Z.D., and Kianji, G., 2016, Massive and prolonged deep carbon emissions associated with continental rifting: Nature Geoscience, v. 9, p. 145–149, doi:10.1038/ngeo2622.

de Leeuw, G.A.M., Hilton, D.R., Güleç, N., and Mutlu, H., 2010, Regional and temporal variations in CO2/3He, 3He/4He and δ13C along the North Anatolian Fault Zone, Turkey: Applied Geochemistry, v. 25, p. 524–539, doi:10.1016/j.apgeochem.2010.01.010.

Levander, A., Schmandt, B., Miller, M.S., Liu, K., Karlstrom, K.E., Crow, R.S., Lee,

C.T.A., and Humphreys, E.D., 2011, Continuing Colorado plateau uplift by delamination-style convective lithospheric downwelling: Nature, v. 472, p. 461–465, doi:10.1038/nature10001.

Lowry, A.R., and Pérez-Gussinyé, M., 2011, The role of crustal quartz in controlling Cordilleran deformation: Nature, v. 471, p. 353–359, doi:10.1038/nature09912.

Mamani, M., Wörner, G., and Sempere, T., 2010, Geochemical variations in igneous rocks of the Central Andean orocline (13 ° S to 18 ° S): Tracing crustal thickening and magma generation through time and space: , p. 162–182, doi:10.1130/B26538.1.

Margirier, A., Audin, L., Robert, X., Herman, F., Ganne, J., and Schwartz, S., 2016, Time and mode of exhumation of the Cordillera Blanca batholith (Peruvian Andes): Journal of Geophysical Research: Solid Earth, v. 121, p. 6235–6249, doi:10.1002/2016JB013055.

Marty, B., and Jambon, A., 1987, C3He in volatile fluxes from the solid Earth: implications for carbon geodynamics: Earth and Planetary Science Letters, v. 83, p. 16–26, doi:10.1016/0012-821X(87)90047-1.

Mitchell, E.C., Fischer, T.P., Hilton, D.R., Hauri, E.H., Shaw, A.M., De Moor, J.M., Sharp, Z.D., and Kazahaya, K., 2010, Nitrogen sources and recycling at subduction zones: Insights from the Izu-Bonin-Mariana arc: Geochemistry, Geophysics, Geosystems, v. 11, doi:10.1029/2009GC002783.

de Moor, J.M., Fischer, T.P., Sharp, Z.D., Hilton, D.R., Barry, P.H., Mangasini, F., and Ramirez, C., 2013, Gas chemistry and nitrogen isotope compositions of cold mantle gases from Rungwe Volcanic Province, southern Tanzania: Chemical Geology, v. 339, p. 30–42, doi:10.1016/j.chemgeo.2012.08.004.

Morche, W., Larico, W., Romero, D., and Torres, V., 2003, Mapa Geológico del Cuadrángulo de Huancavelica 26n : Series A: Carta Geológica Nacional,.

Mörner, N.A., and Etiope, G., 2002, Carbon degassing from the lithosphere: Global and Planetary Change, v. 33, p. 185–203, doi:10.1016/S0921-8181(02)00070-X.

Nelson, S.T., 2000, A simple, practical methodology for routine VSMOW/SLAP normalization of water samples analyzed by continuous flow methods: Rapid Communications in Mass Spectrometry, v. 14, p. 1044–1046, doi:10.1002/1097-0231(20000630)14:12<1044::AID-RCM987>3.0.CO;2-3.

Nelson, S.T., Mayo, A.L., Gilfillan, S., Dutson, S.J., Harris, R.A., Shipton, Z.K., and Tingey, D.G., 2009, Enhanced fracture permeability and accompanying fluid flow in the footwall of a normal fault: The Hurricane fault at Pah Tempe hot springs, Washington County, Utah: Bulletin of the Geological Society of America, v. 121, p.

236–246, doi:10.1130/B26285.1.

Newell, D.L., Crossey, L.J., Karlstrom, K.E., Fischer, T.P., and Hilton, D.R., 2005, Continental-scale links between the mantle and groundwater systems of the western United States: Evidence from travertine springs and regional He isotope data: GSA Today, v. 15, p. 4–10, doi:10.1130/1052-5173(2005)015[4:CSLBTM]2.0.CO;2.

Newell, D.L., Jessup, M.J., Cottle, J.M., Hilton, D.R., Sharp, Z.D., and Fischer, T.P., 2008, Aqueous and isotope geochemistry of mineral springs along the southern margin of the Tibetan plateau: Implications for fluid sources and regional degassing of CO_2: Geochemistry, Geophysics, Geosystems, v. 9, p. n/a-n/a, doi:10.1029/2008GC002021.

Newell, D.L., Jessup, M.J., Hilton, D.R., Shaw, C.A., and Hughes, C.A., 2015, Mantle-derived helium in hot springs of the Cordillera Blanca , Peru : Implications for mantle-to-crust fl uid transfer in a fl at-slab subduction setting: Chemical Geology, v. 417, p. 200–209, doi:10.1016/j.chemgeo.2015.10.003.

O'Nions, R.K., and Oxburgh, E.R., 1988, Helium, volatile fluxes and the development of continental crust: Earth and Planetary Science Letters, v. 90, p. 331–347, doi:10.1016/0012-821X(88)90134-3.

Ozima, M., and Podosek, F.A., 2001, Noble Gas Geochemistry:, doi:10.1017/cbo9780511545986.

Parkhurst, D.L., and Appelo, C.A.J., 2013, Description of Input and Examples for PHREEQC Version 3 — A Computer Program for Speciation , Batch-Reaction , One-Dimensional Transport , and Inverse Geochemical Calculations.: U.S. Geological Survey Techniques and Methods, book 6, chapter A43, doi:10.1016/0029-6554(94)90020-5.

Porter, R., Gilbert, H., Zandt, G., Beck, S., Warren, L., Calkins, J., Alvarado, P., and Anderson, M., 2012, Shear wave velocities in the Pampean flat-slab region from Rayleigh wave tomography: Implications for slab and upper mantle hydration: Journal of Geophysical Research B: Solid Earth, v. 117, p. 1–21, doi:10.1029/2012JB009350.

Ramos, V.A., and Folguera, A., 2009, Andean flat-slab subduction through time: Geological Society, London, Special Publications, v. 327, p. 31–54, doi:10.1144/SP327.3.

Roche, M.A., Bourges, J., Cortes, J., and Mattos, R., 1992, Climatology And Hydrology, *in* Springer, Dordrecht, p. 63–88, doi:10.1007/978-94-011-2406-5_4.

Rosenbaum, G., Giles, D., Saxon, M., Betts, P.G., Weinberg, R.F., and Duboz, C., 2005,

Subduction of the Nazca Ridge and the Inca Plateau: Insights into the formation of ore deposits in Peru: Earth and Planetary Science Letters, v. 239, p. 18–32, doi:10.1016/j.epsl.2005.08.003.

Salata, G.G., Roelke, L.A., and Cifuentes, L.A., 2000, A rapid and precise method for measuring stable carbon isotope ratios of dissolved inorganic carbon: Marine Chemistry, v. 69, p. 153–161, doi:10.1016/S0304-4203(99)00102-4.

Sandeman, H.A., Clark, A.H., and Farrar, E., 1995, An Integrated Tectono-Magmatic Model for the Evolution of the Southern Peruvian Andes (13–20°S) since 55 Ma: International Geology Review, v. 37, p. 1039–1073, doi:10.1080/00206819509465439.

Sano, Y., and Marty, B., 1995, Origin of carbon in fumarolic gas from island arcs: Chemical Geology, v. 199, p. 265–274.

Sano, Y., Takahata, N., Nishio, Y., Fischer, T.P., and Williams, S.N., 2001, Volcanic flux of nitrogen from the Earth: Chemical Geology, v. 171, p. 263–271, doi:10.1016/S0009-2541(00)00252-7.

Sano, Y., and Williams, S.N., 1996, Fluxes of mantle and subducted carbon along convergent plate boundaries: Geophysical Research Letters, v. 23, p. 2749–2752, doi:10.1029/96GL02260.

Scire, A., Zandt, G., Beck, S., Long, M., Wagner, L., Minaya, E., and Tavera, H., 2016, Imaging the transition from flat to normal subduction: Variations in the structure of the Nazca slab and upper mantle under southern Peru and northwestern Bolivia: Geophysical Journal International, v. 204, p. 457–479, doi:10.1093/gji/ggv452.

Scott, B.E., Newell, D.L., Jessup, M.J., Grambling, T., and Shaw, C.A., 2020, Structural controls on crustal fluid circulation and hot spring geochemistry above a flat-slab subduction zone, Peru: Geochemistry, Geophysics, Geosystems, v. 21, doi:10.1029/2020gc008919.

Sharp, Z., 2017, Principles of Stable Isotope Geochemistry, 2nd edition: Principles of Stable Isotope Geochemistry, 2nd edition, v. 136.

Shaw, A.M., Hauri, E.H., Fischer, T.P., Hilton, D.R., and Kelley, K.A., 2008, Hydrogen isotopes in Mariana arc melt inclusions: Implications for subduction dehydration and the deep-Earth water cycle: Earth and Planetary Science Letters, v. 275, p. 138–145, doi:10.1016/j.epsl.2008.08.015.

Sherwood Lollar, B., Ballentine, C.J., and O'Nions, R.K., 1997, The fate of mantle-derived carbon in a continental sedimentary basin: Integration of C/He relationships and stable isotope signatures: Geochimica et Cosmochimica Acta, v. 61, p. 2295–

2307, doi:10.1016/s0016-7037(97)00083-5.

Steinmüller, K., and Huamaní Huaccán, A., 1999, Aguas Termales y Minerales en el Centro del Peru: INGEMMET Boletín, Serie D: Estudio Regionales, p. 53.

Steinmüller, K., and Núñez Juárez, S., 1998, Hidrotermalismo en el Sur del Peru: INGEMMET Boletin, Serie D: Estudio Regionales, v. 19.

Szekely, T., and Trowbridge Grose, L., 1972, Stratigraphy of the Carbonate, Black Shale, and Phosphate of the Pucará Group (Upper Triassic—Lower Jurassic), Central Andes, Peru: GSA Bulletin, v. 83, p. 407–428.

Taylor, H.P., 1977, Water/rock interactions and the origin of H2O in granitic batholiths: Journal of the Geological Society, v. 133, p. 509–558, doi:10.1144/gsjgs.133.6.0509.

USGS, 2006, Chapter A4. Collection of water samples:, doi:10.3133/twri09A4.

Vogel, J.C., Grootes, P.M., and Mook, W.G., 1970, Isotopic fractionation between gaseous and dissolved carbon dioxide: Zeitschrift für Physik, v. 230, p. 225–238, doi:10.1007/BF01394688.

Weiss, R.F., 1974, Carbon dioxide in water and seawater: the solubility of a non-ideal gas: Marine Chemistry, v. 2, p. 203–215, doi:10.1016/0304-4203(74)90015-2.

Weiss, R.F., 1970, Helium isotope effect in solution in water and seawater: Science, v. 168, p. 247–248, doi:10.1126/science.168.3928.247.

Weiss, R.F., 1971, Solubility of Helium and Neon in Water and Seawater: Journal of Chemical and Engineering Data, v. 16, p. 235–241, doi:10.1021/je60049a019.

Williams, S.N., Schaefer, S.J., Marta Lucia Calvache, V., and Lopez, D., 1992, Global carbon dioxide emission to the atmosphere by volcanoes: Geochimica et Cosmochimica Acta, v. 56, p. 1765–1770, doi:10.1016/0016-7037(92)90243-C.

Yamamoto, J., Takahata, N., Sano, Y., Yanagita, M., Arai, S., and Prikhod'ko, V.S., 2020, Nitrogen and noble gas isotopic compositions of mantle xenoliths from Far Eastern Russia: Implications for nitrogen isotopic characteristics of mantle wedge fluid: Earth and Planetary Science Letters, v. 534, p. 116109, doi:10.1016/j.epsl.2020.116109.

Yokochi, R., Marty, B., Chazot, G., and Burnard, P., 2009, Nitrogen in peridotite xenoliths: Lithophile behavior and magmatic isotope fractionation: Geochimica et Cosmochimica Acta, v. 73, p. 4843–4861, doi:10.1016/j.gca.2009.05.054.

Zhao, M., Liu, Z., Li, H.C., Zeng, C., Yang, R., Chen, B., and Yan, H., 2015, Response

of dissolved inorganic carbon (DIC) and δ13CDIC to changes in climate and land cover in SW China karst catchments: Geochimica et Cosmochimica Acta, v. 165, p. 123–136, doi:10.1016/j.gca.2015.05.041.

CHAPTER 4

SHALLOW SUBDUCTION-DERIVED METASOMATISM AT THE ROOT OF ALKALINE BACKARC MAGMATISM IN THE NORTHERN ALTIPLANO[1]

Abstract

Kersantite xenoliths from the Quaternary Quimsachata volcano in Southern Peru exhibit phlogopite hydrogen isotope ratios and trace element patterns that constrain a history of mantle metasomatism during subduction below the northern Altiplano Plateau. These xenoliths are characterized primarily by biotite (up to ~40 modal %) + clinopyroxene (up to ~40 %) + fluorapatite in a partially melted groundmass of microlitic alkali feldspar + plagioclase + minor Fe-Ti oxides, with textural characteristics and major element compositions reflecting a partial cumulate origin. Highly magnesian bulk compositions notably enriched in K_2O and P_2O, similar to other Neogene and Quaternary potassic basalts in the region, suggest that kersantite melts are derived from metasomatized lithospheric mantle characterized by modal enrichments of phlogopite and apatite. Phlogopite in kersantite xenoliths exhibit δD values between -58 ‰ and -38 ‰, with one outlier yielding a value of -74‰, consistent with hydrous minerals and melt inclusions in arc magmas and theoretical predictions for subduction derived fluids. Phlogopite phenocrysts from Quimsachata lavas yield a similar δD value of -57 ‰. Bulk-rock trace element compositions enriched in large ion lithophile elements (e.g., Rb, Ba $>100_{PM}$) and light rare earth elements (e.g., La $>50_{PM}$) as well as prominent Nb and Ta

[1] Paper formatted for publication in *Geochemistry, Geophysics, and Geosystems* with author list:
C.D. Hiett[a], D.L. Newell[a], J.W. Shervais
[a]Utah State University

depletions mirror trace element patterns in Quaternary alkaline basalts and support of the role of subduction-derived fluids or hydrous melts in metasomatism of the underlying lithospheric mantle. Potassic basaltic volcanism > 200 km inboard of the modern arc initiated following a period of shallow subduction in the Oligocene, suggesting that lithospheric alteration resulted from shallow subduction and that melting was triggered upon opening of the mantle wedge. Rejuvenated Quaternary volcanism may be linked to addition of heat to the mantle wedge by the trench-parallel corner flow around the modern Peruvian flat-slab to the north, with magmatic ascent exploiting a lithospheric weakness represented by the Cusco-Vilconata Fault System. Our conclusion that metasomatism occurred contemporaneously with an eastward shift in deformation that established the eastern margin of the plateau provides compelling support for models that invoke rheologic weaking from hydration and metasomatism as a critical process in the growth of the Altiplano Plateau and the evolution of cordillera globally.

1. Introduction

Subduction and orogenesis are central processes in the growth of continental lithosphere and involve a complex interplay of tectonics and magmatism that have proven difficult to untangle in modern systems like the Andes (e.g., Garzione et al., 2017) and ancient systems such as the Mesozoic western North America (e.g., DeCelles, 2004) . Processes leading to metasomatism and volatile enrichment in the deep lithosphere can strongly influence geodynamic variables such as rheology, buoyancy, and melt fertility, with long-term consequences for patterns of deformation, magmatism, and surface uplift both during and following orogenesis (Farmer et al., 2008; Lowry and Pérez-Gussinyé,

2011; Jones et al., 2015). Enrichments of volatiles and metals that can accompany metasomatism are also likely a critical ingredient in the formation of some magmatic ore deposits (Holwell et al., 2019; Rosera et al., 2021). Flat-slab subduction is one process that is recognized for its potential to extensively hydrate and metasomatize the roots of continental margins (Humphreys et al., 2003; Saylor et al., 2023) and is relatively common, occurring along ~10% of the modern global subduction system (Gutscher et al., 2000; Ramos and Folguera, 2009). Identifying the geochemical fingerprint of this process is therefore key to understanding its role in the tectonomagmatic evolution of orogenic belts.

Back arc, intracontinental basaltic magmatism provides a direct way to investigate deep fluid processes and the composition of the deep lithosphere. Potassic alkaline basalts are often interpreted as the first melts of metasomatized mantle (Gibson et al., 1995; Peccerillo, 1999) and can therefore be used to study metasomatic processes. In addition, mantle and crustal xenoliths entrained in these lavas afford direct scrutinization of the lithologies at depth encountered along magma assent paths. Xenoliths may include intrusive rocks without volcanic equivalents exposed at the surface, and thus expand the inventory of igneous rocks that can be used to scrutinize mantle composition, metasomatism, and melting processes.

Major/minor element characteristics of primitive basaltic melts (i.e., melts having undergone little or no differentiation through fractional crystallization or assimilation) are largely controlled by the mineralogy of the mantle source and will reflect any history of melt depletion and/or modal metasomatism in the region sampled by melting. Trace element compositions are especially useful for elucidating melt conditions (e.g.,

Shervais, 1982) or histories of metasomatism (Lee, 2005). Melting processes lead to characteristic enrichment or depletion of various trace elements owing to their relative incompatibilities (Sun et al., 1979), and involvement of aqueous fluids, immiscible melts, or specific phases will mobilize or sequester certain trace elements in distinct ways, for example sequestering Eu in plagioclase cumulates or heavy rare-earth elements (HREE) in residual garnet. Hydrogen isotope ratios (D/H reported as δD values) of geologic materials are also well-suited for identifying the processes responsible for mantle hydration and metasomatism in the source of xenoliths and lavas (e.g., Marshall et al., 2017). Subduction of hydrated oceanic lithosphere provides multiple pathways for water to be introduced into the overlying continental lithosphere, and isotopic fractionation throughout this process results in fluids or melts with δD values that are distinct from hydrogen sourced from the asthenosphere or lower mantle domains. Interactions with various metasomatizing agents, (e.g., subduction fluids/melts, carbonatites, mantle plumes) will result in characteristic isotopic values in the metasomatized lithospheric mantle and any derivative basaltic melts. Isotopic fractionation during crystallization and/or volatile loss (eruption) may shift isotopic values, and identifiable patterns in isotope characteristics may therefore help to elucidate these processes.

The Andean Cordillera is the premier type-example for orogenesis in oceanic-continental convergent margins and provides a modern analogue for studying the chemical and tectonomagmatic evolution of ancient margins across the globe. The Altiplano-Puna Plateau forms the central portion of the orogen, showcasing the dramatic crustal thickening and regional surface uplift that can be attained in these orogenic systems. Deformation and surface uplift has been diachronous across the plateau

throughout the Cenozoic, and numerous mechanisms have been explored to explain patterns of plateau growth, including thermal weakening during pervasive magmatism (Isacks, 1988; Sandeman et al., 1995; James and Sacks, 1999), magmatic thickening (Haschke and Günther, 2003), lower crustal flow (Garzione et al., 2017), and mantle delamination (Kay et al., 1999; Garzione et al., 2006; Calixto et al., 2013). Mid-late Cenozoic episodes of shallow subduction have been linked to dynamic shifts in magmatism and deformation (Isacks, 1988; Sandeman et al., 1995; Lamb and Hoke, 1997; James and Sacks, 1999; Saylor et al., 2023), but hydration and metasomatism of the continental lithosphere that likely accompanied flat-slab subduction (Humphreys, 1995; Jones et al., 2015) has not been thoroughly investigated.

In the northern Altiplano Plateau, geochemical characteristics of Cenozoic alkaline magmatism demonstrate the presence of metasomatized mantle underlying the region (Sandeman et al., 1995; Carlier et al., 2005), yet a clear understanding of lithospheric architecture, the nature of metasomatism, and its impact on the tectonomagmatic history of the margin is lacking. We have assembled a collection of xenoliths from Quaternary alkaline lavas found along the Cusco-Vilconata fault system (CVFS) of southern Peru, including ultramafic and mafic lithologies that have not been previously described from this region that demonstrate significant heterogeneity in the lithospheric mantle below the CVFS. Here we focus on a suite of lamprophyric intrusive igneous xenoliths that were collected from the Quimsachata Volcano (Fig. 1). These include phlogopite-rich foidgabbros, monzogabbros, and gabbros collectively referred to as kersantites (lamprophyres with plagioclase > K-feldspar). We provide a petrologic analysis of these xenoliths and their mantle source through major element compositions

and trace element characteristics. We leverage the abundance of hydrous phases in both xenoliths and the Quimsachata host lavas to measure hydrogen stable isotope ratios of phlogopite, which in conjunction with trace element systematics, allow us to assess the source of metasomatism in the mantle lithosphere below this region of the northern Altiplano.

The resulting geochemical data highlight a subduction-derived origin for metasomatism in the mantle source of kersantite lavas which we argue resulted from shallow subduction below this region in the Oligocene. We conclude that the lithospheric mantle in the northern Altiplano region is at least partially composed of phlogopite- and apatite- bearing metasomatized peridotite, akin to metasomatized peridotite lithologies exhumed in the Italian Alps (Zanetti et al., 1999), and that melting of this altered mantle source is responsible for potassic basaltic volcanism since the cessation of shallow subduction.

2. Geologic Setting

2. 1. Northern Altiplano Plateau

The northern portion of the Altiplano Plateau sits at an average elevation of ~4 km and comprises an active volcanic arc to the west (Western Cordillera) and an extensive fold and thrust belt to the east (Eastern Cordillera, Interandean and Subandean Zones), which together bound the interiorly drained Altiplano basin (Fig. 1). The Andean margin has been a convergent boundary since the Neoproterozoic (Ramos, 2008), but the dramatic crustal shortening that characterizes the modern Andes did not begin until the Cenozoic. In the northern plateau, deformation along the Western Cordillera began in the

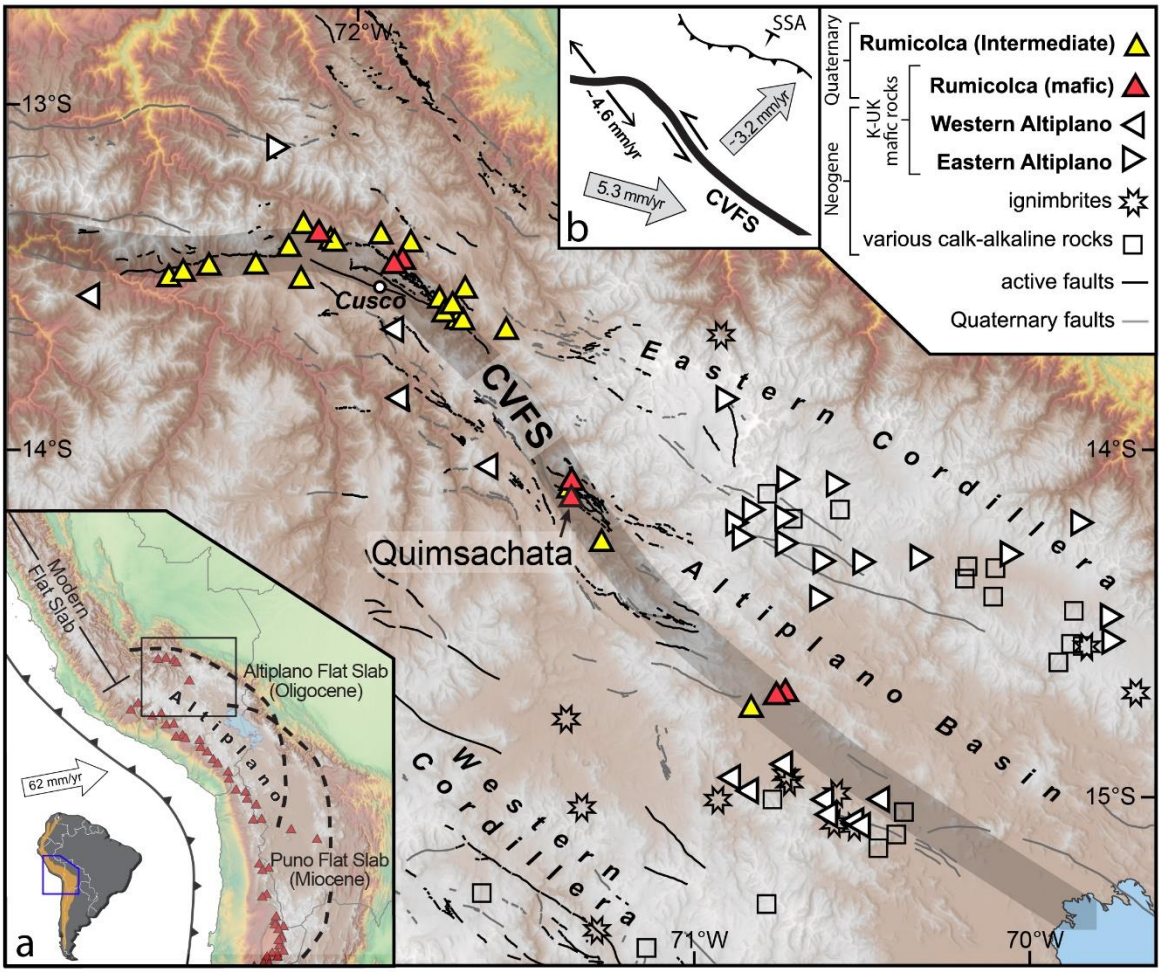

Fig 1. Map of Neogene and Quaternary volcanism of the northern Altiplano region. Quaternary Rumicolca Formation lavas are focused along the trace of the CVFS. The Quimsachata volcano, host of kersantite xenoliths, is highlighted. Older potassic and ultrapotassic (K-UK) mafic rocks comprise the eastern and western Altiplano suites of Carlier et al. (2005). Map location is shown in inset (a) along with major Quaternary volcanoes of the Central Andes (small red triangles) and the inferred extents of the Oligocene Altiplano flat slab and Miocene Puna flat slab (after Ramos and Folguera, 2009). Inset (b) is a schematic representation of convergence velocities of eastern and western Altiplano domains relative to stable South America (SSA) and partitioned by the CVFS (after Villegas-Lanza et al., 2016), demonstrating that the CVFS accommodates oblique-sinistral neotectonic deformation with a greater normal component to the north near Cusco, Peru.

late Cretaceous to early Eocene (Carlotto, 2013), and a cryptic period of deformation in the Eastern Cordillera occurred in the late Eocene (Farrar et al., 1988). Intense west-verging thrusting in the Eastern Cordillera and establishment of the Altiplano hinterland basin primarily occurred in the late Eocene to early Oligocene, coincident with shallowing of the Nazca slab (Isacks, 1988; James and Sacks, 1999; Carlotto, 2013). Active shortening has since propagated towards the Amazonian foreland in the Interandean and Subandean zones along the length of the plateau. Neotectonic activity within the northern plateau interior is focused along the CVFS, also referred to as the Urcos-Ayaviri-Copacabana-Concori Fault System (Sempere et al., 1990). This fault system has a complex slip history but most recently accommodates sinistral transtensional deformation (Carlotto, 2013; Perez and Horton, 2014) and acts as a major structural boundary partitioning Andean deformation between two continental slivers (Villegas-Lanza et al., 2016; Fig. 1).

Surface uplift to attain modern elevations, while diachronous across the plateau, is interpreted to postdate crustal shortening in the northern Altiplano region (Garzione et al., 2006; Kar et al., 2016). Various mechanisms have been proposed to explain modern crustal thicknesses and surface elevations, including lateral flow of lower crustal material from the Eastern and Western Cordilleras into the plateau interior, magmatic underplating, and delamination of the lower lithosphere (see reviews by Allmendinger et al., 1997; Garzione et al., 2017). Trace element ratios (La/Yb, Sr/Y) of potassic backarc volcanics in the northern Altiplano have been used to conclude crustal thickening occurred in the last ~5 Ma, postdating evidence for surface uplift (Garzione et al., 2017). However, these estimates assume that magmatic interaction and trace element

partitioning with residual phases in the lower crust (e.g., plagioclase vs. garnet) is the primary control over these trace element ratios (Profeta et al., 2015). This assumption is questionable if trace element characteristics of the mantle melt source have been altered by slab-derived fluids or melts, as the partitioning effects of residual garnet may be overprinted on already elevated trace element ratios.

The Western Cordillera is currently the axis of calk-alkaline arc volcanism and has been for most of the Phanerozoic (Mamani et al., 2010). In the northern Altiplano, a major inboard migration of magmatism in the late Eocene and Oligocene is recognized as the result of shallow or flat-slab subduction, referred to as the Altiplano flat slab by Ramos and Folguera (2009). The roughly contemporaneous eastward shift in deformation is hypothesized to have resulted from thermal weakening of the foreland lithosphere by the introduction of large volumes of magmatism, either directly resulting from shallow subduction (Isacks, 1988; James and Sacks, 1999) or due to anomalous mantle flow during slab foundering (Sandeman et al., 1995). Others have inferred that deformation and shallow subduction were linked through coupling between the flat slab and Andean lithosphere (Martinod et al., 2010; Horton, 2018), or through more complex stresses resulting from migration of the mantle wedge (Martinod et al., 2020). The effects of hydration and metasomatism on the rheology of the Andean lithosphere has only recently been promoted as acting to influence deformation patterns (Saylor et al., 2023). After shallow subduction ceased below the northern Altiplano, slab shallowing migrated to the south and the Puna flat slab was established below the Southern Altiplano-Puna Plateau from ~ 18 to 12 Ma (Ramos and Folguera, 2009), where it was also followed by development of a regional unconformity inferred to represent reinvigorated exhumation

in the Eastern Cordillera (Saylor et al., 2023). Shallow subduction is a common transient feature along the margin, as evidenced by three occurrences of modern flat slabs below north/central Peru (Fig. 1), Central Chile/Argentina, and Columbia (Ramos and Folguera, 2009).

In the northern Altiplano, arc magmatism was reestablished in the Western Cordillera near the end of the Oligocene, signaling the cessation of shallow subduction. Bimodal volcanism has been prevalent in the back arc region since this time, including ignimbrite eruptions from ca. 23-12 Ma, most frequently >16 Ma, and more punctuated periods of basaltic volcanism that occurred primarily from ca. 30-20 Ma, 6-5 Ma, and <2 Ma. Neogene and Quaternary basaltic rocks are highly alkaline (potassic and ultrapotassic) and include various lamproites, lamprophyres, shoshonites, and latites (Sandeman et al., 1995; Carlier et al., 1997, 2005). This bimodal volcanism has been interpreted as the result of antithetic subduction of the Brazilian shield below the eastern Altiplano, leading to melting of the enriched cratonic lithospheric mantle during interaction with hot asthenosphere and the generation of volatile-rich alkaline basaltic melts (Sandeman et al., 1995). Contemporary bimodal volcanism has also occurred in the Bolivian Altiplano, where lithospheric delamination and asthenospheric flow dynamics have been suggested as the driver of melting (Hoke and Lamb, 2007). We note similarities to bimodal volcanism with highly alkaline mafic endmembers has that occurred during the Oligocene ignimbrite flare-up in the western US, where a connection has been established to lithospheric hydration driven by shallow subduction and subsequent melting after slab removal (Farmer et al., 2008).

The youngest volcanism in the northern plateau interior is a Quaternary suite of mostly intermediate alkaline and calk-alkaline lavas that erupted in close proximity to the CVFS between ~13 and 15°S and are referred to as the Rumicolca Formation (Fig. 1; Carlotto et al., 2011) or Quimsachata volcanics (Mamani et al., 2010). These lavas generally fall into two compositional groups. The first includes a more mafic and highly potassic group of lamproites, lamprophyres (minettes and kersantites), and shoshonites that were the focus of earlier studies (Carlier and Lorand, 1997, 2008; Carlier et al., 2005) and are summarized in more detail below. A second group includes a larger proportion of Rumicolca Formation lavas that exhibit intermediate compositions transitional between alkaline and calk-alkaline varieties. Many of these flows are biotite- and/or amphibole-phyric latites, andesites, and dacites, and were generally referred to as lamprophyres by Chapman et al. (2015). In detail, most of these flows have potassic bulk compositions (1–2 K_2O/Na_2O wt% basis; Foley et al., 1987) with moderate CaO (4-5 wt%), low TiO_2 (<1 wt%), and moderate Al_2O_3 (15–17 wt%) spanning from metaluminous to peraluminous (Mamani et al., 2010; Carlotto et al., 2011). Reported trace elements characteristics, although limited, are similar to their more mafic counterparts along the CVFS, including incompatible element enrichments (e.g., Rb, Ba, Th, La $>100_{PM}$; relative to primitive mantle) with notable negative Nb-Ta anomalies (Mamani et al., 2010; Carlotto et al., 2011).

Xenoliths have not been reported from the more mafic ultrapotassic suite except for a lamproite that contains garnet granulites (Carlier and Lorand, 1997). In contrast, a number of flows from the more felsic group are particularly rich in both crustal and mantle xenoliths. Chapman et al. (2015) described a suite of crustal and mantle xenoliths

collected from four Rumicolca lava flows, focusing on mid-crustal metamorphic lithologies with implications for tectonic burial and reconstructions of tectonic shortening. Igneous and metamorphic xenoliths from the deep crust and mantle were also briefly described, including various peridotites, mafic granulites, and amphibolites.

2.2. Neogene-Quaternary alkaline basalts

Alkaline basalts in the northern plateau are ubiquitously potassic or ultrapotassic ($K_2O/Na_2O > 2$; Foley et al., 1987) and exhibit varying chemistries based their ages and locations either to the east, west, or along the CVFS. The eastern Altiplano suite primarily includes sanidine-phlogopite lamproites, orthopyroxene minettes, and shoshonites with eruption ages between 28 and 20 Ma. Based on the geochemistry of the lamproites, Carlier et al. (2005) suggested the underlying mantle source was most likely a phlogopite-bearing, carbon-rich harzburgite with Archean to Paleoproterozoic model ages. In the western Altiplano, the geochemistry of 30-28 Ma diopside-rich leucitites, tephrites, and trachybasalts are used to infer an underlying mantle source characterized by metasomatized lherzolite or wehrlite with Meso- to Neoproterozoic T_{DM} (depleted mantle) model ages (Carlier et al., 2005). Lavas from both eastern and western domains are highly enriched in incompatible trace elements and display pronounced enrichments in fluid mobile elements (e.g., Ba, Rb, Pb) and relative depletions in Nb and Ta, characteristic of arc-related lavas (e.g., Plank and Langmuir, 1998; Kelemen et al., 2013). These enrichments are more pronounced in eastern Altiplano lavas. Sr and Nd isotopic data also fall towards enriched values on the mantle array. Eastern Altiplano lavas yield

$^{87}Sr/^{86}Sr_i$ and ε_{Nd} values of 0.7100 to 0.7159 and -5.9 to -11.4, respectively, compared to values of 0.7049 to 0.7069 and +0.61 to -6.3 for the western Altiplano.

The alkaline basalts along the CVFS are dated between 1.78 and 0.03 Ma (Kaneoka and Guevara, 1984; Mamani et al., 2010; Carlotto et al., 2011) and include diopside-sanidine-phlogopite lamproites and augite kersantites, minettes, and trachybasalts (Carlier et al., 2005). The lamproites are ultrapotassic ($K_2O/Na_2O > 4$) and display strong incompatible element enrichments similar to the eastern Altiplano lavas, but without notable Nb-Ta depletions. In contrast, augite kersantites, minettes, and trachybasalts are potassic ($K_2O/Na_2O = 1 - 2$), display similarly enriched trace element patterns, but do show clear Nb-Ta anomalies. Sr and Nd isotopic data from both groups cluster to similar values as lavas from the western Altiplano ($^{87}Sr/^{86}Sr_i = 0.7052$ to 0.7062, ε_{Nd} -1.1 to -3.2). Major and trace element characteristics (e.g., CaO concentrations, CaO/Al_2O_3 ratios, large-ion lithophile element (LILE) enrichment) are generally intermediate between the eastern and western Altiplano suites, and as such the CVFS mafic lavas are interpreted to reflect melt input from both eastern and western lithospheric mantle domains. More specifically, the lamproites were hypothesized to have melt source involving mica + clinopyroxene ± apatite ± amphibole, while the melt source of potassic lamprophyres additionally included a larger proportion of olivine or orthopyroxene. Conversely, Chapman et al. (2015) speculated a melting of clinopyroxene-rich lower crustal arc cumulates. Both hypothesized source lithologies described by Carlier et al. (2005) were speculated to have interacted with volatile-rich low viscosity melts, leading to homogenous Sr-Nd isotopic compositions between the ultrapotassic and potassic lavas and potentially explaining discrepancies in high field-

strength element (HFSE) abundances due to HFSE/LILE fractionation during melt percolation (Bedini et al., 1997; Carlier et al., 2005).

The CVFS was ultimately interpreted to separate two distinct lithospheric mantle blocks below the eastern and western Altiplano domains, and younger model ages of CVFS lavas (T_{DM} = 612-864 Ma) compared to both eastern (1130-2485 Ma) and western (837-1241 Ma) domains were interpreted to reflect melt input from the asthenosphere mantle. However, the lithospheric architecture in this region is not fully constrained, and an alternative explanation is that these younger T_{DM} ages along the CVFS are indicative of Neoproterozoic crust/mantle situated between the western edge of the Brazilian shield to the east and the Mesoproterozoic Arequipa terrain to the west (McLeod et al., 2013). Rifting is speculated to have occurred between these older cratonic blocks in the Neoproterozoic (600 – 850 Ma; Ramos, 2008), which could explain the younger observed model ages along the CVFS.

Geophysical investigations highlight a region of anomalously slow seismic velocities in the mantle wedge extending eastward from the volcanic arc to the area below the Quimsachata volcano (Ward et al., 2016). Together with interpretations of arc-parallel flow in the mantle wedge (Wagner et al., 2006) and the southern edge of the modern Peruvian flat slab just north of this region, this mantle anomaly is interpreted to result from deflection of mantle wedge flow leading to a zone of hydrous or partially molten mantle in this region (Ward et al., 2016; Garzione et al., 2017). The southward advance of the Peruvian flat slab implies that this would be a relatively young feature in this location, which may help to explain the localized Quaternary backarc volcanism.

2.3. The Quimsachata and Oroscocha Volcanoes

The Quimsachata volcano is one of the southernmost lavas in the Rumicolca Formation and is the youngest dated lava flow in the region at <0.03 Ma (Kaneoka and Guevara, 1984). This small shield volcano (~4 km wide) is compositionally more akin to the first group of more mafic lavas studied by Carlier et al. (2005). In detail, this flow is a latite (or banakite; Carlier and Lorand, 2008) with SiO_2 = 56.8 wt% and $K_2O + Na_2O$ = 7.25 wt % and with alkali contents dominated by potassium (K_2O/Na_2O wt% = 1.55). It exhibits moderate CaO (5.65 wt%), and TiO_2 (1.27 wt%), and moderate Al_2O_3 (15.0 wt%) (Mamani et al., 2008). Phenocrysts of phlogopite, plagioclase, and orthopyroxene are abundant. Trace element characteristics essentially mirror those reported for other potassic basalts along the CVFS (Carlier et al., 2005; Mamani et al., 2008).

Located five kilometers to the north of the Quimsachata volcano is the 0.64 Ma Oroscocha volcano (Fig. 1; Mamani et al., 2010), which was described in detail by Carlier and Lorand (2008). This smaller extrusive unit (1.5 km^2) consists of multiple rhyolitic lava flows and a smaller summit dome of trachydacite. Mafic “blobs” of kersantite compositions are distributed throughout these flows and represent evidence for mixing of peraluminous granite and lamrpophyric mafic magmas. The dominant mineralogy of the kersantites enclaves, primarily represented by a fine-grained groundmass, include high Ba-Ti phlogopite, diopside, and roughly equal proportions of plagioclase and K-feldspar. Similar to other ultrapotassic mafic lavas studies along the KVFS, these inclusions are highly enriched in LILEs and light rare-earth elements (LREE) and display prominent Nb and Ta negative anomalies.

3. Sampling and Methods

Xenoliths are scarce in the Quimsachata lavas, and most xenoliths noted in the field were granitic lithologies. However, seven xenoliths collected exhibit a similar phlogopite and clinopyroxene-rich, course-grained, mafic igneous lithology best described as phaneritic kersantites. An additional wehrlite xenolith shows dominantly olivine and clinopyroxene but with domains of fine-grain plagioclase, K-feldspar, and phlogopite reminiscent of the seven kersantites xenoliths (Fig. 2). These xenolith samples range in size from ~3 to 6 cm wide. For samples that were too small to perform all analyses, stable isotope and trace element analyses were prioritized over major element analyses. We describe the mineralogy and major element chemistry of the xenoliths to define a likely mantle source lithology for these alkaline melts. In this contribution we focus on stable isotope and trace element evidence for metasomatism in the mantle source of kersantite lavas.

3.1. Petrography and Chemical Analyses

Quimsachata kersantite xenoliths were analyzed petrographically at Utah State University (USU). Mineral compositions and textural characteristics were also assessed using a FEI Quanta FEG 650 field-emission SEM with Oxford EDS detector at the USU Microscopy Core Facility; however, we do not report individual mineral chemistries due to the semi-quantitative nature of this method. An exception are chemical analyses of phlogopite separates analyzed via Inductively Coupled Plasma Mass Spectrometry (ICPMS) and described below.

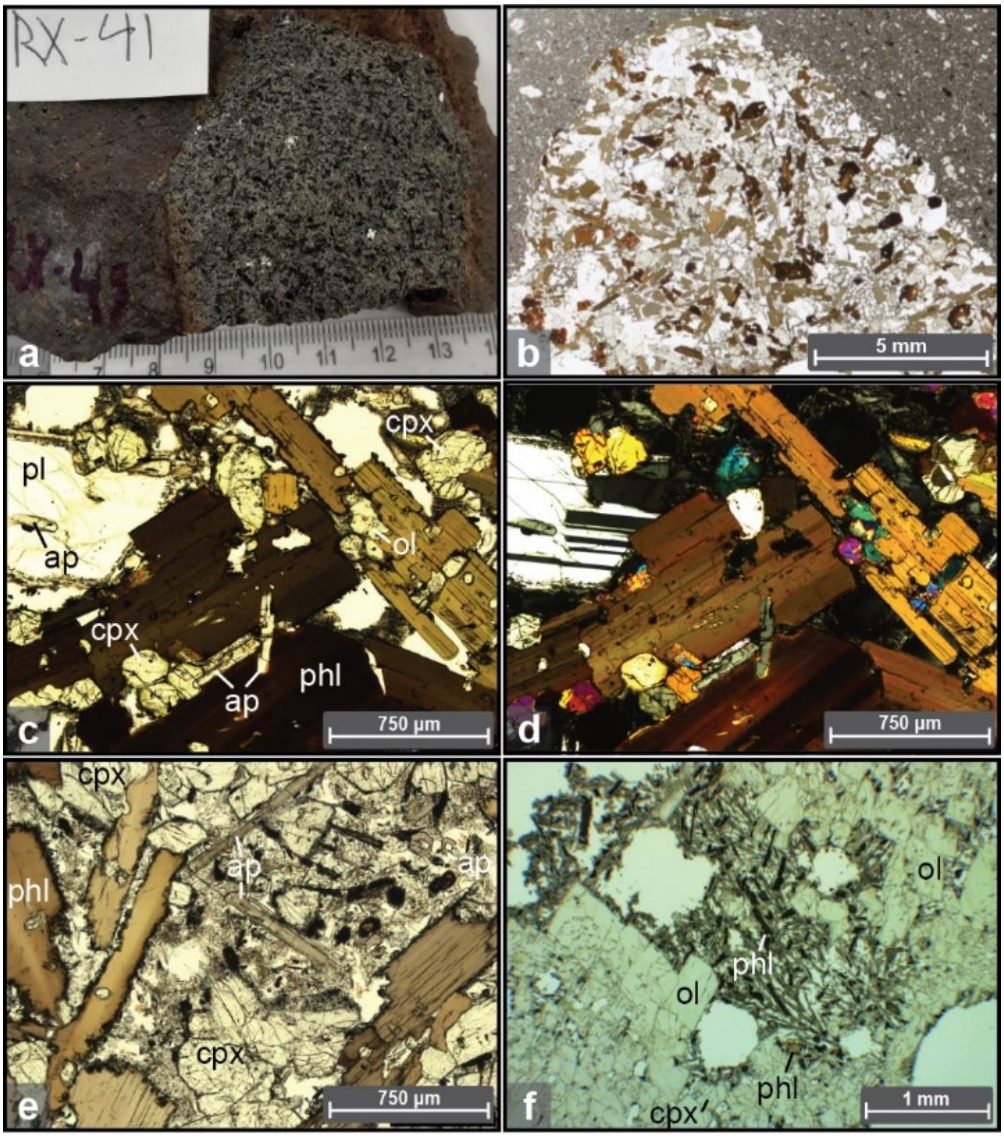

Fig 2. Hand sample photo and photomicrographs of kersantite xenoliths. a) Hand sample photograph of kersantite xenolith CH19RX-41. Scale is labelled in centimeters. b) Plane polarized light (PPL) photomicrograph of sample CH19RX-35 within Quimsachata latite showing course grained biotite rich characteristic of kersantite xenoliths. c) Higher magnification PPL photomicrograph of sample CH19RX-35 showing clinopyroxene, apatite, and rounded (resorbed) olivine included within poikolitic phlogopite. Interstitial plagioclase is partially melted along grain edges. d) Same as (c) in cross polarized light (XPL). e) Kersantite sample CH19RX-41 in PPL displaying euhedral clinopyroxene, partially melted phlogopite, and abundant prismatic apatite. Glassy matrix is composed primarily of plagioclase and alkali-feldspar microlites, enstatite, and ilmenite. f) Wehrlite sample CH19RX-42 comprised primarily of olivine and clinopyroxene, but with domains of phlogopite and glassy matrix of feldspar microlites and oxides. Mineral abbreviations: cpx – clinopyroxene, phl – phlogopite, ap – apatite, pl – plagioclase, ol – olivine

Samples were carefully prepared for bulk rock geochemical analyses to avoid contamination. Exterior rims of xenoliths were sawed away and interiors were gently crushed. Chips of xenoliths were crushed to a fine homogenous powder in an agate mortar and pestle. Bulk rock major element analyses were conducted on fused pellets via wavelength dispersive X-ray fluorescence (WDXRF) spectrometry at the Washington State University Peter Hooper GeoAnalytical Laboratory following standard methods after Johnson et al. (1999).

Bulk rock trace element compositions were determined for the seven xenolith samples and the Quimsachata host lava using an Agilent 8900 triple-quadrupole ICPMS at the Utah State University Geosciences Department. Trace element compositions of phlogopite mineral separates were also measured for six samples with sufficient sample material following the separation procedure outlined below for hydrogen stable isotope analysis. Powdered samples were dissolved in a stepwise acid digestion procedure using trace element grade HNO_3 and HF at 60 – 90 °C. Samples were diluted gravimetrically in dilute HNO_3 and analyzed with an Agilent 6800 Triple Quadrupole ICPMS.

3.2. Hydrogen Stable Isotopes

Hydrogen stable isotopes were measured from phlogopite separates from the seven kersantite xenoliths. Phlogopite from the wehrlite sample was not abundant enough to be analyzed. Phlogopite phenocrysts from Quimsachata lavas were also analyzed for hydrogen isotope characteristics. Material from xenolith interiors or samples of host lava was crushed in agate mortar and pestle and sieved to a size fraction between 75 and 180 μm. Phlogopite was concentrated based on its platy morphology by lightly shaking the

size fraction over a tilted sheet of paper. Phlogopite was then separated from the platy fraction under a binocular microscope, sonicated in pure ethanol for 15 minutes, and dried overnight at 50 °C. Aliquots of 2-6 mg of phlogopite were weighed using a micro balance and loaded into Ag capsules in preparation for isotopic analysis. Aliquots were pyrolyzed in a glassy-carbon reactor at 1450 °C using a Thermo Scientific high temperature conversion elemental analyzer (TC/EA) and the D/H ratio of the produced H_2 gas was analyzed on a Thermo Scientific Delta V Advantage IRMS with Conflow IV interface. Resulting isotope ratios were scale normalized using standards USGS-57 (biotite) and USGS-58 (muscovite) and reported as δD in ‰ relative to VSMOW. Reported δD values have an analytical uncertainty of ± 2 ‰ based on replicate standard analyses.

A series of benzoic acid samples with a range of masses were included in analytical runs to account for linearity effects and to calibrate signal intensity to the mass of H_2 gas produced in each sample. Benzoic acid samples were assumed to quantitatively produce H_2 gas as a function of their mass and stoichiometric H content. A calibration curve relating the calculated mass of H_2 and integrated peak intensity for mass-2 in the benzoic acid suite was then used to evaluate the mass of H_2 produced for each phlogopite aliquot. Calculated H_2 yields of USGS-57 and USGS-58 standards are compared with reported values (Qi et al., 2017) and are accurate within 4 % relative error. Measured H_2 contents are reported as wt% H_2O.

4. Results

Kersantite xenoliths display a ubiquitous assemblage of clinopyroxene (diopside, ~30-40% by volume) and poikilitic phlogopite (20-40%) with interstitial plagioclase (labradorite), prismatic fluorapatite, and minor magnetite, and ilmenite (Fig. 2). One sample contains minor amphibole (likely oxyhornblende). Minor forsterite grains exist as inclusions within phlogopite and in close association with pyroxene and display rounded and embayed grain boundaries, suggesting a xenocristic origin and/or resorption during crystallization. Plagioclase is either partially or wholly melted and recrystallized as smaller feldspar crystallites, presumably during eruption. EDS-SEM analyses of groundmass glasses and feldspar crystallites also suggest that K-feldspar was a significant interstitial phase before partial melting. Phlogopite grains show evidence for partial melting around grain edges, but apatite and clinopyroxene grains maintained a largely euhedral character.

4.1. Major/Minor Element Chemistry

Bulk-rock chemical analyses and calculated normative compositions for five kersantites xenoliths and the wehrlite xenolith are given in Tables 1 and 2. In general, the kersantite samples are highly magnesian (MgO = 9.5 to 15.4 wt%; Mg# = 100Mg/(Mg+Fe) = 68 to 81), low silica (SiO_2 = 45.6 to 49 wt%) and ultrapotassic (K_2O = 3.6 to 5.1 wt%; K_2O/Na_2O = 2.5 to 4.6). On a TAS discrimination diagram (Le Maitre, 1984) these samples fall on a linear trend from more alkaline and lower silica compositions to less alkaline and higher silica compositions, corresponding to foid-gabbro, monzogabbro, and gabbro (Fig. 3). The wehrlite xenolith displays the highest

SiO_2 and lowest alkali compositions of the suite, plotting in the gabbroic diorite field. This relationship is controlled by K_2O contents, which show a strong inverse correlation with SiO_2 ($r^2 = 0.95$, $p = 9x10^{-4}$; Fig. 4). A well-correlated relationship is also seen between SiO_2 and P_2O_5 ($r^2 = 0.91$ or 0.62 excluding or including the wehrlite sample, respectively). Cr and Ni concentrations range from 360 – 1560 ppm and 29 – 88 ppm, respectively, and show relatively weak positive correlations with MgO and Mg# . All five kersantite xenoliths are critically undersaturated with respect to SiO_2 and exhibit compositions with normative nepheline (2.0 to 5.7 wt%), with one sample also exhibiting normative leucite (CH19RX-45; 1.7 wt%).

Compositions of phlogopite phenocrysts measured via ICPMS (Table 3) reveal moderate to highly magnesian compositions with Mg# = 0.62 – 0.79, high TiO_2 (2.9 – 3.9 wt%), and exceptionally high Ba (7000 – 9000 ppm). No F or Cl was detected in phlogopite via EDS-SEM, although significant F^- (~2 wt %) was noted in apatite.

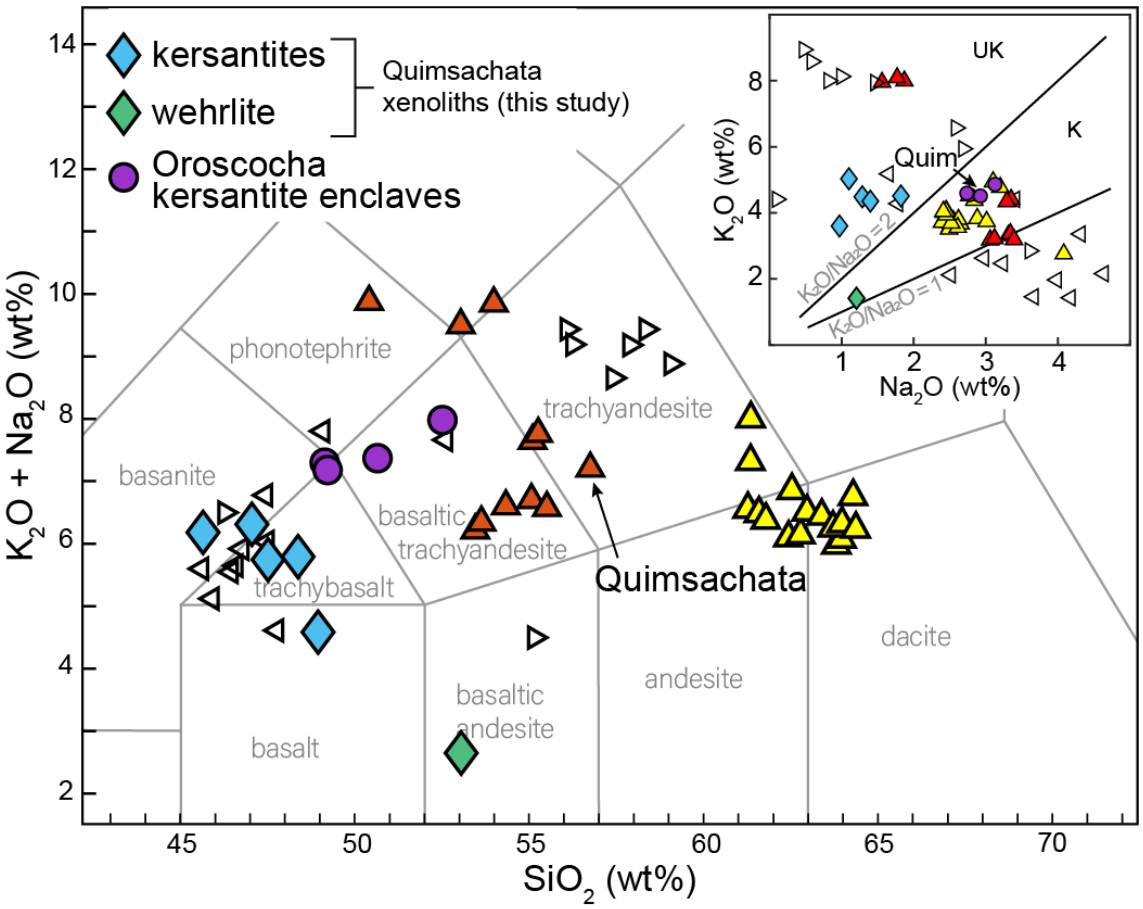

Fig. 3. Total alkali versus silica plot (Le Maitre, 1984) of Quimsachata kersantite xenoliths and other Neogene-Quaternary volcanics discussed in text. Symbols for Rumicolca Formation lavas and eastern and western Altiplano suites are as in Figure 1. Inset shows discrimination of alkali contents (Na_2O vs. K_2O), demonstrating the potassic (K) or ultrapotassic (UK) compositions of kersantite xenoliths and Rumicolca Formation lavas. Compositions of Rumicolca formation lavas and Neogene basalts are provided in Appendix C (Table C4).

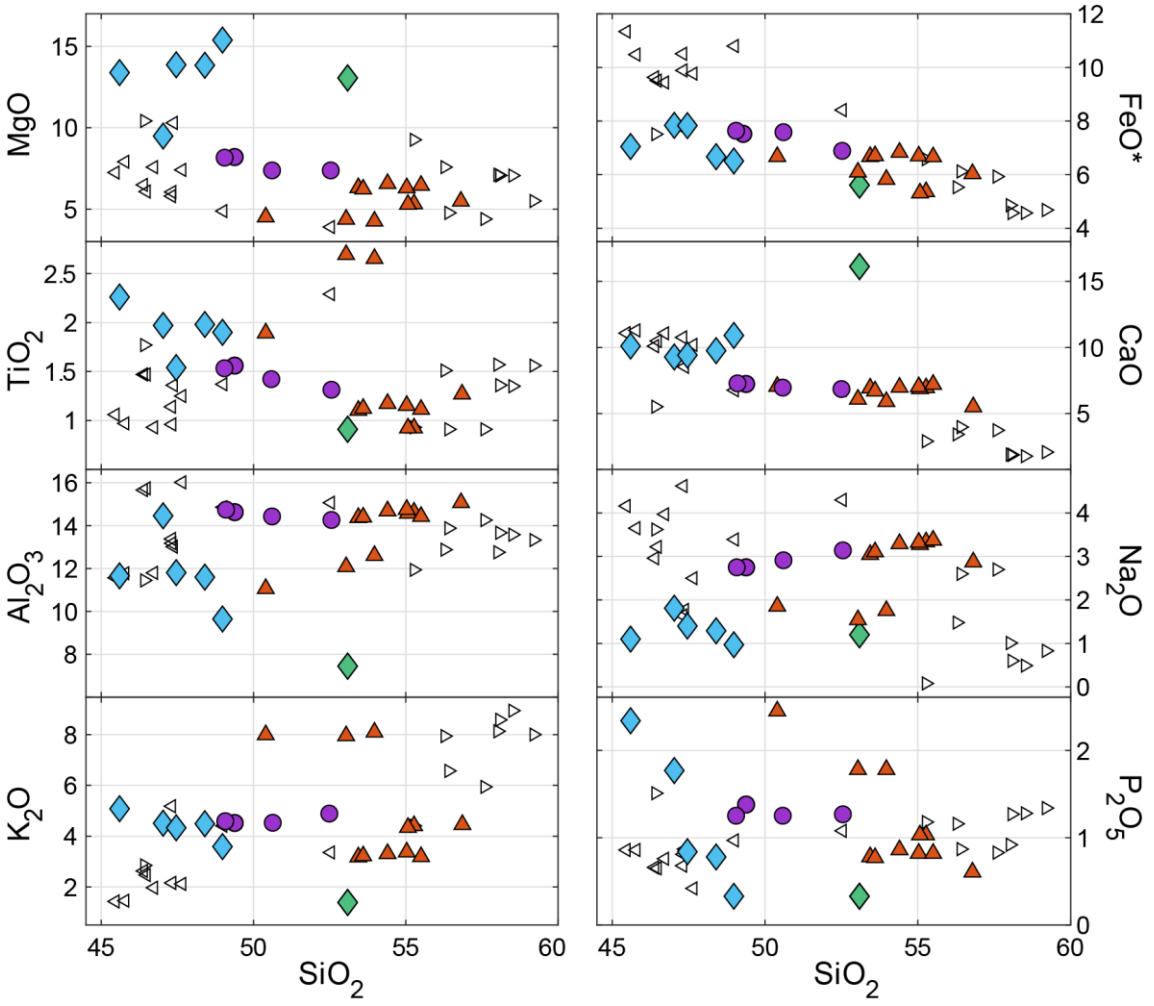

Fig. 4. **Whole-rock major elements versus SiO_2 for Neogene-Quaternary mafic rocks.** Symbols as in Figures 1 and 3. Kersantite xenoliths exhibit low SiO_2 and high MgO compared to other northern Altiplano suites. Major element variability is best explained through variable modal proportions of phenocryst phases (phlogopite, clinopyroxene, apatite), implying some accumulation of cumulate phases.

Table 1. Bulk-rock major and trace element compositions of kersantite and wehrlite xenoliths

	CH19RX-35 kersantite	**CH19RX-39** kersantite	**CH19RX-40** kersantite	**CH19RX-41** kersantite	**CH19RX-44** kersantite	**CH19RX-43** kersantite	**CH19RX-45** kersantite	**CH19RX-42** wehrlite
SiO_2 (wt%)	47.03	-	48.98	48.40	-	47.46	45.60	53.09
TiO_2	1.97	-	1.90	1.98	-	1.54	2.26	0.91
Al_2O_3	14.46	-	9.65	11.60	-	11.81	11.66	7.45
FeO*	7.84	-	6.51	6.67	-	7.83	7.05	5.61
MnO	0.09	-	0.09	0.09	-	0.12	0.09	0.12
MgO	9.49	-	15.39	13.84	-	13.87	13.39	13.06
CaO	9.28	-	10.91	9.76	-	9.42	10.11	16.12
Na_2O	1.81	-	0.97	1.29	-	1.40	1.10	1.20
K_2O	4.51	-	3.59	4.49	-	4.33	5.08	1.39
P_2O_5	1.77	-	0.33	0.78	-	0.84	2.34	0.33
Sum	98.2	-	98.3	98.9	-	98.6	98.7	99.3
LOI %	0.65	-	0.94	0.38	-	0.24	0.28	0.31
Mg#	68.3	-	80.8	78.7	-	75.9	77.2	80.6
Sc (ppm)	26	-	36	29	-	29	29	41
V	194	-	199	179	-	169	216	135
Cr	355	-	1332	1242	-	931	405	1104
Ni	29	-	67	88	-	63	50	50
Cu	9	-	8	6	-	12	8	7
Zn	110	-	77	81	-	92	111	59
Ga	20	-	13	15	-	17	17	11
Rb	137	122	131	168	55	134	157	40
Sr	2101	1336	526	677	720	1420	1154	642
Y	15.45	17.91	11.31	12.54	13.58	18.32	17.40	15.34
Zr	136	260	100	131	153	246	158	139
Nb	11.07	14.81	7.66	8.11	9.41	16.99	10.62	7.52
Cs	1.649	1.606	2.045	1.652	0.592	1.164	1.020	0.648
Ba	3750	2442	3057	2661	1746	2690	3448	865

Table 1 continued.

	CH19RX-35 kersantite	**CH19RX-39** kersantite	**CH19RX-40** kersantite	**CH19RX-41** kersantite	**CH19RX-44** kersantite	**CH19RX-43** kersantite	**CH19RX-45** kersantite	**CH19RX-42** wehrlite
La	66.19	80.97	29.92	38.34	44.87	81.15	83.74	36.40
Ce	138.6	162.7	63.3	84.5	90.6	161.5	178.1	77.5
Pr	16.89	19.09	7.97	10.43	10.98	18.71	21.75	9.72
Nd	67.83	73.79	33.12	43.09	43.41	72.15	87.86	40.51
Sm	11.41	12.56	6.43	8.06	7.77	12.07	15.01	7.90
Eu	3.19	3.18	1.84	2.00	2.11	3.12	3.57	2.19
Gd	7.55	8.46	4.60	5.63	5.52	8.14	9.71	5.88
Tb	0.769	-	0.508	-	0.716	-	-	0.693
Dy	3.47	4.50	2.57	3.14	3.13	4.47	4.59	3.37
Ho	0.537	0.713	0.401	0.501	0.618	0.709	0.706	0.578
Er	1.29	1.82	1.00	1.26	1.37	1.82	1.65	1.40
Tm	0.131	0.202	0.102	0.134	0.273	0.212	0.181	0.182
Yb	0.953	1.335	0.806	0.894	1.11	1.40	1.09	1.12
Lu	0.097	0.165	0.089	0.102	0.226	0.175	0.132	0.144
Hf	3.60	6.30	2.90	2.91	4.09	6.14	3.72	3.96
Ta	0.488	1.324	0.374	-	0.456	-	-	0.380
Pb	16.17	18.19	13.13	5.71	21.97	12.48	8.68	10.10
Th	8.25	14.36	6.16	6.11	8.40	12.28	9.81	7.04
U	1.69	2.41	2.58	1.06	1.64	2.08	1.62	1.15

Major oxides reported in weight percent (wt%), trace elements in parts per million (ppm)

FeO* = total Fe reported as FeO

Mg# = molar 100Mg/(Mg+Fe)

Table 2. Normative mineralogy of kersantite xenoliths

	CH19RX-35	CH19RX-40	CH19RX-41	CH19RX-43	CH19RX-45	CH19RX-42
Plagioclase	26.2	16.0	15.3	14.5	11.9	21.0
Orthoclase	26.6	21.2	26.5	25.6	27.8	8.2
Nepheline	3.9	2.0	4.4	5.7	5.0	0.0
Leucite	0.0	0.0	0.0	0.0	1.7	0.0
Diopside	14.3	32.8	25.1	23.3	19.3	53.5
Hypersthene	0.0	0.0	0.0	0.0	0.0	10.4
Olivine	17.8	20.6	20.5	23.0	21.8	2.4
Ilmenite	3.7	3.6	3.8	2.9	4.3	1.7
Magnetite	1.9	1.6	1.6	1.9	1.7	1.4
Apatite	4.1	0.8	1.8	2.0	5.4	0.8
Zircon	0.0	0.0	0.0	0.1	0.0	0.0
Chromite	0.1	0.3	0.3	0.2	0.1	0.2
Total	98.6	98.7	99.3	99.0	99.0	99.5

values are in weight percent

Table 3. Hydrogen isotope ratios, water contents, and compositions of phlogopite from kersantite xenoliths and Quimsachata lavas

	CH19RX-35	CH19RX-39	CH19RX-40	CH19RX-41	CH19RX-44	CH19RX-43	CH19RX-45	Quimsachata
δD	-38.34	-42.48	-52.71	-49.72	-49.41	-76.97	-57.66	-56.85
wt% H2O	1.52	2.08	2.26	2.11	1.89	1.91	1.22	1.35
TiO_2 (wt %)	3.4	3.6	3.6	3.3	-	2.9	3.9	-
Al_2O_3	11.7	13.8	11.2	12.7	-	13.5	13.3	-
FeO*	12.4	10.0	7.5	8.4	-	10.4	9.2	-
MgO	11.5	14.6	15.1	17.8	-	15.1	17.0	-
MnO	0.07	0.09	0.05	0.06	-	0.11	0.06	-
K_2O	14.1	16.5	14.0	16.0	-	15.1	16.5	-
Na_2O	0.9	0.9	0.8	1.0	-	1.3	0.7	-
Mg#	62	72	78	79	-	72	77	-
Cr (ppm)	295	606	962	1742	-	323	468	-
Ga	21.5	17.5	13.3	15.4	-	18.4	17.5	-
Ge	9.705	7.625	6.303	6.721	-	7.972	7.178	-
Rb	259	299	263	307	-	253	316	-
Sr	542	369	272	280	-	667	312	-
Y	8.775	2.216	1.718	2.527	-	5.219	1.264	-
Zr	51.3	59.8	22.6	50.6	-	97.4	40.6	-
Nb	13.6	12.3	7.8	9.4	-	18.2	11.0	-
Cs	2.42	2.16	2.23	2.39	-	2.03	2.25	-
Ba	8212	8855	7934	6956	-	7609	8676	-
La	39.9	13.2	2.50	8.39	-	27.2	5.15	-
Ce	87.9	24.5	5.54	16.3	-	51.4	9.98	-
Pr	11.0	2.70	0.76	1.94	-	5.69	1.18	-
Nd	45.2	9.74	3.33	7.77	-	21.01	4.59	-
Sm	7.35	1.44	0.697	1.40	-	3.19	0.773	-
Eu	2.46	1.20	1.04	1.05	-	1.62	1.18	-
Gd	4.72	0.946	0.570	1.019	-	2.19	0.539	-
Tb	0.460	0.094	0.063	0.107	-	0.233	0.054	-
Dy	2.03	0.481	0.345	0.546	-	1.10	0.272	-

Table 3 continued.

	CH19RX-35	CH19RX-39	CH19RX-40	CH19RX-41	CH19RX-44	CH19RX-43	CH19RX-45	Quimsachata
Ho	0.300	0.073	0.056	0.088	-	0.177	0.038	-
Er	0.690	0.188	0.148	0.240	-	0.451	0.109	-
Tm	0.080	0.021	0.014	0.031	-	0.059	0.011	-
Yb	0.470	0.110	0.113	0.202	-	0.382	0.065	-
Lu	0.055	0.021	0.014	0.023	-	0.052	0.011	-
Hf	1.375	1.474	0.683	1.336	-	2.486	1.100	-
Ta	0.515	0.512	0.380	0.435	-	0.729	0.441	-
Pb	14.91	4.55	7.59	-	-	22.4	3.40	-
Th	2.80	2.53	0.419	1.83	-	4.19	1.12	-
U	0.605	0.470	0.162	0.401	-	0.753	0.218	-

all elements/oxides measured via ICPMS

major oxides are in weight percent, trace elements are in parts per million

analytical error for major oxides < 11% based on BHVO-1 standard analyses, CaO omitted due to larger error, SiO_2 not measured

4.2. Trace Element Chemistry

Trace element compositions are provided in Table 1. Analytical accuracy is within 5% relative error for most trace elements, and less than 10% for Hf and Eu, based on analyses of the USGS BHVO-1 standard. All samples exhibit broadly similar trace element characteristics and are overall highly enriched in incompatible elements relative to primitive mantle compositions, including both LILEs and LREEs. Fluid mobile LILEs are notably enriched above other incompatible elements; Rb Ba and Pb show concentrations up to 176, 4843, and 25 ppm, respectively. Primitive mantle (PM) normalized concentrations for Ba, Rb, Pb, and La are up to 600_{PM}, 200_{PM}, 150_{PM}, and 100_{PM}, respectively (Fig. 5). Pronounced negative anomalies are seen for Nb and Ta in all samples, with slight negative anomalies in Zr and Hf in all but one sample. Trace element characteristics (e.g., Ba concentrations, La/Yb ratios), show an apparent relationship with major element chemistry. For example, the most mafic samples with highest K_2O and P_2O_5 contents commonly display the greatest LILE and LREE abundances, as well higher ratios of La/Yb and Sr/Y that are characteristic of incompatible element enrichment (Fig. 5).

4.3. Hydrogen Stable Isotopes

Measured δD values of the kersantite xenoliths and alkaline lavas are given in Table 3. Two or three phlogopite aliquots were run for each sample, with standard deviations for each sample < 2 ‰ (excluding one duplicate with sd = 4 ‰). All but one xenolith sample exhibited δD values between -58 ‰ and -38 ‰, with the outlier yielding a value of -74 ‰. Phlogopite phenocrysts from Quimsachata lavas yield a similar δD

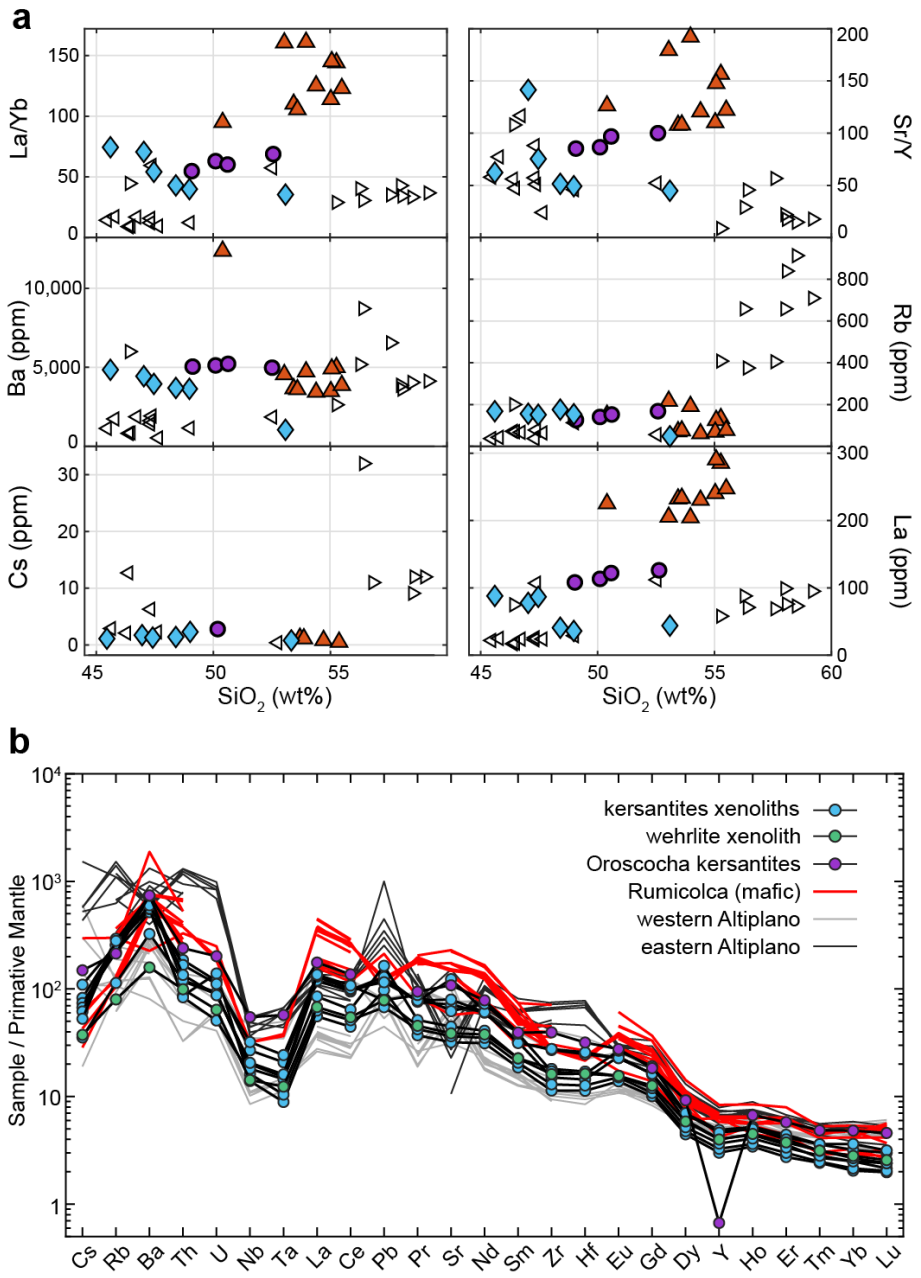

Fig. 5. Whole-rock trace element compositions of kersantite xenoliths and Neogene-Quaternary potassic basalts of the northern Altiplano region. a) Whole rock trace element concentrations versus SiO_2. Linear relationships are seen for some trace elements (Ba, La) and characteristic ratios (La/Yb), mirroring major element trends and implying a control by modal mineralogy. b) Primitive mantle normalized trace element concentrations for kersantite xenoliths and related potassic mafic rocks demonstrating enrichments in LILE and LREE, with notable depletions in HFSE (Nb, Ta), which are characteristics of the input of subduction-derived fluids or melts.

values of -57 ‰. Isotopic values do not show a clear relationship to major or trace element compositions.

Kersantite xenolith hosted phlogopite exhibit anomalously low hydrogen contents, with a range from 1.2 to 2.3 wt% H_2O. Quimsachata biotite phenocrysts contain 1.4 wt% H_2O. A typical phlogopite with similar compositions contains ~4 wt% H_2O. There is no correlation between H contents and δD values, but H contents do show a clear relationship with major element compositions (Fig. 6). For example, H_2O content shows a strong positive correlation with whole-rock SiO_2 ($r^2 = 0.95$) and negative correlations with P_2O_5 ($r^2 = 0.98$) and K_2O ($r^2 = 0.72$).

5. Discussion

Potassic alkaline basalts represent a diverse subgroup of alkaline basalts, lending to an exhaustive list of potential petrogenetic models for their formation and continued scrutiny of their origin (Foley and Peccerillo, 1992; Farmer, 2013). Potassic arc magmas, often categorized into the absorakite-shoshonite-banakite series (Iddings, 1895), have long been recognized as a volumetrically minor but common feature of subduction systems, typically occurring as the furthest inboard magmatism from the trench where the depth to the subducting slab is greater (Hatherton and Dickinson, 1969). Primitive potassic arc basalts have been suggested to form through low degrees of partial melting in the deeper portions of subduction zones, where melting may involve K-metasomatized mantle wedge material dragged down along the subduction interface to depths beyond the zone of calk-alkaline melt production (Wyllie and Sekine, 1982; Tatsumi and Eggins, 1995). These basalts are generally associated with chains of alkaline volcanoes within

island arc systems, which contrasts with the monogenetic nature and temporally and spatially punctuated formation of Rumicolca Formation lavas. Furthermore, Quimsachata kersantites and other potassic basalts of southern Peru exhibit distinctly different chemistries compared to island arc-type alkaline basalts, including lower Na_2O and significantly higher TiO_2, K_2O and P_2O_5 (Bloomer et al., 1989; Gill and Whelan, 1989).

Potassic alkaline basalts are also found in various continental settings such as Tibet (Miller et al., 1999), eastern China (Zhang et al., 2007), Italy (Peccerillo, 1999) and western North America (Kempton et al., 1991). These basalts commonly share similar geochemical signatures with island arc basalts, including LILE and LREE enrichment, HFSE depletions, positive Pb anomalies, high $^{87}Sr/^{86}Sr$ ratios and low εNd values, but are characterized by higher K_2O (~3—7.5 wt%). Combined with the observation that these rocks often occur in regions with relatively recent histories of subduction, they are commonly interpreted to represent partial melts from metasomatized continental lithospheric mantle. Metasomatic histories may include multistage evolution of depletion and enrichment, but fluid and/or melt metasomatism with a subduction affinity is often invoked as a major contributor to their formation. In many cases, these alkaline provinces postdate subduction, and delayed melting of the metasomatized (and hydrated) lithospheric mantle may be triggered due to its lowered melting temperature (Harry and Leeman, 1995). Mechanisms triggering melting include delamination or convective thinning of the lithospheric mantle Turner et al., 1996; Chung et al., 1998; Farmer et al., 2002), extension (Kempton et al., 1991), or asthenosphere return flow following removal of a flat-slab or underthrust lithosphere (Farmer et al., 2008). Recent experimental studies demonstrate that generation metasomatizing melts, interaction with mantle peridotite, and

eruption of potassic basalts can also occur contemporaneously (Mallik et al., 2015; Cruz-Uribe et al., 2018; Codillo et al., 2018). For example, melting of subducted sediments, mélange, or oceanic crust yields intermediate to felsic potassic melt compositions (Rapp et al., 1999; Castro and Gerya, 2008; Cruz-Uribe et al., 2018), and subsequent reaction with peridotite converts olivine to orthopyroxene and stabilizes phlogopite, buffering the reacted melt to ultrapotassic mafic compositions (Mallik et al., 2015).

In the Quimsachata kersantites, low abundances of basaltic components such as FeO, Al_2O_3, and Na_2O are consistent with melting of a harzburgitic mantle source such as that commonly envisioned for average subcontinental lithospheric mantle (e.g., McDonough, 1990). Exceptionally high K_2O and P_2O_5 concentrations, as well as incompatible trace element enrichments, suggest that the depleted mantle source was re-enriched by metasomatizing fluids/melts rich in these elements prior to or during generation of the kersantite melts. Likely K- and P-bearing mantle phases are phlogopite (± K-rich amphibole) and apatite, both of which are expected to be stable at lithospheric mantle conditions (Ayers and Watson, 1991; Fumagalli et al., 2009) and have been observed in samples of metasomatized lithospheric mantle (Zanetti et al., 1999; O'Reilly and Griffin, 2000; Chen and Zhou, 2005; Morishita et al., 2008). The range of K_2O contents in kersantite samples (3.6 to 5.1 wt%) is consistent with melt reaction buffering by phlogopite based on experimental melts of phlogopite-bearing peridotites (Condamine and Médard, 2014; Condamine et al., 2016) and peridotite fluxed with potassic high-silica melts (Mallik et al., 2015). This explanation is consistent with prior studies of potassic lavas from this region (Carlier et al., 2005), as well as interpretations for the genesis of potassic alkali basalts globally (Boettcher and O'Neil, 1980; Foley et al., 1987;

Kempton et al., 1991; Gibson et al., 1995; Zhang et al., 1995; Miller et al., 1999; Peccerillo, 1999; Downes et al., 2004).

Quimsachata kersantite xenoliths share compositional and mineralogical similarities with kersantites enclaves found within the nearby Oroscocha lavas described by Carlier and Lorand (2008). Oroscocha kersantites exhibit slightly higher Na_2O and lower CaO and MgO, perhaps owing to contamination by felsic host magma, but are also enriched in K_2O and P_2O_5 with a similarly high normative abundance of phlogopite, clinopyroxene, plagioclase, K-feldspar, and apatite. The kersantite enclaves of Oroscocha were interpreted to have formed from the intrusion of potassic basaltic melts into a felsic subvolcanic magma chamber, where they mingled with the peraluminous granite and partially crystallized shortly before eruption (Carlier and Lorand, 2008). This interpretation suggests intrusion of kersantite lavas into the upper crust at the time of Oroscoha eruption (ca. 0.64 Ma; Mamani et al., 2010). Eruption of Quimsachata lavas along a similar magma assent path would have then entrained these xenoliths at 0.03 Ma (Kaneoka and Guevara, 1984).

5.1. Geochemical Variability

5.1.1. Major/trace element variability

The small sample size of kersantite xenoliths make it difficult to assess controls on chemical variability with certainty. Nonetheless, bulk compositions do appear to show interpretable and systematic relationships in some of their major and trace element characteristics. Chemical variability is not readily explained through typical differentiation mechanisms of fractional crystallization or crustal assimilation. Increased

SiO_2 concentrations correspond to either lower (Al_2O_3, K_2O, trace elements) or similar (Na_2O) concentrations in these elements, opposite of the trends expected for assimilation of felsic crustal material or mixing with a felsic magma (Grove et al., 1988). Compositional variability is also difficult to explain through progressive loss of cumulate phases. Weak positive relationships between MgO and Ni or Cr imply that some olivine and clinopyroxene fractionation may have occurred, but similar correlations are lacking between MgO and other major oxides. Plagioclase fractionation would lead to decreasing CaO with increasing SiO_2, as well as characteristic negative Eu anomalies, neither of which are observed. Fractionation through removal of clinopyroxene and/or phlogopite, which is more likely to control differentiation of high-K magmas (Bucholz et al., 2014a, 2014b), is also inconsistent with the geochemical variability in these samples. Fractionation of clinopyroxene with the observed diopsidic compositions together with phlogopite would decrease MgO while increasing SiO_2 in the evolving melt (Bucholz et al., 2014a), opposite of the observed relationships. Fractionation of phlogopite may be in part responsible for decreasing K_2O with increased SiO_2; however, modelled fractionation of magmas with similar compositions do not support fractionation through removal of phlogopite alone, and instead predict an increase in K_2O in more evolved magmas (Bucholz et al., 2014a).

Based on the chemical variability and textural characteristics of the rocks, we suggest that crystal accumulation, rather than fractionation, is most likely controlling the major element variability in these xenoliths. Clinopyroxenes exhibit glomerophyric textures in some samples, supportive of crystal accumulation, although the wide spacing between liquidous clinopyroxenes and abundant glassy groundmass (mesostasis) suggest

only a partial cumulate origin. Trends in bulk-rock compositions are explained well by mixing of phenocrystic phlogopite (9-11% K_2O, ~40% SiO_2) and clinopyroxene (no K_2O, ~53% SiO_2), with additional contribution of a "melt" endmember (plagioclase and mesostasis). This interpretation is consistent with the few other occurrences of similar mica-clinopyroxenites that have been interpreted as cumulates in the fractionation of alkaline magma series elsewhere (Buhlmann et al., 2000; Downes et al., 2004; Bucholz et al., 2014b). Relationships between trace elements and major elements are scattered but follow a general relationship where samples with lowest silica and highest K_2O or P_2O_5 display higher abundances of incompatible trace elements. REE abundances and LREE/HREE ratios (e.g., La/Yb) display strong negative correlations with silica content (Fig. 5). These trends can be explained by modal proportions of phases like phlogopite and apatite. Phlogopite is enriched in Ba and Rb and has higher average La/Yb and Sr/Y values compared to bulk rock compositions, explaining the association of these bulk-rock trace element compositions and K_2O. La and other LREE, which are not concentrated in phlogopite, may be controlled by greater abundances of apatite or Ti-rich phases in samples with the lowest silica.

5.1.2. Potential hydrogen isotope modification

Fractional crystallization or accumulation of cumulate phases is unlikely to modify hydrogen isotope ratios, as fractionation factors between hydrous phases and melt are too small to significantly impact δD values of the system (DePaolo, 1981; Sharp, 2017b). Crustal assimilation has a greater potential to modify isotopic compositions given the variable δD values of crustal material (~ 0 to -100 ‰ e.g., Sheppard, 1986), which can extend to even lower values for rocks that have been hydrothermally altered with

meteoric fluids (Taylor, 1978). However, significant assimilation of crustal H is unsupported by lack of major element evidence for crustal contamination, and δD values do not show a consistent trend with major oxides that would indicate crustal contamination (e.g., SiO_2, K_2O, Al_2O_3), so we rule this out as a major control on hydrogen isotope compositions.

Hydrogen loss from phlogopite, either as H_2 (dehydrogenation) or H_2O (dehydration), is another possible mechanism that can modify both water content and H isotope values of kersantite xenoliths. The vesicular character of the xenoliths is evidence for gas/vapor production during melting of interstitial feldspars, presumably during entrainment and eruption of Quimsachata lavas, and the anomalously low H_2O contents of phlogopite suggests that H-loss may have occurred. Evidence for dehydrogenation of biotite is observed in silicic magmatic systems (Feeley and Sharp, 1996; Underwood et al., 2012), and is promoted at high fO_2 conditions where the reaction proceeds via $OH^- + Fe^{2+} \rightarrow [O^{2-} + Fe^{3+}] + 1/2H_2$, or with oxidation/replacement of a different octahedral cation (Eugster and Wones, 1962; Righter et al., 2002). Dehydrogenation favors diffusive loss of H over D (Suzuoki and Epstein, 1976; Richet et al., 1977), which results in trends of increasing δD values with decreasing H contents in phlogopite phenocrysts (Feeley and Sharp, 1996; Underwood et al., 2012). Hydrogen loss from dehydration reactions proceed via $2OH^- \rightarrow O^{2-} + H_2O$, leading to hydroxyl-site vacancies and ultimately mineral decomposition at high degrees of dehydration (Miyagi et al., 1998). This reaction favors loss of D over H (Suzuoki and Epstein, 1976; Underwood et al., 2012), which would result in a trend of decreasing δD values with decreasing H_2O contents in phlogopite phenocrysts. No relationship between δD and H_2O contents is apparent in our

samples. Although we cannot entirely rule out that some post crystallization H-loss has occurred, this mechanism does not readily explain the variability in δD or H_2O contents of phlogopite samples (Fig. 6a).

Phlogopite H_2O contents show a strong negative correlation with bulk rock P_2O_5 (r^2 = 0.98) as well as a strong positive correlation with SiO_2 (r^2 = 0.95) (Fig. 6b). A weaker negative correlation is also seen with K_2O (r^2 = 0.72). A similar relationship was seen between phlogopite H_2O contents and SiO_2 by Feeley and Sharp (1997) and used as evidence for variable phlogopite dehydrogenation as a function of melt temperature, with lower silica systems experiencing greater phlogopite degassing at higher temperatures. However, given the inconsistent relationship between δD values and H_2O contents of phlogopite, we do not favor a similar explanation. Another possibility is that the low water content in phlogopite is the result of apatite crystallization and water uptake before the crystallization of phlogopite. Textural relationships show that apatite crystallized as a liquidus phase followed by phlogopite, and the relatively high abundance of apatite (normative values up to 5.4 wt %) may be sufficient to reduce the amount of water remaining during phlogopite formation. Although apatite does exhibit relatively high F^- contents (up to ~3 wt %, XRF-EDS observation), samples with lower phlogopite H_2O contents, and higher apatite contents show less F^- (~2.5 wt %, EDS data), and would therefore be able to reduce the residual water contents in the melt. This may be more likely if the melt was already relatively dry, which is supported by low LOI values (< 0.94 wt %) in these samples and low H_2O contents in other alkaline potassic basalts (Bucholz et al., 2014a) as compared to arc basalts globally (1.5 – 6 wt %; Grove et al., 2003; Jagoutz and Schmidt, 2013).

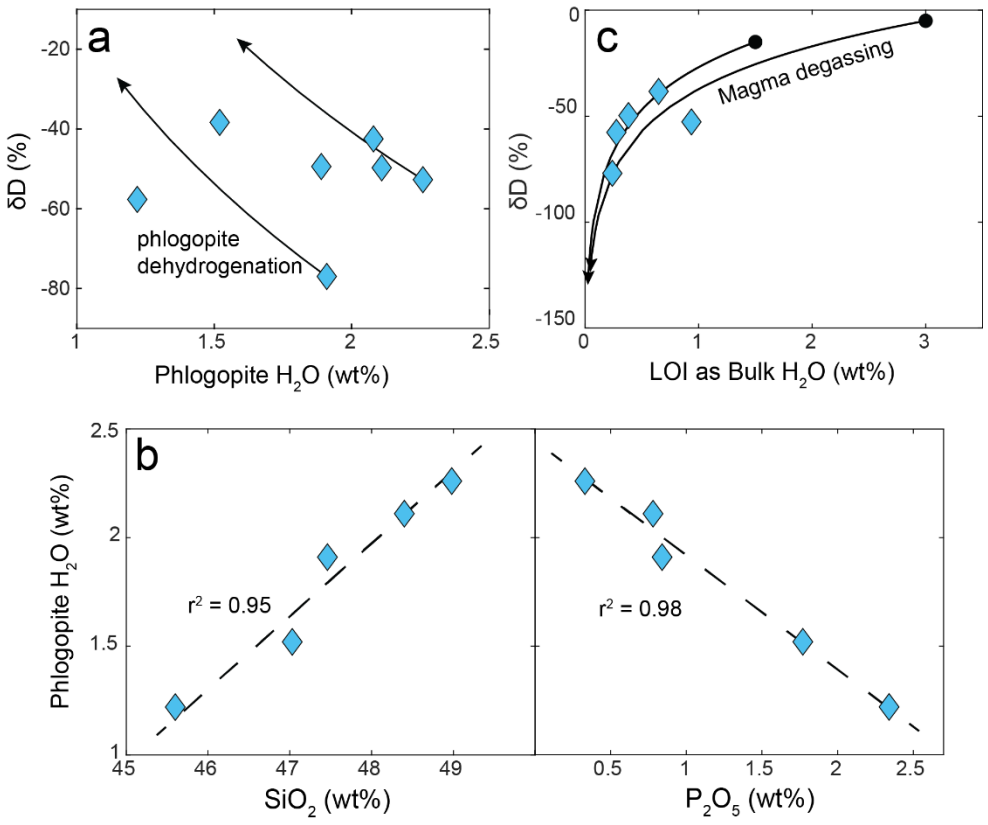

Fig. 6. Relationships between δD values, phlogopite water contents, and bulk-rock volatile contents. a) Phlogopite δD values do not show a clear relationship to phlogopite water contents, as would be expected if dehydrogenation or dehydration were the primary explanation for low water contents in phlogopite. Example δD fractionation trends resulting from dehydrogenation are shown. Trajectories were calculated using equation (1) with arbitrary starting δD and water contents, and a fractionation factor ($100\ln\alpha = 0.897$) from Underwood et al., (2012). **b)** Strong correlations between phlogopite water contents and bulk-rock SiO_2 and P_2O_5 **c)** Phlogopite δD values versus bulk-rock LOI (as a proxy for bulk-rock water contents), showing that lower δD values may be due to fractionation during magma degassing (see text for discussion).

Low volatile contents of the bulk rock samples may also be a function of water loss during degassing of kersantite magmas before/during crystallization, which can also impact the δD values in the phlogopite. Isotopically heavier water is favored to degas

from a melt, resulting in a decrease in δD values of the residual water (Kyser and O'Neil, 1984; Hauri, 2002). Fractionation is sensitive to water speciation in the melt (H_2O vs OH^-), and lower water contents will lead to higher proportions of OH^- (Newman et al., 1988). Kersantite xenoliths exhibit a weak relationship between bulk-rock LOI and phlogopite δD values (Fig. 6c), suggesting that magma degassing may be responsible for the lowest and most mantle-like δD values in the xenoliths suite and implying initially higher δD values of the undegassed kersantite magmas. Using LOI values as a proxy for water contents and assuming open-system behavior, we can model the decrease in δD values as a function of magmatic degassing using the Rayleigh fractionation equation (Sharp, 2017b):

$$\delta D_f = \delta D_i + (1000 + \delta D_i) \times (F^{(\alpha-1)}-1) \quad (1)$$

where δD_f is the value of the dissolved H_2O/OH^-, δD_i is the initial undegassed value, F is the fraction of H_2O remaining, and α is the isotopic fractionation factor (vapor-melt). Using a fractionation factor of 1.03 for average water contents of ~0.5 wt % (Newman et al., 1988), a range of reasonable initial water contents of 1.5 to 3 % (Bucholz et al., 2014a), and varying the initial δD value to best fit the data, we can model our data with initial δD values of -15 to -5 ‰ (Fig. 6c). The lowest δD value of -77 ‰ is achieved with ~90 % of the water degassed from the magma, while δD values from the other samples are achieved with 55 to 83 % degassing. This simple model can reproduce our data ranges with reasonable inputs, supporting the possibility of progressive degassing as a control on lower δD values. However, we note that without knowledge of the initial H_2O contents, and given the dependence of α on variable H_2O/OH^- throughout degassing, that these are qualitative initial δD values and degassing percentages.

5.2. Mantle metasomatism

Potential processes responsible for upper mantle metasomatism include interaction with subduction-related fluids/melts, introduction of fluids/melts during interaction with plume-type lower mantle material, or long-term infiltration of asthenosphere-derived fluids (Downes, 2001). Given that the northern Altiplano lithosphere has resided in a subduction zone environment since at least the Paleozoic, subduction processes are the most likely culprit. However, older episodes of enrichment are still plausible given the Proterozoic age of the lithosphere in this region, including the proximal Mesoproterozoic Arequipa terrain Amazonian craton. Long-term refertilization of depleted lithospheric mantle through asthenosphere-derived fluids/melts has been invoked in some cratonic regions McDonough, 1990), but is not considered here.

5.2.1. Trace element perspective

Enrichment in LILEs, notably for the most fluid mobile elements (e.g., Rb, Ba), together with LREE enrichment and distinct Nb-Ta anomalies are characteristic of igneous rocks formed in a subduction setting or in mantle lithologies interpreted to have been metasomatized by slab-derived fluids/melts (Plank and Langmuir, 1998). Fluids released by a dehydrating oceanic lithosphere become enriched in fluid mobile (e.g., LILE, Pb, Th) or generally incompatible elements (e.g., LREE > HREE) as they percolate through the subducting slab and into the overlying mantle. Low HFSE/LILE ratios in arc rocks are generally attributed the lower mobilities of HFSE in aqueous fluids, and Nb and Ta are generally regarded to be sequestered in residual rutile within the subducting oceanic lithosphere (Kelemen et al., 2014). Enrichments of LILE and LREE in Quimsachata kersantites (e.g., Rb, Ba $>100_{PM}$, La $>50_{PM}$) as well as prominent Nb and Ta

depletions are strongly supportive of the role of subduction-derived fluids or hydrous melts in metasomatism of the kersantite mantle source.

Metasomatism by siliceous or carbonatitic melts from other mantle sources (e.g., mantle plumes) is also associated with incompatible element enrichment; however, several differences are apparent. For example, metasomatism by carbonatitic melts is associated with extreme Zr depletions, relative depletions in middle-REEs that result in U-shaped REE patterns, and anomalously low Ti/Eu ratios, which are not observed in these samples (e.g., Downes, 2001). Metasomatism by siliceous melts derived from the asthenosphere or lower mantle will lack dramatic fluid mobile element enrichments and Nb-Ta depletions that are associated with subduction-related metasomatism.

5.2.2. Hydrogen isotope perspective

Hydrogen isotopes offer an additional and independent line of evidence for assessing sources of metasomatism because isotopic fractionation of water carried into the mantle during subduction leads to disparate isotopic compositions between slab-derived fluids, residual subducted lithosphere, and upper and lower mantle reservoirs. A key feature of this process is isotopic fractionation between hydrous minerals and aqueous fluids. Associated mineral-water fractionation factors (expressed as $1000\ln\alpha$) are generally negative for prominent hydrous phases in subduction systems (i.e., the mineral is D-depleted relative to the fluids; $1000\ln\alpha_{\text{mineral-H2O}} < 0$) but decrease in magnitude with higher temperature (Suzuoki and Epstein, 1976; Sakai and Tsutsumi, 1978; Graham et al., 1984; Vennemann and O'Neil, 1996; Saccocia et al., 2009). Water is exchanged between aqueous fluids and hydrous minerals at least two times in this process, first during

hydrothermal alteration of the oceanic lithosphere by seawater, and second during dehydration of subducting lithosphere releasing fluids into the mantle wedge. The second step is essentially a reversal of the first but with a smaller magnitude of isotopic fractionation owing to higher temperatures, resulting in slab-derived fluids that are D-depleted relative to seawater. Estimates of the average δD value of subducting oceanic lithosphere range from -30 to -50 ‰ (Shaw et al., 2008) considering observations from both altered oceanic crust and serpentinized oceanic mantle (Magaritz and Taylor, 1976; Agrinier et al., 1995). Aqueous fluids produced during subsequent dehydration of the oceanic lithosphere at subduction zone conditions are expected to exhibit δD values between -15 and -40 ‰ (Kempton et al., 1988; Shaw et al., 2008; Marshall et al., 2017). This range is similar to observations from hydrous melt inclusions in arc-lavas (Shaw et al., 2008), bononite glasses (Dobson and O'Neil, 1987), hydrous phenocrysts in andesites (Miyagi and Matsubaya, 2003), and the sublithospheric component of fumarole gases (Allard, 1983; Giggenbach, 1992) (Fig. 7).

We emphasize that both aqueous fluids or hydrous melts generated from subducting oceanic lithosphere will exhibit δD values that are higher than H derived from the upper mantle (-80 ± 10 ‰; Kyser and O'Neil, 1984). In the case of aqueous fluids, subsequent hydration reactions that produce secondary phlogopite, amphibole, chlorite, and serpentine result in equilibrium hydrogen isotope fractionations of -20 to 5 ‰, -39 to -18 ‰, -30 ‰, and -20 to -14 ‰, respectively, at mantle wedge temperatures between 400 and 700 °C (Suzuoki and Epstein, 1976; Saccocia et al., 2009). Mantle metasomatism by slab-derived hydrous fluids is therefore expected to result in hydrous minerals with δD values ranging from -55 to -10 ‰ (phlogopite), -74 to -32 ‰

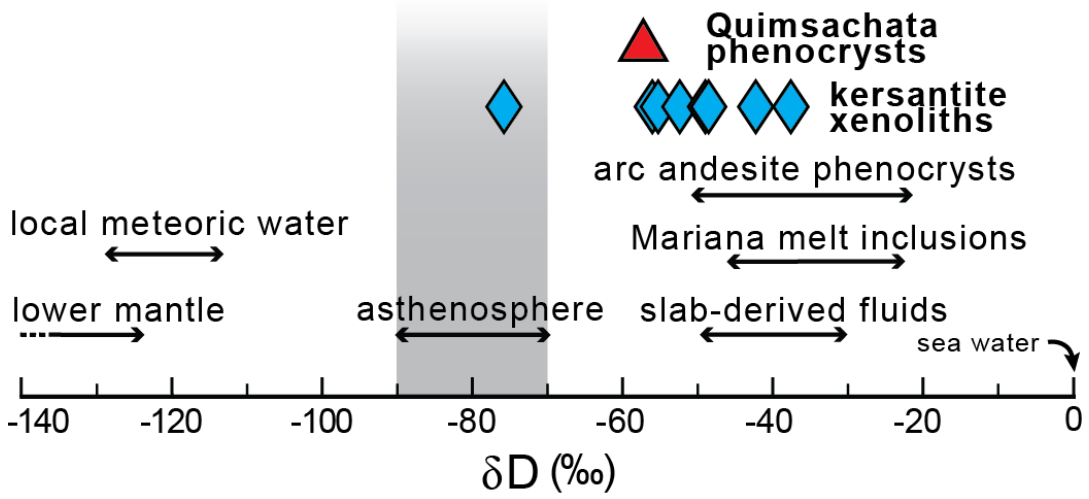

Fig. 7. **Phlogopite δD values of kersantite xenoliths and Quimsachata phenocrysts**, demonstrating values that are distinct from mantle sources (excluding one sample) and trend towards with theoretical estimates for δD values of subduction derived fluid (Kempton et al., 1988; Shaw et al., 2008; Marshall et al., 2017) and reported δD values in volcanic arc materials. Data sources are provided in the text.

(amphibole), -65 to -45 ‰ (chlorite), and -55 to -29 ‰ (serpentine). Although these fractionation factors are poorly constrained at mantle conditions (e.g., Suzuoki and Epstein, 1976 compared to Kuroda et al., 1988), and factors such as mineral chemistry can influence fractionation (Suzuoki and Epstein, 1976), we emphasize that the anticipated δD values are significantly D-enriched compared to upper mantle hydrogen (-80 ± 10 ‰; Kyser and O'Neil, 1984). In the case of slab-derived melts, the small stable isotope fractionations associated with melting (Shaw et al., 2008; Bindeman et al., 2012) would not significantly alter the hydrogen isotope composition, and the resulting melts are anticipated to exhibit δD values between -15 and -40 ‰.

Constraints on the hydrogen isotope ratios of deep mantle sources are scarce but reveal a significantly D-depleted mantle domain compared to the asthenosphere, with δD values ranging from -218 to -125 ‰ (Deloule et al., 1991; Hauri, 2002; Hallis et al.,

2015). One exception is δD values up to -36 ‰ reported from basalt glasses along the Easter-Salas y Gomez seamount chain (Kingsley et al., 2002), which have been attributed to mantle wedge material being recycled into the deep mantle (Shaw et al., 2008). The low δD values ascribed to most OIB sources may be a feature of recycled oceanic crust subducted into the deep mantle. Continued release of D-enriched slab-derived fluids is expected to lead to increasingly negative δD values for remaining water in the subducting slab, potentially to values below -200 ‰ after extensive dehydration (Shaw et al., 2008). Alternatively, these low δD values may be a function of primordial mantle source (Hallis et al., 2015; Sharp, 2017a).

Phlogopite from kersantite xenoliths exhibit δD values up to -38 ‰ (avg = -52 ± 13 ‰), demonstrating D/H ratios that are clearly elevated compared to the current H isotopic composition of both upper and lower mantle reservoirs, and that fall within the range estimated for fluids derived from dehydrating oceanic lithosphere. Phlogopite phenocrysts from Quimsachata lavas (-57 ‰) also exhibit a similarly D-enriched character. These results provide evidence for a slab-derived component involved in metasomatism in the source of both kersantite lavas and related potassic basalts like Quimsachata, consistent with interpretations of trace element characteristics and K_2O and P_2O_5 enrichment.

5.2.3. Model for mantle metasomatism and kersantite genesis

Major element patterns, trace element characteristics, and hydrogen isotope ratios each provide evidence for a history of subduction-derived metasomatism in the northern Altiplano mantle lithosphere. Higher concentrations of TiO_2, Al_2O_3, and FeO* associated

with the highest K_2O and P_2O suggests metasomatism by hydrous melts, as these elements are generally immobile in aqueous fluids. Hydrous melts can be produced either through melting of oceanic crust, sediments, or mélange material, especially in hot subduction systems (Peacock et al., 1994), or through melting of mantle wedge material altered by slab derived aqueous fluids. In both scenarios, melts will carry characteristic subduction signatures such as enrichments in K, P, and fluid-mobile incompatible elements.

Hydrous melts could be introduced into the overlying lithosphere in subduction systems in several ways. In a typical subduction geometry, hydrous melting in a forearc wedge allows for introduction of melts into the continental lithosphere apart from the more extensive mantle melting and generation of arc magmatism that occurs at greater depths in the subduction system (e.g., Selverstone and Sharp, 2011). In a shallow or flat-slab geometry, closing of the mantle wedge restricts or prohibits arc volcanism, and hydrous fluids are transferred directly into the overlying continental lithosphere leading to hydration and metasomatism (Humphreys et al., 2003; Hiett et al., 2021). Slab sediments and/or mélange material may also be accreted to the base of the continental lithosphere during flat-slab subduction (Ducea and Chapman, 2018). After re-steepening of the subducting slab, hydrated mantle wedge material or accreted slab material would be rapidly heated by renewed convection of hot asthenosphere, initiating melting of hydrated peridotite or slab-material (Johnson and Plank, 2000; Hirschmann, 2006). The produced melts could then migrate upwards and interact with harzburgite or dunnite lithologies, enriching the depleted mantle lithosphere in K, P, incompatible trace elements, and slab-derived H_2O.

We suggest that metasomatism of the Altiplano lithosphere most likely occurred during the recent episode of shallow subduction in the late Eocene-Oligocene. The close association between the initiation of Neogene basaltic volcanism and the cessation of shallow subduction in the late Oligocene suggests that mantle metasomatism in the northern Altiplano occurred because of mantle hydration and/or accretion of slab material during this episode of shallow subduction. Rejuvenated Quaternary melting of this metasomatized mantle source demands a recent thermal perturbation to explain delayed melting. The shear wave velocity structure imaged by Ward et al. (2016) includes a low velocity anomaly in the upper mantle just to the south of the Quimsachata volcano. This anomaly was interpreted to represent hydrous or partially molten mantle localized at region where the Nazca slab transitions from flat subduction in the north to steep subduction to the south. The southward advance of the modern Peruvian flat slab implies that this is a recent feature, and may provide a mechanism for melting of the overlying lithospheric mantle (Garzione et al., 2017) Age constraints for Rumicolca lavas are limited, but lavas are generally older in the north near Cusco, while Quimsachata and nearby Oroscocha are the youngest Rumicolca lava flows, consistent with this model (Kaneoka and Guevara, 1984; Carlier et al., 2005; Mamani et al., 2010).

6. Implications for Andean Tectonics and Cordillera Globally

Metasomatism has been suggested as a critical process controlling the composition of the lithospheric mantle globally (Kelemen et al., 1992; Prouteau et al., 2001), and evidence for hydrous melt metasomatism has been observed in both convergent margins, (e.g., Cascades, Ertan and Leeman, 1996; North China Craton, Chen and Zhou, 2005; interior Western US, Carlson et al., 2004; Downes et al., 2004, and

intraplate settings (e.g., central Europe, Rizzo et al., 2021; Canary Islands, Wulff-Pedersen et al., 1996). A potential analogue for the mantle source of kersantite lavas envisioned here is the Finero ultramafic complex within the Ivrea Verbano Zone of the Italian Alps. The phlogopite-peridotite portion of the Finero complex comprises spinel harzburgite and subordinate lherzolite, dunite, clinopyroxenites, and chromitites, with variable abundance of phlogopite and amphibole. Apatite and carbonate-bearing lithologies are also associated with distinct peridotite and pyroxenite layers (Zannetti 1999, Moriishita et al 2003b, 2008). These rocks are generally interpreted as the result of mixing and recrystallization resulting from both channelized and pervasive melt infiltration into a previously depleted peridotite. Evidence including trace element systematics (e.g., Zanetti et al., 1999; Cannaò et al., 2022) and stable isotopes (Selverstone and Sharp, 2011; Cannaò et al., 2022) repeatedly reveal an apparent subduction fingerprint imparted by the metasomatizing volatile-rich melt, although the potential multi-stage history of metasomatism is still under scrutiny (Grieco et al., 2001; Bussolesi et al., 2019) and other geodynamic environments have been proposed (Zaccarini et al., 2004). We note that the range, and especially the higher δD values, of Finero phlogopite (-76 to -29 ‰) and amphibole (-87 to -34 ‰) reported by Hartmann and Wedepohl (1993) and Selverstone and Sharp (2011) overlap with those reported in this study.

The kersantite xenoliths studied here, and by association the Neogene potassic basalts described in earlier studies (Carlier et al., 2005) are suggested to represent melts from a metasomatized mantle source akin to the Finero phlogopite peridotite, suggesting that similarly metasomatized mantle material is widespread in the northern Altiplano

lithosphere. More detailed petrologic analysis and modelling is necessary to constrain the specific mantle compositions and melt conditions involved in kersantite magmagenesis, but we emphasize similarities to the general characteristics displayed at Finero, including subduction-derived hydrous melt metasomatism resulting in modal metasomatism producing phlogopite and apatite. Lithologic variability of the Altiplano lithosphere such as that seen in Finero, together with the preexisting tectonic structure and chemical heterogeneity of the Andean lithospheric mantle (Carlier et al., 2005), may help to explain the compositional variability among kersantite xenoliths and the diversity of potassic and ultrapotassic basalts in southern Peru more broadly. Although modern volcanism in the northern Altiplano backarc has been punctuated, low volume, and restricted to the CVFS in the last ~2 Ma, geochemical evidence for active mantle degassing observed from geothermal systems suggests that the lithospheric mantle across the broader region is experiencing partial melting and/or dehydration (Hiett et al., 2021, 2022). Geophysical evidence also supports the existence of partial melt at mid-crustal depths throughout this region (Ma and Clayton, 2014). Together, these observations suggest that potassic volcanism along the CVFS is a manifestation of a more widespread melting at depth across the northern Altiplano Plateau.

Recent work has demonstrated that growth of the Altiplano-Puna Plateau has been intimately tied to subduction dynamics, with patterns of deformation and orogen widening tracking the southward advance of Cenozoic shallow subduction (Martinod et al., 2020; Saylor et al., 2023). Thermal weakening due to concurrent inboard migration arc magmatism has been proposed as a causal link between shallow subduction and deformation (Isacks, 1988; James and Sacks, 1999), but widespread metasomatism will

also act to weaken upper mantle or lower crust rheology through enhanced ductile deformation mechanisms associated with infiltration of hydrous melts or increased water contents in nominally anhydrous minerals (Liao et al., 2017; Tommasi et al., 2017). Aqueous fluid metasomatism and production of weak phases like serpentine or talc, although not directly evident in the geochemistry of Altiplano lavas, would also significantly weaken the Altiplano lithosphere (Hyndman and Peacock, 2003). Introduction of volatiles into the continental lithosphere, together with any subsequent melting, may also modulate the thermal state of the continental lithosphere through enthalpy changes associated with hydration reactions and enabling advective heat transfer (Berry et al., 2022), which together with alteration or melting of dense phases like garnet (e.g., Jones et al., 2015), could contribute to lithospheric buoyancy and surface uplift. Saylor et al. (2023) connect patterns of deformation across the central Andes with southward migration of mid-Cenozoic shallow subduction, citing subduction-derived metasomatism as a likely link between the two. The metasomatism of the Altiplano lithosphere highlighted by this study, which we argue occurred contemporaneously with a dramatic shift in deformation patterns within the region, provides compelling support for this model. Similar considerations of metasomatism during shallow subduction have gained substantial traction for explaining enigmatic deformation, uplift, and magmatism in the North American Cordillera in the early Cenozoic (e.g., Humphreys et al., 2003; Farmer et al., 2008; Jones et al., 2015). Results from this study highlight that hydration and metasomatism during shallow subduction is a global phenomenon and should be taken into consideration when trying to unravel the Cenozoic tectonic and magmatic evolution of the Andean Cordillera and other regions with dynamic subduction histories.

References

Agrinier, P., Hékinian, R., Bideau, D., & Javoy, M. (1995). O and H stable isotope compositions of oceanic crust and upper mantle rocks exposed in the Hess Deep near the Galapagos Triple Junction. *Earth and Planetary Science Letters*, *136*(3–4), 183–196. https://doi.org/10.1016/0012-821X(95)00159-A

Allard, P. (1983). The origin of hydrogen, carbon, sulfur, nitrogen and rare gases in volcanic exhalations: Evidences from isotope geochemistry (1). In *Forecasting Volcanic Events*.

Allmendinger, R. W., Jordan, T. E., Kay, S. M., & Isacks, B. L. (1997). The evolution of the Altiplano-Puna plateau of the Central Andes. *Annual Review of Earth and Planetary Sciences*, *25*, 139–174. https://doi.org/10.1146/ANNUREV.EARTH.25.1.139

Ayers, J. C., & Watson, E. B. (1991). Solubility of apatite, monazite, zircon, and rutile in supercritical aqueous fluids with implications for subduction zone geochemistry. *Philosophical Transactions - Royal Society of London, A*, *335*(1638). https://doi.org/10.1098/rsta.1991.0052

Bedini, R. M., Bodinier, J. L., Dautria, J. M., & Morten, L. (1997). Evolution of LILE-enriched small melt fractions in the lithospheric mantle: A case study from the East African Rift. *Earth and Planetary Science Letters*, *153*(1–2). https://doi.org/10.1016/s0012-821x(97)00167-2

Berry, M. A., Lowry, A. R., Ma, X., Kanda, R. V. S., & Schutt, D. L. (2022). Wet roots of high elevation in the western United States. *Earth and Planetary Science Letters*, *584*. https://doi.org/10.1016/j.epsl.2022.117483

Bindeman, I. N., Kamenetsky, V. S., Palandri, J., & Vennemann, T. (2012). Hydrogen and oxygen isotope behaviors during variable degrees of upper mantle melting: Example from the basaltic glasses from Macquarie Island. *Chemical Geology*, *310–311*. https://doi.org/10.1016/j.chemgeo.2012.03.031

Bloomer, S. H., Stern, R. J., Fisk, E., & Geschwind, C. H. (1989). Shoshonitic volcanism in the northern Mariana Arc. 1. Mineralogic and major and trace element characteristics. *Journal of Geophysical Research*, *94*(B4), 4469–4496. https://doi.org/10.1029/JB094IB04P04469

Boettcher, A. L., & O'Neil, J. R. (1980). Stable isotope, chemical, and petrographic studies of high-pressure amphiboles and micas: evidence for metasomatism in the mantle source regions of alkali basalts and kimberlites. *American Journal of Science*, *280-A*, 594–621.

Bucholz, C. E., Jagoutz, O., Schmidt, M. W., & Sambuu, O. (2014a). Fractional crystallization of high-K arc magmas: biotite- versus amphibole-dominated

fractionation series in the Dariv Igneous Complex, Western Mongolia. *Contributions to Mineralogy and Petrology*, *168*(5). https://doi.org/10.1007/s00410-014-1072-9

Bucholz, C. E., Jagoutz, O., Schmidt, M. W., & Sambuu, O. (2014b). Phlogopite- and clinopyroxene-dominated fractional crystallization of an alkaline primitive melt: petrology and mineral chemistry of the Dariv Igneous Complex, Western Mongolia. *Contributions to Mineralogy and Petrology*, *167*(4). https://doi.org/10.1007/s00410-014-0994-6

Buhlmann, A. L., Cavell, P., Burwash, R. A., Creaser, R. A., & Luth, R. W. (2000). Minette bodies and cognate mica-clinopyroxenite xenoliths from the Milk River area, southern Alberta: Records of a complex history of the northernmost part of the Archean Wyoming craton. *Canadian Journal of Earth Sciences*, *37*(11), 1629–1650. https://doi.org/10.1139/E00-058/ASSET/IMAGES/GR.GIF

Bussolesi, M., Grieco, G., & Tzamos, E. (2019). Olivine–Spinel Diffusivity Patterns in Chromitites and Dunites from the Finero Phlogopite-Peridotite (Ivrea-Verbano Zone, Southern Alps): Implications for the Thermal History of the Massif. *Minerals 2019, Vol. 9, Page 75*, *9*(2), 75. https://doi.org/10.3390/MIN9020075

Calixto, F. J., Sandvol, E., Kay, S., Mulcahy, P., Heit, B., Yuan, X., Coira, B., Comte, D., & Alvarado, P. (2013). Velocity structure beneath the southern Puna plateau: Evidence for delamination. *Geochemistry, Geophysics, Geosystems*, *14*(10), 4292–4305. https://doi.org/10.1002/ggge.20266

Cannaò, E., Tiepolo, M., Fumagalli, P., Grieco, G., & Agostini, S. (2022). Metasomatism in the Finero Phlogopite Peridotite: New insights from C and N concentrations and δ13C - δ11B signatures. *Chemical Geology*, *614*, 121181. https://doi.org/10.1016/J.CHEMGEO.2022.121181

Carlier, G., & Lorand, J. P. (2008). Zr-rich accessory minerals (titanite, perrierite, zirconolite, baddeleyite) record strong oxidation associated with magma mixing in the south Peruvian potassic province. *Lithos*, *104*(1–4), 54–70. https://doi.org/10.1016/j.lithos.2007.11.008

Carlier, G., Lorand, J. P., Audebaud, E., & Kienast, J. R. (1997). Petrology of an unusual orthopyroxene-bearing minette suite from southeastern Peru, Eastern Andean Cordillera: Al-rich lamproites contaminated by peraluminous granites. *Journal of Volcanology and Geothermal Research*, *75*(1–2), 59–87. https://doi.org/10.1016/S0377-0273(96)00035-2

Carlier, G., Lorand, J. P., Liégeois, J. P., Fornari, M., Soler, P., Carlotto, V., & Cárdenas, J. (2005). Potassic-ultrapotassic mafic rocks delineate two lithospheric mantle blocks beneath the southern Peruvian Altiplano. *Geology*, *33*(7), 601–604. https://doi.org/10.1130/G21643.1

Carlier, G., & Lorand, J.-P. (1997). First occurrence of diopside sanidine phlogopite lamproite in the Andean Cordillera: the Huacancha and Morojarja dikes, southern Peru. *Canadian Journal of Earth Sciences*, *34*(8), 1118–1127. https://doi.org/10.1139/e17-090

Carlotto, V. (2013). Paleogeographic and tectonic controls on the evolution of Cenozoic basins in the Altiplano and Western Cordillera of southern Peru. *Tectonophysics*, *589*. https://doi.org/10.1016/j.tecto.2013.01.002

Carlotto, V., Cardenas, J., & Carlier, G. (2011). Geologia del Cuadrangulo de Cusco Hoja 28-s. *Instituto Geológico Minero y Metalúrgico Boletin 138, Serie A, Carta Geologica Nacional, Escala 1:50,000*.

Carlson, R. W., Irving, A. J., Schulze, D. J., & Hearn, B. C. (2004). Timing of Precambrian melt depletion and Phanerozoic refertilization events in the lithospheric mantle of the Wyoming Craton and adjacent Central Plains Orogen. *Lithos*, *77*(1-4 SPEC. ISS.), 453–472. https://doi.org/10.1016/j.lithos.2004.03.030

Castro, A., & Gerya, T. V. (2008). Magmatic implications of mantle wedge plumes: Experimental study. *Lithos*, *103*(1–2). https://doi.org/10.1016/j.lithos.2007.09.012

Chapman, A. D., Ducea, M. N., McQuarrie, N., Coble, M., Petrescu, L., & Hoffman, D. (2015). Constraints on plateau architecture and assembly from deep crustal xenoliths, northern Altiplano (SE Peru). *Bulletin of the Geological Society of America*, *127*(11–12), 1777–1797. https://doi.org/10.1130/B31206.1

Chen, L. H., & Zhou, X. H. (2005). Subduction-related metasomatism in the thinning lithosphere: Evidence from a composite dunite-orthopyroxenite xenolith entrained in Mesozoic Laiwu high-Mg diorite, North China Craton. *Geochemistry, Geophysics, Geosystems*, *6*(6). https://doi.org/10.1029/2005GC000938

Chung, S. L., Lo, C. H., Lee, T. Y., Zhang, Y., Xie, Y., Li, X., Wang, K. L., & Wang, P. L. (1998). Diachronous uplift of the Tibetan plateau starting 40 Myr ago. *Nature*, *394*(6695). https://doi.org/10.1038/29511

Codillo, E. A., Le Roux, V., & Marschall, H. R. (2018). Arc-like magmas generated by mélange-peridotite interaction in the mantle wedge. *Nature Communications 2018 9:1*, *9*(1), 1–11. https://doi.org/10.1038/s41467-018-05313-2

Condamine, P., & Médard, E. (2014). Experimental melting of phlogopite-bearing mantle at 1 GPa: Implications for potassic magmatism. *Earth and Planetary Science Letters*, *397*. https://doi.org/10.1016/j.epsl.2014.04.027

Condamine, P., Médard, E., & Devidal, J. L. (2016). Experimental melting of phlogopite-peridotite in the garnet stability field. *Contributions to Mineralogy and Petrology*, *171*(11). https://doi.org/10.1007/s00410-016-1306-0

Cruz-Uribe, A. M., Marschall, H. R., Gaetani, G. A., & Le Roux, V. (2018). Generation of alkaline magmas in subduction zones by partial melting of mélange diapirs-An experimental study. *Geology*, *46*(4). https://doi.org/10.1130/G39956.1

DeCelles, P. G. (2004). Late Jurassic to Eocene evolution of the Cordilleran thrust belt and foreland basin system, western U.S.A. *American Journal of Science*, *304*(2). https://doi.org/10.2475/ajs.304.2.105

Deloule, E., Albarède, F., & Sheppard, S. M. F. (1991). Hydrogen isotope heterogeneities in the mantle from ion probe analysis of amphiboles from ultramafic rocks. *Earth and Planetary Science Letters*, *105*(4). https://doi.org/10.1016/0012-821X(91)90191-J

DePaolo, D. J. (1981). Trace element and isotopic effects of combined wallrock assimilation and fractional crystallization. *Earth and Planetary Science Letters*, *53*(2). https://doi.org/10.1016/0012-821X(81)90153-9

Dobson, P. F., & O'Neil, J. R. (1987). Stable isotope compositions and water contents of boninite series volcanic rocks from Chichi-jima, Bonin Islands, Japan. *Earth and Planetary Science Letters*, *82*(1–2). https://doi.org/10.1016/0012-821X(87)90108-7

Downes, H. (2001). Formation and modification of the shallow sub-continental lithospheric mantle: A review of geochemical evidence from ultramatic xenolith suites and tectonically emplaced ultramafic massifs of Western and Central Europe. *Journal of Petrology*, *42*(1). https://doi.org/10.1093/petrology/42.1.233

Downes, H., Macdonald, R., Upton, B. G. J., Cox, K. G., Bodinier, J. L., Mason, P. R. D., James, D., Hill, P. G., & Hearn, B. C. (2004). Ultramafic Xenoliths from the Bearpaw Mountains, Montana, USA: Evidence for Multiple Metasomatic Events in the Lithospheric Mantle beneath the Wyoming Craton. *Journal of Petrology*, *45*(8), 1631–1662. https://doi.org/10.1093/PETROLOGY/EGH027

Ducea, M. N., & Chapman, A. D. (2018). Sub-magmatic arc underplating by trench and forearc materials in shallow subduction systems; A geologic perspective and implications. In *Earth-Science Reviews* (Vol. 185). https://doi.org/10.1016/j.earscirev.2018.08.001

Ertan, I. E., & Leeman, W. P. (1996). Metasomatism of Cascades subarc mantle: Evidence from a rare phlogopite orthopyroxenite xenolith. *Geology*, *24*(5). https://doi.org/10.1130/0091-7613(1996)024<0451:MOCSME>2.3.CO;2

Eugster, H. P., & Wones, D. R. (1962). Stability relations of the ferruginous biotite, annite. *Journal of Petrology*, *3*(1). https://doi.org/10.1093/petrology/3.1.82

Farmer, G. L. (2013). Continental Basaltic Rocks. In *Treatise on Geochemistry: Second Edition* (Vol. 4). https://doi.org/10.1016/B978-0-08-095975-7.00303-X

Farmer, G. L., Bailley, T., & Elkins-Tanton, L. T. (2008). Mantle source volumes and the origin of the mid-Tertiary ignimbrite flare-up in the southern Rocky Mountains, western U.S. *Lithos*, *102*(1–2), 279–294. https://doi.org/10.1016/j.lithos.2007.08.014

Farmer, G. L., Glazner, A. F., & Manley, C. R. (2002). Did lithospheric delamination trigger late Cenozoic potassic volcanism in the southern Sierra Nevada, California? *Bulletin of the Geological Society of America*, *114*(6). https://doi.org/10.1130/0016-7606(2002)114<0754:DLDTLC>2.0.CO;2

Farrar, E., Clark, A. H., Kontak, D. J., & Archibald, D. A. (1988). Zongo-San Gabán zone: Eocene foreland boundary of the Central Andean orogen, northwest Bolivia and southeast Peru. *Geology*, *16*(1). https://doi.org/10.1130/0091-7613(1988)016<0055:ZSGNZE>2.3.CO;2

Feeley, T. C., & Sharp, Z. D. (1996). Chemical and hydrogen isotope evidence for in situ dehydrogenation of biotite in silicic magma chambers. *Geology*, *24*(11). https://doi.org/10.1130/0091-7613(1996)024<1021:CAHIEF>2.3.CO;2

Foley, S. F., Venturelli, G., Green, D. H., & Toscani, L. (1987). The ultrapotassic rocks: Characteristics, classification, and constraints for petrogenetic models. *Earth Science Reviews*, *24*(2), 81–134. https://doi.org/10.1016/0012-8252(87)90001-8

Foley, S., & Peccerillo, A. (1992). Potassic and ultrapotassic magmas and their origin. *LITHOS*, *28*(3–6). https://doi.org/10.1016/0024-4937(92)90005-J

Fumagalli, P., Zanchetta, S., & Poli, S. (2009). Alkali in phlogopite and amphibole and their effects on phase relations in metasomatized peridotites: A high-pressure study. *Contributions to Mineralogy and Petrology*, *158*(6), 723–737. https://doi.org/10.1007/S00410-009-0407-4/FIGURES/11

Garzione, C. N., McQuarrie, N., Perez, N. D., Ehlers, T. A., Beck, S. L., Kar, N., Eichelberger, N., Chapman, A. D., Ward, K. M., Ducea, M. N., Lease, R. O., Poulsen, C. J., Wagner, L. S., Saylor, J. E., Zandt, G., & Horton, B. K. (2017). Tectonic Evolution of the Central Andean Plateau and Implications for the Growth of Plateaus. *Annual Review of Earth and Planetary Sciences*, *45*(1), 529–559. https://doi.org/10.1146/annurev-earth-063016-020612

Garzione, C. N., Molnar, P., Libarkin, J. C., & MacFadden, B. J. (2006). Rapid late Miocene rise of the Bolivian Altiplano: Evidence for removal of mantle lithosphere. *Earth and Planetary Science Letters*, *241*(3–4), 543–556. https://doi.org/10.1016/j.epsl.2005.11.026

Gibson, S. A., Thompson, R. N., Leonardos, O. H., Dickin, A. P., & Mitchell, J. G. (1995). The Late Cretaceous Impact of the Trindade Mantle Plume: Evidence from Large-volume, Mafic, Potassic Magmatism in SE Brazil. *Journal of Petrology*, *36*(1), 189–229. https://doi.org/10.1093/PETROLOGY/36.1.189

Giggenbach, W. F. (1992). Isotopic shifts in waters from geothermal and volcanic systems along convergent plate boundaries and their origin. *Earth and Planetary Science Letters*, *113*(4). https://doi.org/10.1016/0012-821X(92)90127-H

Gill, J., & Whelan, P. (1989). Early rifting of an oceanic island arc (Fiji) produced shoshonitic to tholeiitic basalts. *Journal of Geophysical Research*, *94*(B4), 4561–4578. https://doi.org/10.1029/JB094IB04P04561

Graham, C. M., Harmon, R. S., & Sheppard, S. M. F. (1984). Experimental hydrogen isotope studies: hydrogen isotope exchange between amphibole and water. *American Mineralogist*, *69*(1–2).

Grieco, G., Ferrario, A., Von Quadt, A., Koeppel, V., & Mathez, E. A. (2001). The Zircon-Bearing Chromitites of the Phlogopite Peridotite of Finero (Ivrea Zone, Southern Alps): Evidence and Geochronology of a Metasomatized Mantle Slab. *Journal of Petrology*, *42*(1), 89–101. https://doi.org/10.1093/PETROLOGY/42.1.89

Grove, T. L., Elkins-Tanton, L. T., Parman, S. W., Chatterjee, N., Müntener, O., & Gaetani, G. A. (2003). Fractional crystallization and mantle-melting controls on calc-alkaline differentiation trends. *Contributions to Mineralogy and Petrology*, *145*(5). https://doi.org/10.1007/s00410-003-0448-z

Grove, T. L., Kinzler, R. J., Baker, M. B., Donnelly-Nolan, J. M., & Lesher, C. E. (1988). Assimilation of granite by basaltic magma at Burnt Lava flow, Medicine Lake volcano, northern California: Decoupling of heat and mass transfer. *Contributions to Mineralogy and Petrology*, *99*(3). https://doi.org/10.1007/BF00375365

Gutscher, M. A., Spakman, W., Bijwaard, H., & Engdahl, E. R. (2000). Geodynamics of flat subduction: Seismicity and tomographic constraints from the Andean margin. *Tectonics*, *19*(5), 814–833. https://doi.org/10.1029/1999TC001152

Hallis, L. J., Huss, G. R., Nagashima, K., Taylor, G. J., Halldórsson, S. A., Hilton, D. R., Mottl, M. J., & Meech, K. J. (2015). Evidence for primordial water in Earth's deep mantle. *Science*, *350*(6262). https://doi.org/10.1126/science.aac4834

Harry, D. L., & Leeman, W. P. (1995). Partial melting of melt metasomatized subcontinental mantle and the magma source potential of the lower lithosphere. *Journal of Geophysical Research*, *100*(B6). https://doi.org/10.1029/94JB03065

Haschke, M., & Günther, A. (2003). Balancing crustal thickening in arcs by tectonic vs. magmatic means. *Geology*, *31*(11), 933–936. https://doi.org/10.1130/G19945.1

Hatherton, T., & Dickinson, W. R. (1969). Relationship between andesitic volcanism and seismicity in Indonesia, the Lesser Antilles, and other island arcs. *J Geophys Res*, *74*(22). https://doi.org/10.1029/jb074i022p05301

Hauri, E. (2002). SIMS analysis of volatiles in silicate glasses, 2: Isotopes and abundances in Hawaiian melt inclusions. *Chemical Geology*, *183*(1–4). https://doi.org/10.1016/S0009-2541(01)00374-6

Hiett, C. D., Newell, D. L., & Jessup, M. J. (2021). 3He evidence for fluid transfer and continental hydration above a flat slab. *Earth and Planetary Science Letters*, *556*, 116722. https://doi.org/10.1016/j.epsl.2020.116722

Hiett, C. D., Newell, D. L., Jessup, M. J., Grambling, T. A., Scott, B. E., & Upin, H. E. (2022). Deep CO2 and N2 emissions from Peruvian hot springs: Stable isotopic constraints on volatile cycling in a flat-slab subduction zone. *Chemical Geology*, *595*, 120787. https://doi.org/10.1016/J.CHEMGEO.2022.120787

Hirschmann, M. M. (2006). Water, melting, and the deep Earth H2O cycle. *Annual Review of Earth and Planetary Sciences*, *34*. https://doi.org/10.1146/annurev.earth.34.031405.125211

Hoke, L., & Lamb, S. (2007). Cenozoic behind-arc volcanism in the Bolivian Andes, South America: implications for mantle melt generation and lithospheric structure. *Journal of the Geological Society*, *164*(4), 795–814. https://doi.org/10.1144/0016-76492006-092

Holwell, D. A., Fiorentini, M., McDonald, I., Lu, Y., Giuliani, A., Smith, D. J., Keith, M., & Locmelis, M. (2019). A metasomatized lithospheric mantle control on the metallogenic signature of post-subduction magmatism. *Nature Communications*, *10*(1). https://doi.org/10.1038/s41467-019-11065-4

Horton, B. K. (2018). Tectonic Regimes of the Central and Southern Andes: Responses to Variations in Plate Coupling During Subduction. *Tectonics*, *37*(2). https://doi.org/10.1002/2017TC004624

Humphreys, E. D. (1995). Post-Laramide removal of the Farallon slab, western United States. *Geology*, *23*(11), 987–990. https://doi.org/10.1130/0091-7613(1995)023<0987:PLROTF>2.3.CO;2

Humphreys, E., Hessler, E., Dueker, K., Farmer, G. L., Erslev, E., & Atwater, T. (2003). How Laramide-Age Hydration of North American Lithosphere by the Farallon Slab Controlled Subsequent Activity in the Western United States. *International Geology Review*, *45*(7), 575–595. https://doi.org/10.2747/0020-6814.45.7.575

Hyndman, R. D., & Peacock, S. M. (2003). Serpentinization of the forearc mantle. *Earth and Planetary Science Letters*, *212*(3–4), 417–432. https://doi.org/10.1016/S0012-821X(03)00263-2

Iddings, J. P. (1895). Absarokite-Shoshonite-Banakite Series. *The Journal of Geology*, *3*(8). https://doi.org/10.1086/607398

Isacks, B. L. (1988). Uplift of the central Andean Plateau and bending of the Bolivian Orocline. *Journal of Geophysical Research*, *93*(B4), 3211–3231. https://doi.org/10.1029/JB093iB04p03211

Jagoutz, O., & Schmidt, M. W. (2013). The composition of the foundered complement to the continental crust and a re-evaluation of fluxes in arcs. *Earth and Planetary Science Letters*, *371–372*, 177–190. https://doi.org/10.1016/J.EPSL.2013.03.051

James, D., & Sacks, I. (1999). Cenozoic formation of central Andes: a geophysical perspective. In *Geology and Ore Deposits of the Central Andes* (pp. 1–25).

Johnson, D. M., Hooper, P. R., & Conrey, R. M. (1999). XRF analysis of rocks and minerals for major and trace elements on a single low dilution Li-tetraborate fused bead. *Advances in X-Ray Analysis*, *41*(C).

Johnson, M. C., & Plank, T. (2000). Dehydration and melting experiments constrain the fate of subducted sediments. *Geochemistry, Geophysics, Geosystems*, *1*(12). https://doi.org/10.1029/1999GC000014

Jones, C. H., Mahan, K. H., Butcher, L. A., Levandowski, W. B., & Farmer, G. L. (2015). Continental uplift through crustal hydration. *Geology*, *43*(4), 355–358. https://doi.org/10.1130/G36509.1

Kaneoka, I., & Guevara, C. (1984). K-Ar age determinations of late Tertiary and Quaternary Andean volcanic rocks, Southern Peru. *Geochemical Journal*, *18*(5), 233–239. https://doi.org/10.2343/geochemj.18.233

Kar, N., Garzione, C. N., Jaramillo, C., Shanahan, T., Carlotto, V., Pullen, A., Moreno, F., Anderson, V., Moreno, E., & Eiler, J. (2016). Rapid regional surface uplift of the northern Altiplano plateau revealed by multiproxy paleoclimate reconstruction. *Earth and Planetary Science Letters*, *447*, 33–47. https://doi.org/10.1016/j.epsl.2016.04.025

Kay, S. M., Mpodozis, C., & Coira, . (1999). Neogene magmatism, tectonism, and mineral deposits of the Central Andes (22 to 33 S latitude). *Society of Economic Geologists, Special Publication*, *7*, 27–59.

Kelemen, P. B., Dick, H. J. B., & Quick, J. E. (1992). Formation of harzburgite by pervasive melt/rock reaction in the upper mantle. *Nature*, *358*(6388). https://doi.org/10.1038/358635a0

Kelemen, P. B., Hanghøj, K., & Greene, A. R. (2013). One View of the Geochemistry of Subduction-Related Magmatic Arcs, with an Emphasis on Primitive Andesite and Lower Crust. In *Treatise on Geochemistry: Second Edition* (Vol. 4). https://doi.org/10.1016/B978-0-08-095975-7.00323-5

Kempton, P. D., Fitton, J. G., Hawkesworth, C. J., & Ormerod, D. S. (1991). Isotopic and trace element constraints on the composition and evolution of the lithosphere

beneath the southwestern United States. *Journal of Geophysical Research*, *96*(B8). https://doi.org/10.1029/91jb00373

Kempton, P. D., Harmon, R. S., Stosch, H. G., Hoefs, J., & Hawkesworth, C. J. (1988). Open-system O-isotope behaviour and trace element enrichment in the sub-Eifel mantle. *Earth and Planetary Science Letters*, *89*(3–4). https://doi.org/10.1016/0012-821X(88)90116-1

Kingsley, R. H., Schilling, J.-G., Dixon, J. E., Swart, P., Poreda, R., & Simons, K. (2002). D/H ratios in basalt glasses from the Salas y Gomez mantle plume interacting with the East Pacific Rise: Water from old D-rich recycled crust or primordial water from the lower mantle? *Geochemistry, Geophysics, Geosystems*, *3*(4). https://doi.org/10.1029/2001gc000199

Kuroda, Y., Matsuo, S., & Yamada, T. (1988). D/H fractionation during dehydration of hornblende, mica and volcanic glass. *Journal of Mineralogy, Petrology and Economic Geology*, *83*(3). https://doi.org/10.2465/ganko.83.85

Kyser, T. K., & O'Neil, J. R. (1984). Hydrogen isotope systematics of submarine basalts. *Geochimica et Cosmochimica Acta*, *48*(10). https://doi.org/10.1016/0016-7037(84)90392-2

Lamb, S., & Hoke, L. (1997). Origin of the high plateau in the central Andes, Bolivia, South America. *Tectonics*, *16*(4), 623–649. https://doi.org/10.1029/97TC00495

Le Maitre, R. W. (1984). A proposal by the iugs subcommission on the systematics of igneous rocks for a chemical classification of volcanic rocks based on the total alkali silica (TAS) diagram. *Australian Journal of Earth Sciences*, *31*(2). https://doi.org/10.1080/08120098408729295

Lee, C. A. (2005). Trace Element Evidence for Hydrous Metasomatism at the Base of the North American Lithosphere and Possible Association with Laramide Low-Angle Subduction. *The Journal of Geology*, *113*(6), 673–685. https://doi.org/10.1086/449327

Liao, J., Wang, Q., Gerya, T., & Ballmer, M. D. (2017). Modeling Craton Destruction by Hydration-Induced Weakening of the Upper Mantle. *Journal of Geophysical Research: Solid Earth*, *122*(9), 7449–7466. https://doi.org/10.1002/2017JB014157

Lowry, A. R., & Pérez-Gussinyé, M. (2011). The role of crustal quartz in controlling Cordilleran deformation. *Nature*, *471*(7338), 353–359. https://doi.org/10.1038/nature09912

Ma, Y., & Clayton, R. W. (2014). The crust and uppermost mantle structure of Southern Peru from ambient noise and earthquake surface wave analysis. *Earth and Planetary Science Letters*, *395*, 61–70. https://doi.org/10.1016/j.epsl.2014.03.013

Magaritz, M., & Taylor, H. P. (1976). Oxygen, hydrogen and carbon isotope studies of the franciscan formation, Coast Ranges, California. *Geochimica et Cosmochimica Acta*, *40*(2), 215–234. https://doi.org/10.1016/0016-7037(76)90179-4

Mallik, A., Nelson, J., & Dasgupta, R. (2015). Partial melting of fertile peridotite fluxed by hydrous rhyolitic melt at 2–3 GPa: implications for mantle wedge hybridization by sediment melt and generation of ultrapotassic magmas in convergent margins. *Contributions to Mineralogy and Petrology*, *169*(5). https://doi.org/10.1007/s00410-015-1139-2

Mamani, M., Tassara, A., & Wörner, G. (2008). Composition and structural control of crustal domains in the central Andes. *Geochemistry, Geophysics, Geosystems*, *9*(3). https://doi.org/10.1029/2007GC001925

Mamani, M., Wörner, G., & Sempere, T. (2010). *Geochemical variations in igneous rocks of the Central Andean orocline (13 ° S to 18 ° S): Tracing crustal thickening and magma generation through time and space*. *1*, 162–182. https://doi.org/10.1130/B26538.1

Marshall, E. W., Barnes, J. D., & Lassiter, J. C. (2017). The role of serpentinite-derived fluids in metasomatism of the Colorado Plateau (USA) lithospheric mantle. *Geology*, *45*(12), 1103–1106. https://doi.org/10.1130/G39444.1

Martinod, J., Gérault, M., Husson, L., & Regard, V. (2020). Widening of the Andes: An interplay between subduction dynamics and crustal wedge tectonics. In *Earth-Science Reviews* (Vol. 204). https://doi.org/10.1016/j.earscirev.2020.103170

Martinod, J., Husson, L., Roperch, P., Guillaume, B., & Espurt, N. (2010). Horizontal subduction zones, convergence velocity and the building of the Andes. *Earth and Planetary Science Letters*, *299*(3–4). https://doi.org/10.1016/j.epsl.2010.09.010

McDonough, W. F. (1990). Constraints on the composition of the continental lithospheric mantle. *Earth and Planetary Science Letters*, *101*(1), 1–18. https://doi.org/10.1016/0012-821X(90)90119-I

McLeod, C. L., Davidson, J. P., Nowell, G. M., de Silva, S. L., & Schmitt, A. K. (2013). Characterizing the continental basement of the central andes: Constraints from bolivian crustal xenoliths. *Bulletin of the Geological Society of America*, *125*(5–6), 985–997. https://doi.org/10.1130/B30721.1

Miller, C., Schuster, R., Klötzli, U., Frank, W., & Purtscheller, F. (1999). Post-collisional potassic and ultrapotassic magmatism in SW Tibet: Geochemical and Sr-Nd-Pb-O isotopic constraints for mantle source characteristics and petrogenesis. *Journal of Petrology*, *40*(9), 1399–1424. https://doi.org/10.1093/PETROJ/40.9.1399

Miyagi, I., & Matsubaya, O. (2003). Hydrogen isotopic composition of hornblende and biotite phenocrysts from Japanese island arc volcanoes: Evaluation of alteration process of the hydrogen isotopic ratios by degassing and re-equilibration. *Journal of*

Volcanology and Geothermal Research, *126*(1–2). https://doi.org/10.1016/S0377-0273(03)00148-3

Miyagi, I., Matsubaya, O., & Nakashima, S. (1998). Change in D/H ratio, water content and color during dehydration of hornblende. *Geochemical Journal*, *32*(1). https://doi.org/10.2343/geochemj.32.33

Morishita, T., Hattori, K. H., Terada, K., Matsumoto, T., Yamamoto, K., Takebe, M., Ishida, Y., Tamura, A., & Arai, S. (2008). Geochemistry of apatite-rich layers in the Finero phlogopite–peridotite massif (Italian Western Alps) and ion microprobe dating of apatite. *Chemical Geology*, *251*(1–4), 99–111. https://doi.org/10.1016/J.CHEMGEO.2008.02.018

Newman, S., Epstein, S., & Stolper, E. (1988). Water, carbon dioxide, and hydrogen isotopes in glasses from the ca. 1340 A.D. eruption of the Mono Craters, California: Constraints on degassing phenomena and initial volatile content. *Journal of Volcanology and Geothermal Research*, *35*(1–2), 75–96. https://doi.org/10.1016/0377-0273(88)90007-8

O'Reilly, S. Y., & Griffin, W. L. (2000). Apatite in the mantle: Implications for metasomatic processes and high heat production in Phanerozoic mantle. *Lithos*, *53*(3–4). https://doi.org/10.1016/S0024-4937(00)00026-8

Peacock, S. M., Rushmer, T., & Thompson, A. B. (1994). Partial melting of subducting oceanic crust. *Earth and Planetary Science Letters*, *121*(1–2). https://doi.org/10.1016/0012-821X(94)90042-6

Peccerillo, A. (1999). Multiple mantle metasomatism in central-southern Italy: Geochemical effects, timing and geodynamic implications. *Geology*, *27*(4). https://doi.org/10.1130/0091-7613(1999)027<0315:MMMICS>2.3.CO;2

Perez, N. D., & Horton, B. K. (2014). Oligocene-Miocene deformational and depositional history of the Andean hinterland basin in the northern Altiplano plateau, southern Peru. *Tectonics*, *33*(9), 1819–1847. https://doi.org/10.1002/2014TC003647

Plank, T., & Langmuir, C. H. (1998). The chemical composition of subducting sediment and its consequences for the crust and mantle. *Chemical Geology*, *145*(3–4). https://doi.org/10.1016/S0009-2541(97)00150-2

Profeta, L., Ducea, M. N., Chapman, J. B., Paterson, S. R., Gonzales, S. M. H., Kirsch, M., Petrescu, L., & DeCelles, P. G. (2015). Quantifying crustal thickness over time in magmatic arcs. *Scientific Reports*, *5*. https://doi.org/10.1038/srep17786

Prouteau, G., Scaillet, B., Pichavant, M., & Maury, R. (2001). Evidence for mantle metasomatism by hydrous silicic melts derived from subducted oceanic crust. *Nature*, *410*(6825), 197–200. https://doi.org/10.1038/35065583

Qi, H., Coplen, T. B., Gehre, M., Vennemann, T. W., Brand, W. A., Geilmann, H., Olack, G., Bindeman, I. N., Palandri, J., Huang, L., & Longstaffe, F. J. (2017). New biotite and muscovite isotopic reference materials, USGS57 and USGS58, for δ2H measurements–A replacement for NBS 30. *Chemical Geology*, *467*. https://doi.org/10.1016/j.chemgeo.2017.07.027

Ramos, V. A. (2008). The Basement of the Central Andes: The Arequipa and Related Terranes. *Annual Review of Earth and Planetary Sciences*, *36*(1), 289–324. https://doi.org/10.1146/annurev.earth.36.031207.124304

Ramos, V. A., & Folguera, A. (2009). Andean flat-slab subduction through time. *Geological Society, London, Special Publications*, *327*(1), 31–54. https://doi.org/10.1144/SP327.3

Rapp, R. P., Shimizu, N., Norman, M. D., & Applegate, G. S. (1999). Reaction between slab-derived melts and peridotite in the mantle wedge: Experimental constraints at 3.8 GPa. *Chemical Geology*, *160*(4). https://doi.org/10.1016/S0009-2541(99)00106-0

Richet, P., Bottinga, Y., & Javoy, M. (1977). A Review of Hydrogen, Carbon, Nitrogen, Oxygen, Sulphur, and Chlorine Stable Isotope Fractionation Among Gaseous Molecules. *Annual Review of Earth and Planetary Sciences*, *5*(1). https://doi.org/10.1146/annurev.ea.05.050177.000433

Righter, K., Dyar, M. D., Delaney, J. S., Vennemann, T. W., Hervig, R. L., & King, P. L. (2002). Correlations of octahedral cations with OH-, O2-, Cl-, and F- in biotite from volcanic rocks and xenoliths. *American Mineralogist*, *87*(1). https://doi.org/10.2138/am-2002-0115

Rizzo, A. L., Faccini, B., Casetta, F., Faccincani, L., Ntaflos, T., Italiano, F., & Coltorti, M. (2021). Melting and metasomatism in West Eifel and Siebengebirge Sub-Continental Lithospheric Mantle: Evidence from concentrations of volatiles in fluid inclusions and petrology of ultramafic xenoliths. *Chemical Geology*, *581*. https://doi.org/10.1016/j.chemgeo.2021.120400

Rosera, J. M., Gaynor, S. P., & Coleman, D. S. (2021). Spatio-temporal shifts in magmatism and mineralization in Northern Colorado beginning in the late eocene. *Economic Geology*, *116*(4). https://doi.org/10.5382/ECONGEO.4815

Saccocia, P. J., Seewald, J. S., & Shanks, W. C. (2009). Oxygen and hydrogen isotope fractionation in serpentine-water and talc-water systems from 250 to 450 °C, 50 MPa. *Geochimica et Cosmochimica Acta*, *73*(22). https://doi.org/10.1016/j.gca.2009.07.036

Sakai, H., & Tsutsumi, M. (1978). D/H fractionation factors between serpentine and water at 100° to 500°C and 2000 bar water pressure, and the D/H ratios of natural

serpentines. *Earth and Planetary Science Letters*, *40*(2). https://doi.org/10.1016/0012-821X(78)90093-6

Sandeman, H. A., Clark, A. H., & Farrar, E. (1995). An Integrated Tectono-Magmatic Model for the Evolution of the Southern Peruvian Andes (13–20°S) since 55 Ma. *International Geology Review*, *37*(12), 1039–1073. https://doi.org/10.1080/00206819509465439

Saylor, J. E., Sundell, K. E., Perez, N. D., Hensley, J. B., McCain, P., Runyon, B., Alvarez, P., Cárdenas, J., Usnayo, W. P., & Valer, C. S. (2023). Basin formation, magmatism, and exhumation document southward migrating flat-slab subduction in the central Andes. *Earth and Planetary Science Letters*, *606*, 118050. https://doi.org/10.1016/J.EPSL.2023.118050

Selverstone, J., & Sharp, Z. D. (2011). Chlorine isotope evidence for multicomponent mantle metasomatism in the Ivrea Zone. *Earth and Planetary Science Letters*, *310*(3–4), 429–440. https://doi.org/10.1016/J.EPSL.2011.08.034

Sempere, T., Herail, G., Oller, J., & Bonhomme, M. G. (1990). Late Oligocene-Early Miocene major tectonic crisis and related basins in Bolivia. *Geology*, *18*(10). https://doi.org/10.1130/0091-7613(1990)018<0946:LOEMMT>2.3.CO;2

Sharp, Z. (2017). Principles of Stable Isotope Geochemistry, 2nd edition. *Principles of Stable Isotope Geochemistry, 2nd Edition*, *136*(1).

Sharp, Z. D. (2017). Nebular ingassing as a source of volatiles to the Terrestrial planets. *Chemical Geology*, *448*. https://doi.org/10.1016/j.chemgeo.2016.11.018

Shaw, A. M., Hauri, E. H., Fischer, T. P., Hilton, D. R., & Kelley, K. A. (2008). Hydrogen isotopes in Mariana arc melt inclusions: Implications for subduction dehydration and the deep-Earth water cycle. *Earth and Planetary Science Letters*, *275*(1–2), 138–145. https://doi.org/10.1016/j.epsl.2008.08.015

Sheppard, S. M. F. (1986). Characterization and isotopic variations in natural waters. *Reviews in Mineralogy*, *16*.

Shervais, J. W. (1982). TiV plots and the petrogenesis of modern and ophiolitic lavas. *Earth and Planetary Science Letters*, *59*(1). https://doi.org/10.1016/0012-821X(82)90120-0

Sun, S. S., Nesbitt, R. W., & Sharaskin, A. Y. (1979). Geochemical characteristics of mid-ocean ridge basalts. *Earth and Planetary Science Letters*, *44*(1). https://doi.org/10.1016/0012-821X(79)90013-X

Suzuoki, T., & Epstein, S. (1976). Hydrogen isotope fractionation between OH-bearing minerals and water. *Geochimica et Cosmochimica Acta*, *40*(10). https://doi.org/10.1016/0016-7037(76)90158-7

Tatsumi, Y., & Eggins, S. (1995). Subduction zone magmatism. *Subduction Zone Magmatism*. (1), Wiley.

Taylor, H. P. (1978). Oxygen and hydrogen isotope studies of plutonic granitic rocks. *Earth and Planetary Science Letters*, *38*(1). https://doi.org/10.1016/0012-821X(78)90131-0

Tommasi, A., Langone, A., Padrón-Navarta, J. A., Zanetti, A., & Vauchez, A. (2017). Hydrous melts weaken the mantle, crystallization of pargasite and phlogopite does not: Insights from a petrostructural study of the Finero peridotites, southern Alps. *Earth and Planetary Science Letters*, *477*, 59–72. https://doi.org/10.1016/J.EPSL.2017.08.015

Turner, S., Arnaud, N., Liu, J., Rogers, N., Hawkesworth, C., Harris, N., Kelley, S., Van Calsteren, P., & Deng, W. (1996). Post-collision, shoshonitic volcanism on the Tibetan plateau: Implications for convective thinning of the lithosphere and the source of ocean island basalts. *Journal of Petrology*, *37*(1). https://doi.org/10.1093/petrology/37.1.45

Underwood, S. J., Feeley, T. C., & Clynne, M. A. (2012). Hydrogen isotope investigation of amphibole and biotite phenocrysts in silicic magmas erupted at Lassen Volcanic Center, California. *Journal of Volcanology and Geothermal Research*, *227–228*. https://doi.org/10.1016/j.jvolgeores.2012.02.019

Vennemann, T. W., & O'Neil, J. R. (1996). Hydrogen isotope exchange reactions between hydrous minerals and molecular hydrogen: I. A new approach for the determination of hydrogen isotope fractionation at moderate temperatures. *Geochimica et Cosmochimica Acta*, *60*(13). https://doi.org/10.1016/0016-7037(96)00103-2

Villegas-Lanza, J. C., Chlieh, M., Cavalié, O., Tavera, H., Baby, P., Chire-Chira, J., & Nocquet, J. M. (2016). Active tectonics of Peru: Heterogeneous interseismic coupling along the Nazca megathrust, rigid motion of the Peruvian Sliver, and Subandean shortening accommodation. *Journal of Geophysical Research: Solid Earth*, *121*(10). https://doi.org/10.1002/2016JB013080

Wagner, L. S., Beck, S., Zandt, G., & Ducea, M. N. (2006). Depleted lithosphere, cold, trapped asthenosphere, and frozen melt puddles above the flat slab in central Chile and Argentina. *Earth and Planetary Science Letters*, *245*(1–2). https://doi.org/10.1016/j.epsl.2006.02.014

Ward, K. M., Zandt, G., Beck, S. L., Wagner, L. S., & Tavera, H. (2016). Lithospheric structure beneath the northern Central Andean Plateau from the joint inversion of ambient noise and earthquake-generated surface waves. *Journal of Geophysical Research: Solid Earth*, *121*(11). https://doi.org/10.1002/2016JB013237

Wulff-Pedersen, E., Neumann, E. R., & Jensen, B. B. (1996). The upper mantle under La Palma, Canary Islands: Formation of Si - K - Na-rich melt and its importance as a metasomatic agent. *Contributions to Mineralogy and Petrology*, *125*(2–3). https://doi.org/10.1007/s004100050210

Wyllie, P. J., & Sekine, T. (1982). The formation of mantle phlogopite in subduction zone hybridization. *Contributions to Mineralogy and Petrology*, *79*(4), 375–380. https://doi.org/10.1007/BF01132067/METRICS

Zaccarini, F., Stumpfl, E. F., & Garuti, G. (2004). Zirconolite and Zr–Th–U minerals in chromitites of the Finero complex, western Alps, Italy: evidence for carbonatite-type metasomatism in a subcontinental mantle plume. *The Canadian Mineralogist*, *42*(6), 1825–1845. https://doi.org/10.2113/GSCANMIN.42.6.1825

Zanetti, A., Mazzucchelli, M., Rivalenti, G., Vannucci, R., Zanetti, A., Vannucci, R., Mazzucchelli, M., & Rivalenti, G. (1999). The Finero phlogopite-peridotite massif: an example of subduction-related metasomatism. *Contrib Mineral Petrol*, *134*.

Zhang, M., Hu, P., Niu, Y., & Su, S. (2007). Chemical and stable isotopic constraints on the nature and origin of volatiles in the sub-continental lithospheric mantle beneath eastern China. *Lithos*, *96*(1–2), 55–66. https://doi.org/10.1016/j.lithos.2006.10.006

Zhang, M., Suddaby, P., Thompson, R. N., Thirlwall, M. F., & Menzies, M. A. (1995). Potassic Volcanic Rocks in NE China: Geochemical Constraints on Mantle Source and Magma Genesis. *Journal of Petrology*, *36*(5), 1275–1303. https://doi.org/10.1093/PETROLOGY/36.5.1275

CHAPTER 5

METASOMATISM AND MELTING OF CORDILLERAN LITHOSPHERE RESULTING FROM SEDIMENT RELAMINATION DURING SHALLOW SUBDUCTION[1]

Abstract

Neogene and Quaternary potassic lavas erupted ≤ 200km inboard of the modern volcanic arc in southern Peru, including a Quaternary suite of xenolith-bearing latites, andesites, and dacites that outcrop along the Cusco-Vilconata Fault System (CVFS). Mantle xenoliths collected from a latite lava flow near Huarocondo, Peru include phlogopite- and calcite-rich orthopyroxenites and harzburgites that sample melt metasomatized lithospheric mantle characterized by orthopyroxene and phlogopite growth at the expense of olivine. Calcite-rich inclusions within neoformed orthopyroxene crystals evidence an immiscible carbonate melt phase involved in metasomatism, and stable isotope analyses of calcite yield $\delta^{13}C$ and $\delta^{18}O$ values of -2.49 to +0.77 $‰_{VPDB}$ and +15.8 to +16.4 $‰_{VSMOW}$, respectively, which are interpreted to reflect an input of subducted carbonate sediments in the metasomatizing melt. Characteristic arc-like trace element patterns, including fluid mobile and incompatible element enrichments (e.g., Cs, Rb, Pb > 10^2 × primitive mantle) with notable Nb-Ta depletions further support a subduction influence. Lavas from both mafic and intermediate suites yield surprisingly similar trace element patterns that mirror mantle xenoliths but with larger magnitudes of

[1] Paper formatted for publication in *AGU Advances* with author list:
C.D. Hiett[a], D.L. Newell[a], J.W. Shervais
[a]Utah State University

enrichment. Trace element characteristics, together with constraints implied by the presence of mantle xenoliths, rule out an origin through igneous differentiation for intermediate alkaline lavas. Instead, we suggest that these lavas are derived from melting of sediments accreted to the base of the lithosphere during shallow subduction. We propose a model in which melting of relaminated sediments or mélange material produces silicic alkaline melts, which react with peridotite in the lithospheric mantle to produce phlogopite-orthopyroxenites and alkaline basaltic melts. This reaction can explain the observed xenolith suite and Neogene-Quaternary high-K basaltic volcanism, while the intermediate lavas may represent sediment melts that ascended to the surface with minimal reaction or differentiation by exploiting the oblique-extensional CVFS. These observations inform on mass transfer processes during shallow subduction and resulting melting and metasomatism in the lithospheric mantle, with implications for rheologic weakening, volatile cycling, and critical mineral bearing magmatism in the Altiplano Plateau and Cordilleran regions globally.

1. Introduction

The geochemistry of potassic basalts and mantle xenoliths each provide a means for scrutinizing the evolution of the continental lithosphere and testing models for subduction-derived mass transfer and mantle metasomatism. Potassic lavas display a diverse range of geochemical characteristics that reflect often complex histories of melt depletion and metasomatism in their mantle source regions, yet the nature of metasomatizing agents and their geodynamic context can be difficult to resolve. New perspectives on the generation of potassic lavas come from recent experimental studies that test the current paradigm of arc magmagenesis via hydrous flux melting of the

mantle wedge, demonstrating that the observed spectrum of potassic and calk-alkaline arc magmas can also be explained by metasomatic reactions involving melts of subducted material and mantle peridotite (Mallik et al., 2015; Cruz-Uribe et al., 2018; Codillo et al., 2018). Within the context of continental volcanism, these experiments provide a provocative explanation for potassic basalts with arc-like geochemical signatures and mantle xenoliths that display evidence for subduction-derived melt metasomatism. Continental potassic volcanism often postdates subduction or continental collision by tens of Ma (e.g., Miller et al., 1999) or even up to 2 Ga (e.g., Buhlmann et al., 2000), attesting to the preservation of metasomatized mantle and/or subducted material incorporated into the continental lithosphere and its delayed melting long after the cessation of subduction.

The Andean Cordillera is the premier type-example for arc magmatism and orogenesis in oceanic-continental convergent margins and an ideal setting to scrutinize the chemical evolution of formative continental lithosphere. At the heart of the Andes lies the Altiplano-Puna Plateau, showcasing the dramatic crustal thickening and regional surface uplift that can be attained in these orogenic systems. Neogene through Quaternary potassic volcanism has occurred across the plateau interior, generally initiating after periods of shallow subduction (Carlier et al., 2005; Hoke and Lamb, 2007; Ramos and Folguera, 2009). In southern Peru, detailed geochemical investigation of ultrapotassic lavas has highlighted a heterogeneous metasomatized lithospheric mantle below the northern Altiplano Plateau (Carlier et al., 2005). However, the nature of that metasomatism is unconstrained, and alternative explanations for potassic lavas have been proposed, including melting of lower crustal arc-cumulates (Chapman et al., 2015).

Furthermore, the petrogenesis of the most abundant Quaternary alkaline volcanics, a suite of xenolith-rich intermediate alkaline lavas, has not been adequately addressed.

We sampled mantle and lower crustal xenoliths from four Quaternary alkaline lava flows across southern Peru to investigate the metasomatic history of the northern Altiplano lithosphere and improve constraints on the formation of recent potassic magmatism in the region. Here we describe a suite of carbonate- and phlogopite-bearing ultramafic xenoliths collected from a latite lava flow near Huarocondo, Peru, which we interpreted as samples of melt metasomatized subcontinental lithospheric mantle (SCLM) that underlies the region. We present new stable isotope values of carbonate ($\delta^{13}C$, $\delta^{18}O$) and phlogopite (δD), mineral major element compositions, and trace element characteristics that ultimately show evidence for metasomatism by silicic slab-derived melts, providing physical validation to recent experimental results (Mallik et al., 2015). Major and trace element geochemistry of the alkaline host lavas are used to assess the disparate compositions of intermediate and mafic alkaline lavas, and with consideration of their xenolith-rich nature and the geodynamic history of the region, we argue that intermediate potassic lavas are primitive melts of slab-derived material accreted to the base of the lithosphere during shallow subduction. In this model, potassic basalts represent the evolved melts produced by reaction between silicic lavas and lithospheric mantle peridotite, and phlogopite- and orthopyroxene-rich ultramafic xenoliths represent the residual altered mantle.

Surprisingly high abundances of carbon and fluorine in these ultramafic xenoliths suggest that these processes can also enrich the SCLM in volatiles, exerting important controls on arc volatile cycling, lithosphere rheology, and priming the lithosphere for

critical mineral bearing magmatism. These arguments highlight the need to reimagine the evolution of the lithospheric mantle and consider the long-term impacts of melting and metasomatism resulting from the accretion/underplating of slab material during shallow subduction.

2. Geologic Setting

The Altiplano-Puna Plateau represents the keystone tectonomorphic feature of the Andean Cordillera (Fig. 1). Deformation and surface uplift have been diachronous across the plateau throughout the Cenozoic, and numerous mechanisms have been explored to explain patterns of plateau growth (e.g., Garzione et al., 2017). In the northern plateau, a major inboard migration of magmatism in the late Eocene and Oligocene is interpreted as the result of shallow or flat-slab subduction (Ramos and Folguera, 2009; Saylor et al., 2023). The roughly contemporaneous eastward shift in deformation is hypothesized to have resulted from either thermal weakening of the foreland lithosphere by the resulting magmatism (Sandeman et al., 1995; James and Sacks, 1999), basal coupling between the subducting slab and Andean lithosphere (Martinod et al., 2010; Horton, 2018), dynamic stresses during mantle wedge migration (Martinod et al., 2020), or mechanical weaking from hydration and metasomatism (Saylor et al., 2023). Surface uplift between ~ 9 – 5 Ma was likely decoupled from crustal shortening and attributed to magmatic addition, mid/lower crustal flow, or mantle delamination (Garzione et al., 2017 and references therein).

Arc magmatism has been relatively continuous along the Andean Cordillera since at least the late Paleozoic, with the Western Cordillera as the axis of calk-alkaline arc

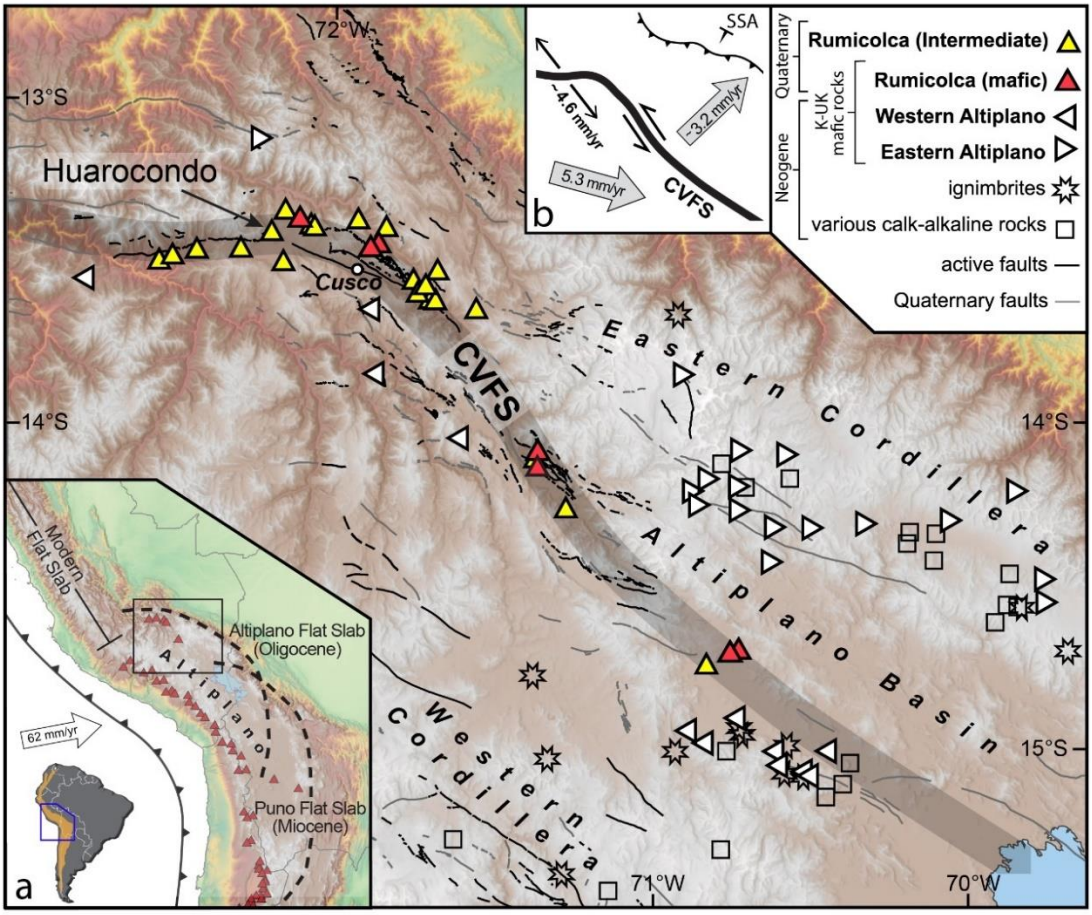

Figure 1. Map of Neogene and Quaternary volcanism of the northern Altiplano region. Quaternary Rumicolca Formation lavas are focused along the trace of the CVFS. The Huarocondo volcano is highlighted. Older potassic and ultrapotassic (K-UK) mafic rocks comprise the eastern and western Altiplano suites of Carlier et al. (2005). Map location is shown in inset (a) along with major Quaternary volcanoes of the Central Andes (small red triangles) and the inferred extents of the Oligocene Altiplano flat slab and Miocene Puna flat slab (after Ramos and Folguera, 2009). Inset (b) is a schematic representation of convergence velocities of eastern and western Altiplano domains relative to stable South America (SSA) and partitioned by the CVFS (after Villegas-Lanza et al., 2016), demonstrating that the CVFS accommodates oblique-sinistral neotectonic deformation with a greater normal component to the north near Cusco, Peru.

volcanism until the inboard migration of magmatism during late Eocene – Oligocene in the northern Altiplano (Mamani et al., 2010). Arc magmatism was reestablished in the western Cordillera near the end of the Oligocene in this region, and bimodal volcanism has been prevalent in the backarc region since this time, including ignimbrite eruptions from ca. 23-12 Ma, most frequently >16 Ma, and more punctuated periods of basaltic volcanism that occurred from ca. 30-20 Ma, 6-5 Ma, and <2 Ma (Mamani et al., 2010). Neogene basaltic rocks are generally highly potassic and include various lamproites, lamprophyres, and shoshonites (Carlier and Lorand, 1997, 2008; Carlier et al., 1997, 2005). These mafic units are enriched in incompatible trace elements, particularly fluid mobile elements (e.g., Ba, Rb, Pb), and most display relative depletions in Nb and Ta, characteristic of arc-related lavas (Pearce, 1982; Kelemen et al., 2013). Radiogenic isotope characteristics (Sr-Nd) show variable crustal or metasomatic enrichment (Carlier et al., 2005), and were used to divide these rocks into three suites based on their location in the eastern Altiplano, western Altiplano, or along the Cuzco-Vilcanota fault system (CVFS; Fig. 1). Eastern and western Altiplano alkaline basalts were interpreted as melts of distinct metasomatized mantle domains, with the CFVS representing the boundary between these two lithospheric domains.

Here we focus on the Quaternary suite of alkaline and calk-alkaline lavas in the northern plateau interior, which crop out as small monogenetic flows or domal structures in close proximity to the CVFS (Fig. 1), referred to as the Rumicolca Formation (Carlotto et al., 2011) or Quimsachata volcanics (Mamani et al., 2010). Rumicolca Formation lavas generally fall into two compositional groups. One group includes seven occurrences of lamproite, lamprophyre and shoshonite lavas described by Carlier et al. (2005) and

Carlier & Lorand (2008, 1997). These potassic basalts exhibit compositions intermediate between eastern and western Altiplano suites and were interpreted to reflect melting from both domains along their tectonic boundary. A second group constituting a larger proportion of Rumicolca Formation lavas (>30 flows) that exhibit intermediate silica contents and are transitional between alkaline (latites) and calc-alkaline compositions (andesites and dacites). The petrogenesis of these lavas has received less attention due to their apparently more evolved chemistry. Interestingly though, it is this group that includes lavas with abundant lower crustal and mantle xenoliths.

Most of these flows are biotite- or amphibole-phyric latites, andesites, and dacites with potassic bulk compositions (1 – 2 K_2O/Na_2O by wt%; Foley et al., 1987), moderate CaO (4-5 wt%), low TiO_2 (<1 wt%), and moderate Al_2O_3 (15 – 17 wt%) spanning from metaluminous to peraluminous (Mamani et al., 2010; Carlotto et al., 2011). Trace elements characteristics are nearly identical to their more mafic counterparts along the CVFS (Carlier et al., 2005), including enrichments in large ion lithophile elements (LILE) and light rare earth elements (LREE) 10^2 to 10^3 × primitive mantle, as well as prominent Nb-Ta depletions (Mamani et al., 2010; Carlotto et al., 2011). Chapman et al. (2015) described a suite of mid-lower crustal (amphibolite, granulite) and upper mantle (peridotite) xenoliths collected from four Rumicolca lava flows but focused on mid-crustal metamorphic lithologies with implications for tectonic burial and reconstructions of tectonic shortening.

3. Xenolith Description

Xenoliths detailed here were collected from an intermediate composition Rumicolca Formation lava flow near Huarocondo, Peru (Fig 1). Samples of volcanic host rock were also collected for bulk rock chemical analysis. Here we focus on a suite of ultramafic xenoliths that include phlogopite- and calcite-bearing orthopyroxenites, and carbonate-bearing harzburgites. We also include observations from a calcite-bearing wehrlite and phlogopite schist that share similar geochemical characteristics and speak to the heterogeneity of alteration in the lithosphere. Brief descriptions of individual xenolith samples are provided in Table C.1.

Orthopyroxenite and harzburgite xenoliths share abundant jaggedly interlocking orthopyroxene crystals with minor spinel and chromite, but contain variable amounts of olivine and phlogopite (Fig. 2). Based on textural and compositional similarities of orthopyroxene and olivine, these xenoliths are likely derived from the same lithology but with differing modal abundances due to their small size (~ 2 – 4 cm wide). Rounded grain boundaries of olivine in contact with orthopyroxene (Fig. 2b,c) suggest that orthopyroxene and likely phlogopite were formed in a reaction at the expense of olivine. Orthopyroxene in these samples contains small globular inclusions (up to 1mm, most < 300μm) consisting primarily of calcite with variable amounts of olivine and minor chromite and spinel (Fig. 2, C.2). Smaller melt pockets of Fe-rich silicate melts and Fe-Ni sulfides were also observed (Fig. C.2). Abundant interstitial calcite is found in one fine-grained orthopyroxenite, where the orthopyroxene is displays an acicular radiating habit. Phlogopite is present in two xenoliths in large masses of fine-grained crystals (Fig. 2a), and as a small, isolated pocket in the finer grained sample. Samples appear to have

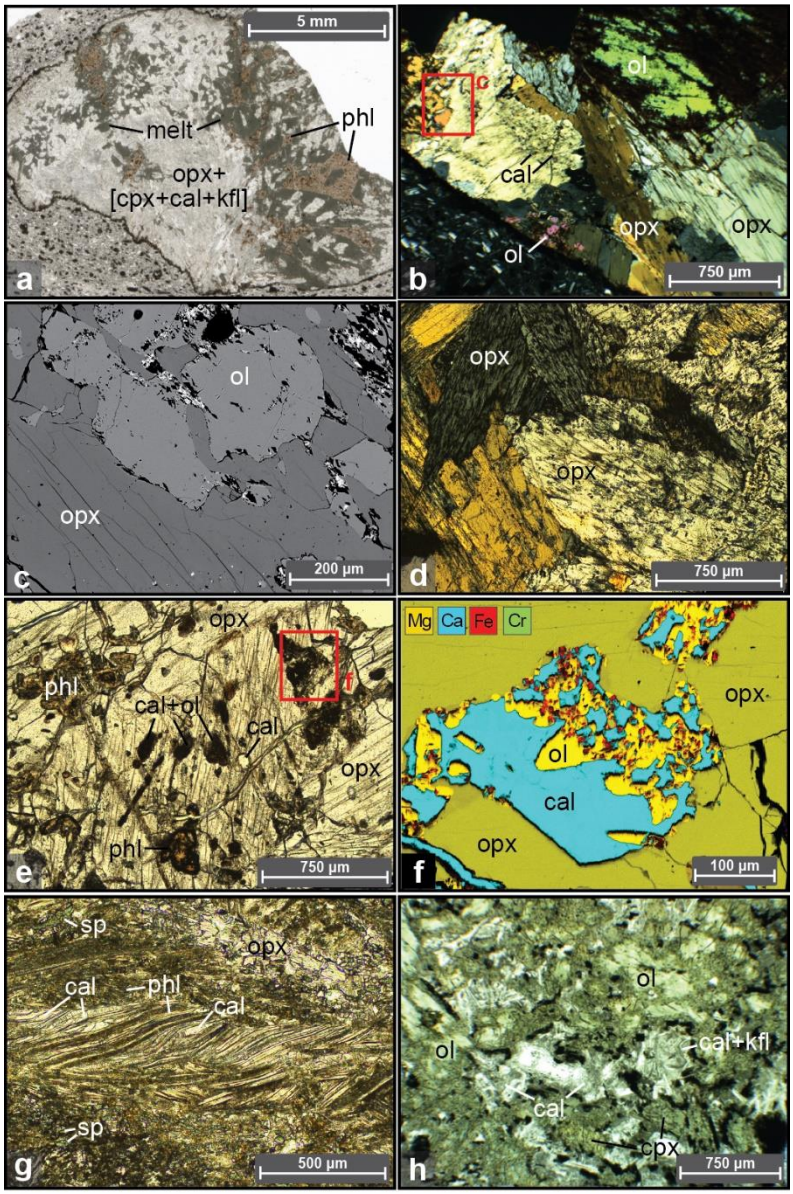

Figure 2. Photomicrographs, backscatter electron (BSE) images, and chemical maps of xenoliths discussed in text. a) low magnification plane polarized light (PPL) image of phlogopite-orthopyroxenite xenolith (CH19RX-66) displaying large heterogenous domains of phlogopite and orthopyroxene. Turbid melt domains are localized around phlogopite, and orthopyroxene exhibits a secondary assemblage of clinopyroxene, K-feldspar, and remobilized calcite, primarily along orthopyroxene cleavage planes. b) Cross polarized light (XPL) image of harzburgite xenolith (CH19RX-49) displaying jaggedly intergrown orthopyroxene and rounded olivine, consistent with orthpyroxene growth and olivine consumption during metasomatism. c) BSE image of area shown in b), showing olivine orthopyroxene contact. d) Orthopyroxenite xenolith (CH19RX-46) displaying similar jagged grain boundaries (XPL), e) Phlogopite-orthopyroxenite (CH19RX-69) showing intergrown orthopyroxene grain boundaries, small phlogopite

clusters, and multiple ~200 μm wide inclusions of calcite and olivine. Crosscutting veins of calcite are apparent, interpreted to have formed during decompression/xenolith entrainment. (PPL) f) Electron microprobe (EMP) chemical map of area highlighted in e) showing calcite and olivine inclusion. Olivine in this inclusion contain up to 1.3 wt% NiO. g) Phlogopite schist (CH19RX-47) displaying shear fabrics with abundant interstitial calcite (PPL). h) Calcite bearing wehrlite xenolith (CH19RX-71) exhibiting uralitic amphibole rims on clinopyroxene and olivine with interstitial fine grained calcite and plagioclase. Mineral abbreviations: cal–calcite, cpx–clinopyroxene, ol–olivine, opx–orthopyroxene, phl–phlogopite, sp–spinel. Enlarged versions and additional photomicrographs, backscatter electron (BSE) images, and chemical maps are provided in the supplementary material.

been variably altered and/or melted (Fig. 2a), presumably during entrainment in ascending host magmas, during which veins of calcite formed that crosscut mineral grains (Fig. 2e). A secondary assemblage of potassium feldspar, plagioclase, and clinopyroxene in association with calcite is observed in three samples that we interpret as forming at this time. Olivine in these samples displays variable iddingsite alteration, likely due to interaction with hydrothermal and/or deuteric fluids during eruption or weathering at surface conditions. A similar orthopyroxenite xenolith was recovered from another latite flow near Oropesa, Peru, but was not included in geochemical analyses due to evidence of extensive surface alteration.

Other calcite-rich xenoliths include a phlogopite schist showing protomylonitic shear textures and phlogopite compositions similar to the orthopyroxenite/harzburgite suite and an altered calcite-rich wehrlite. The phlogopite schist is composed dominantly of phlogopite and calcite with lesser spinel. Phlogopite is strongly foliated and locally displays shear textures, with interstitial calcite between phlogopite grains concentrated in zones with shear fabrics. The altered wehrlite is dominantly olivine and clinopyroxene,

minor magnetite and apatite, with interstitial calcite and small feldspar grains focused within fine-grained altered domains. Euralitic amphibole rims on clinopyroxene grains and the absence of obvious melt reaction textures is distinct from the orthopyroxene-rich xenoliths and suggests that calcite mineralization and metasomatism may have been facilitated by aqueous and/or CO_2-rich fluids rather than melts.

4. Results & Discussion

4.1. Xenolith suite

Xenoliths were analyzed for mineral compositions (excluding the wehrlite and phlogopite schist), bulk-rock trace element concentrations, and stable isotope compositions of calcite ($\delta^{13}C$ and $\delta^{18}O$ values) and phlogopite (δD values) as outlined in the supplementary methods. Major element analyses measured via electron microprobe are provided in supplementary table C.2. Orthopyroxene is enstatite (En85 to En91; Wo < 3), and olivine is forsterite (Fo87 to Fo91). Phlogopite (Mg# = 90–95) exhibit nearly complete fluorophlogopite compositions (9–11 wt % F^-). Calcite found within inclusions and veins is essentially a pure Ca endmember, and associated olivine is more Fe-rich (Fo84) than primary olivine, with exceptionally high NiO contents (up to 1.3 wt %).

Trace element concentrations for xenoliths and Rumicolca lava flows (Tables C.3, C.4) reveal primitive mantle (PM) normalized values characteristic of metasomatism by subduction-derived fluids/melts (Fig. 3a). All xenolith samples are enriched in LILE and LREE relative to heavy rare earth elements (HREE) and high field strength elements (HFSE). Common negative anomalies for Nb and Ta are observed, whereas Zr and Hf show inconsistent depletion or enrichment patterns with no apparent lithologic control

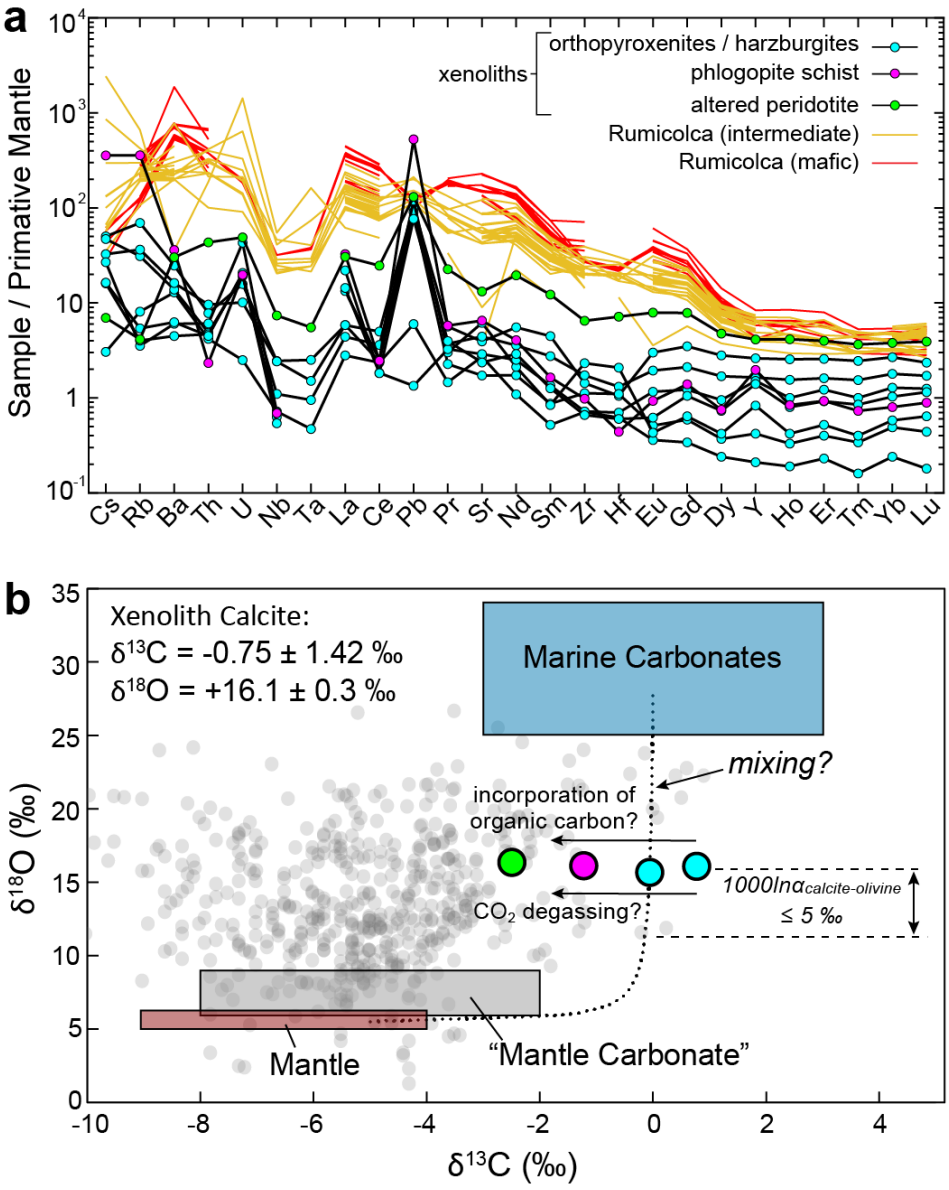

Figure 3. Primitive mantle trace element compositions of xenoliths and Rumicolca lavas and C-O stable isotope ratios of xenolith hosted calcite. a) Primitive mantle normalized trace element compositions of xenoliths and Rumicolca Formation lavas showing characteristic arc-like patterns of LILE and LREE enrichment and Nb-Ta depletions. b) Measured $\delta^{13}C$ (VPDB) and $\delta^{18}O$ (VSMOW) values of xenolith hosted calcite. $\delta^{13}C$ values overlap with those of marine carbonates, and $\delta^{18}O$ values are intermediate between mantle-derived carbon and marine carbonates, reflecting mixing of these two endmembers (see text for discussion). Mantle carbonate box gives range of expected $\delta^{13}C$ and $\delta^{18}O$ values for magmatic carbonates crystallized from pristine mantle melts (Giuliani et al., 2014). Range of values for mantle carbon are from Boettcher and O'Neil (1980) and Deines (2002). Grey dots are a global compilation of kimberlite hosted carbonates from Giuliani et al (2014).

over this difference. These arc-like characteristics reflect the influence of fluids/melts enriched in fluid mobile (LILE) and more incompatible (LREE) elements, whereas HFSE (particularly Nb and Ta), may be preferentially sequestered within the subducting lithosphere (Kelemen et al., 2013). PM normalized HREE concentrations <1 for half of the samples attest to melt depletion prior to metasomatism, typical of upper mantle peridotites (McDonough, 1990). Trace element enrichments are unlikely to be derived solely during metasomatism with alkaline magmas during eruption, as we see similar trace element enrichments in samples despite variability or absence of late stage clinopyroxene and feldspar growth.

Carbon and oxygen isotope ($\delta^{13}C$, $\delta^{18}O$) values of xenolith-hosted calcite range from -2.5 to +0.8 ‰ (VPDB) and +15.8 to +16.4 ‰ (VSMOW), respectively (Fig. 3b, Table B.5). Values of $\delta^{13}C$ near 0 ‰ are consistent with subducted marine carbonates, whereas $\delta^{18}O$ values fall between marine carbonate (~+30 ‰ VSMOW) and mantle values (+5 to +6 ‰ VSMOW; Boettcher & O'Neil, 1980). These values are distinct from primary mantle carbonates but overlap with $\delta^{13}C$ and $\delta^{18}O$ values from kimberlite-hosted carbonates that have been altered by hydrothermal or deuteric fluids during eruption (Fig. 3b; Giuliani et al., 2014). We consider such fluid alteration as an unlikely control over the isotopic composition of xenolith-hosted calcite, as this process would lead to coupled $\delta^{18}O$-$\delta^{13}C$ modification (Giuliani et al., 2014), which is not observed among the four analyzed samples. We interpret calcite $\delta^{18}O$ and $\delta^{13}C$ values as reflecting original isotopic composition of calcite enclosed within orthopyroxene during melt metasomatism. Mixing between sediment-derived melts (including a marine carbonate component) and mantle-derived melts would produce intermediate $\delta^{18}O$ values while

maintaining the $\delta^{13}C$ of the sediment due to the low abundance of C in mantle lithologies (Fig. 3b; Deines, 2002). The consistent $\delta^{18}O$ values are likely a function of isotopic equilibrium and buffering by silicate minerals at mantle temperatures, as isotopic partitioning between calcite and common mantle mineral phases has equilibrium oxygen isotope fractionations between 1.5–5 ($1000\ln\alpha_{calcite\text{-}mineral}$) at 700–1000 °C (Chiba et al., 1989; Zheng and Zhao, 2003). This suggests that calcite was in equilibrium with silicates having a $\delta^{18}O$ value of 10 – 14 ‰, > 4 ‰ above mantle values, perhaps indicating that the bulk system had these $\delta^{18}O$ values after mixing. The consistent isotopic character between calcite from two orthopyroxenite samples, the carbonated peridotite, and mylonitic phlogopite schist suggests a common carbon source in these disparate lithologies. The ~3 ‰ variability in $\delta^{13}C$ may reflect either minor contributions from organic carbon in slab-sediments or fractionation during CO_2 degassing/exsolution from the metasomatizing melt, which would lead to progressively lower $\delta^{13}C$ values in the residual melt (Demény and Harangi, 1996). Isotopic fractionation driven by degassing upon eruption (i.e. formation of calcite veins) is unlikely given the lack of $\delta^{18}O$ variability that would accompany $\delta^{13}C$ modification during degassing.

Hydrogen isotopes (δD values) of phlogopite in one orthopyroxenite and the phlogopite shist exhibit values of -197 and -165 ‰ (VSMOW), respectively, which are anomalously low compared to upper mantle-derived hydrogen (-80 ± 10 ‰; Boettcher & O'Neil, 1980) or slab-derived fluids (-15 to -40 ‰; Kempton et al., 1988; Marshall et al., 2017; Shaw et al., 2008). Such low δD values are hypothesized for residual water within subducting oceanic lithosphere after extensive dehydration (Shaw et al., 2008). However, dehydration of the extent needed to achieve these low values in the subducting slab is

expected in the deeper regions of subduction systems, and δD values of biotite in Rumicolca lava phenocrysts and kersantite xenoliths recovered from the Quimsachata volcano are more positive (up to -38 ‰; Ch. 3), suggesting slab-derived water with characteristic D-enriched values (Shaw et al., 2008). An alternative explanation is that xenoliths in Huambutio lava interacted with meteoric water during or after eruption, which have present-day δD values of ~ -120 ‰ in this region (Hiett et al., 2022). Hydrothermal alteration is consistent with iddingsite alteration of olivine and lower K_2O/Na_2O in Huarocondo lava (Fig. 4) that may be due to fluid-rock interaction (Gibson et al., 1995). Isotopic fractionation between biotite and water is unconstrained at temperatures < 300°C but is anticipated to result in δD values lower than -120 ‰ (Suzuoki and Epstein, 1976; Vennemann and O'Neil, 1996). Low δD values may also be a function of the extremely high F^- contents in phlogopite, which could affect isotopic fractionation during crystallization or volatile loss, although the effects of F^- on H-isotope behavior has not been studied to our knowledge.

4.2. Rumicolca lavas

New bulk rock chemical analyses combined with previous data from Quaternary Rumicolca lavas (Figs. 4, 5, Table C.4) demonstrate two distinct populations of intermediate and mafic composition potassic rocks. These lavas yield trace element patterns that mirror arc-like trends measured in xenoliths but with higher magnitude enrichments (Fig. 2). Surprisingly, trace element compositions of intermediate xenolith-bearing lavas overlap those of the mafic suite but with slightly lower enrichments (e.g., Ba, Th, LREEs), which is not expected if their intermediate character were generated through typical magmatic differentiation mechanisms of assimilation and fractional

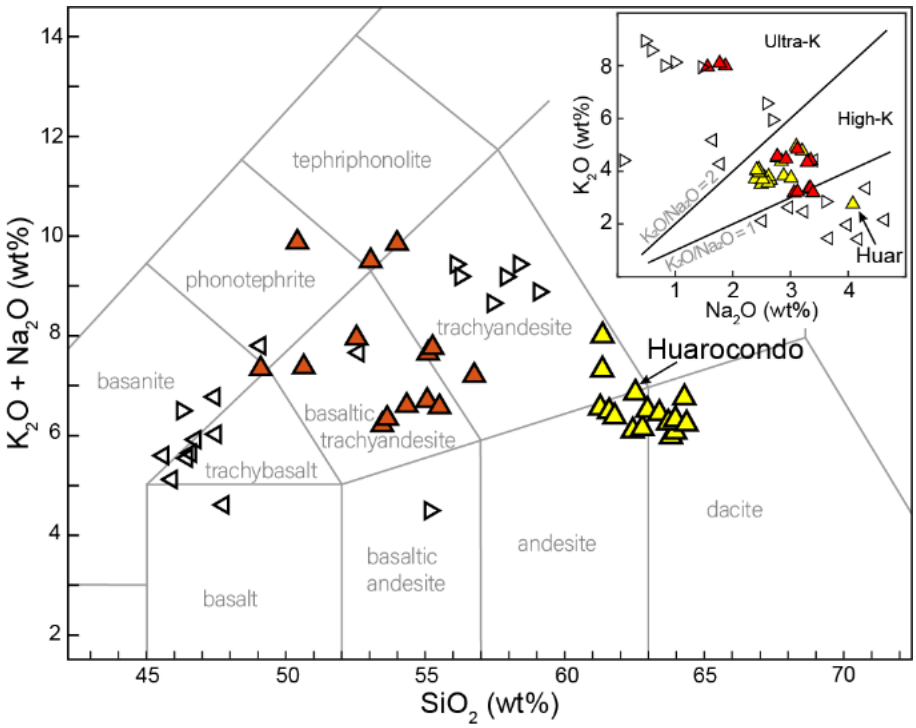

Figure 4. Total alkali versus silica plot (Le Maitre, 1984) of Rumicolca lavas and Neogene western Alitplano and eastern Altiplano suites. Key for symbols is given in Figure 1. Inset shows discrimination of alkali contents (Na_2O vs. K_2O), demonstrating the potassic (K) or ultrapotassic (UK) compositions of kersantite xenoliths and Rumicolca Formation lavas.

crystallization (AFC). Similar patterns are also seen in older eastern and western Altiplano potassic basalts but with variable magnitudes of LILE and LREE enrichment (Fig. C.2; Carlier et al., 2005).

Major element characteristics of the mafic suite (high K_2O, MgO, P_2O_5, low FeO, Na_2O), together with trace element enrichment patterns, implicate a phlogopite- or K-amphibole-rich mantle source that was previously melt-depleted and re-enriched through metasomatizing melts with a subduction affinity, akin to the orthopyroxenite and harzburgite xenoliths described here and consistent with earlier studies (Carlier et al., 2005). Compositions of the intermediate suite have been presumed as a function of

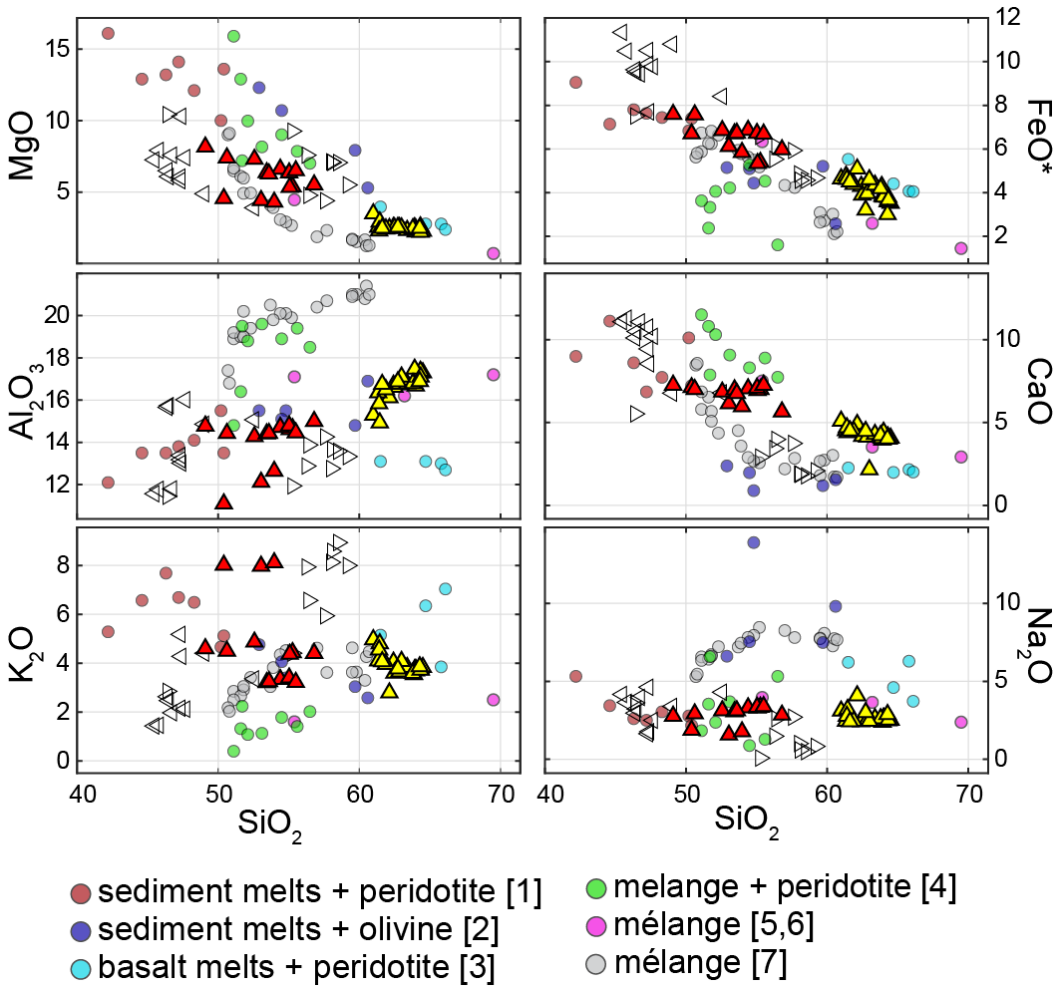

Figure 5. Major element compositions of Rumicolca lavas compared to experimental melt products of hybridized slab material and peridotite. Legend lists the starting mixtures replicated by melting experiments. Major element chemistry of intermediate Rumicolca lavas generally agree with compositions of melts derived from mélange material (especially study 5 & 6), as well as melts of hybridized basalt melts and peridotite (study 3). It is worth noting that these high silica melts from ref. 3 represent hybridization with high melt-rock ratios. Compositions of the mafic suite agree most closely with melts derived through sediment melt and peridotite interaction (study 1). Experimental studies: 1–Mallik et al., 2015, 2–Pirard and Hermann, 2015, 3–Rapp et al., 1999, 4–Codillo et al. 2018, 5–Castro et al., 2013, 6–Castro and Gerya 2018, 7–Cruz Uribe et al., 2018.

magmatic differentiation (AFC) or mixing between mafic and felsic endmembers (Carlier et al., 2005; Carlier and Lorand, 2008), which is difficult to reconcile with the abundance of mantle xenoliths and the trace element characteristics of the two suites. The presence of mantle xenoliths is incompatible with differentiation through fractional crystallization, as any gravitational or mechanical separation of cumulate phases would also remove any entrained xenoliths, and significant crustal assimilation is unlikely without the latent heat supplied by fractional crystallization (e.g., Bohrson and Spera, 2001). Overlapping trace element patterns strongly imply a genetic relationship, but differentiation through AFC processes are expected to lead to greater enrichments in the evolved (intermediate) suite, which is opposite of the observed relationship. Furthermore, mixing between basaltic melts with a crustal-derived felsic melt would dramatically shift trace element patterns away from the mafic melt. Although AFC processes are complex and compositional evolution can be difficult to predict (Bohrson and Spera, 2001), we argue that the remarkably similar trace element patterns between the intermediate and mafic Rumicolca suites make differentiation from primary basaltic melts or mixing with crustal melts highly unlikely. The petrogenesis of the intermediate Rumicolca lavas therefore needs to be reassessed, and we suggest that these melts may represent a key link between mafic potassic lavas and metasomatized ultramafic xenoliths.

5. Accretion, Melting, and Metsomatism of Slab Material

Data from the ultramafic xenolith suite and both groups of Rumicolca lavas suggest that subduction-metasomatized mantle material is present in the SCLM below the northern Altiplano and has been involved in Neogene-Quaternary potassic magmatism. The enigmatic intermediate-composition Rumicolca lavas provide a novel explanation

coupling mantle metasomatism and bimodal potassic magmatism. Experimental work in the last decade is shifting our perspective of melt-rock interaction in the mantle wedge, demonstrating that melts of slab-derived material can interact with peridotite to generate a broad range of alkaline and calk-alkaline magmas (Codillo et al., 2018 and refs therein). Melting of subducted sediments or mélange material is anticipated under hot mantle wedge conditions (Schmidt et al., 2004) and the produced melts will yield intermediate to felsic high-K compositions (Castro and Gerya, 2008; Cruz-Uribe et al., 2018). Subsequent reaction with peridotite converts olivine to orthopyroxene and stabilizes phlogopite, buffering the reacted melt to ultrapotassic mafic compositions (Mallik et al., 2015). Results from these experimental studies are compared with compositions of Rumicolca lavas in Figure 5. If the Altiplano is a natural example of this process, the intermediate-composition Rumicolca lavas may represent primary melts of subducted sediments or mélange material. In this model, potassic and ultrapotassic mafic lavas are produced by reaction of these felsic melts with mantle peridotite, and phlogopite orthopyroxenites and harzburgite xenoliths are samples of the residual altered peridotite (Fig. 6).

Both mafic and intermediate Rumicolca suites are constrained to the trace of the CVFS, suggesting that this structure represents a lithosphere-scale weakness that allowed melts to ascend from the mantle. The CVFS has an overall oblique sinistral sense of deformation (Carlotto et al., 2011), with geodetic data supporting a greater component of extension in the Cusco region where the fault system trends E-W (Villegas-Lanza et al., 2016), coincident with the highest density of Quaternary potassic volcanism (Fig 1). Rapid ascent through lithosphere may have promoted rapid ascent of sediment-derived

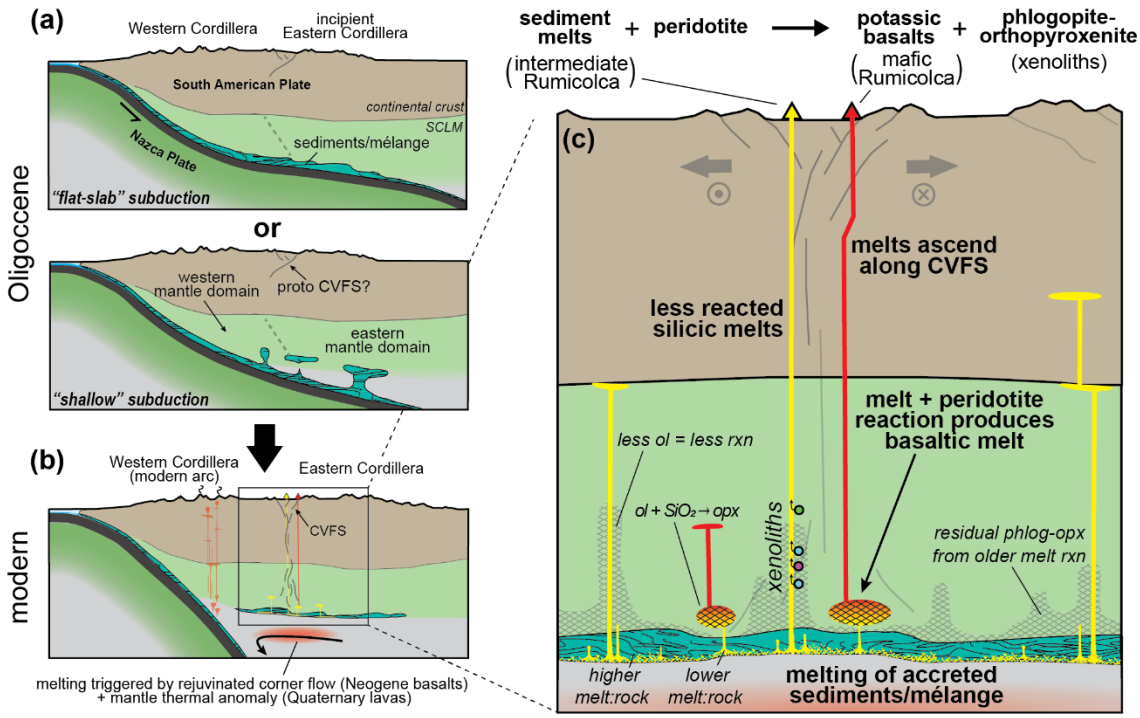

Figure 6. Schematic illustration of the proposed model for mantle metasomatism and Quaternary potassic volcanism in the northern Altiplano Plateau. Panel a) shows two possible scenarios explaining relamination of subducted sediments to the base of the continental lithosphere. Panel b) shows modern tectonic configuration and melting of relaminated sediments after opening of the asthenospheric wedge. Panel c) illustrates sediment derived silicic melts interacting with SCLM to form residual phlogopite-orthopyroxenite and potassic basaltic melts. The consumption of silica is noted by the simplified reaction $ol + SiO_2 \rightarrow opx$; readers are directed to Mallik et al (2015) for a more detailed discussion of this melt reaction. Melts avoiding conversion to basaltic compositions may be due to ascent through residual orthopyroxene rich SCLM or higher melt-rock ratios.

melts and minimal reaction with mantle peridotite, but the question remains as to why basaltic magmas were generated in some cases, forming a bimodal distribution of Quaternary melt compositions. Melt compositions produced during reaction between silicic slab-derived melts and mantle peridotite are highly sensitive to melt-rock ratios, so intermediate lavas may represent higher volumes sediment-derived melts intruded into the SCLM, while potassic basalts may be the result of lower melt-rock ratios and a more

pronounced influence of peridotite-melt reaction. A second possibility is that high silica compositions were maintained where melts ascended through previously altered mantle, which would have a diminished capacity to buffer melts towards mafic compositions via conversion of olivine to orthopyroxene.

Carbon from the sediment/mélange melts was apparently trapped within the forming orthopyroxene as calcite inclusions, retaining stable isotope signatures that reflect mixing of subducted sediment and mantle melts. The uniform composition and mosaic textures of calcite in the inclusions are consistent with trapping of an immiscible carbonate melt phase (Demény and Harangi, 1996; Roedder, 2015). Immiscibility between alkaline-silicate melts and carbonate melts is observed at high temperatures (e.g., >1220°C at 1.7GPa for kamafugite-carbonatite melts; Martin et al., 2012), and is dramatically enhanced by high F^- abundances (Thompson et al., 2007). Partitioning of Ni into the carbonate melt phase may explain associated olivine with NiO contents up to 1.3 wt % found within the inclusions, which to our knowledge is the highest ever recorded. However, we are unaware of any experimental constraints on Ni partitioning between silicate and carbonate melts.

Trace element characteristics of the subducted sediment-derived melts were imparted on the altered SCLM and maintained within the resulting mafic magmas. Most incompatible trace elements are slightly more enriched in the mafic basalts, consistent with their affinity to remain in the evolving melt as it is partially consumed during reaction with mantle peridotite. Positive Pb, Zr, and Hf anomalies observed in xenolith samples are mirrored by complimentary depletions in the mafic lavas, and significant positive or negative anomalies are absent in the intermediate lavas. This observation

implies that Pb, Zr, and Hf were scavenged from the felsic slab-derived magmas that evolved towards basaltic compositions during reaction with mantle peridotites.

Trace element and stable isotope characteristics of the calcite-bearing wehrlite sample essentially mirror those of the other xenoliths despite absence of melt-reaction textures, implying that slab-derived metasomatism was heterogeneous and not limited to melt-reactions, but also involved H_2O-CO_2 fluid phases. Lower $\delta^{13}C$ values are inconsistent with CO_2 degassed/exsolved from a carbonated melt with $\delta^{13}C$ values measured in the other samples because isotopic fractionation leads to fluid phases enriched in ^{13}C relative to the melt (Giuliani et al., 2014). This suggests that isotopic variability of carbon from slab sediments is the most likely explanation for the overall $\delta^{13}C$ variability in xenolith hosted calcite.

The spatially and temporally isolated eruption of Rumicolca lavas >200 km inboard of the modern volcanic arc suggests that mantle melting in this region is disconnected from modern subduction zone processes. The initiation of backarc magmatism closely followed the cessation of Oligocene shallow subduction, pointing towards a causal explanation. We suggest that shallow subduction led to the alteration of the overlying lithosphere, but in addition to metasomatism and hydration by slab-derived fluids (Humphreys, 1995; Hiett et al., 2021), we envision accretion of material from the subduction interface onto the base of the continental lithosphere. If subduction was particularly flat, or perhaps even erosive to the overlying lithosphere (Axen et al., 2018) this could be accomplished through abandonment of mélange material upon slab steepening. Alternatively, if a thin mantle wedge existed over a shallowly subducting Nazca plate, diapirism of slab sediments could transfer material upwards to the base of

the continental lithosphere (e.g., Behn et al., 2011). Return of hot asthenosphere upon the resumption of steep subduction would raise temperatures of underplated sediments above their solidus (<800°C below 3.5Ga; Schmidt et al., 2004), leading to melting of the accreted/underplated material, metasomatic reaction with overlying peridotites, and formation of older ultrapotassic basalts across the northern Altiplano.

Delayed mantle melting ~25 Ma after the cessation of shallow subduction and generation of the Quaternary Rumicolca formation has been linked to a thermal anomaly in the asthenospheric wedge below this region, which may be related to trench parallel asthenospheric flow deflected by the southward advancing modern Peruvian flat slab (Garzione et al., 2017). This interpretation places the thermal anomaly as a southward progressing transient feature, which would have re-initiated melting of the previously altered lithosphere after migrating below the northern Altiplano region. That older potassic volcanism has not migrated from the north in step with this thermal anomaly suggests that altered continental lithosphere below the northern altiplano was a prerequisite for alkaline volcanism, as the lithosphere further north was not affected by Oligocene shallow subduction.

5.1. Global implications

Investigations of potassic basalts or metasomatized mantle xenoliths regularly invoke metasomatizing melts or altered mantle lithologies which are either not preserved in the geologic record or not accessible for study. In contrast, the Quaternary volcanism and entrained mantle xenoliths described here represent an unprecedented window into deep mantle metasomatism, as the complete suite of reactants and products involved in

sediment melting, mantle metasomatism, and derivative high-K basaltic melts are available. Furthermore, this work provides physical validation to recent experimental work showing that reactions between slab-derived melts and mantle peridotite may be a critical process for generating the diverse range of arc volcanism as well as more obscure volcanics in backarc and continental settings. Near-primitive melts of subducted sediments have been invoked in the generation of high-Mg andesites in volcanic arcs (e.g., Tatsumi, 2001), but to our knowledge this is the first study to document similar volcanism in a continental or backarc setting originating from melting of sediments accreted to the base of the lithosphere.

Accretion or underplating of slab material below the Altiplano has not been documented, but similar processes have been invoked in geodynamic models (e.g., Currie et al., 2007; Castro and Gerya, 2008) and observed in other Cordilleran regions globally, where this process may be facilitated by shallow subduction or diapirism in the mantle wedge (termed “re-lamination”; Behn et al., 2011; Ducea & Chapman, 2018). The accretion of slab sediments and their delayed melting, resulting from shifting subduction geometries should be considered as an additional mechanism for explaining enigmatic potassic volcanism or lithospheric alteration in continental margins worldwide. For example, petrologic studies of potassic basalts in Tibet reveal a complex metasomatic history in the Tibetan mantle with a distinct input of subducted sediments, but the mechanisms responsible for metasomatism and formation of associated felsic potassic rocks remain uncertain (Miller et al., 1999). Accretion or underplating of slab material, with subsequent melting and reaction with the lithospheric mantle, may be a contributing factor in the petrogenesis of these rocks and is consistent with observations of accreted

mélange material in the region now exposed within metamorphic core complexes (Kapp et al., 2000).

The xenolith suite described here highlights potential impacts of this process on both the rheology of the deep lithosphere and priming the mantle for generating critical-mineral bearing magmatism. The calcite-bearing phlogopite xenolith displaying foliation and shear textures demonstrates that mantle deformation can be localized in relatively weak mica rich domains, possibly aided by volatiles like CO_2, thus representing significant weakened rheology in the continental lithosphere. This observation contrasts with conclusions based on exhumed phlogopite-peridotites in the Italian Alps (Tommasi et al., 2017), although rheological weakening in those rocks is still evident and suggested to results from hydrous melt infiltration. Xenolith hosted calcite also lends credence to the sequestration of carbon within the deep lithosphere during subduction, which is an important yet poorly constrained piece of the long-term carbon cycle (Kelemen and Manning, 2015). Recent work has shown that metasomatic enrichment of the lithosphere may be a prerequisite for some ore-bearing magmatic systems, including enrichment in metals (Holwell et al., 2019) and volatiles such and fluorine (Rosera et al., 2022). The observation of Ni-rich sulfide melt inclusions, as well as the extremely high fluorine contents of metasomatic phlogopite, speaks to the ability of this metasomatism to prime the mantle lithosphere to participate in critical mineral bearing melt generation.

References

Axen, G. J., van Wijk, J. W., & Currie, C. A. (2018). Basal continental mantle lithosphere displaced by flat-slab subduction. *Nature Geoscience 2018 11:12*, *11*(12), 961–964. https://doi.org/10.1038/s41561-018-0263-9

Behn, M. D., Kelemen, P. B., Hirth, G., Hacker, B. R., & Massonne, H. J. (2011). Diapirs as the source of the sediment signature in arc lavas. *Nature Geoscience 2011 4:9*, *4*(9), 641–646. https://doi.org/10.1038/ngeo1214

Boettcher, A. L., & O'Neil, J. R. (1980). Stable isotope, chemical, and petrographic studies of high-pressure amphiboles and micas: evidence for metasomatism in the mantle source regions of alkali basalts and kimberlites. *American Journal of Science, 280-A*, 594–621.

Bohrson, W. A., & Spera, F. J. (2001). Energy-constrained open-system magmatic processes II: Application of energy- constrained assimilation - Fractional crystallization (EC-AFC) model to magmatic systems. *Journal of Petrology*, *42*(5). https://doi.org/10.1093/petrology/42.5.1019

Buhlmann, A. L., Cavell, P., Burwash, R. A., Creaser, R. A., & Luth, R. W. (2000). Minette bodies and cognate mica-clinopyroxenite xenoliths from the Milk River area, southern Alberta: Records of a complex history of the northernmost part of the Archean Wyoming craton. *Canadian Journal of Earth Sciences*, *37*(11), 1629–1650. https://doi.org/10.1139/E00-058/ASSET/IMAGES/GR.GIF

Carlier, G., & Lorand, J. P. (2008). Zr-rich accessory minerals (titanite, perrierite, zirconolite, baddeleyite) record strong oxidation associated with magma mixing in the south Peruvian potassic province. *Lithos*, *104*(1–4), 54–70. https://doi.org/10.1016/j.lithos.2007.11.008

Carlier, G., Lorand, J. P., Audebaud, E., & Kienast, J. R. (1997). Petrology of an unusual orthopyroxene-bearing minette suite from southeastern Peru, Eastern Andean Cordillera: Al-rich lamproites contaminated by peraluminous granites. *Journal of Volcanology and Geothermal Research*, *75*(1–2), 59–87. https://doi.org/10.1016/S0377-0273(96)00035-2

Carlier, G., Lorand, J. P., Liégeois, J. P., Fornari, M., Soler, P., Carlotto, V., & Cárdenas, J. (2005). Potassic-ultrapotassic mafic rocks delineate two lithospheric mantle blocks beneath the southern Peruvian Altiplano. *Geology*, *33*(7), 601–604. https://doi.org/10.1130/G21643.1

Carlier, G., & Lorand, J.-P. (1997). First occurrence of diopside sanidine phlogopite lamproite in the Andean Cordillera: the Huacancha and Morojarja dikes, southern Peru. *Canadian Journal of Earth Sciences*, *34*(8), 1118–1127. https://doi.org/10.1139/e17-090

Carlotto, V., Cardenas, J., & Carlier, G. (2011). Geologia del Cuadrangulo de Cusco Hoja 28-s. *Instituto Geológico Minero y Metalúrgico Boletin 138, Serie A, Carta Geologica Nacional, Escala 1:50,000*.

Castro, A., & Gerya, T. V. (2008). Magmatic implications of mantle wedge plumes: Experimental study. *Lithos*, *103*(1–2). https://doi.org/10.1016/j.lithos.2007.09.012

Chapman, A. D., Ducea, M. N., McQuarrie, N., Coble, M., Petrescu, L., & Hoffman, D. (2015). Constraints on plateau architecture and assembly from deep crustal xenoliths, northern Altiplano (SE Peru). *Bulletin of the Geological Society of America*, *127*(11–12), 1777–1797. https://doi.org/10.1130/B31206.1

Chiba, H., Chacko, T., Clayton, R. N., & Goldsmith, J. R. (1989). Oxygen isotope fractionations involving diopside, forsterite, magnetite, and calcite: Application to geothermometry. *Geochimica et Cosmochimica Acta*, *53*(11). https://doi.org/10.1016/0016-7037(89)90174-9

Codillo, E. A., Le Roux, V., & Marschall, H. R. (2018). Arc-like magmas generated by mélange-peridotite interaction in the mantle wedge. *Nature Communications 2018 9:1*, *9*(1), 1–11. https://doi.org/10.1038/s41467-018-05313-2

Cruz-Uribe, A. M., Marschall, H. R., Gaetani, G. A., & Le Roux, V. (2018). Generation of alkaline magmas in subduction zones by partial melting of mélange diapirs-An experimental study. *Geology*, *46*(4). https://doi.org/10.1130/G39956.1

Currie, C. A., Beaumont, C., & Huismans, R. S. (2007). The fate of subducted sediments: A case for backarc intrusion and underplating. *Geology*, *35*(12). https://doi.org/10.1130/G24098A.1

Deines, P. (2002). The carbon isotope geochemistry of mantle xenoliths. *Earth-Science Reviews*, *58*(3–4), 247–278. https://doi.org/10.1016/S0012-8252(02)00064-8

Demény, A., & Harangi, S. (1996). Stable isotope studies and processes of carbonate formation in Hungarian alkali basalts and lamprophyres: Evolution of magmatic fluids and magma-sediment interactions. *Lithos*, *37*(4). https://doi.org/10.1016/0024-4937(95)00029-1

Ducea, M. N., & Chapman, A. D. (2018). Sub-magmatic arc underplating by trench and forearc materials in shallow subduction systems; A geologic perspective and implications. In *Earth-Science Reviews* (Vol. 185). https://doi.org/10.1016/j.earscirev.2018.08.001

Foley, S. F., Venturelli, G., Green, D. H., & Toscani, L. (1987). The Ultrapotassic Rocks: Characteristics, Classification, and Constraints for Petrogenetic models. *Earth-Science Reviews*, *24*, 81–134.

Garzione, C. N., McQuarrie, N., Perez, N. D., Ehlers, T. A., Beck, S. L., Kar, N., Eichelberger, N., Chapman, A. D., Ward, K. M., Ducea, M. N., Lease, R. O., Poulsen, C. J., Wagner, L. S., Saylor, J. E., Zandt, G., & Horton, B. K. (2017). Tectonic Evolution of the Central Andean Plateau and Implications for the Growth of Plateaus. *Annual Review of Earth and Planetary Sciences*, *45*(1), 529–559. https://doi.org/10.1146/annurev-earth-063016-020612

Gibson, S. A., Thompson, R. N., Leonardos, O. H., Dickin, A. P., & Mitchell, J. G. (1995). The Late Cretaceous Impact of the Trindade Mantle Plume: Evidence from Large-volume, Mafic, Potassic Magmatism in SE Brazil. *Journal of Petrology*, *36*(1), 189–229. https://doi.org/10.1093/PETROLOGY/36.1.189

Giuliani, A., Phillips, D., Kamenetsky, V. S., Fiorentini, M. L., Farquhar, J., & Kendrick, M. A. (2014). Stable isotope (C, O, S) compositions of volatile-rich minerals in kimberlites: A review. In *Chemical Geology* (Vols. 374–375). https://doi.org/10.1016/j.chemgeo.2014.03.003

Hiett, C. D., Newell, D. L., & Jessup, M. J. (2021). 3He evidence for fluid transfer and continental hydration above a flat slab. *Earth and Planetary Science Letters*, *556*, 116722. https://doi.org/10.1016/j.epsl.2020.116722

Hiett, C. D., Newell, D. L., Jessup, M. J., Grambling, T. A., Scott, B. E., & Upin, H. E. (2022). Deep CO2 and N2 emissions from Peruvian hot springs: Stable isotopic constraints on volatile cycling in a flat-slab subduction zone. *Chemical Geology*, *595*, 120787. https://doi.org/10.1016/J.CHEMGEO.2022.120787

Hoke, L., & Lamb, S. (2007). Cenozoic behind-arc volcanism in the Bolivian Andes, South America: implications for mantle melt generation and lithospheric structure. *Journal of the Geological Society*, *164*(4), 795–814. https://doi.org/10.1144/0016-76492006-092

Holwell, D. A., Fiorentini, M., McDonald, I., Lu, Y., Giuliani, A., Smith, D. J., Keith, M., & Locmelis, M. (2019). A metasomatized lithospheric mantle control on the metallogenic signature of post-subduction magmatism. *Nature Communications*, *10*(1). https://doi.org/10.1038/s41467-019-11065-4

Horton, B. K. (2018). Tectonic Regimes of the Central and Southern Andes: Responses to Variations in Plate Coupling During Subduction. *Tectonics*, *37*(2). https://doi.org/10.1002/2017TC004624

Humphreys, E. D. (1995). Post-Laramide removal of the Farallon slab, western United States. *Geology*, *23*(11), 987–990. https://doi.org/10.1130/0091-7613(1995)023<0987:PLROTF>2.3.CO;2

James, D., & Sacks, I. (1999). Cenozoic formation of central Andes: a geophysical perspective. In *Geology and Ore Deposits of the Central Andes* (pp. 1–25).

Kapp, P., Yin, A., Manning, C. E., Murphy, M., Harrison, T. M., Spurlin, M., Lin, D., Xi-Guang, D., & Cun-Ming, W. (2000). Bluechist-bearing metamorphic core complexes in the Qiangtang block reveal deep crustal structure of northern Tibet. *Geology*, *28*(1). https://doi.org/10.1130/0091-7613(2000)28<19:BMCCIT>2.0.CO;2

Kelemen, P. B., Hanghøj, K., & Greene, A. R. (2013). One View of the Geochemistry of Subduction-Related Magmatic Arcs, with an Emphasis on Primitive Andesite and Lower Crust. In *Treatise on Geochemistry: Second Edition* (Vol. 4). https://doi.org/10.1016/B978-0-08-095975-7.00323-5

Kelemen, P. B., & Manning, C. E. (2015). Reevaluating carbon fluxes in subduction zones, what goes down, mostly comes up. *Proceedings of the National Academy of Sciences of the United States of America*, *112*(30), E3997–E4006. https://doi.org/10.1073/pnas.1507889112

Kempton, P. D., Harmon, R. S., Stosch, H. G., Hoefs, J., & Hawkesworth, C. J. (1988). Open-system O-isotope behaviour and trace element enrichment in the sub-Eifel mantle. *Earth and Planetary Science Letters*, *89*(3–4). https://doi.org/10.1016/0012-821X(88)90116-1

Le Maitre, R. W. (1984). A proposal by the iugs subcommission on the systematics of igneous rocks for a chemical classification of volcanic rocks based on the total alkali silica (TAS) diagram. *Australian Journal of Earth Sciences*, *31*(2). https://doi.org/10.1080/08120098408729295

Mallik, A., Nelson, J., & Dasgupta, R. (2015). Partial melting of fertile peridotite fluxed by hydrous rhyolitic melt at 2–3 GPa: implications for mantle wedge hybridization by sediment melt and generation of ultrapotassic magmas in convergent margins. *Contributions to Mineralogy and Petrology*, *169*(5). https://doi.org/10.1007/s00410-015-1139-2

Mamani, M., Wörner, G., & Sempere, T. (2010). *Geochemical variations in igneous rocks of the Central Andean orocline (13 ° S to 18 ° S): Tracing crustal thickening and magma generation through time and space*. *1*, 162–182. https://doi.org/10.1130/B26538.1

Marshall, E. W., Barnes, J. D., & Lassiter, J. C. (2017). The role of serpentinite-derived fluids in metasomatism of the Colorado Plateau (USA) lithospheric mantle. *Geology*, *45*(12), 1103–1106. https://doi.org/10.1130/G39444.1

Martin, L. H. J., Schmidt, M. W., Mattsson, H. B., Ulmer, P., Hametner, K., & Günther, D. (2012). Element partitioning between immiscible carbonatite-kamafugite melts with application to the Italian ultrapotassic suite. *Chemical Geology*, *320–321*. https://doi.org/10.1016/j.chemgeo.2012.05.019

Martinod, J., Gérault, M., Husson, L., & Regard, V. (2020). Widening of the Andes: An interplay between subduction dynamics and crustal wedge tectonics. In *Earth-Science Reviews* (Vol. 204). https://doi.org/10.1016/j.earscirev.2020.103170

Martinod, J., Husson, L., Roperch, P., Guillaume, B., & Espurt, N. (2010). Horizontal subduction zones, convergence velocity and the building of the Andes. *Earth and Planetary Science Letters*, *299*(3–4). https://doi.org/10.1016/j.epsl.2010.09.010

McDonough, W. F. (1990). Constraints on the composition of the continental lithospheric mantle. *Earth and Planetary Science Letters*, *101*(1), 1–18. https://doi.org/10.1016/0012-821X(90)90119-I

Miller, C., Schuster, R., Klötzli, U., Frank, W., & Purtscheller, F. (1999). Post-collisional potassic and ultrapotassic magmatism in SW Tibet: Geochemical and Sr-Nd-Pb-O isotopic constraints for mantle source characteristics and petrogenesis. *Journal of Petrology*, *40*(9), 1399–1424. https://doi.org/10.1093/PETROJ/40.9.1399

Pearce, J. A. (1982). Trace element characteristics of lavas from destructive plate boundaries. *Andesites: Orogenic Andesites and Related Rocks*.

Ramos, V. A., & Folguera, A. (2009). Andean flat-slab subduction through time. *Geological Society, London, Special Publications*, *327*(1), 31–54. https://doi.org/10.1144/SP327.3

Roedder, E. (2015). Silicate liquid immiscibility in magmas. In *Evolution of the Igneous Rocks: Fiftieth Anniversary Perspectives*. https://doi.org/10.2307/j.ctt13x1dkm.5

Rosera, J. M., Frazer, R. E., Mills, R. D., Jacob, K., Gaynor, S. P., Coleman, D. S., & Farmer, L. G. (2022). Fluorine-rich mafic lower crust in the southern Rocky Mountains: the role of pre-enrichment in generating Fluorine-rich silicic magmas and porphyry Mo Deposits. *American Mineralogist, in press.*

Sandeman, H. A., Clark, A. H., & Farrar, E. (1995). An Integrated Tectono-Magmatic Model for the Evolution of the Southern Peruvian Andes (13–20°S) since 55 Ma. *International Geology Review*, *37*(12), 1039–1073. https://doi.org/10.1080/00206819509465439

Saylor, J. E., Sundell, K. E., Perez, N. D., Hensley, J. B., McCain, P., Runyon, B., Alvarez, P., Cárdenas, J., Usnayo, W. P., & Valer, C. S. (2023). Basin formation, magmatism, and exhumation document southward migrating flat-slab subduction in the central Andes. *Earth and Planetary Science Letters*, *606*, 118050. https://doi.org/10.1016/J.EPSL.2023.118050

Schmidt, M. W., Vielzeuf, D., & Auzanneau, E. (2004). Melting and dissolution of subducting crust at high pressures: the key role of white mica. *Earth and Planetary Science Letters*, *228*(1–2), 65–84. https://doi.org/10.1016/J.EPSL.2004.09.020

Shaw, A. M., Hauri, E. H., Fischer, T. P., Hilton, D. R., & Kelley, K. A. (2008). Hydrogen isotopes in Mariana arc melt inclusions: Implications for subduction dehydration and the deep-Earth water cycle. *Earth and Planetary Science Letters*, *275*(1–2), 138–145. https://doi.org/10.1016/j.epsl.2008.08.015

Suzuoki, T., & Epstein, S. (1976). Hydrogen isotope fractionation between OH-bearing minerals and water. *Geochimica et Cosmochimica Acta*, *40*(10). https://doi.org/10.1016/0016-7037(76)90158-7

Tatsumi, Y. (2001). Geochemical modeling of partial melting of subducting sediments and subsequent melt-mantle interaction: Generation of high-Mg andesites in the Setouchi volcanic belt, southwest Japan. *Geology*, *29*(4). https://doi.org/10.1130/0091-7613(2001)029<0323:GMOPMO>2.0.CO;2

Thompson, A. B., Aerts, M., & Hack, A. C. (2007). Liquid immiscibility in silicate melts and related systems. *Reviews in Mineralogy and Geochemistry*, *65*. https://doi.org/10.2138/rmg.2007.65.4

Tommasi, A., Langone, A., Padrón-Navarta, J. A., Zanetti, A., & Vauchez, A. (2017). Hydrous melts weaken the mantle, crystallization of pargasite and phlogopite does not: Insights from a petrostructural study of the Finero peridotites, southern Alps. *Earth and Planetary Science Letters*, *477*, 59–72. https://doi.org/10.1016/J.EPSL.2017.08.015

Vennemann, T. W., & O'Neil, J. R. (1996). Hydrogen isotope exchange reactions between hydrous minerals and molecular hydrogen: I. A new approach for the determination of hydrogen isotope fractionation at moderate temperatures. *Geochimica et Cosmochimica Acta*, *60*(13). https://doi.org/10.1016/0016-7037(96)00103-2

Villegas-Lanza, J. C., Chlieh, M., Cavalié, O., Tavera, H., Baby, P., Chire-Chira, J., & Nocquet, J. M. (2016). Active tectonics of Peru: Heterogeneous interseismic coupling along the Nazca megathrust, rigid motion of the Peruvian Sliver, and

Subandean shortening accommodation. *Journal of Geophysical Research: Solid Earth*, *121*(10). https://doi.org/10.1002/2016JB013080

Zheng, Y.-F., & Zhao, Z.-F. (2003). Calculation of oxygen isotope fractionation in magmatic rocks. *Chemical Geology*, *193*(1–2).

CHAPTER 6

CONCLUSIONS

The preceding four chapters encompass a unique combination of geochemical investigations that analyze volatile cycling and metasomatism in two instances of flat slab subduction in the central Andes. This work trades space for time by investigating both modern and ancient flat-slab settings, affording study of fluid-lithosphere interaction ranging from the surface to the deep mantle, and bridging the time from active shallow subduction to 25 Ma after. Below I individually summarize the key conclusions from the geochemical survey of thermal springs, which detail the modern signature of mantle and crustal degassing in active and ancient flat-slab settings of central and Southern Peru (Chapters 2 and 3), and geochemical analyses from xenoliths and Quaternary lavas, which serve to record of the influence of flat-slab subduction in the deep lithosphere in the ancient flat-setting of southern Peru (Chapters 4 and 5). Finally, I incorporate these ideas into a wholistic set of conclusions and reflect on their implications for continental tectonics.

INSIGHT FROM THERMAL SPRINGS IN A MODERN FLAT-SLAB SETTING

Mantle volatile emissions observed in thermal springs across the Peruvian Andes provide evidence for ongoing slab-to-lithosphere fluid transfer and continental hydration in an active flat-slab setting. Our analyses of He, CO_2, and N_2 geochemical systematics reveal both mantle and crustal volatile contributions in thermal spring gases throughout our study area. In the absence of recent magmatism, mantle volatile fluxes are best explained by slab-derived fluids mobilizing volatiles from the lithospheric mantle

through ongoing metasomatic reactions. Assuming binary mixing between crustal helium and a lithospheric mantle source, $^{3}He/^{4}He$ ratios ranging from 0.26 to 2.40 R_C/R_A imply 4 – 39 % mantle-derived helium present in thermal spring gases. Relationships between $\delta^{13}C$ of CO_2 and dissolved inorganic carbon and $^{3}He/^{4}He$ evidences a prominent mantle CO_2 component that is overprinted by crustal sources, with concentrations of deeply sourced carbon in some thermal springs that are comparable to springs from the volcanic region of central Italy (Chiodini et al., 2004). Similarly, coupled δN - N_2/He systematics imply a modest mantle N_2 contribution overprinted by sedimentary N_2 sources. Mantle volatile fluxes require persistent replenishment of fluids to the base of the continental lithosphere and implicate the existence of hydrated pathways to promote sustained deep fluid transport through the thick Andean lithosphere. Mantle volatile signatures are overprinted by crustal degassing, reflecting dilution and mixing with crustal fluids that inform on mantle-to surface volatile transit times and the influence of tectonism in the subducting slab and continental lithosphere. The time dependent ingrowth of radiogenic ^{4}He during ascent of mantle fluids through continental crust suggests minimum mantle to surface transit times ranging from 648 ka to 1.03 Ma. Corresponding estimates of vertical continuous flow rates are 49 – 771 mm/year, which are up to five times higher than flow rates calculated for mantle fluids transiting major strike-slip fault systems (e.g., Newell et al., 2023). Regional variability in $^{3}He/^{4}He$ ratios reflects the influence of slab morphology and continental tectonics over fluid productivity and mobility and provides a novel means to study these processes. For example, elevated $^{3}He/^{4}He$ ratios observed above a suspected tear in the Nazca slab imply increased slab dehydration or partial melting of in response to asthenosphere interaction with the tearing slab, confirming the

existence of this enigmatic feature.

Unexpectedly similar mantle volatile signatures are observed in the volcanically active backarc region of Southern Peru, where an episode of shallow subduction occurred in the Oligocene. This observation implies ongoing fluid production in the lithospheric mantle, either released during crystallization of partial melts at depth or during dehydration reactions in the SCLM and lower crust, with both processes being expected consequences of hydrated lithosphere re-equilibrating with asthenosphere after episodes of flat-slab subduction.

Geochemical modelling of carbon sources across the spring transect are used to distinguish deep CO_2 sources from CO_2 derived through carbonate dissolution in geothermal systems, affording a quantitative estimate of atmospheric carbon fluxes resulting from crustal and mantle degassing. The resulting carbon flux from analyzed springs with available discharge measurements is $3x10^8$ mol yr^{-1}. When scaled to all reported thermal springs in Peru, these results imply a total CO_2 emissions from Peruvian thermal springs that may approach $2x10^9$ mol yr^{-1}, or ~0.2 % of global emissions from subaerial volcanism. Regional CO_2 emissions may be 10 to 100 times greater when considering CO_2 diffusely lost along fault zones or temporarily dissolved near-surface aquifers. Considering that flat slab subduction constitutes ~10% of the modern global subduction system, this research affirms that amagmatic CO_2 fluxes from volcanic gaps associated with flat slab subduction are a critical and underappreciated piece of the global geologic carbon cycle.

INSIGHT FROM XENOLITHS AND ALKALINE LAVAS IN AN ANCIENT FLAT-SLAB SETTING

Geochemical analysis of xenolith and potassic basalts in the northern Altiplano Plateau converge on the conclusion that a portion of the lithospheric mantle in this region has been chemically modified through subduction-derived melt metasomatism, with geodynamic considerations and the timing of potassic volcanism linking metasomatism with Oligocene shallow subduction. Kersantite xenoliths share similar major and trace element characteristics with Neogene-Quaternary potassic basalts in the region, including high MgO, K_2O and P_2O_5 and incompatible trace elements. Abundant phlogopite in these samples afford hydrogen isotope analyses that yield δD values that are distinct from mantle hydrogen and consistent with H_2O sourced from slab-derived fluids or melts. Calcite- and phlogopite-bearing orthopyroxenite and harzburgite xenoliths show chemical and textural evidence for metasomatism by high-K siliceous melts, consistent with the inferred mantle source of potassic basaltic volcanism. Calcite $\delta^{13}C$ and $\delta^{18}O$ values suggest that carbon was sourced from subducted marine carbonates, and trace element patterns are indicative of slab-derived fluid enrichment, collectively implicating melts of subducted sediments as a metasomatizing agent. Abundant carbon and fluorine in mantle xenoliths provides valuable insight into volatile enrichment of the lithospheric mantle during shallow subduction, with implications for weakened rheology, carbon cycling, and the generation of critical mineral-bearing magmatism.

An analysis of new and previously reported compositions of Quaternary Rumicolca Formation volcanics in the northern Altiplano region reveal a bimodal distribution of potassic basalts (*sensu lato*; including lamprophyres, lamproites, and

shoshonites) and intermediate alkaline and calc-alkaline lavas (including latites, andesites, and dacites). Overlapping trace element characteristics in both suites, and observations of mantle xenoliths in the intermediate suite, preclude previous assumptions that intermediate lavas are derived through differentiation or contamination of basaltic melts. Instead, these observations inspire a model in which intermediate lavas represent melts of subducted sediments/mélange material. A portion of these silicic alkaline melts experienced limited interaction with mantle peridotites through some combination of high melt-rock ratios, migration through previously modified mantle, and/or rapid ascent through the oblique extensional Cusco-Vilconata Fault system. In this model, potassic basaltic melts are formed through metasomatic reactions between silicic melts and mantle peridotite, and phlogopite- and orthopyroxene- enriched peridotite is left as the residual mantle lithology. I conclude that subducted crustal material was transferred to the base of the lithosphere during shallow subduction, and that subsequent melting of accreted sediments was triggered first by the opening of the mantle wedge at the end of the Oligocene and again by the arrival of a mantle thermal anomaly in the Quaternary. Active volcanism is localized along the Cusco Vilconata Fault system, but melting of accreted sediments and subsequent metasomatism in the lithospheric mantle is likely widespread, which is supported by the presence of mantle volatiles in thermal springs throughout this region.

IMPLICATIONS FOR CONTINENTAL TECTONICS

Results from the geochemical survey of Peruvian springs represents the first direct observations of slab-to-lithosphere fluid transfer and metasomatism in a modern flat-slab setting. This conclusion lends support to models of fluid transfer and continental

hydration resulting from flat slab subduction (Humphreys et al., 2003; Jones et al., 2015), extends these ideas to the Andean Cordillera, and provides a novel means to investigate these enigmatic tectonic systems. Mantle volatile fluxes implicate vertically extensive hydrated flow paths through the entire lithospheric column, and their ubiquitous presence across the study area demonstrate the laterally extensive nature of fluid transfer both parallel and perpendicular to the continental margin. These results affirm that hydration and metasomatism can extend far into the continental lithosphere, enabling phase changes that can increase crustal and mantle buoyancy and lead to surface uplift (e.g., Jones et al., 2015). Extensive fluid advection during shallow subduction, together with advection of fluids and melts following the return to steeper subduction, also has implications for the thermal state and buoyancy of the continental lithosphere (Berry et al., 2022). The conclusion that tectonic features such as slab tears locally amplify fluid transfer or potentially allow for localized melt infiltration in an otherwise amagmatic flat slab setting has implications for chemical heterogeneity in the lithospheric mantle and enigmatic magmatic patterns, for example supporting models that propose a similar origin to the Colorado Mineral Belt in the Western U.S. Cordillera (Chapin, 2012).

Volcanism and mantle degassing in the northern Altiplano region highlight the protracted influence of flat-slab subduction in a continental margin, and xenoliths provide a valuable window into resulting chemical evolution of the lithospheric mantle. The interpretation that Neogene-Quaternary basaltic volcanism, and by extension the associated ignimbrite volcanism, occurred in response to the Oligocene episode of shallow subduction draws parallels with the Cenozoic “ignimbrite flare-up” in the Western U.S. (Humphreys et al., 2003; Farmer et al., 2008). Furthermore, this work

expands upon these ideas by demonstrating that shallow subduction can lead to tectonic underplating of slab material that participates in melting following shallow subduction. Evidence for melt-metasomatism and the generation of phlogopite- and orthopyroxene-rich mantle lithologies helps to constrain the compositional and rheologic evolution of the lithospheric mantle, which is an important step for refining geodynamic and geochemical models of continental lithosphere globally.

A recent model for the tectonic evolution of the Altiplano-Puna Plateau highlights a systematic southward progression of magmatic patterns, exhumation of the Eastern Cordillera, and sedimentation that ultimately link orogenic widening and the establishment of the Altiplano-Puna Plateau to the southward migration of shallow subduction (Saylor et al., 2023). This models proposes that shallow subduction set the stage for plateau formation through hydration and weakening of the Eastern Cordillera lithosphere, enabling ductile shortening in the lower crust and upper mantle and facilitating subsequent mantle delamination or convective removal in the central and southern plateau. Results from this work provide direct support for this link between shallow subduction, lithospheric weakening, and plateau development. Furthermore, these results provide additional mechanisms that explain the nature of lithospheric weaking, showing that shallow subduction not only leads to continental hydration, but also infiltration of potassic siliceous melts that consume olivine and precipitate enstatite and phlogopite in the lithospheric mantle. Mantle enrichment of phlogopite may be especially pertinent to models of deformation and surface uplift considering its relatively low density (2.7 g/cm, as opposed to 3.22 g/cm for forsterite) and its expectedly weaker rheology. Although no experimental data constrain the rheologic effect of phlogopite

crystallization in peridotite, evidence from mantle xenoliths presented in this study suggests that phlogopite can indeed participate in mantle deformation.

REFERENCES

Berry, M.A., Lowry, A.R., Ma, X., Kanda, R.V.S., and Schutt, D.L., 2022, Wet roots of high elevation in the western United States: Earth and Planetary Science Letters, v. 584, doi:10.1016/j.epsl.2022.117483.

Chapin, C.E., 2012, Origin of the Colorado Mineral Belt: Geosphere, v. 8, p. 28–43, doi:10.1130/GES00694.1.

Chiodini, G., Cardellini, C., Amato, A., Boschi, E., Caliro, S., Frondini, F., and Ventura, G., 2004, Carbon dioxide Earth degassing and seismogenesis in central and southern Italy: Geophysical Research Letters, v. 31, p. n/a-n/a, doi:10.1029/2004GL019480.

Farmer, G.L., Bailley, T., and Elkins-Tanton, L.T., 2008, Mantle source volumes and the origin of the mid-Tertiary ignimbrite flare-up in the southern Rocky Mountains, western U.S.: Lithos, v. 102, p. 279–294, doi:10.1016/j.lithos.2007.08.014.

Humphreys, E., Hessler, E., Dueker, K., Farmer, G.L., Erslev, E., and Atwater, T., 2003, How Laramide-Age Hydration of North American Lithosphere by the Farallon Slab Controlled Subsequent Activity in the Western United States: International Geology Review, v. 45, p. 575–595, doi:10.2747/0020-6814.45.7.575.

Jones, C.H., Mahan, K.H., Butcher, L.A., Levandowski, W.B., and Farmer, G.L., 2015, Continental uplift through crustal hydration: Geology, v. 43, p. 355–358, doi:10.1130/G36509.1.

Newell, D.L., Benowitz, J.A., Regan, S.P., and Hiett, C.D., 2023, Roadblocks and speed limits: Mantle-to-surface volatile flux through the lithospheric-scale Denali fault, Alaska: Geology, v. 51, p. 576–580, doi:10.1130/G51068.1.

Saylor, J.E., Sundell, K.E., Perez, N.D., Hensley, J.B., McCain, P., Runyon, B., Alvarez, P., Cárdenas, J., Usnayo, W.P., and Valer, C.S., 2023, Basin formation, magmatism, and exhumation document southward migrating flat-slab subduction in the central Andes: Earth and Planetary Science Letters, v. 606, p. 118050, doi:10.1016/J.EPSL.2023.118050.

APPENDICES

APPENDIX A

Supporting Information for Chapter 2

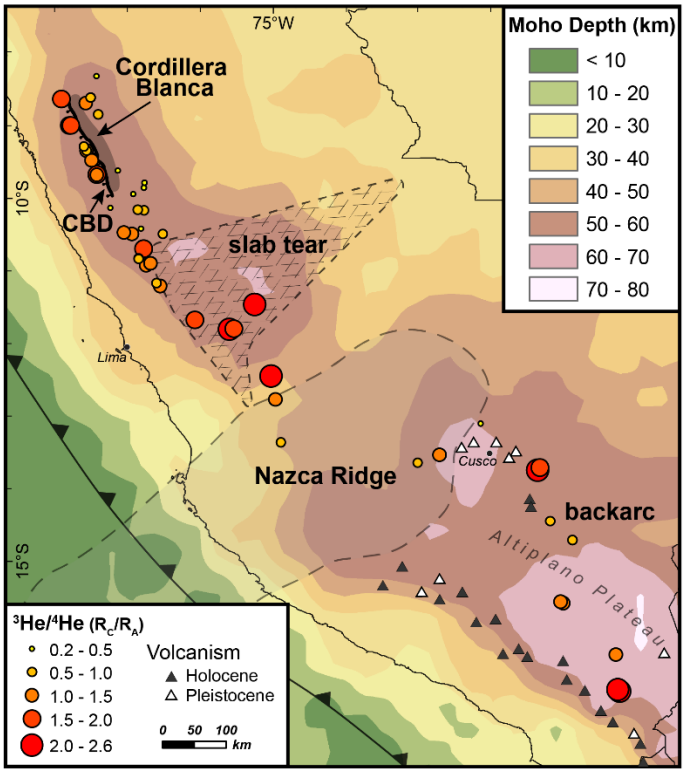

Supplementary Figure A.1. $^{3}He/^{4}He$ ratios (reported as R_C/R_A) from thermal springs in southern Peru overlain on a map of Moho depth. Contours of Moho depth were derived from an inverse distance weighting interpolation of data points provided by Bishop et al. (2017) and references therein. No clear relationship is observed between $^{3}He/^{4}He$ ratios and crustal thickness, suggesting that this is not a primary control on the observed data pattern.

Supplementary Table A1. Helium isotope data for Peruvian thermal springs, including helium concentrations and gas ratios.

Sample ID	sample type	R_A	X[a]	R_C/R_A[b] (± 1σ)	$CO_2/^3He$	TDIC (mol/kgH_2O)	$[^4He]_M$ (cm^{3}STP/gH_2O)	$[^4He]_C$[c] (cm^{3}STP/gH_2O)	He/Ne
Flat slab									
DNCB17-2	water	0.88	8.36	0.86 ± 0.03	4.51E+11	4.60E-03	2.36E-07	2.08E-07	2.63
DNCB17-6	water	1.10	34	1.10 ± 0.04	3.84E+10	3.33E-03	1.42E-06	1.38E-06	10.69
DNCB17-7b	water	0.64	4.89	0.55 ± 0.02	4.33E+11	1.58E-03	1.46E-07	1.16E-07	1.52
DNCB17-9	water	0.63	5.81	0.55 ± 0.02	4.95E+11	2.18E-03	1.69E-07	1.40E-07	1.81
DNCB17-13	water	0.36	184	0.35 ± 0.01	7.79E+10	1.05E-02	6.70E-06	6.66E-06	54.19
DNCB17-21	water	0.34	158	0.34 ± 0.01	7.37E+10	9.08E-03	6.43E-06	6.39E-06	49.51
DNCB17-24	water	1.01	10.3	0.26 ± 0.01	3.51E+11	1.64E-03	3.46E-07	3.12E-07	3.39
DNCB17-25	water	0.33	13.3	0.33 ± 0.01	1.08E+13	1.42E-02	7.61E-08	7.04E-08	4.34
DNCB17-30	water	0.37	42.5	0.35 ± 0.01	1.34E+12	1.67E-02	6.35E-07	6.20E-07	13.33
DNCB17-36	water	0.54	12	0.46 ± 0.02	1.64E+11	2.79E-03	7.02E-07	6.44E-07	3.74
DNCB17-37	water	0.57	21.4	0.55 ± 0.02	2.47E+11	4.45E-03	6.04E-07	5.76E-07	6.98
DNCB17-38	water	0.38	59.3	0.53 ± 0.02	3.06E+10	5.01E-03	5.44E-06	5.35E-06	19.89
DN18AP-01	water	0.89	1.65	0.71 ± 0.02	2.81E+13	2.23E-02	4.94E-08	1.94E-08	0.55
DN18AP-02	gas	0.82	2.83	0.72 ± 0.03	1.54E+16	5.71E-02	1.40E-10	9.03E-11	0.68
DN18AP-03	water	1.29	181	1.29 ± 0.03	7.93E+09	4.51E-03	7.77E-06	7.72E-06	53.61
DN18AP-05	gas	0.56	5.66	0.47 ± 0.02	8.24E+16	5.35E-02	2.94E-11	2.42E-11	1.48
DN19CP-11	water	1.18	85.5	1.18 ± 0.04	4.12E+10	7.89E-03	2.87E-06	2.84E-06	28.18
DN19CP-14	gas	0.45	5.09	0.32 ± 0.01	5.02E+11	1.27E-03	1.72E-07	1.38E-07	1.74
DN19CP-20	water	0.99	0.904	0.99 ± 0.04[†]	1.76E+12	3.08E-03	3.10E-08[†]	3.10E-08	0.28
DN19CP-30	water	2.39	187	2.40 ± 0.08	2.45E+10	1.63E-02	4.86E-06	4.84E-06	59.27
DN19CP-31	water	1.45	1.05	1.45 ± 0.05[†]	9.42E+12	1.89E-02	2.42E-08[†]	2.42E-08	0.35
slab tear region									
DN19CP-1	water	1.21	36.3	1.21 ± 0.04	8.22E+10	5.32E-03	9.60E-07	9.33E-07	11.73

Sample ID	sample type	R_A	X[a]	R_C/R_A[b] (± 1σ)	$CO_2/^3He$	TDIC (mol/kgH_2O)	$[^4He]_M$ (cm^{3}STP/ gH_2O)	$[^4He]_C$[c] (cm^{3}STP/ gH_2O)	He/Ne
DN19CP-02	water	1.25	38.5	1.26 ± 0.04	7.68E+10	5.49E-03	1.02E-06	9.96E-07	12.44
DN19CP-04	gas	1.37	68.7	1.38 ± 0.05	6.30E+11	2.42E-02	4.95E-07	4.88E-07	19.87
DN19CP-05	water	0.83	22.9	0.82 ± 0.03	1.22E+12	1.67E-02	3.04E-07	2.91E-07	7.00
DN19CP-06	gas	0.77	171	0.77 ± 0.03	1.23E+13	2.95E-02	5.52E-08	5.48E-08	49.21
DN19CP-08	gas	1.55	667	1.55 ± 0.06	3.25E+12	2.73E-02	9.45E-08	9.44E-08	203.61
DN19CP-10	gas	0.90	1590	0.90 ± 0.03	3.91E+12	2.39E-02	1.19E-07	1.19E-07	506.31
DN19CP-24	gas	1.37	1.98	1.74 ± 0.06	3.34E+13	2.84E-02	1.73E-08	8.58E-09	0.64
DN19CP-26	gas	2.06	278	2.07 ± 0.08	1.13E+13	5.19E-02	3.89E-08	3.87E-08	80.38
DN19CP-27	gas	1.68	7850	1.68 ± 0.06	9.40E+12	4.90E-02	5.43E-08	5.43E-08	2199.31
DN19CP-34	gas	1.85	5.42	2.04 ± 0.08	4.49E+13	5.12E-02	1.20E-08	9.77E-09	1.40
DN19CP-38	water	0.83	1.77	0.60 ± 0.02	4.87E+13	1.96E-02	2.69E-08	1.17E-08	0.57
DN19CP-39	gas	1.06	61.8	1.06 ± 0.04	1.97E+12	1.76E-02	1.50E-07	1.48E-07	21.05
*CBD fault zone & adjacent hanging wall**									
DN13CB05	water	1.05	5.43	1.06 ± 0.24	1.03E+13	3.82E-02	7.08E-08	5.77E-08	1.87
DN13CB06	water	1.80	36.9	1.82 ± 0.55	3.91E+13	4.16E-02	9.89E-09	9.63E-09	12.72
DN13CB07	water	0.70	5.07	0.62 ± 0.17	2.73E+13	1.98E-02	2.40E-08	1.93E-08	1.69
DN13CB08a	water	1.24	3.65	1.33 ± 0.31	4.22E+12	1.03E-02	4.18E-08	3.03E-08	1.21
DN13CB08b	water	0.90	3.51	0.85 ± 0.24	1.92E+13	2.36E-02	3.32E-08	2.38E-08	1.16
DN13CB09	water	1.27	13.2	1.30 ± 0.30	2.44E+12	1.96E-02	1.10E-07	1.02E-07	4.40
DN13CB11g	gas	1.95	36.7	1.98 ± 0.40	-	-	-	-	12.27
DN13CB11w	water	1.66	5.28	1.81 ± 0.46	6.85E+12	1.90E-02	3.13E-08	2.53E-08	1.73
DN13CB14	water	1.78	53.7	1.79 ± 0.40	6.09E+11	1.26E-02	1.94E-07	1.90E-07	16.53
Backarc									
DN18AP-06	gas	2.39	12.5	2.51 ± 0.09	1.42E+12	1.33E-02	7.09E-08	6.52E-08	3.80

Sample ID	sample type	R_A	X[a]	R_C/R_A[b] (± 1σ)	$CO_2/^3He$	TDIC (mol/kgH_2O)	$[^4He]_M$ (cm^{3}STP/ gH_2O)	$[^4He]_C$[c] (cm^{3}STP/ gH_2O)	He/Ne
DN18AP-07	gas	1.94	221	1.94 ± 0.07	4.52E+12	2.27E-02	4.54E-08	4.52E-08	63.33
DN18AP-08	gas	0.90	25.5	0.90 ± 0.03	3.56E+14	3.46E-02	1.97E-09	1.89E-09	7.24
DN18AP-09	gas	0.96	1.82	0.92 ± 0.03	6.06E+13	5.35E-02	3.73E-08	1.68E-08	0.45
DN18AP-10	water	1.13	7.9	1.15 ± 0.03	3.95E+13	2.61E-02	1.15E-08	1.00E-08	2.61
DN18AP-11	gas	1.35	2110	1.35 ± 0.05	6.16E+10	7.72E-03	1.63E-06	1.63E-06	653.36
DN18AP-12	gas	1.34	1950	1.34 ± 0.05	4.00E+10	7.49E-03	2.45E-06	2.44E-06	583.02
DN18AP-13	gas	2.30	59.6	2.32 ± 0.08	3.49E+12	2.33E-02	5.14E-08	5.05E-08	17.73
DN18AP-14	gas	2.51	269	2.52 ± 0.09	2.16E+12	2.65E-02	8.54E-08	8.51E-08	75.48

* previously reported analyses described in Newell et al. (2015)

† value uncorrected for air contamination due to X<1.5

[a] $X = (He/Ne)_{measured} / (He/Ne)_{air} \times ß_{Ne}/ß_{He}$; ß = Bunsen coefficient from (Weiss, 1971): groundwater recharge temperature of 5 – 25 °C depending on altitude

[b] corrected for air contamination using $R_C/R_A = [(R_A \times X) - 1] / (X - 1)$

[c] dissolved He concentrations are air corrected using $[He]_C = [He]_M \times (X - 1) / X$

Supplementary Table A2. Raw He and Ne gas concentrations and conversion factors used to calculate dissolved gas concentrations.

Sample ID	$[^4He]_M$ (cm^3/cm^3)	[Ne] (cm^3/cm^3)	P[a] (atm)	I[b] (mol/kgH_2O)	K_m^{He} [c] (kgH_2O/mol)	K_m^{Ne} [c] (kgH_2O/mol)	H^{cp} *He* [d] (mol/L/atm)	H^{cp} *Ne* [d] (mol/L/atm)
Flat slab								
DN18AP-02	2.02E-08	2.65E-08	0.81	1.43E-01	0.222	0.238	3.48E-04	3.87E-04
DN18AP-05	5.12E-09	3.17E-09	0.66	9.70E-02	0.222	0.234	3.55E-04	3.88E-04
DN19CP-14	3.37E-05	1.95E-05	0.57	4.08E-03	0.238	0.231	3.65E-04	3.62E-04
slab tear region								
DN19CP-04	7.86E-05	3.67E-06	0.71	5.15E-02	0.222	0.235	3.63E-04	3.91E-04
DN19CP-06	8.15E-06	1.61E-07	0.77	4.50E-02	0.228	0.229	3.60E-04	3.71E-04
DN19CP-08	1.58E-05	7.42E-08	0.68	5.99E-02	0.225	0.230	3.59E-04	3.74E-04
DN19CP-10	2.05E-05	3.97E-08	0.66	3.83E-02	0.231	0.229	3.60E-04	3.67E-04
DN19CP-24	3.34E-06	4.89E-06	0.59	6.42E-02	0.222	0.233	3.60E-04	3.85E-04
DN19CP-26	6.87E-06	7.55E-08	0.65	1.11E-01	0.225	0.254	3.57E-04	4.04E-04
DN19CP-27	9.26E-06	3.59E-09	0.64	4.91E-02	0.231	0.270	3.72E-04	4.36E-04
DN19CP-34	1.72E-06	1.06E-06	0.80	1.23E-01	0.228	0.263	3.56E-04	4.10E-04
DN19CP-39	2.79E-05	1.34E-06	0.61	3.21E-02	0.240	0.232	3.58E-04	3.55E-04
Backarc								
DN18AP-06	1.48E-05	3.86E-06	0.57	9.94E-02	0.241	0.232	3.45E-04	3.49E-04
DN18AP-07	8.93E-06	1.33E-07	0.58	4.52E-02	0.226	0.230	3.61E-04	3.84E-04
DN18AP-08	3.83E-07	5.01E-08	0.60	8.96E-02	0.227	0.229	3.52E-04	3.72E-04
DN18AP-09	6.91E-06	1.28E-05	0.61	9.53E-02	0.236	0.281	3.64E-04	4.42E-04
DN18AP-11	3.58E-04	5.55E-07	0.57	1.77E-01	0.254	0.239	3.26E-04	3.22E-04
DN18AP-12	5.29E-04	8.90E-07	0.57	1.76E-01	0.238	0.231	3.32E-04	3.38E-04
DN18AP-13	1.16E-05	6.28E-07	0.55	2.16E-01	0.232	0.229	3.27E-04	3.40E-04
DN18AP-14	1.75E-05	2.11E-07	0.55	6.67E-02	0.222	0.235	3.61E-04	3.98E-04

Partial pressures used in equation (1) are calculated by multiplying the fractional gas concentration by total atmospheric pressure

[a] Total atmospheric pressure calculated from spring elevation

[b] Ionic strength of spring water from geochemical modelling in PHREEQC (Parkhurst and Appelo, 2013)

[c] Tempurature dependent Sechenov (salting) parameters calculated from the emperical relationships presented in Smith and Kennedy (1983)

[d] Henery's law coefficients as a function of tempurature and salinity. Tempurature dependence calculated using the van't Hoff equation and constants presented in Sander (2015). Salting-out coefficient (i.e. H^{cp}/H_0^{cp}, where H_0^{cp} is the Henry's law coeficient in pure water) is calculated as $\log(H^{cp}/H_0^{cp}) = \log(\alpha/\alpha_0) = -K_m*I$ (where α is the Bunsen coefficient; Sander, 2015; Smith and Kennedy, 1982)

Supplementary Table A.3. Relative gas abundances in Peruvian thermal springs.

Sample ID	CO_2	He	H_2	Ar	O_2	N_2	CH_4	CO	total
					(mol %)				
Flat slab									
DNCB17-2*	44.242	-	0.000	-	-	51.238	0.187	0.000	95.67
DNCB17-6	38.928	0.544	0.046	1.618	2.236	56.226	0.402	0.000	100.00
DNCB17-7b	53.387	0.000	0.039	0.857	4.051	40.948	0.718	0.000	100.00
DNCB17-13	76.641	0.000	0.031	0.593	1.102	21.597	0.036	0.000	100.00
DNCB17-21	48.797	0.282	0.331	0.919	0.790	48.870	0.010	0.000	100.00
DNCB17-24*	23.301	-	0.000	-	-	69.218	1.511	0.000	94.03
DNCB17-25	95.386	0.093	0.004	0.092	0.789	3.614	0.022	0.000	100.00
DNCB17-30	87.200	0.103	0.019	0.340	0.682	11.638	0.018	0.000	100.00
DNCB17-32*	89.409	-	0.026	-	-	8.545	0.068	0.000	98.05
DN18AP-02	51.158	0.039	0.142	0.610	8.917	39.135	0.000	0.000	100.00
DN18AP-05	44.073	0.040	0.166	0.638	10.621	44.462	0.000	0.000	100.00
DN19CP-11	1.406	0.011	0.000	0.961	21.401	76.221	0.000	0.000	100.00
DN19CP-14	4.031	0.006	0.000	1.559	0.007	93.715	0.679	0.000	100.00
DN19CP-30	7.891	0.020	0.000	0.932	18.863	72.294	0.000	0.000	100.00
DN19CP-31*	29.375	-	0.000	-	-	56.667	0.000	0.000	86.04
slab tear region									
DN19CP-01	49.852	0.054	0.000	1.908	3.104	44.005	1.051	0.000	99.97
DN19CP-02*	9.141	-	0.000	-	-	75.307	0.045	0.000	84.49
DN19CP-05	17.455	0.047	0.000	0.986	18.132	63.066	0.000	0.315	100.00
DN19CP-8	89.119	0.012	0.000	0.193	0.337	10.190	0.149	0.000	100.00
DN19CP-10	91.672	0.010	0.000	0.123	0.514	7.530	0.096	0.054	100.00
DN19CP-24	88.517	0.003	0.000	0.307	0.453	10.581	0.138	0.000	100.00
DN19CP-26	90.094	0.005	0.000	0.183	0.326	9.203	0.076	0.112	100.00
DN19CP-34	68.749	0.026	0.000	0.565	0.342	30.314	0.002	0.002	100.00

Sample ID	CO_2	He	H_2	Ar	O_2	N_2	CH_4	CO	total
					(mol %)				
DN19CP-38	83.147	0.009	0.000	0.333	2.775	13.734	0.002	0.001	100.00
DN19CP-39	69.004	0.020	0.000	0.685	0.193	29.055	1.038	0.000	100.00
CBD fault zone & adjacent hanging wall									
DNCB15-07	93.658	0.180	0.102	0.083	0.624	5.343	0.001	0.010	100.00
DNCB15-08	74.948	0.032	0.211	0.378	0.491	23.919	0.010	0.011	100.00
DNCB15-9B	10.690	0.047	0.044	2.212	0.538	86.467	0.003	0.000	100.00
DNCB15-11	17.222	0.085	0.033	1.910	0.112	80.639	0.000	0.000	100.00
DNCB15-12	96.050	0.439	0.004	0.167	0.354	2.968	0.019	0.000	100.00
Backarc									
DN18AP-06	66.586	0.051	0.158	0.316	5.040	27.184	0.666	0.000	100.00
DN18AP-07	89.727	0.007	0.569	0.136	0.535	8.840	0.141	0.045	100.00
DN18AP-08	96.954	0.003	0.020	0.003	0.481	2.494	0.045	0.000	100.00
DN18AP-09	20.875	0.001	0.009	0.737	17.603	60.773	0.000	0.000	100.00
DN18AP-11	66.464	0.165	0.249	0.222	0.439	32.387	0.074	0.000	100.00
DN18AP-12	49.109	0.103	0.184	0.450	4.453	45.647	0.054	0.000	100.00
DN18AP-13	78.589	0.007	0.063	0.177	0.645	20.323	0.196	0.000	100.00
DN18AP-14	90.057	0.009	0.226	0.090	0.233	9.325	0.060	0.000	100.00

*gas chromatograph data only

Supplementary Table A.4. Peruvian thermal spring locations and field parameters.

Spring	Sample ID	Latitude	Longitude	Elevation (m)	T (°C)	pH	Conductivity (µS)
Flat slab							
Pomabamba laundry	DNCB17-2	-8.8260	-77.4600	2910	50.5	6.62	-
Chilhuan	DNCB17-6	-8.6720	-77.6340	3304	36.5	7.02	-
Rupac	DNCB17-7b	-8.5960	-77.5680	2360	63.8	6.04	200
Rupac	DNCB17-9	-8.5950	-77.5660	2443	61.5	6.18	230
Jocos Peinado	DNCB17-13	-8.2950	-77.4880	1591	40.6	6.31	3332
Chavin	DNCB17-21	-9.6110	-77.1820	3214	41.0	7.47	1406
Conococha	DNCB17-24	-10.1290	-77.2890	4026	28.0	7.98	233
Azulmina	DNCB17-25	-9.9380	-76.9630	3870	70.7	5.96	1452
Taurimpampa	DNCB17-30	-9.8470	-76.8170	3244	45.3	6.24	1387
Banos (Batan)	DNCB17-32	-10.0480	-76.7220	3390	64.7	5.71	940
Conoc (La Union)	DNCB17-36	-9.7810	-76.8050	3175	42.2	6.68	377
Machaycancha	DNCB17-37	-10.1640	-76.8110	3835	44.6	6.40	568
Janac	DNCB17-38	-10.1540	-76.9020	4343	51.5	6.48	720
Licapa	DN18AP-01	-13.3689	-74.8778	4103	20.2	6.53	1312
Santo Tomás	DN18AP-02	-13.6525	-72.9448	1693	39.9	6.12	11310
Ccónocc	DN18AP-03	-13.5431	-72.6387	1850	31.8	6.84	3260
Lares	DN18AP-05	-13.1107	-72.0545	3281	45.4	5.96	7170
Macanacoto	DN19CP-11	-10.4911	-76.5472	3404	27.4	6.62	2490
Pumarinri	DN19CP-14	-10.4201	-76.8584	4358	68.4	6.63	295
Conoc (Oyon)	DN19CP-20	-10.4744	-77.0953	2237	51.4	7.53	2110
Aguas Calientes	DN19CP-30	-12.4576	-75.0199	3017	22.6	6.89	1342
Huancavelica	DN19CP-31	-12.7815	-74.9557	3671	26.3	6.78	1203
slab tear region							
Picoy	DN19CP-01	-10.9019	-76.7212	3262	57.0	6.35	1948

Spring	Sample ID	Latitude	Longitude	Elevation (m)	T (°C)	pH	Conductivity (µS)
Huancahuasi	DN19CP-02	-10.9000	-76.7209	3252	61.8	6.33	1942
Huancachin	DN19CP-04	-10.9300	-76.7803	2760	43.9	6.02	3590
Banos de Fierro	DN19CP-05	-10.8321	-76.8892	2169	47.9	5.86	2920
Banos de Tingo	DN19CP-06	-10.8377	-76.8918	2143	57.2	5.90	4250
Rupay	DN19CP-08	-10.6952	-76.8208	3043	53.3	6.23	4290
Tambochaca	DN19CP-10	-10.4911	-76.5471	3311	60.9	6.35	3610
Yuali	DN19CP-24	-11.6822	-76.0941	4168	45.9	6.20	5640
Acaya	DN19CP-26	-11.8130	-75.6057	3452	28.9	6.13	8170
Huajal	DN19CP-27	-11.8061	-75.5449	3479	20.9	6.11	3170
Uchubamba	DN19CP-34	-11.4682	-75.2510	1819	24.3	6.18	8770
Santa Catallina	DN19CP-38	-11.1740	-76.6370	3109	40.1	6.49	4074
San Jose de Banos	DN19CP-39	-11.2145	-76.5848	3839	70.1	5.80	2161
CBD fault zone & adjacent hanging wall							
Olleros	DN13CB05	-9.6683	-77.4626	3453	20.4	6.65	23200
Olleros	DN13CB06	-9.6673	-77.4633	3432	47.8	6.49	21500
Merced	DN13CB07	-9.2591	-77.6119	3002	38.4	5.03	723
Chancos	DN13CB08a	-9.3196	-77.5752	2863	47.6	6.22	6020
Chancos	DN13CB08b	-9.3196	-77.5752	2863	47.6	6.22	6020
Monterrey	DN13CB09	-9.4684	-77.5354	2989	46.4	5.89	6240
Huancarhuaz	DN13CB11g	-8.9437	-77.7846	2721	73.3	6.22	5120
Huancarhuaz	DN13CB11w	-8.9437	-77.7846	2721	73.3	6.22	5120
Aquilina	DN13CB14	-8.6129	-77.8836	1930	78.3	6.26	2130
Huancarhuaz	DNCB15-7	-8.9437	-77.7846	2721	73.3	6.22	5120
Huancarhuaz	DNCB15-08	-8.9415	-77.7853	2721	69.9	6.40	5750
Aqulina	DNCB15-9b	-8.6129	-77.8836	1884	78.3	6.26	2130
Aticara	DNCB15-11	-8.6125	-77.8836	2662	78.0	6.40	170
Pumapampa	DNCB15-12	-9.8803	-77.2864	4185	19.2	5.95	3970

Spring	Sample ID	Latitude	Longitude	Elevation (m)	T (°C)	pH	Conductivity (µS)
Backarc							
Upis	DN18AP-06	-13.7501	-71.2752	4418	71.0	6.54	9010
Pacchanta	DN18AP-07	-13.7174	-71.2420	4308	54.2	5.96	3270
La Raya	DN18AP-08	-14.4507	-71.0730	4054	56.4	6.09	7020
Pichacani-Santa Rosa	DN18AP-09	-14.7090	-70.7544	3931	16.6	6.15	6760
Collpa Apacheta	DN18AP-10	-16.2676	-70.1422	4106	54.0	5.98	4820
Pinaya	DN18AP-11	-15.5667	-70.8866	4386	80.5	6.15	15160
Pinaya	DN18AP-12	-15.5669	-70.8877	4379	68.5	6.09	14610
Crucero	DN18AP-13	-16.7418	-70.1165	4572	62.0	5.98	18760
Punta Perdida-Pastogrande	DN18AP-14	-16.7626	-70.0893	4614	43.2	5.31	6290

References

Bishop, B.T., Beck, S.L., Zandt, G., Wagner, L., Long, M., Antonijevic, S.K., Kumar, A., and Tavera, H., 2017, Causes and consequences of flat-slab subduction in southern Peru: Geosphere, v. 13, p. 1392–1407, doi:10.1130/GES01440.1.

Newell, D.L., Jessup, M.J., Hilton, D.R., Shaw, C.A., and Hughes, C.A., 2015, Mantle-derived helium in hot springs of the Cordillera Blanca, Peru : Implications for mantle-to-crust fluid transfer in a flat-slab subduction setting: Chemical Geology, v. 417, p. 200–209, doi:10.1016/j.chemgeo.2015.10.003.

Parkhurst, D.L., and Appelo, C.A.J., 2013, Description of Input and Examples for PHREEQC Version 3 — A Computer Program for Speciation , Batch-Reaction , One-Dimensional Transport , and Inverse Geochemical Calculations.: U.S. Geological Survey Techniques and Methods, book 6, chapter A43, doi:10.1016/0029-6554(94)90020-5.

Sander, R., 2015, Compilation of Henry's law constants (version 4.0) for water as solvent: Atmospheric Chemistry and Physics, v. 15, p. 4399–4981, doi:10.5194/acp-15-4399-2015.

Smith, S.P., and Kennedy, B.M., 1983, The solubility of noble gases in water and in NaCl brine: Geochimica et Cosmochimica Acta, v. 47, p. 503–515, doi:10.1016/0016-7037(83)90273-9.

Weiss, R.F., 1971, Solubility of Helium and Neon in Water and Seawater: Journal of Chemical and Engineering Data, v. 16, p. 235–241, doi:10.1021/je60049a019.

APPENDIX B

Supporting Information for Chapter 3

This supplementary material contains one figure (Figs. B.1) and six tables (Table B.1 – B.6) providing relevant geochemical data and field parameters for Peruvian thermal springs discussed in this study.

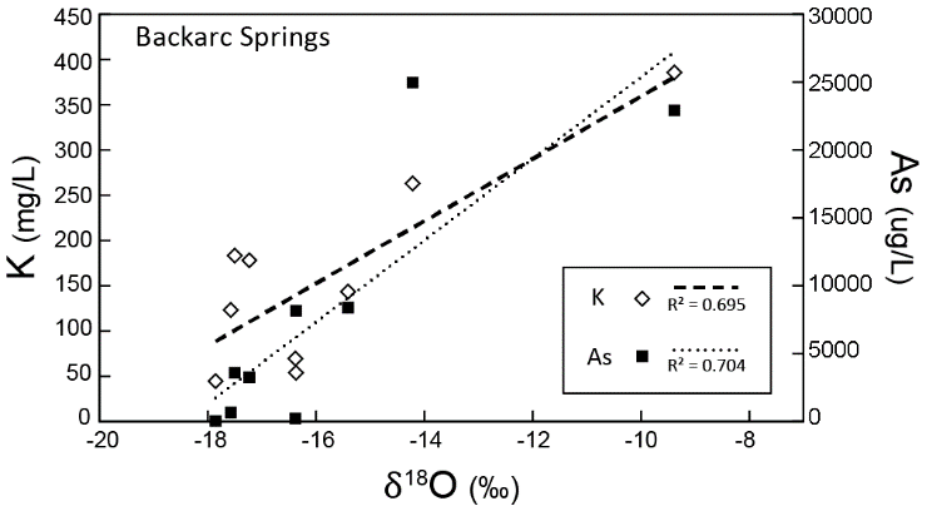

Supplementary Figure B.1. Plot of K and As concentrations versus $\delta^{18}O$ values for springs from the backarc region. Positive correlations suggest that high-temperature fluid interaction with silicates and other minerals is responsible for increases in K and As concentrations and higher $\delta^{18}O$ values in these springs. Both correlations have an r^2 value of 0.70.

Supplementary Table B.1. Stable isotope data (C, N, O, H, He) and volatile abundances for Peruvian hot springs, including calculated nitrogen source mixing ratios.

Spring	gas collected?	DIC*	C_{carb}	C_{ext}	$\delta^{13}C$ [a]	$\delta^{13}C_{ext}$	$CO_2/^3He$*	log P_{CO2}	$\delta^{15}N$	N_2/He*	f_a	f_s	f_m	% S^b	$\delta^{18}O$	δ^2H	$^3He/^4He$*	C/N_2*	He/Ar*
		mmol/ kgH_2O	mmol/ kgH_2O	mmol/ kgH_2O	‰ VPDB	‰ VPDB		atm	‰ AIR						‰ VSMOW	‰ VSMOW	R_C/R_A		
Flat Slab																			
DNCB17-01															-14.3†	-104†			
DN17CB-02		4.6	0.7	3.9	-3.4†	-4.3	4.5E+11	-1.153							-14.5†	-110†	0.86	0.86	
DN17CB-06		3.3	0.2	3.2	-10.2†	-10.8	3.8E+10	-1.712		103					-14.9†	-110†	1.10	0.69	0.34
DN17CB-7B		1.6	0.0	1.6	-9.3†	-9.4	4.3E+11	-1.205							-15.2†	-107†	0.55		
DN17CB-09		2.2	0.1	2.1	-8.2†	-8.8	4.9E+11	-1.139							-15.3†	-113†	0.55		
DN17CB-13		10.5	2.7	7.8	-2.2†	-3.6	7.8E+10	-0.718							-13.8†	-103†	0.35	1.30	0.00
DN17CB-21		9.1	3.7	5.4	-2.7†	-6.0	7.4E+10	-1.690							-14.6†	-116†	0.34	3.55	0.00
DN17CB-24		1.6	0.5	1.2	-12.6†	-18.5	3.5E+11	-2.958							-14.9†	-118†	0.26	0.34	
DN17CB-25		14.2	2.5	11.7	-1.8†	-2.7	1.1E+13	-0.194		39					-16.0†	-124†	0.33	26.40	1.01
DN17CB-30		16.7	4.1	12.6	-1.9†	-3.1	1.3E+12	-0.418		113					-14.4†	-114†	0.35	7.49	0.30
DN17CB-32		17.2	1.5	15.7	-3.5†	-4.1		-0.066							-16.8†	-130†		10.46	
DN17CB-36		2.8	1.0	1.8	-6.0†	-10.6	1.6E+11	-1.471							-15.3†	-118†	0.46		
DN17CB-37		4.5	0.9	3.6	-8.0†	-10.4	2.5E+11	-1.074							-16.1†	-120†	0.55		
DN17CB-38		5.0	0.8	4.2	-7.7†	-9.5	3.1E+10	-1.029							-16.6†	-125†	0.53		
DN10AP-01		22.3	5.8	16.5	-0.3	-1.1	2.8E+13	-0.671							-16.3	-118	0.71		
DN18AP-02	X	57.1	17.1	40.0	-4.8	-7.7	1.5E+16	0.087	2.02	1014	0.47	0.39	0.14	73	-15.1	-112	0.72	1.31	0.06
DN18AP-03		4.5	1.5	3.0	-6.4	-10.6	7.9E+09	-1.519							-14.7	-113	1.29		
DN18AP-04[c]		1.8			-7.0			-1.599	1.29						-14.8	-109			
DN18AP-05	X	53.5	16.5	37.1	-12.5	-18.9	8.2E+16	0.182		1348					-14.6	-111	0.47	0.99	0.06
DN19CP-11		7.9	0[d]	7.9	-10.6	-10.6	4.1E+10	-1.129	0.88	6748	0.84	0.14	0.02	88	-14.1	-106	1.18	0.02	0.01
DN19CP-14	X	1.3	0.3	1.0	-7.3	-9.6	5.0E+11	-1.598	0.35	15902	0.94	0.05	0.01	88	-15.8	-114	0.32	0.04	0.00
DN19CP-20		3.1	0[d]	3.1	-6.5	-6.5	1.8E+12	-2.147							-13.1	-98	0.99		
DN19CP-22		6.0	0[d]	6.0	-8.8	-8.8		-0.793							-12.8	-95			

DN19CP-30		16.3	6.3	10.0	-2.9	-6.0	2.4E+10	-1.047	1.07	3656	0.8	0.2	0.0	83	-14.7	-112	2.40	0.11	0.02
DN19CP-31		18.9	6.3	12.6	-3.4	-6.1	9.4E+12	-0.877	1.25						-15.7	-118	1.45	0.52	
DN19CP-32															-15.7	-118			
slab tear region																			
DN19CP-01		5.3	0.2	5.2	-6.9	-7.2	8.2E+10	-0.906	0.79	817	0.6	0.2	0.2	57	-15.7	-114	1.21	1.13	0.03
DN19CP-02		5.5	0.2	5.3	-6.6	-6.9	7.7E+10	-0.848	0.96						-15.6	-114	1.26	0.12	
DN19CP-04	X	24.2	3.6	20.6	-8.9	-10.8	6.3E+11	-0.059	1.29						-13.5	-101	1.38		
DN19CP-05		16.7	0.9	15.8	-7.4	-8.0	1.2E+12	-0.250	1.08	1348	0.7	0.2	0.1	68	-12.7	-95	0.82	0.28	0.05
DN19CP-06	X	29.5	1.5	28.0	-11.1	-11.8	1.2E+13	0.051	3.80						-11.2	-86	0.77		
DN19CP-08	X	27.3	4.3	23.0	-8.2	-10.0	3.3E+12	-0.169	-0.50	819	0.76	0.06	0.18	24	-15.2	-113	1.55	8.75	0.06
DN19CP-09		1.9	0.2	1.7	-5.9	-6.6		-1.763							-16.1	-119			
DN19CP-10	X	23.9	5.8	18.0	-3.8	-5.7	3.9E+12	-0.231	1.90	776	0.41	0.41	0.19	68	-14.6	-111	0.90	12.17	0.08
DN19CP-23		3.6	0.9	2.7	-8.6	-12.1		-1.645							-13.0	-96			
DN19CP-24	X	28.4	0[d]	28.4	-7.0	-7.0	3.3E+13	-0.184	1.77	3549	0.68	0.28	0.04	88	-15.6	-117	1.74	8.37	0.01
DN19CP-25															-15.7	-119			
DN19CP-26	X	51.9	10.0	41.9	-5.5	-7.2	1.1E+13	-0.046	0.43	1690	0.79	0.12	0.09	59	-15.8	-120	2.07	9.79	0.03
DN19CP-27	X	49.0	6.3	42.7	-6.0	-7.2	9.4E+12	-0.121	4.35						-16.4	-123	1.68		
DN19CP-28															-14.6	-114			
DN19CP-29															-16.0	-121			
DN19CP-34	X	51.2	7.2	43.9	-5.1	-6.3	4.5E+13	-0.121	2.26	1169	0.47	0.41	0.12	77	-9.4	-69	2.04	2.27	0.05
DN19CP-38		19.6	3.5	16.1	-4.5	-5.9	4.9E+13	-0.552	1.64	1586	0.61	0.30	0.09	77	-12.7	-96	0.60	6.05	0.03
DN19CP-39	X	17.6	0.5	17.1	-6.9	-7.1	2.0E+12	-0.056	1.15	1465	0.67	0.23	0.10	70	-15.6	-115	1.06	2.37	0.03
CBD fault zone & adjacent hanging wall																			
DN13CB04															-7.8[§]	-81[§]			
DN13CB05		38.2	10.0	28.2	-7.8[§]	-11.3	1.00E+13	-0.441							-6.4[§]	-74[§]	1.06		
DN13CB06		41.6	7.8	33.8	-10.3[§]	-13.1	3.90E+13	-0.184							-4.9[§]	-80[§]	1.82		
DN13CB07		19.8	1.1	18.7	-6.3[§]	-6.8	2.70E+13	0.461							-12.6[§]	-94[§]	0.62		
DN13CB08a		10.3			-9.1[§]		4.20E+12										1.33		

DN13CB08b		23.6	3.3	20.2	-9.7[§]	-11.6	1.90E+13	-0.167						-10.5[§]	-86[§]	0.85		
DN13CB09		19.6	1.6	18.0	-10.0[§]	-11.1	2.40E+12	-0.089						-10.2[§]	-88[§]	1.30		
DN13CB11g	X															1.98		
DN13CB11w		19.0	1.6	17.5	-13.6[§]	-15.0	6.90E+12	-0.074								1.81		
DN13CB13														-13.0[§]	-99[§]			
DN13CB14		12.6	0[d]	12.6	-10.7[§]	-10.7	6.10E+11	-0.244						-14.2[§]	-107[§]	1.79		
DNCB15-5														-14.4[†]	-103[†]			
DNCB15-7										30				-13.6[†]	-106[†]		17.53	2.17
DNCB15-08										750				-12.6[†]	-94[†]		3.13	0.08
DNCB15-9b										1857				-14.4[†]	-113[†]		0.12	0.02
DNCB15-10														-14.3[†]	-103[†]			
DNCB15-11										953				-13.1[†]	-94[†]		0.21	0.04
DNCB15-12										7				-14.7[†]	-111[†]		32.36	2.63
DNCB15-13														-6.3[†]	-79[†]			
Backarc																		
DN18-AP-06	X	13.3	1.7	11.5	-6.3	-7.6	1.4E+12	-0.571		535				-14.2	-126	2.51	2.45	0.16
DN18-AP-07	X	22.7	0[d]	22.7	-7.9	-7.9	4.5E+12	-0.106		1202				-16.4	-127	1.94	10.15	0.05
DN18-AP-08	X	34.6	5.1	29.5	-10.6	-12.7	3.6E+14	0.022	1.30	887	0.53	0.30	0.16	64.89	-17.6	-132	0.90	38.87	0.84
DN18-AP-09	X	53.5	13.0	40.6	-9.9	-13.7	6.1E+13	-0.162	3.72	41265	0.47	0.53	0.00	100.00	-16.4	-128	0.92	0.34	0.00
DN18-AP-10		26.1	2.6	23.5	-3.0	-3.6	4.0E+13	-0.061							-17.9	-138	1.15		
DN18-AP-11	X	7.7	1.1	6.6	-4.8	-5.9	6.2E+10	-0.520	0.89	196	0.00	0.67	0.76	46.87	-17.5	-141	1.35	2.05	0.74
DN18-AP-12	X	7.5	0.1	7.3	-4.7	-4.8	4.0E+10	-0.574	2.40	441	0.09	0.58	0.33	63.60	-17.2	-133	1.34	1.08	0.23
DN18-AP-13	X	23.3	4.2	19.2	-6.5	-8.3	3.5E+12	-0.071	0.34	3039	0.87	0.08	0.05	63.56	-9.4	-120	2.32	3.87	0.04
DN18-AP-14	X	26.5	1.9	24.6	-6.5	-7.2	2.2E+12	0.026		999					-15.4	-131	2.52	9.66	0.10

*reported in Hiett et al. (2021)
[†] repoted in Scott et al. (2020)
[§] reported in Newell et al. (2015)
[a] $\delta^{13}C$ refers to modelled $\delta^{13}C_i$ for bubbling springs and $\delta^{13}C_{DIC}$ for non-bubbling springs
[b] $\%S = f_s / (f_s + f_m) \times 100$

[c] C_{carb} and C_{ext} not calculated due to anomalously high salinity, likely due to proximity to nearby evaporite deposits
[d] Springs with SO_4^{2-} concentrations that exceed Ca^{2+} + Mg^{2+}, resulting in negative C_{carb}. C_{carb} set to 0

Supplementary Table B.2. Parameters used for modelling carbon isotope fractionation during degassing to derive initial carbon isotope values ($\delta^{13}C_i$)

Spring	T	pH	$\delta^{13}C_{DIC}$	$\delta^{13}C_{CO2}$	DIC	CO_2 (aq)	HCO_3^-	HCO_3^- = 1-X	CO_2 (aq) = X	1000 lnK_0[a]	1000 lnK_1[b]	$\varepsilon_{(DIC-CO2)}$[c]	$\alpha_{(CO2-DIC)}$[d]	$\delta^{13}C_i$	f[e]
	°C		‰ VPDB	‰ VPDB	mol/ kgH2O	mol/ kgH2O	mol/ kgH2O							‰ VPDB	
Flat Slab															
DN18AP-02	39.9	6.12	-2.5	-6.4	0.057	0.034	0.029	0.46	0.54	-0.846	6.674	2.58011	0.99742	-4.8	0.4
DN18AP-05	45.4	5.96	-9.0	-13.0	0.054	0.038	0.022	0.37	0.63	-0.848	6.290	1.77472	0.99823	-12.5	0.14
DN19CP-14	68.4	6.63	-7.3	-10.2	0.001	0.000	0.001	0.71	0.29	-0.856	4.881	3.21579	0.99679	-7.27	1
slab tear region															
DN19CP-04	43.9	6.02	-5.0	-9.7	0.024	0.014	0.010	0.43	0.57	-0.847	6.393	2.27113	0.99773	-8.85	0.185
DN19CP-06	57.2	5.9	-7.3	-11.3	0.030	0.019	0.010	0.35	0.65	-0.852	5.530	1.39834	0.99860	-11.08	0.065
DN19CP-08	53.3	6.23	-5.0	-9.6	0.027	0.012	0.014	0.55	0.45	-0.851	5.773	2.79517	0.99721	-8.15	0.32
DN19CP-10	60.9	6.35	-1.8	-5.8	0.024	0.009	0.014	0.60	0.40	-0.854	5.309	2.86983	0.99713	-3.84	0.488
DN19CP-24	45.9	6.2	-3.7	-8.5	0.028	0.014	0.014	0.52	0.48	-0.848	6.256	2.86115	0.99714	-6.96	0.32
DN19CP-26	28.9	6.13	-1.6	-7.0	0.052	0.027	0.022	0.48	0.52	-0.841	7.506	3.13770	0.99687	-5.45	0.29
DN19CP-27	20.9	6.11	-1.4	-7.1	0.049	0.029	0.019	0.41	0.59	-0.837	8.170	2.84856	0.99716	-6.02	0.195
DN19CP-34	24.3	6.18	-2.4	-7.4	0.051	0.026	0.022	0.50	0.50	-0.839	7.881	3.48337	0.99652	-5.10	0.458
DN19CP-39	70.1	5.8	-3.8	-6.9	0.018	0.012	0.005	0.30	0.70	-0.857	4.788	0.81075	0.99919	-6.85	0.02
CBD fault zone & adjacent hanging wall															

DN13CB11	73.3		-10.8	-14.5	0.019	0.006	0.007	0.53	0.47	-0.857	4.632	2.04608	0.99796	-13.6	0.25
Backarc															
DN18AP-06	71.0	6.54	-5.9	-9.1	0.013	0.004	0.010	0.69	0.31	-0.857	4.739	3.02925	0.99698	-6.3	0.875
DN18AP-07	54.2	5.96	-5.5	-8.8	0.023	0.015	0.087	0.37	0.63	-0.847	6.435	1.84583	0.99816	-7.9	0.27
DN18AP-08	56.4	6.09	-8.3	-11.6	0.035	0.021	0.017	0.44	0.56	-0.852	5.579	1.98749	0.99801	-10.6	0.32
DN18AP-09	16.6	6.15	-7.9	-11.9	0.054	0.036	0.023	0.40	0.60	-0.835	8.550	2.90819	0.99710	-9.9	0.5
DN18AP-11	80.5	6.15	-3.2	-5.7	0.008	0.004	0.004	0.48	0.52	-0.860	4.247	1.59131	0.99841	-4.8	0.37
DN18AP-12	68.5	6.09	-2.7	-5.6	0.007	0.005	0.004	0.46	0.55	-0.856	4.875	1.75271	0.99825	-4.7	0.325
DN18AP-13	62.0	5.98	-3.7	-7.1	0.023	0.015	0.011	0.41	0.59	-0.854	5.244	1.62818	0.99837	-6.5	0.18
DN18AP-14	43.2	5.31	-5.1	-6.5	0.026	0.026	0.003	0.11	0.89	-0.847	6.442	-0.04242	1.00004	-6.5	1

[a] $K_0 = (^{13}C/^{12}C)H_2CO_3 / (^{13}C/^{12}C)CO_2$; $1000\ln K_0 = -0.91 + (0.0063 \times 10^6/T^2)$ (Dienes and Langmuir, 1974)

[b] $K_1 = (^{13}C/^{12}C)HCO_3^- / (^{13}C/^{12}C)CO_2$; $1000\ln K_1 = -4.54 + (1.099 \times 10^6/T^2)$ (Dienes and Langmuir, 1974)

[c] $\varepsilon = x(1000\ln K0)+(1-x)(1000\ln K1)$

[d] α (CO2-DIC) =exp(-ε (DIC-CO2)/1000)

[e] fraction of DIC remaining after degassing

Supplementary Table B.3. O and H isotopic data for meteoric water samples

Sample ID	Latitude	Longitude	Elevation	$\delta^{18}O$	$\delta^{2}H$
			m	‰ VSMOW	‰ VSMOW
DNCB17-3†	-8.8246	-77.4608	2893	-14.4	-95
DNCB17-8†	-8.5960	-77.5680	2360	-13.9	-104
DNCB17-22†	-9.6108	-77.1822	3205	-15.2	-120
DNCB17-26†	-9.9380	-76.9630	3870	-15.4	-119
DN18AP-06 MW	-13.7501	-71.2752	4418	-18.2	-122
DN18AP10 MW	-16.2676	-70.1422	4106	-15.8	-120
DN18AP11 MW	-15.5667	-70.8866	4386	-17.9	-125
DN18AP14 MW	-16.7626	-70.0893	4614	-16.5	-113
Lake Titicaca	-15.8360	-70.0140	3821	-5.5	-53
DN19CP03	-10.9000	-76.7209	3252	-15.3	-113
DN19CP07	-10.8377	-76.8918	2143	-14.8	-110
DN19CP12	-10.4911	-76.5472	3404	-13.8	-103
DN19CP16	-10.4201	-76.8584	4358	-14.7	-110
DN19CP17	-10.3594	-76.9616	3910	-15.6	-115
DN19CP33	-12.7802	-74.9635	3690	-15.0	-115
DN19CP35	-11.4682	-75.7510	1819	-12.1	-85
DN19CP36	-11.4909	-75.2751	2093	-10.9	-72
DN19CP37	-11.6049	-75.3369	3766	-14.3	-107
DN19CP40	-11.2145	-76.5848	3839	-14.9	-112

† repoted in Scott et al. (2020)

Supplementery Table B.4. Major element concentrations (mg/L) for Peru thermal springs. Minimum reporting limits (MRL) are provided.

Sample ID	Na	Mg	K	Ca	Si	HCO_3	Cl	SO_4
MRL (mg/L)	0.10	0.03	0.1	0.08	0.25	0.05	0.02	0.02
Flat Slab								
DNCB17-2†	45.4	10.84	7.2	19.95	29.43	198	18.37	25.41
DNCB17-6†	62.8	5.50	3.5	47.88	17.64	173	24.39	120.35
DNCB17-9†	9.8	7.58	3.2	12.88	23.20	62	1.29	49.74
DNCB17-13†	114.4	108.05	30.8	535.99	10.27	371	227.65	1451.64
DNCB17-21†	67.3	42.04	8.2	191.58	9.70	532	72.84	267.49
DNCB17-24†	24.8	2.14	2.3	15.97	10.21	99	17.69	1.35
DNCB17-25†	98.0	24.19	17.8	148.98	27.59	316	150.07	211.10
DNCB17-30†	96.4	14.60	18.1	153.49	25.35	526	165.14	29.53
DNCB17-32†	97.5	12.02	17.5	49.33	18.41	248	143.11	17.56
DNCB17-36†	18.7	10.85	3.7	32.63	13.55	124	25.32	22.55
DNCB17-37†	21.7	9.15	6.2	70.65	21.43	161	16.39	122.34
DNCB17-38†	20.1	10.82	6.7	91.65	38.84	198	21.67	184.46
DN18AP-01	70.0	24.47	8.2	224.51	nm	90	77.56	847.67
DN18AP-02	1922.6	96.33	296.4	674.05	nm	3096	353.76	1751.02
DN18AP-03	381.3	87.96	10.0	295.49	nm	614	911.82	222.75
DN18AP-04	16283.5	182.08	-	1649.28	nm	30023	1954.40	68.06
DN18AP-05	893.9	137.80	100.3	585.29	nm	1915	366.74	1330.28
DN19CP-11	315.4	19.66	5.8	207.47	19.50	336	64.39	968.36
DN19CP-14	8.0	3.00	2.2	38.66	26.31	55	0.90	79.83
DN19CP-20	234.9	15.88	20.7	136.54	19.96	183	240.30	490.84
DN19CP-22	194.9	21.88	18.3	149.94	16.24	134	205.03	555.28
DN19CP-30	28.5	33.86	4.6	242.09	6.79	793	33.98	113.44
DN19CP-31	114.4	31.59	22.0	296.85	14.38	885	179.87	228.84
CBD fault zone & adjacent hanging wall								
DN13CB02§	3.3	0.39	0.5	2.30	8.18	22	1.42	0.74
DN13CB05§	4948.0	48.00	694.0	330.00	-	2103	7369.00	16.00
DN13CB06§	4714.0	38.20	690.0	285.00	-	2030	6553.00	85.00
DN13CB07§	82.1	9.40	11.8	33.04	16.10	260	76.50	9.60
DN13CB08b§	1079.0	17.30	175.9	150.80	49.50	953	1372.00	111.00
DN13CB09§	1297.0	9.77	174.2	51.40	-	538	1708.00	3.32
DN13CB11§	1164.0	2.74	162.5	70.00	79.00	780	1468.00	38.40
DN13CB13§	223.0	12.90	22.8	73.60	16.70	192	57.50	384.00
DN13CB14§	431.0	1.22	28.1	29.50	48.90	489	282.00	148.00
slab tear region								
DN19CP-01	76.9	39.53	9.3	330.54	19.91	195	33.64	932.47
DN19CP-02	73.7	38.74	8.1	335.18	20.91	198	35.93	940.05
DN19CP-04	240.1	71.32	35.9	469.70	15.57	635	356.01	1058.75
DN19CP-05	282.5	67.01	47.0	163.29	22.66	330	416.22	571.34
DN19CP-06	473.7	61.28	83.9	175.86	24.35	555	744.18	518.20
DN19CP-08	389.0	55.56	42.0	524.20	17.60	915	451.25	1064.44
DN19CP-09	16.7	18.86	7.0	106.35	20.66	95	3.83	314.64
DN19CP-10	398.8	51.36	70.7	175.09	19.02	879	665.95	61.57
DN19CP-23	28.1	11.27	2.8	96.98	7.55	159	24.04	190.88
DN19CP-24	681.6	34.48	120.8	281.27	48.28	903	796.51	1093.05
DN19CP-26	1080.8	172.19	62.5	660.32	5.00	1501	1590.31	1302.22
DN19CP-27	155.5	116.17	42.2	390.12	6.43	1220	132.57	792.69
DN19CP-34	1343.2	124.74	76.6	720.72	8.69	1538	1770.42	1526.71
DN19CP-38	524.4	21.87	63.1	177.17	12.54	793	941.91	176.81
DN19CP-39	194.4	30.44	18.2	271.20	23.46	317	213.66	721.09
Backarc								
DN18AP-06	1498.5	23.69	262.9	265.80	nm	2671	562.62	593.99
DN18AP-07	421.9	19.52	54.0	263.39	nm	490	832.21	532.11
DN18AP-08	1255.6	42.14	123.1	396.35	nm	1782	623.00	1014.73
DN18AP-09	1158.1	114.84	69.5	433.70	nm	1938	247.09	1454.03
DN18AP-10	844.9	43.03	44.5	268.50	nm	1159	560.58	643.49
DN18AP-11	3350.5	33.49	183.1	365.45	nm	5034	900.07	247.49
DN18AP-12	3240.1	33.39	178.0	357.31	nm	5014	974.53	228.93
DN18AP-13	4616.2	26.36	385.5	152.99	nm	6931	70.39	637.30
DN18AP-14	1297.3	5.73	143.5	73.14	nm	2174	19.54	198.00

(nm) not measured; (-) below MRL

† reported in Scott et al. (2020)

§ reported in Newell et al. (2015)

Supplementery Table B.5. Minor element concentrations (µg/L) for Peru thermal springs. Minimum reporting limits (MRL) are provided.

Sample ID	Be	Al	V	Cr	Mn	Fe	Co	Ni	Cu	Zn	As	Se	Sr	Cd	Sb	Ba	Ti	Pb	U
MRL	0.03	4	0.25	0.05	0.15	7	0.25	0.4	0.8	2.5	0.2	0.1	1	0.15	2.4	1	0.1	0.35	0.06
Flat Sab																			
DN17CB-01†	0.08	-	-	1.52	175.18	75	-	-	-	4.3	2.1	-	424	-	-	273	-	-	-
DN17CB-02†	0.08	-	-	-	160.52	18	-	-	-	-	4.1	-	412	-	-	268	-	-	-
DN17CB-06†	0.08	-	-	-	296.83	-	-	-	-	-	2.3	-	482	-	-	55	-	-	-
DN17CB-07a†	-	-	-	-	263.63	911	4.38	3.7	-	48.9	7.6	-	66	-	-	111	0.3	-	-
DN17CB-07b†	0.13	-	-	-	261.66	3280	2.86	3.5	-	12.5	22.1	-	68	-	-	118	0.2	-	-
DN17CB-09†	-	-	-	-	315.75	2287	-	-	-	10.0	16.5	-	72	-	-	133	0.1	-	-
DN17CB-13†	4.75	-	-	1.20	4.58	60	-	-	-	-	210.2	-	6023	-	-	21	-	-	-
DN17CB-21†	0.07	-	-	-	160.26	50	0.36	-	-	3.9	0.8	-	2844	-	10.9	49	0.2	-	-
DN17CB-24†	-	-	-	-	57.78	190	-	-	-	3.0	36.4	-	140	-	-	37	-	-	-
DN17CB-25†	0.75	9	-	-	873.78	1916	-	-	-	12.4	9.1	-	2702	-	6.9	100	2.8	-	-
DN17CB-30†	0.08	-	-	18.63	76.13	307	-	0.4	1.2	3.9	125.7	-	897	-	5.8	889	0.2	-	-
DN17CB-32†	0.19	5	-	-	316.40	267	-	-	-	3.0	244.7	-	825	-	12.8	723	1.9	-	-
DN17CB-36†	-	-	-	-	179.58	113	-	-	-	-	52.7	-	437	-	3.4	256	-	-	-
DN17CB-37†	0.14	-	-	-	333.83	458	-	-	-	3.5	597.8	-	916	-	3.8	73	-	-	-
DN17CB-38†	0.08	4	-	-	189.87	388	-	-	-	-	17.3	-	2200	-	-	98	-	-	-
DN18AP-01	-	-	-	-	-	-	-	-	-	52.0	47.6	-	nm	-	-	105	1.4	22.68	nm
DN18AP-02	-	-	-	-	561.43	3140	-	-	-	173.1	4719.5	-	nm	-	-	123	24.1	-	nm
DN18AP-03	-	-	-	-	-	80	-	-	-	263.5	10.1	1.9	nm	-	-	20	3.7	-	nm
DN18AP-04	-	-	-	-	826.82	-	-	-	-	-	-	-	nm	-	-	-	-	-	nm
DN18AP-05	5.85	-	-	-	618.18	7261	-	-	-	20.3	709.6	-	nm	-	-	89	13.7	-	nm
DN19CP-11	-	-	-	0.99	240.56	587	-	-	-	-	187.5	-	7811	-	-	15	-	-	-
DN19CP-14	-	49	-	-	285.22	287	-	-	-	38.2	5.6	-	747	-	-	114	-	1.10	-
DN19CP-20	-	71	-	-	1410.11	47	5.35	-	-	51.2	5.6	-	1998	-	-	30	0.7	1.31	-
DN19CP-22	-	-	-	-	2081.11	9326	10.14	7.9	-	422.0	50.0	-	1860	-	7.6	27	-	1.50	-
DN19CP-30	-	-	-	-	31.56	302	-	-	-	-	127.2	-	582	-	-	70	-	-	-
DN19CP-31	-	-	-	-	137.72	62	-	-	-	-	100.6	-	1686	-	-	58	-	-	-
slab tear region																			
DN19CP-01	-	135	-	3.59	893.99	778	3.76	855.6	30.3	87.0	26.6	-	7360	-	14.8	46	-	7.07	-
DN19CP-02	-	52	-	-	767.83	585	-	-	6.3	37.1	18.7	-	7370	-	7.2	40	-	1.49	-
DN19CP-04	-	55	-	0.70	103.01	60	-	-	22.2	30.3	-	-	7310	-	11.2	35	-	1.58	-
DN19CP-05	-	105	-	-	1882.73	9016	17.77	15.6	11.1	213.9	43.0	-	2217	-	11.7	55	0.8	2.46	-
DN19CP-06	-	45	-	-	889.97	2884	-	-	8.8	33.8	35.2	-	3084	-	10.0	65	0.8	1.30	-
DN19CP-08	2.40	88	-	-	330.15	1286	-	-	-	-	840.8	-	11102	-	3.8	47	-	0.82	-
DN19CP-09	-	41	-	-	626.11	1377	-	-	6.3	20.5	12.1	-	1926	-	-	50	-	2.98	-
DN19CP-10	-	45	-	-	516.10	858	-	-	-	-	244.9	-	2564	-	31.0	360	5.6	0.70	-
DN19CP-23	-	-	-	-	3.48	38	-	-	-	-	18.7	-	821	-	15.2	49	-	1.19	3.88

DN19CP-24	3.51	-	-	-	88.51	1348	-	-	-	-	25.2	-	5026	-	12.2	42	5.8	-	-
DN19CP-26	-	-	-	-	29.53	276	-	-	-	-	52.3	-	6271	-	-	-	-	-	-
DN19CP-27	-	39	-	-	734.01	710	-	-	-	32.4	259.4	-	5478	-	-	44	-	-	-
DN19CP-34	-	-	-	-	484.92	1498	-	-	-	-	3647.6	-	11796	-	-	-	-	-	-
DN19CP-38	-	42	-	-	1984.72	41	-	-	-	-	17.4	-	3595	-	-	102	-	-	-
DN19CP-39	-	37	-	-	1107.03	963	-	-	-	-	95.8	-	6301	-	88.9	49	-	-	-
CBD fault zone & adjacent hanging wall																			
DN13CB02[§]	-	14	-	-	0.73	14	-	-	2.0	-	-	-	nm	-	-	-	-	-	-
DN13CB05[§]	1.04	41	6.12	0.43	411	12345	-	1.1	16.6	-	2106.6	7.5	nm	-	-	1123	-	-	-
DN13CB06[§]	1.29	46	5.87	0.32	347	6570	-	0.9	15.3	-	10806.1	6.9	nm	-	-	554	1.4	-	-
DN13CB07[§]	0.62	-	-	-	1096	8565	-	-	-	6.3	2.4	-	nm	-	-	44	-	-	-
DN13CB08b[§]	1.67	-	2.70	-	180	197	-	-	1.7	-	621.7	2.4	nm	-	6.3	249	0.5	-	-
DN13CB09[§]	0.55	-	2.06	-	1787	155	-	-	2.0	-	1.3	3.0	nm	-	-	1200	-	-	-
DN13CB11[§]	5.62	-	2.31	-	443	449	-	-	1.7	-	1654.9	3.0	nm	-	36.0	646	9.3	-	-
DN13CB13[§]	3.70	-	-	-	2931	1957	13.73	19.3	-	5532.0	389.7	-	nm	1.47	178.9	25	17.0	9.82	-
DN13CB14[§]	3.83	30	-	-	77.4	399	-	-	-	5.9	1496.1	-	nm	-	21.7	92	1.2	-	2.08
DNCB15-05[†]	-	107	-	-	1.70	24	-	-	-	-	-	-	10	-	-	1	0.1	-	nm
DNCB15-08[†]	12.36	-	-	-	566.26	1111	-	-	-	6.8	1851.2	2.3	5099	-	40.4	876	15.1	-	nm
DNCB15-10[†]	8.73	12	-	-	109.76	607	-	-	-	6.1	2634.2	-	2544	-	39.5	154	2.2	-	nm
DNCB15-11[†]	-	21	0.73	-	0.24	-	-	0.5	2.2	8.0	38.2	-	61	-	-	-	-	-	nm
DNCB15-12[†]	6.46	213	-	-	1708.53	8452	0.32	0.9	-	6.1	9.4	0.2	2913	-	-	447	-	-	nm
DNCB15-13[†]	0.52	-	-	-	1077.29	194	-	-	-	-	4.1	1.9	11698	-	-	1126	-	-	nm
Backarc																			
DN18AP-06	4.83	-	-	-	54.46	479	-	-	-	-	24954.8	-	nm	-	-	108	-	-	nm
DN18AP-07	10.1	-	-	-	104.37	705	-	-	-	-	8153.9	-	nm	-	-	38	4.6	-	nm
DN18AP-08	8.66	-	-	-	319.76	3548	-	-	-	-	668.3	-	nm	-	45.6	59	8.3	-	nm
DN18AP-09	1.30	-	-	-	3245.64	20782	26.22	18.9	21.9	45.5	227.3	-	nm	-	-	44	1.1	-	nm
DN18AP-10	-	-	-	1.17	1394.25	2029	-	-	-	-	38.0	-	nm	-	-	54	-	-	nm
DN18AP-11	-	-	-	-	460.64	354	-	-	-	-	3587.1	-	nm	-	-	115	12.2	-	nm
DN18AP-12	-	-	-	-	521.70	252	-	-	-	-	3252.4	-	nm	-	-	100	12.4	-	nm
DN18AP-13	-	-	-	-	321.66	501	-	-	-	-	22907.3	-	nm	-	1331.4	1142	52.6	-	nm
DN18AP-14	-	-	-	-	4306.74	9506	-	-	-	-	8386.9	-	nm	-	-	649	7.2	-	nm

(nm) not measured; (-) below MRL

[†] reported in Scott et al. (2020)

[§] reported in Newell et al. (2015)

Supplementary Table B.6. Peruvian hot spring locations and field parameters.

Spring	Sample ID	Latitude	Longitude	Elevation	T	pH	Conductivity	Discharge*
				m	°C		µS	L/s
Flat slab								
Pomabamba	DNCB17-01	-8.8255	-77.4595	2901	48.8	6.50	460	
Pomabamba	DNCB17-2	-8.8257	-77.4600	2910	50.5	6.62	468	4.5
Chilhuan	DNCB17-6	-8.6717	-77.6336	3304	36.5	7.02	607	
Rupac	DNCB17-7b	-8.5960	-77.5680	2360	63.8	6.04	200	
Rupac	DNCB17-9	-8.5950	-77.5660	2443	61.5	6.18	230	
Jocos Peinado	DNCB17-13	-8.2955	-77.4881	1591	40.6	6.31	3332	5.0
Chavin	DNCB17-21	-9.6110	-77.1820	3214	41.0	7.47	1406	
Conococha	DNCB17-24	-10.1290	-77.2890	4026	28.0	7.98	233	
Azulmina	DNCB17-25	-9.9380	-76.9630	3870	70.7	5.96	1452	1.0
Taurimpampa	DNCB17-30	-9.8470	-76.8170	3244	45.3	6.24	1387	0.1
Banos (Batan)	DNCB17-32	-10.0480	-76.7220	3390	64.7	5.71	940	
Conoc (La Union)	DNCB17-36	-9.7810	-76.8050	3175	42.2	6.68	377	0.1
Machaycancha (Conog)	DNCB17-37	-10.1640	-76.8110	3835	44.6	6.40	568	0.5
Janac	DNCB17-38	-10.1540	-76.9020	4343	51.5	6.48	720	
Licapa	DN18AP-01	-13.3689	-74.8778	4103	20.2	6.53	1312	
Santo Tomás	DN18AP-02	-13.6525	-72.9448	1693	39.9	6.12	11310	1.0
Ccónocc	DN18AP-03	-13.5431	-72.6387	1850	31.8	6.84	3260	10.0
Sauceda	DN18AP-04	-13.5010	-72.4984	2308	27.8	6.16	85800	0.5
Lares	DN18AP-05	-13.1107	-72.0545	3281	45.4	5.96	7170	8.0
Macanacoto	DN19CP-11	-10.4911	-76.5472	3404	27.4	6.62	2490	
Pumarinri	DN19CP-14	-10.4201	-76.8584	4358	68.4	6.63	295	
Conoc (Oyon)	DN19CP-20	-10.4744	-77.0953	2237	51.4	7.53	2110	1.0
Yahuar Cocha	DN19CP-22	-10.4709	-77.0967	2087	40.1	5.97	1959	1.5
Aguas Calientes	DN19CP-30	-12.4576	-75.0199	3017	22.6	6.89	1342	1.0
Huancavelica	DN19CP-31	-12.7815	-74.9557	3671	26.3	6.78	1203	1.0
Baños de Incas	DN19CP-32	-12.7815	-74.9557	3671	-	-	-	
slab tear region								
Picoy	DN19CP-01	-10.9019	-76.7212	3262	57.0	6.35	1948	0.2
Huancahuasi	DN19CP-02	-10.9000	-76.7209	3252	61.8	6.33	1942	5.0
Huancachin	DN19CP-04	-10.9300	-76.7803	2760	43.9	6.02	3590	2.0

Banos de Fierro	DN19CP-05	-10.8321	-76.8892	2169	47.9	5.86	2920	1.0
Banos de Tingo	DN19CP-06	-10.8377	-76.8918	2143	57.2	5.90	4250	2.0
Rupay	DN19CP-08	-10.6952	-76.8208	3043	53.3	6.23	4290	0.2
Viroc	DN19CP-09	-10.6851	-76.8086	3484	54.5	6.91	776	2.0
Tambochaca	DN19CP-10	-10.4911	-76.5471	3311	60.9	6.35	3610	1.0
Surco	DN19CP-23	-11.8667	-76.4231	2111	16.7	6.78	712	0.5
Yuali	DN19CP-24	-11.6822	-76.0941	4168	45.9	6.20	5640	1.0
Matachico	DN19CP-25	-11.7968	-75.5910	3437	19.7	6.03	7720	
Acaya	DN19CP-26	-11.8130	-75.6057	3452	28.9	6.13	8170	5.0
Huajal	DN19CP-27	-11.8061	-75.5449	3479	20.9	6.11	3170	1.0
Pachacayo 1	DN19CP-28	-11.7564	-75.7198	3566	-	-	-	
Pachacayo 2	DN19CP-29	-11.7540	-75.7223	3561	17.5	6.98	1547	
Uchubamba	DN19CP-34	-11.4682	-75.2510	1819	24.3	6.18	8770	5.0
Santa Catallina	DN19CP-38	-11.1740	-76.6370	3109	40.1	6.49	4074	1.0
San Jose de Banos	DN19CP-39	-11.2145	-76.5848	3839	70.1	5.80	2161	0.5
CBD fault zone & adjacent hanging wall								
Olleros 1	DN13CB04	-9.6686	-77.463	3464	17.6	6.32	15,870	
Olleros 2b	DN13CB05	-9.6683	-77.4626	3453	20.4	6.65	23200	5.0
Olleros 4	DN13CB06	-9.6673	-77.4633	3432	47.8	6.49	21500	5.5
Merced	DN13CB07	-9.2591	-77.6119	3002	38.4	5.03	723	4.0
Chancos	DN13CB08a	-9.3196	-77.5752	2863	47.6	6.22	6020	2.0
Chancos	DN13CB08b	-9.3196	-77.5752	2863	47.6	6.22	6020	5.0
Monterrey	DN13CB09	-9.4684	-77.5354	2989	46.4	5.89	6240	4.0
Huancarhuaz	DN13CB11g	-8.9437	-77.7846	2721	73.3	6.22	5120	
Huancarhuaz	DN13CB11w	-8.9437	-77.7846	2721	73.3	6.22	5120	9.0
Shangol	DN13CB13	-8.9846	-77.8170	2214	39.6	6.01	1025	
Aquilina	DN13CB14	-8.6129	-77.8836	1930	78.3	6.26	2130	12.0
Huancarhuaz	DNCB15-7	-8.9437	-77.7846	2721	73.3	6.22	5120	
Huancarhuaz	DNCB15-08	-8.9415	-77.7853	2721	69.9	6.40	5750	
Aqulina	DNCB15-9b	-8.6129	-77.8836	1884	78.3	6.26	2130	
Pacatque	DNCB15-10	-8.6125	-77.8836	1941	88.9	6.84	2280	
Aticara	DNCB15-11	-8.6125	-77.8836	2662	78.0	6.40	170	
Pumapampa	DNCB15-12	-9.8803	-77.2864	4185	19.2	5.95	3970	
Recuay	DNCB15-13	-9.7181	-77.4590	3415	16.9	6.81	14380	
Backarc								

Upis	DN18AP-06	-13.7501	-71.2752	4418	71.0	6.54	9010	
Pacchanta	DN18AP-07	-13.7174	-71.2420	4308	54.2	5.96	3270	3.0
La Raya	DN18AP-08	-14.4507	-71.0730	4054	56.4	6.09	7020	5.0
Pichacani-Santa Rosa	DN18AP-09	-14.7090	-70.7544	3931	16.6	6.15	6760	2.5
Collpa Apacheta	DN18AP-10	-16.2676	-70.1422	4106	54.0	5.98	4820	2.0
Pinaya	DN18AP-11	-15.5667	-70.8866	4386	80.5	6.15	15160	1.5
Pinaya	DN18AP-12	-15.5669	-70.8877	4379	68.5	6.09	14610	1.5
Crucero	DN18AP-13	-16.7418	-70.1165	4572	62.0	5.98	18760	4.0
Punta Perdida-Pastogrande	DN18AP-14	-16.7626	-70.0893	4614	43.2	5.31	6290	2.5

* Reported discharge measurements from Steinmüller and Huamaní Huaccán (1999), Huamaní Huaccán (2000), and Huamaní Huaccán and Valenzuala Ortiz (2001)

REFERENCES

Deines, P., Langmuir, D., and Harmon, R.S., 1974, Stable carbon isotope ratios and the existence of a gas phase in the evolution of carbonate ground waters: Geochimica et Cosmochimica Acta, v. 38, p. 1147–1164, doi:10.1016/0016-7037(74)90010-6.

Hiett, C.D., Newell, D.L., and Jessup, M.J., 2021, 3He evidence for fluid transfer and continental hydration above a flat slab: Earth and Planetary Science Letters, v. 556, p. 116722, doi:10.1016/j.epsl.2020.116722.

Huamaní Huaccán, A., 2000, Aguas Termales y Minerales en el Norte del Perú: INGEMMET Boletin, Serie D: Estudio Regionales.

Huamaní Huaccán, A., and Valenzuala Ortiz, G., 2001, Aguas Termales y Minerales en el Suroriente del Peru: INGEMMET Boletin, Serie D: Estudio Regionales, p. 124.

Newell, D.L., Jessup, M.J., Hilton, D.R., Shaw, C.A., and Hughes, C.A., 2015, Mantle-derived helium in hot springs of the Cordillera Blanca , Peru : Implications for mantle-to-crust fl uid transfer in a fl at-slab subduction setting: Chemical Geology, v. 417, p. 200–209, doi:10.1016/j.chemgeo.2015.10.003.

Scott, B.E., Newell, D.L., Jessup, M.J., Grambling, T., and Shaw, C.A., 2020, Structural controls on crustal fluid circulation and hot spring geochemistry above a flat-slab subduction zone, Peru: Geochemistry, Geophysics, Geosystems, v. 21, doi:10.1029/2020gc008919.

Steinmüller, K., and Huamaní Huaccán, A., 1999, Aguas Termales y Minerales en el Centro del Peru: INGEMMET Boletín, Serie D: Estudio Regionales, p. 53.

APPENDIX C

Supporting Information for Chapter 4

SUPPLEMENTARY METHODS

Petrography and Chemical Analyses

Quimsachata kersantite xenoliths were analyzed petrographically at Utah State University (USU). Mineral compositions and textural characteristics were also assessed using a FEI Quanta FEG 650 field-emission SEM with Oxford EDS detector at the USU Microscopy Core Facility.

Reported mineral compositions and chemical maps were obtained via electron microprobe (EMP) analysis performed with a JEOL 8230 Superprobe at the University of Colorado, Boulder. All analyses were performed with an acceleration voltage of 15 keV, beam current of 20 nA, and a beam diameter of 2 μm. Standards consisted of natural and synthetic minerals from Astimex Inc. and the Smithsonian microbeam standard suite. A ZAF matrix correction was applied to all analyses. Compositional data for each sample acquired from the EMP analyses was produced in weight percent oxides, and approximately 3-5 spot analyses were taken from multiple grains of each mineral.

Bulk rock trace element compositions were determined for xenolith and lava samples via solution inductively coupled plasma mass spectrometry (ICPMS) at the USU Geosciences Department. Samples were carefully prepared for bulk rock geochemical analyses to avoid contamination. Exterior rims of xenoliths were sawed away and interiors were gently crushed. Chips of xenoliths were crushed to a fine homogenous powder in an agate mortar and pestle. Powdered samples were dissolved in a stepwise acid digestion procedure using trace element grade HNO_3 and HF at 60 – 90 °C. Samples were diluted gravimetrically in dilute HNO_3 and analyzed with an Agilent 6800 Triple Quadrupole ICPMS. Analytical accuracy is within 5% relative all trace elements, and less than 10% for Cr, Mn, Cu, Ga, and Cs, based on analyses of the USGS BHVO-1 standard.

Stable Isotope Analyses

Phlogopite δD

Material from xenolith interiors was crushed in agate mortar and pestle and sieved to a size fraction between 75 and 180 μm. Phlogopite was concentrated based on its platy morphology by lightly shaking the size fraction over a tilted sheet of paper. Phlogopite was further concentrated from the platy fraction under a binocular microscope; pure phlogopite separates were difficult to achieve and separates were ultimately a mixture of phlogpite and bulk rock material, and the proportion of phlogopite was estimated to calculate sample mass required for analysis. Separates were sonicated in pure ethanol for 15 minutes, and dried overnight at 50 °C. Aliquots of 5-10 mg of phlogopite (+bulk rock material) were weighed using a micro balance and loaded into Ag capsules in preparation for isotopic analysis. Aliquots were pyrolyzed in a glassy-

carbon reactor at 1450 °C using a Thermo Scientific high temperature conversion elemental analyzer (TC/EA) and the D/H ratio of the produced H_2 gas was analyzed on a Thermo Scientific Delta V Advantage continuous flow isotope ratio mass spectrometer (CF-IRMS) with Conflow IV interface at the USU Department of Geosciences Stable Isotope Laboratory. Resulting isotope ratios were calibrated using international standards USGS-57 and USGS-58 and reported as δD in ‰ relative to VSMOW. Reported δD values have an analytical uncertainty of ± 2 ‰ based on replicate standard analyses.

Calcite $\delta^{13}C$ and $\delta^{18}O$

Pieces weighing ~0.5 – 2 g where sawed from calcite-rich portions of xenolith interiors and crushed in agate mortar and pestal. Estimates of calcite abundance were made via representative thin section petrography and observation under binocular microscope, and aliquots of ~0.8 – 2.4 mg of material were weighed to provide ~100 μg of calcite for analysis. The $\delta^{13}C$ and $\delta^{18}O$ of carbonate powders were analyzed at the USU Department of Geosciences Stable Isotope Laboratory via CF-IRMS with Thermo Scientific Gasbench II interphase following the phosphoric acid method (McCrea, 1950). Results were calibrated using international standards NBS-19 ($\delta^{13}C$, $\delta^{18}O$), NBS-18 ($\delta^{13}C$, $\delta^{18}O$), and USGS 44 ($\delta^{13}C$) and reported relative to VPDB. Analytical uncertainties of $\delta^{13}C$ and $\delta^{18}O$ values are ± 0.1 ‰ based on replicate standard analyses.

References

McCrea, J. M. (1950). On the isotope chemistry of carbonates and a paleotemperature scale. The Journal of Chemical Physics,18(6),849–857

SUPPLEMENTARY FIGURES

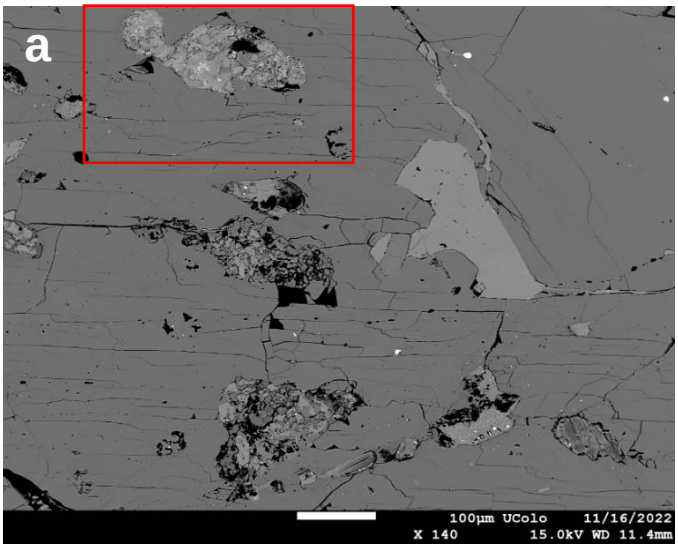

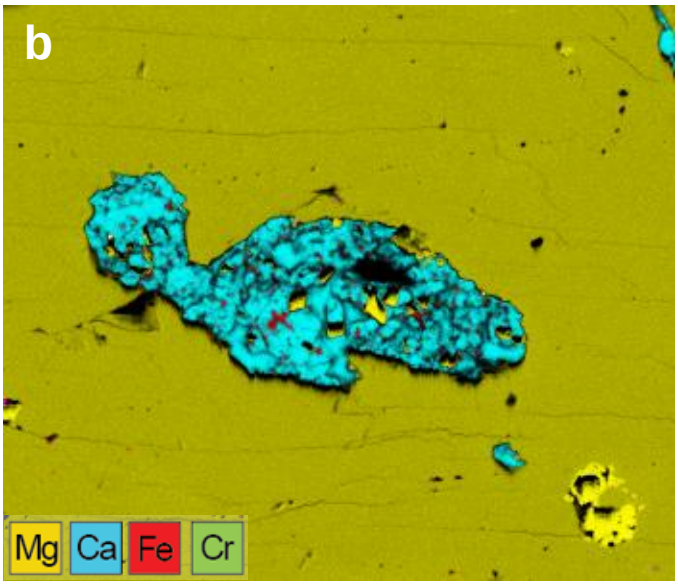

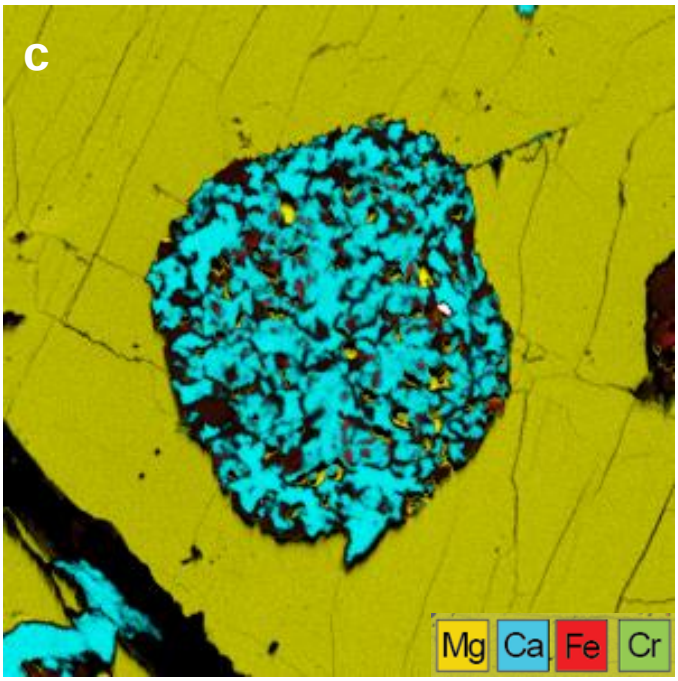
c
Mg
Ca
Fe
Cr

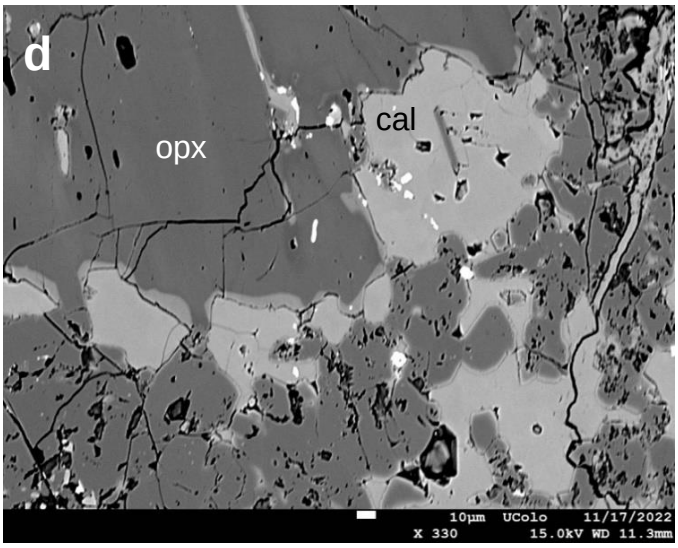
d
opx
cal
10µm UColo 11/17/2022
X 330 15.0kV WD 11.3mm

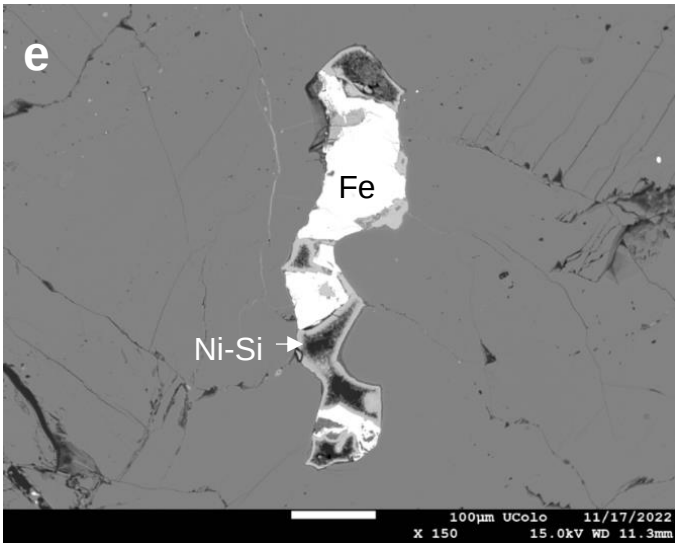
e
Fe
Ni-Si
100µm UColo 11/17/2022
X 150 15.0kV WD 11.3mm

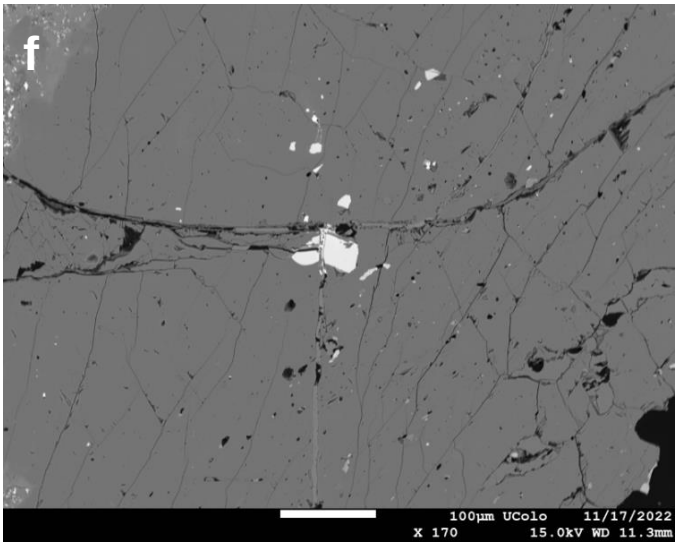
f
100µm UColo 11/17/2022
X 170 15.0kV WD 11.3mm

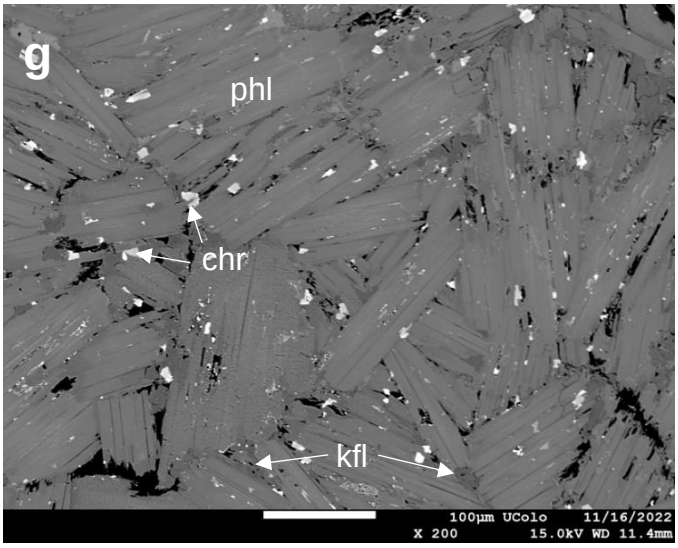
g
phl
chr
kfl
100µm UColo 11/16/2022
X 200 15.0kV WD 11.4mm

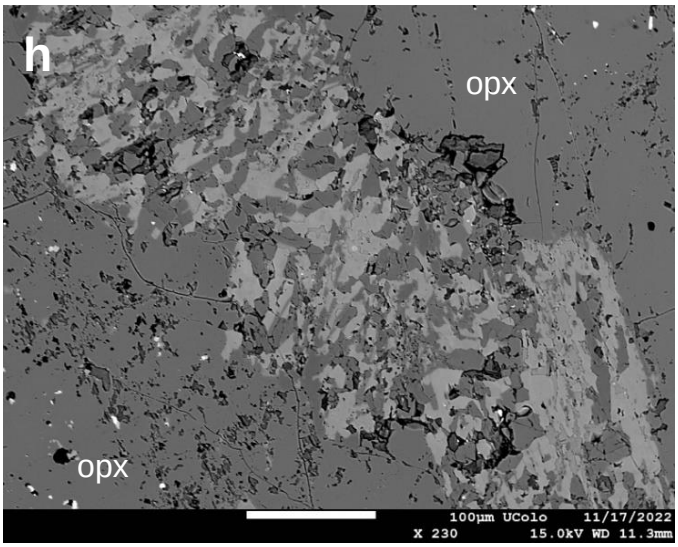
h
opx
opx
100µm UColo 11/17/2022
X 230 15.0kV WD 11.3mm

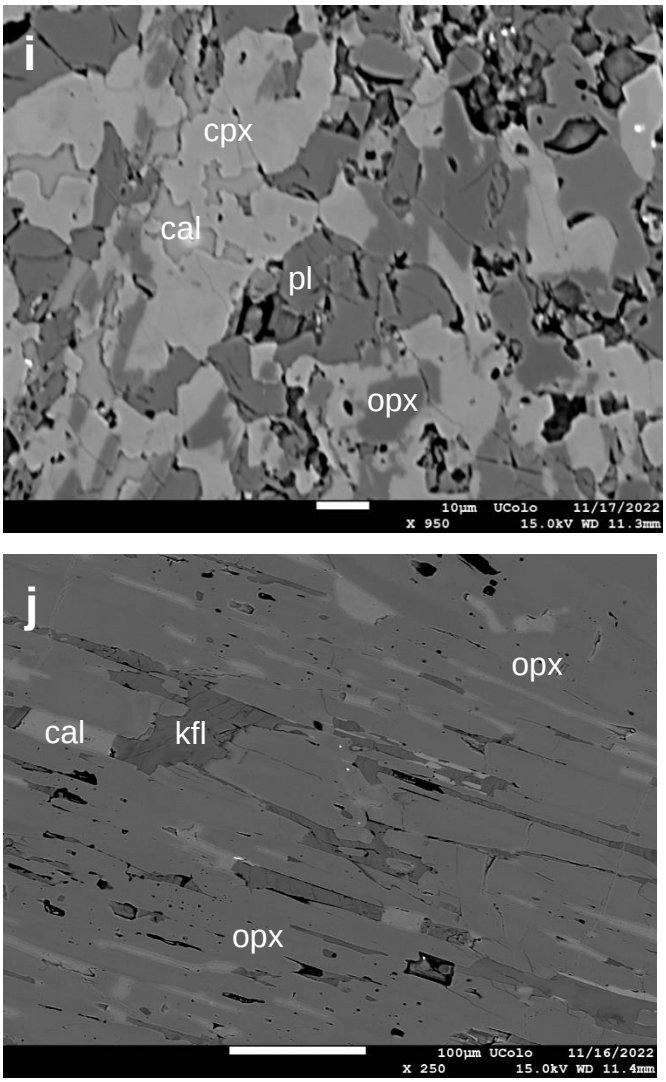

Figure C.1. Additional photomicrographs, BSE images, and chemical maps of xenoliths discussed in the text. a) Calcite inclusions in orthopyroxene, BSE image. c) Caclite inclusion element map, location shown in a). c) Calcite inclusion element map. d) Calcite inclusions in enstatite demonstrating mosaic texture of calcite. e) Large nickel silicate and Fe composite melt inclusion in enstatite. f) Fe-Al rich melt inclusions in enstatite. g) domain of phlogopite, chromite, and interstitial secondary K-feldspar in orthopyroxenite sample. h) Secondary mineral assemblage of calcite, orthopyroxene, clinopyroxene, and plagioclase hosted in orthopyroxene. i) higher magnification view of h). j) Secondary alteration assemblage of K-feldspar and calcite in orthopyroxene. Mineral abbreviations: cal–calcite, chr–chromite, cpx–clinopyroxene, kfl–K-feldspar, opx–orthopyroxene, phl–phlogopite, pl–plagioclase

.

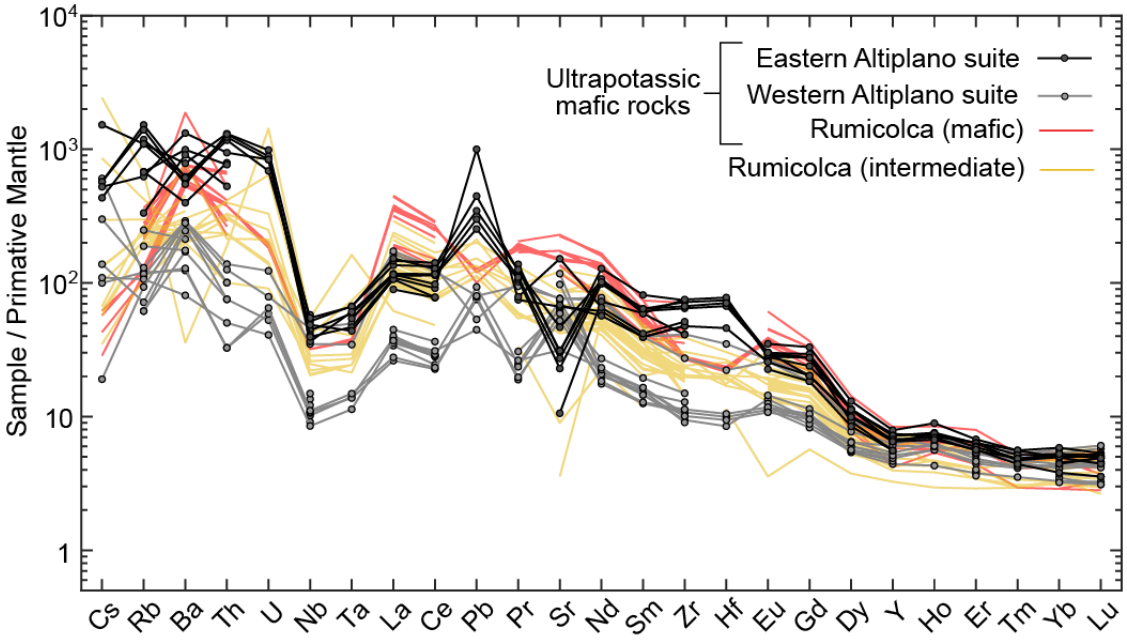

Figure C.2. Primitive mantle normalized trace element compositions of Rumicolca lavas compared to Eastern Altiplano and Western Altiplano Neogene potassic basalts.

SUPPLEMENTARY TABLES

Table C1. Lithology, primary mineralogy, and observations of individual xenoliths discussed in text.

Sample ID	lithology	Primary Mineralogy	Notes
Orthopyroxenite Suite			
CH19RX-48	Harzburgite	enstatite + olivine + spinel	Jagged interlocking enstatite. Olivine is rounded/resorbed at contact with enstatite. Olivine altered to iddingsite. Localized turbid domains of secondary cpx + plagioclase+ calcite. Enstatite contains small inclusions of calcite, Ni-S melt inclusions, and Fe-Al-rich melt inclusions
CH19RX-49	Harzburgite	enstatite + olivine + spinel	Same observations as CH19RX-48
CH19RX-66	Phlogopite orthopyroxenite - heavily altered	enstatite + flourophlogopite + calcite + spinel + melt, secondary diopside + K-feldspar	Jagged interlocking enstatite heavily altered to calcite + K-felsdpar + cpx, primarily along cleavage. Near melt, opx has recrystallize to larger opx+cpx intergrowths. Melt domains localized near phlogopite. Cross cutting calcite veins.
CH19RX-69	Phlogopite orthopyroxenite	enstatite + flourophlogopite + calcite + spinel	Jagged interlocking enstatite. Clusters of phlogopite. Contains abundant small inclusions primarily of calcite and olivine. Cross cutting calcite veins.
CH19RX-70	Olivine orthopyroxenite - fine grained, altered	enstatite + calcite + spinel + olivine + minor flourophlogopite	Enstitite displays fine-grained, acicular, radiating habit. Small rounded olivine crystals, largely altered to iddingsite. Calcite is interstitial throughout or found filling in small pockets/globules
CH19RX-46	Orthopyroxenite	enstatite, minor spinel + melt	Jagged interlocking enstatite. Turbid melt domains.
other carbonated lithologies			
CH19RX-47	Sheared phlogopite schist with calcite	phlogopite + calcite + spinel + minor enstatite; secondary plagioclase	Strongly foliated phlogopite with isolated shear textures. Small spinel crystals throughout. Interstitial calcite throughout, most prominent in regions displaying shear fabrics.
CH19RX-71	Carbonated peridotite with plagioclase?	olivine + diopside + minor apatite; secondary: calcite, plagioclase, amphibole(?)	Carbonate and plagioclase found in zones with grungy primary diopside and olivine. Amphibole(?) as uralitic rims on diopside.

Table C.2. Mineral compositions of phlogopite orthopyroxenite and harzburgite xenoliths.

Sample	**CH19RX-48**		**CH19RX-49**		**CH19RX-66**		**CH19RX-69**	
Phase[1]	***opx***	***ol***	***opx***	***ol***	***opx***	***phlog***	***opx***	***phlog***
	n=3	*n=3*	*n=4*	*n=4*	*n=5*	*n=7*	*n=4*	*n=4*
SiO_2	57.83	40.73	57.28	40.16	56.92	39.69	57.90	40.10
TiO_2	0.02	0.00	0.00	0.02	0.01	0.31	0.01	0.43
Al_2O_3	0.33	0.00	0.57	0.00	0.63	13.29	0.13	12.80
FeO*	6.12	8.79	7.90	11.98	7.22	3.50	6.43	3.18
MnO	0.17	0.14	0.17	0.12	0.22	0.02	0.14	0.02
MgO	35.60	50.37	34.06	47.75	33.46	24.91	35.24	25.56
CaO	0.09	0.01	0.08	0.01	0.99	0.05	0.11	0.08
Na_2O	0.01	0.00	0.01	0.00	0.03	0.97	0.00	1.04
K_2O	0.00	0.00	0.01	0.00	0.01	9.47	0.00	9.19
NiO	0.09	0.53	0.06	0.34	0.22	0.18	0.23	0.17
Cr_2O_3	0.05	0.00	0.03	0.01	0.25	1.26	0.14	1.12
Cl	0.00	0.00	0.00	0.00	0.00	0.10	0.00	0.08
F	0.00	0.00	0.01	0.02	0.02	9.94	0.00	10.24
Total	100.31	100.58	100.17	100.41	99.99	99.48	100.34	99.67
Si	1.98	0.99	1.98	0.99	1.98	2.87	1.99	2.89
Ti	0.00	0.00	0.00	0.00	0.00	0.02	0.00	0.02
Al	0.01	0.00	0.02	0.00	0.03	1.13	0.01	1.09
Fe	0.18	0.18	0.23	0.25	0.21	0.21	0.18	0.19
Mn	0.00	0.00	0.00	0.00	0.01	0.00	0.00	0.00
Mg	1.82	1.83	1.76	1.76	1.73	2.68	1.81	2.74
Ca	0.00	0.00	0.00	0.00	0.04	0.00	0.00	0.01
Na	0.00	0.00	0.00	0.00	0.00	0.14	0.00	0.15
K	0.00	0.00	0.00	0.00	0.00	0.88	0.00	0.85
Ni	0.00	0.01	0.00	0.01	0.01	0.01	0.01	0.01
Cr	0.00	0.00	0.00	0.00	0.01	0.11	0.01	0.09
Total	4.01	3.01	4.01	3.01	4.01	8.04	4.01	8.03
Oxygen	6	4	6	4	6	11	6	11
Mg#	91.20	91.08	88.49	87.66	89.19	92.69	90.71	93.41
Wo	0.17	-	0.15	-	1.86	-	0.20	-
En	91.04	-	88.35	-	87.53	-	90.53	-
Fs	8.79	-	11.50	-	10.61	-	9.27	-

*FeO as total Fe

Table C.3. Trace element compositions of xenolith samples

Lithology	harzburgite		phlogopite orthopyroxenite		
Sample	RX-48	RX-49	RX-66mp	RX-66c	RX-69
V	72	93	32	21	18
Cr	1828	1359	3927	1532	1762
Mn	1146	1115	1245	1598	1327
Co	88.2	110.5	64.0	63.7	71.7
Ni	1682	1223	1463	1445	1718
Cu	31.1	36.9	57.9	32.6	27.5
Zn	173	185	200	134	240
Ga	3.04	3.37	6.07	3.31	5.34
Rb	2.41	3.23	41.67	18.16	22.20
Sr	57.4	46.9	78.3	86.3	34.3
Y	6.472	6.000	11.234	7.112	1.798
Zr	7.6	6.9	15.0	15.2	10.0
Nb	0.411	0.357	1.611	0.758	1.625
Cs	0.337	0.343	1.053	0.955	0.657
Ba	29.6	41.3	163.0	90.1	107.6
La	9.314	14.234	3.777	2.852	3.790
Ce	3.063	3.043	8.358	6.094	4.011
Pr	0.828	1.007	1.433	0.945	0.573
Nd	3.142	3.620	6.911	4.501	2.159
Sm	0.548	0.511	1.816	1.169	0.349
Eu	0.178	0.096	0.462	0.312	0.074
Gd	0.662	0.571	1.898	1.150	0.295
Tb	0.089	0.069	0.303	0.173	0.035
Dy	0.639	0.490	1.890	1.142	0.252
Ho	0.149	0.119	0.380	0.235	0.049
Er	0.534	0.401	1.124	0.733	0.171
Tm	0.068	0.058	0.167	0.109	0.023
Yb	0.565	0.453	1.183	0.710	0.198
Lu	0.084	0.078	0.159	0.120	0.030
Hf	0.198	0.169	0.298	0.298	0.272
Ta	0.000	0.000	0.093	0.035	0.061
Pb	0.202	11.49	15.45	13.57	12.90
Th	0.372	0.357	0.620	0.374	0.766
U	0.405	0.420	0.321	0.392	0.206

Table C.3 continued.

Lithology	olivine-spinel orthopyroxenite	orthopyroxenite	wehrlite	phlogopite schist
Sample	**RX-70**	**RX-46**	**RX-71**	**RX-47**
V	60	44	109	175
Cr	3215	2034	35	1275
Mn	714	820	1809	489
Co	80.6	83.6	20.5	96.5
Ni	1364	1969	32	750
Cu	79.8	9.8	29.5	48.6
Zn	242	104	233	435
Ga	3.89	3.83	12.80	14.34
Rb	2.12	4.86	2.49	214.67
Sr	122.6	54.1	262.4	129.6
Y	3.564	0.884	17.706	8.453
Zr	24.4	7.4	68.1	10.3
Nb	0.468	0.472	4.850	0.453
Cs	0.564	0.064	0.146	7.486
Ba	39.8	85.1	199.5	237.9
La	8.639	1.817	19.824	21.128
Ce	4.189	3.932	41.342	4.125
Pr	0.764	0.372	5.745	1.466
Nd	2.651	1.368	24.342	5.063
Sm	0.342	0.211	4.966	0.664
Eu	0.067	0.056	1.216	0.143
Gd	0.347	0.187	4.264	0.757
Tb	0.038	0.020	0.580	0.079
Dy	0.282	0.164	3.200	0.504
Ho	0.062	0.028	0.617	0.125
Er	0.228	0.099	1.742	0.405
Tm	0.027	0.011	0.248	0.049
Yb	0.258	0.108	1.673	0.351
Lu	0.043	0.012	0.264	0.060
Hf	0.588	0.176	2.027	0.125
Ta	0.000	0.017	0.204	0.000
Pb	17.92	0.899	19.60	79.11
Th	0.482	0.332	3.450	0.185
U	0.873	0.051	0.993	0.401

Table C.4. New and previously reported major and trace element compositions of Neogene and Quaternary alkaline lavas from Southern Peru

Volcanic Suite	Rumicolca (Intermediate)	Rumicolca (Intermediate)	Rumicolca (Intermediate)	Rumicolca (Intermediate)	Rumicolca (Intermediate)	Rumicolca (Intermediate)	Rumicolca (Intermediate)
Data Source	Our data	Our data	Our data	Mamani et al., (2010)	Mamani et al., (2010)	Mamani et al., (2010)	Mamani et al., (2010)
Classification	Latite	Latite	Andesite	Dacite	Dacite	Dacite	Rhyolite
SampleID	Huarocando	Oropesa	Huambutio	SHO-01-74	SHO-01-67	8_11_01	SHO-01-66-1
SiO2 (wt%)	62.13	60.99	62.42	64.00	64.50	64.30	72.70
TiO_2	1.04	0.82	0.83	0.82	0.81	0.82	0.24
Al_2O_3	16.12	15.29	16.71	16.90	17.30	17.30	14.50
FeO*	5.09	4.64	4.30	*3.88*	*3.52*	*3.59*	*1.56*
Fe_2O_3*	*5.66*	*5.15*	*4.78*	4.31	3.91	3.99	1.73
MnO	0.08	0.07	0.07	0.07	0.07	0.07	0.06
MgO	2.46	3.49	2.53	2.41	2.27	2.27	0.50
CaO	4.89	5.09	4.42	4.17	4.06	4.14	1.01
Na_2O	4.08	3.10	2.42	2.62	2.51	2.55	3.78
K_2O	2.79	4.97	4.05	3.75	3.83	3.79	4.38
P_2O_5	0.35	0.59	0.38	0.33	0.35	0.35	0.28
LOI %	0.66	0.12	1.38				
Mg#	46.28	57.28	51.21	52.56	53.49	52.99	36.41
Sc (ppm)	9.08	12.36	12.95	9.00	13.00	15.00	6.00
V	99.88	113.60	115.24	108.00	105.00	108.00	12.00
Cr	36.8	106.2	66.3	60	46	44	17
Co							
Ni	30.10	46.55	11.39	11.00	11.00	11.00	6.00
Cu	20.16	15.81	9.59	7.00	9.00	9.00	-4.00
Zn	80.10	96.78	97.96	89.00	101.00	101.00	55.00
Rb	64.30	139.23	123.11	114.70	116.40	160.90	
Sr	1241.64	1713.37	1074.17	839.10	835.40	1308.20	
Y	18.70	30.44	26.41	21.00	18.10	28.00	
Zr	249.04	305.40	243.81	207.50	214.40	253.20	
Nb	16.28	18.80	14.57	13.40	13.70	17.10	
Cs	0.73	2.76	2.11	1.30	1.20	1.40	
Ba	1320	2006	1324	1337.70	1601.50	1600.00	
La	66.737	153.999	90.824	61.80	63.50	106.90	
Ce	123.941	282.808	175.388	130.40	135.30	206.60	
Pr	13.759	33.784	20.689	14.60	15.20	25.20	
Nd	50.919	126.566	78.038	56.00	58.30	90.00	
Sm	8.187	19.882	12.815	9.10	9.30	15.30	
Eu	2.259	4.794	3.010	2.00	2.00	2.90	
Gd	5.822	12.353	8.639	6.50	6.40	12.00	
Tb	0.786	1.597	1.153	0.80	0.70	1.10	
Dy	3.518	6.161	5.338	4.20	3.80	6.00	
Ho	0.636	1.045	0.930	0.70	0.70	0.90	
Er	1.650	2.543	2.409	1.80	1.50	2.90	
Tm	0.230	0.336	0.323	0.30	0.20	0.30	
Yb	1.437	2.034	2.153	1.70	1.40	2.10	
Lu	0.199	0.278	0.300	0.20	0.20	0.30	
Hf	4.802	4.981	5.747	5.40	5.60	7.20	
Ta	0.791	1.081	0.899	0.90	0.90	1.00	
Pb	16.958	29.990	20.205	16.50	18.60	22.90	
Th	7.989	31.706	24.007	18.40	18.70	25.20	
U	1.846	6.684	3.993	2.80	2.90	3.90	
La/Yb	46.43	75.72	42.19	36.35	45.36	50.90	
Sr/Y	66.41	56.29	40.67	39.96	46.15	46.72	

Table C.4 Continued.

Volcanic Suite	Rumicolca (Intermediate)	Rumicolca (Intermediate)	Rumicolca (Intermediate)	Rumicolca (Intermediate)	Rumicolca (Intermediate)	Rumicolca (Intermediate)	Rumicolca (Intermediate)
Data Source	Carlotto et al., (2011)	Carlotto et al., (2011)	Carlotto et al., (2011)	Carlotto et al., (2011)	Carlotto et al., (2011)	Carlotto et al., (2011)	Carlotto et al., (2011)
Classification	Andesite	Andesite	Dacite	Dacite	Andesite	Dacite	Latite
SampleID	Cz20	Cz21	OR10	OR10b	Cz18	Ti1	Orop1
SiO2 (wt%)	62.49	62.84	64.33	63.92	61.34	63.87	61.45
TiO_2	0.77	0.78	0.79	0.80	0.81	0.81	0.83
Al_2O_3	16.61	16.76	17.37	17.47	16.35	16.78	14.93
FeO*	*3.90*	*3.96*	*3.79*	*3.84*	*4.76*	*4.29*	*4.64*
Fe_2O_3*	4.33	4.40	4.21	4.27	5.29	4.77	5.16
MnO	0.06	0.06	0.06	0.06	0.07	0.06	0.05
MgO	2.50	2.52	2.57	2.51	2.54	2.45	2.92
CaO	4.17	4.12	4.01	3.94	4.52	4.05	4.40
Na_2O	2.50	2.52	2.48	2.39	2.45	2.49	3.20
K_2O	3.60	3.65	3.74	3.74	4.10	3.54	4.80
P_2O_5	0.40	0.40	0.32	0.32	0.45	0.39	0.48
LOI %	1.74	1.05	0.80	0.62	0.74	0.32	1.21
Mg#	53.35	53.15	54.74	53.80	48.75	50.43	52.85
Sc (ppm)	12.00	12.00			14.00	13.00	12.00
V	101.00	95.00	99.00	100.00	117.00	111.00	110.00
Cr							
Co	6.00				9.00	6.00	11.00
Ni	17.00	10.00	11.00	12.00	27.00	14.00	29.00
Cu							
Zn							
Rb	137.00	128.00	116.00	119.00	143.00	123.00	157.00
Sr	960.00	952.00	913.00	901.00	1099.00	1099.00	1340.00
Y	23.00	22.00	32.00	28.00	29.00	26.00	25.00
Zr	206.00	205.00	86.00	94.00	231.00	203.00	288.00
Nb	14.00	13.00	13.00	12.00	15.00	13.00	14.00
Cs							
Ba	1583.00	1611.00	1708.00	1688.00	1439.00	1304.00	1595.00
La	78.30	76.84			97.58	79.62	109.86
Ce	140.49	138.72			174.43	144.18	195.08
Pr							
Nd	63.08	61.02			82.79	67.06	91.90
Sm	11.21	11.17			14.37	12.02	15.99
Eu	2.51	2.44			3.22	2.64	3.46
Gd	7.72	7.60			9.71	8.35	10.11
Tb							
Dy	4.66	4.53			5.63	5.12	5.29
Ho							
Er	2.16	2.08			2.68	2.35	2.40
Tm							
Yb	1.87	1.76			2.37	2.05	1.97
Lu	0.32	0.30			0.39	0.33	0.34
Hf							
Ta							
Pb							
Th							
U							
La/Yb	41.87	43.66			41.17	38.84	55.77
Sr/Y	41.74	43.27	28.53	32.18	37.90	42.27	53.60

Table C.4 continued.

Volcanic Suite	Rumicolca (Intermediate)	Rumicolca (Intermediate)	Rumicolca (Intermediate)	Rumicolca (Intermediate)	Rumicolca (Intermediate)	Rumicolca (Intermediate)	Rumicolca (Intermediate)
Data Source	Carlotto et al., (2011)	Carlotto et al., (2011)	Carlotto et al., (2011)	Carlotto et al., (2011)	Carlotto et al., (2011)	Carlotto et al., (2011)	Carlotto et al., (2011)
Classification	Latite	Dacite	Dacite	Dacite	Dacite	Andesite	Andesite
SampleID	Orop2	Cz22	Ms21	Rumi2	Rumi1	Or9	Ca1
SiO2 (wt%)	61.40	64.00	63.39	63.79	64.34	61.88	62.99
TiO_2	0.81	0.75	0.83	0.81	0.81	0.84	0.84
Al_2O_3	15.83	16.67	16.78	16.79	17.10	16.50	17.10
FeO*	*4.61*	*3.81*	*4.35*	*4.19*	*3.67*	*4.39*	*4.60*
Fe_2O_3*	5.12	4.23	4.83	4.66	4.08	4.88	5.11
MnO	0.06	0.07	0.06	0.06	0.05	0.06	0.03
MgO	2.29	2.22	2.32	2.43	2.20	2.43	2.50
CaO	4.69	4.42	4.29	4.22	4.00	4.48	2.16
Na_2O	2.77	2.65	2.62	2.61	2.52	2.45	2.45
K_2O	4.55	3.69	3.83	3.59	3.72	3.96	4.08
P_2O_5	0.50	0.40	0.34	0.38	0.38	0.37	0.44
LOI %	1.35	0.59	0.21	0.22	0.38	1.69	1.78
Mg#	46.98	50.97	48.76	50.81	51.65	49.66	49.22
Sc (ppm)	14.00	13.00	13.00	13.00	11.00	10.00	12.00
V	109.00	103.00	106.00	110.00	107.00	111.00	121.00
Cr							
Co	8.00	5.00	9.00	7.00	6.00	6.00	6.00
Ni	15.00	14.00	15.00	14.00	13.00	12.00	10.00
Cu							
Zn							
Rb	150.00	134.00	120.00	121.00	132.00	118.00	137.00
Sr	1700.00	962.00	71.00	971.00	997.00	945.00	993.00
Y	32.00	23.00	25.00	22.00	21.00	26.00	28.00
Zr	270.00	199.00	219.00	198.00	191.00	232.00	241.00
Nb	14.00	12.00	7.00	12.00	12.00	13.00	14.00
Cs							
Ba	1846.00	1559.00	1504.00	1300.00	1364.00	1279.00	1300.00
La	136.24	73.48	76.70	66.56	76.91	82.92	84.44
Ce	233.41	134.49	142.00	122.67	140.71	157.90	166.70
Pr							
Nd	109.58	60.97	65.85	55.15	63.98	75.51	75.82
Sm	19.19	11.18	12.03	10.01	11.46	12.37	13.21
Eu	4.30	2.52	2.78	2.18	2.55	2.72	2.91
Gd	12.07	7.57	8.50	6.97	7.61	8.70	8.91
Tb							
Dy	6.37	4.66	5.06	4.37	4.49	5.38	5.58
Ho							
Er	2.92	2.17	2.24	2.08	2.00	2.65	2.78
Tm							
Yb	2.49	1.92	2.04	1.84	1.66	2.38	2.36
Lu	0.41	0.31	0.36	0.29	0.26	0.34	0.37
Hf							
Ta							
Pb							
Th							
U							
La/Yb	54.71	38.27	37.60	36.17	46.33	34.84	35.78
Sr/Y	53.13	41.83	2.84	44.14	47.48	36.35	35.46

Table C.4 continued.

Volcanic Suite	Rumicolca (Intermediate)	Rumicolca (Intermediate)	Rumicolca (Intermediate)	Rumicolca (Intermediate)	Rumicolca (Intermediate)	Rumicolca (mafic)	Rumicolca (mafic)
Data Source	Carlotto et al., (2011)	Carlotto et al., (2011)	Carlotto et al., (2011)	Carlier and Lorand (2008)	Carlier and Lorand (2008)	Our data	Mamani et al., (2010)
Classification	Andesite	Dacite	Andesite	Trachydacite	Rhyolite	latite / banakite	latite / banakite
SampleID	Ms22	Rc1	Rc2	Oroscocha trachydacite	Oroscocha rhyolite	Quimsachata	SHO-01-65 (Quimsachata)
SiO2 (wt%)	61.62	64.28	62.73	67.3	73.11		56.80
TiO_2	0.83	0.61	0.61	0.53	0.2		1.27
Al_2O_3	16.75	16.89	16.87	14.85	14.38		15.00
FeO*	*4.50*	*3.01*	*3.21*	*2.72*	1.1		*5.97*
Fe_2O_3*	5.00	3.34	3.57	3.02	0.27		6.63
MnO	0.06	0.05	0.05	0.06	0.06		0.09
MgO	2.47	2.47	2.54	1.61	0.36		5.51
CaO	4.50	4.02	4.47	2.24	0.88		5.65
Na_2O	2.41	2.88	3.01	3.35	3.69		2.84
K_2O	4.07	3.86	3.77	5.09	4.23		4.41
P_2O_5	0.38	0.40	0.50	0.43	0.25		0.61
LOI %	1.43	0.57	1.01	1.34	0.97		
Mg#	49.46	59.43	58.50	51.3	36.8		62.21
Sc (ppm)	14.00	8.00	9.00				22.00
V	117.00	76.00	87.00	42.00	11.00		116.00
Cr				57	8	190.2	197
Co	9.00	4.00	4.00	6.00	1.25		
Ni	18.00	7.00	5.00	15.00	3.20		51.00
Cu							11.00
Zn							98.00
Rb	130.00	154.00	142.00	254.00	397.00	179.03	176.50
Sr	1078.00	1756.00	2505.00	866.00	179.00	1137.45	1326.00
Y	25.00	18.00	21.00	17.00	14.00	27.00	22.30
Zr	221.00	152.00	150.00			320.38	341.20
Nb	8.00	14.00	14.00	27.00	36.00	17.36	23.80
Cs				18.00	51.00	6.221	4.30
Ba	1341.00	2271.00	2968.00	1480.00	236.00	1489.74	1961.50
La	81.37	145.50	188.00	96.00	40.00	101.869	116.10
Ce	149.10	257.00	333.00	185.00	81.00	196.261	225.50
Pr				20.00	8.50	21.493	27.00
Nd	69.04	106.10	138.00	69.00	28.00	76.894	92.60
Sm	12.46	14.50	18.27	11.00	4.82	12.086	15.00
Eu	2.87	3.20	4.10	2.12	0.55	2.672	2.90
Gd	8.42	10.20	12.61	6.38	3.09	7.549	11.70
Tb				0.80	0.48		1.00
Dy	4.95	4.56	5.52	3.69	2.53	4.153	5.20
Ho				0.57	0.44	0.672	0.80
Er	2.23	1.77	2.13	1.51	1.27	1.769	2.40
Tm				0.21	0.20	0.206	0.20
Yb	2.02	1.44	1.58	1.37	1.47	1.442	1.70
Lu	0.35	0.21	0.23	0.20	0.21	0.179	0.20
Hf				6.00	3.23	7.534	9.40
Ta				2.73	6.00	0.000	1.20
Pb						31.781	31.80
Th				33.00	15.00	26.144	27.60
U				13.00	29.00	5.057	4.80
La/Yb	40.28	101.04	118.99			70.63	68.29
Sr/Y	43.12	97.56	119.29			42.13	59.46

Table C.4 continued.

Volcanic Suite	Rumicolca (mafic)	Rumicolca (mafic)	Rumicolca (mafic)	Rumicolca (mafic)	Rumicolca (mafic)	Rumicolca (mafic)	Rumicolca (mafic)
Data Source	Mamani et al., (2010)	Calier et al. (2005)	Calier et al. (2005)	Calier et al. (2005)	Calier et al. (2005)	Calier et al. (2005)	Calier et al. (2005)
Classification	Kersantite (Oroschoch a enclaves)	Diopside phlogopite lamproite	Diopside phlogopite lamproite	Diopside phlogopite lamproite	Augite kersantite (Oroschoch a enclaves)	Augite kersantite (Oroschoch a enclaves)	Augite kersantite (Oroschoch a enclaves)
SampleID	SHO-01-66-2	12	13	14	15	16	17
SiO2 (wt%)	50.10	50.40	53.04	53.97	49.09	52.57	50.62
TiO_2	1.50	1.90	2.70	2.66	1.54	1.31	1.41
Al_2O_3	14.50	11.10	12.12	12.64	14.78	14.28	14.43
FeO*	*7.22*	*6.70*	*6.12*	*5.85*	*7.59*	*6.85*	*7.57*
Fe_2O_3*	8.02	7.45	6.80	6.50	8.44	7.61	8.41
MnO	0.12	0.09	0.06	0.06	0.12	0.12	0.12
MgO	7.87	4.56	4.42	4.30	8.16	7.30	7.40
CaO	6.99	7.11	6.14	5.96	7.26	6.84	7.00
Na_2O	2.79	1.87	1.56	1.77	2.77	3.12	2.92
K_2O	4.81	8.02	7.98	8.12	4.60	4.87	4.50
P_2O_5	1.28	2.46	1.79	1.79	1.25	1.27	1.25
LOI %		3.97	2.35	2.20	0.41	0.61	0.68
Mg#	66.03	55.00	56.00	57.00	66.00	65.00	64.00
Sc (ppm)	20.00	13.00	16.00	12.00	21.00	19.00	21.00
V	158.00	103.00	127.00	124.00	156.00	133.00	144.00
Cr	325	65	225	121	346	327	355
Co							
Ni	98.00	57.00	67.00	91.00	90.00	126.00	110.00
Cu	16.00						
Zn	92.00						
Rb	140.60	152.00	219.00	194.00	132.00	168.00	152.00
Sr	2413.70	4562.00	3414.00	3466.00	2364.00	2686.00	2708.00
Y	27.90	36.00	19.00	18.00	28.00	27.00	28.00
Zr	409.80	746.00	472.00	466.00	372.00	291.00	413.00
Nb	30.50	192.00	180.00	169.00	37.00	43.00	40.00
Cs	2.80						
Ba	5121.90	12389.00	4580.00	4753.00	5043.00	4927.00	5167.00
La	113.40	226.00	206.00	205.00	107.00	125.00	122.00
Ce	217.80	426.00	366.00	368.00	219.00	253.00	222.00
Pr	24.50	52.00		43.00			
Nd	93.30	199.00	154.00	157.00	90.00	94.00	99.00
Sm	14.50	30.00	19.00	20.00	16.00	17.00	17.00
Eu	3.60	9.40	5.30	5.40	4.27	4.26	4.36
Gd	10.40	20.00	13.00	15.00	11.00	11.00	12.00
Tb	1.10	2.10		1.33			
Dy	5.60	9.60	5.20	5.90	6.10	5.80	6.10
Ho	0.90	1.26		0.80			
Er	2.00	3.48	2.17	1.93	2.62	2.64	2.53
Tm	0.30	0.36		0.20			
Yb	1.80	2.37	1.28	1.27	1.97	1.83	2.03
Lu	0.30	0.35	0.22	0.19	0.38	0.38	0.34
Hf	8.60						
Ta	1.50						
Pb	20.00						
Th	17.00	42.00	33.00	33.00	21.00	23.00	18.00
U	4.30						
La/Yb	63.00	95.36	160.94	161.42	54.31	68.31	60.10
Sr/Y	86.51	126.72	179.68	192.56	84.43	99.48	96.71

Table C.4 continued.

Volcanic Suite	Rumicolca (mafic)	Rumicolca (mafic)	Rumicolca (mafic)	Rumicolca (mafic)	Rumicolca (mafic)	Rumicolca (mafic)	Rumicolca (mafic)
Data Source	Calier et al. (2005)	Calier et al. (2005)	Calier et al. (2005)	Calier et al. (2005)	Calier et al. (2005)	Calier et al. (2005)	Calier et al. (2005)
Classification	Augite minette	Augite minette	Augite trachybasalt	Augite trachybasalt	Augite trachybasalt	Augite trachybasalt	Augite trachybasalt
SampleID	18	19	20	21	22	23	24
SiO2 (wt%)	55.27	55.07	54.40	53.44	55.03	53.60	55.50
TiO_2	0.93	0.93	1.18	1.11	1.16	1.13	1.12
Al_2O_3	14.66	14.61	14.72	14.41	14.79	14.43	14.46
FeO*	*5.39*	*5.34*	*6.86*	*6.70*	*6.72*	*6.73*	*6.69*
Fe_2O_3*	5.99	5.94	7.62	7.45	7.47	7.48	7.43
MnO	0.08	0.08	0.10	0.10	0.09	0.10	0.08
MgO	5.37	5.33	6.61	6.36	6.35	6.27	6.50
CaO	7.00	6.93	7.04	6.98	7.08	6.76	7.26
Na_2O	3.35	3.29	3.31	3.06	3.34	3.12	3.39
K_2O	4.44	4.37	3.34	3.21	3.40	3.25	3.22
P_2O_5	1.04	1.04	0.87	0.79	0.83	0.78	0.83
LOI %	0.55	0.54	0.77	0.61	0.41	1.22	0.38
Mg#	64.00	64.00	63.00	63.00	63.00	62.00	63.00
Sc (ppm)	15.00	15.00	13.00	13.00	13.00	13.00	17.00
V	125.00	125.00	139.00	135.00	124.00	137.00	137.00
Cr	85	86	305	293	288	278	308
Co							
Ni	43.00	41.00	151.00	185.00	173.00	128.00	183.00
Cu							
Zn							
Rb	136.00	127.00	63.00	73.00	71.00	77.00	79.00
Sr	4550.00	4446.00	3026.00	3028.00	2985.00	2928.00	3430.00
Y	29.00	30.00	25.00	28.00	27.00	27.00	28.00
Zr	292.00	292.00	290.00	295.00	282.00	288.00	281.00
Nb	24.00	24.00	21.00	21.00	21.00	21.00	20.00
Cs			0.90	1.30	0.60	1.20	
Ba	5028.00	4938.00	3461.00	3688.00	3500.00	3623.00	3890.00
La	286.00	291.00	231.00	233.00	241.00	234.00	248.00
Ce	475.00	485.00	427.00	427.00	449.00	425.00	413.00
Pr			45.00	48.00	50.00	47.00	
Nd	205.00	208.00	166.00	172.00	173.00	170.00	175.00
Sm	30.00	30.00	22.00	23.00	23.00	21.00	26.00
Eu	7.00	6.90	5.60	5.90	6.00	5.70	5.60
Gd	18.00	18.00	14.00	14.00	14.00	14.00	15.00
Tb			1.41	1.53	1.48	1.57	
Dy	7.00	7.10	6.90	6.90	6.80	7.60	6.40
Ho			0.83	0.97	0.84	0.94	
Er	2.86	2.95	2.49	2.72	2.71	2.80	2.71
Tm			0.28	0.31	0.31	0.30	
Yb	1.98	2.00	1.84	2.11	2.11	2.21	2.01
Lu	0.38	0.36	0.28	0.34	0.25	0.32	0.34
Hf			6.40	6.70	6.10	6.50	
Ta			1.36	1.35	1.41	1.39	
Pb			18.00	19.00	15.00	19.00	
Th	54.00	52.00	30.00	30.00	30.00	30.00	31.00
U			4.03	3.72	3.95	3.98	
La/Yb	144.44	145.50	125.54	110.43	114.22	105.88	123.38
Sr/Y	156.90	148.20	121.04	108.14	110.56	108.44	122.50

Table C.4 continued.

Volcanic Suite	Rumicolca (mafic)	Weatern Altiplano (K-UK mafic)	Weatern Altiplano (K-UK mafic)	Weatern Altiplano (K-UK mafic)	Weatern Altiplano (K-UK mafic)	Weatern Altiplano (K-UK mafic)	Weatern Altiplano (K-UK mafic)
Data Source	Carlier and Lorand (2008)	Calier et al. (2005)	Calier et al. (2005)	Calier et al. (2005)	Calier et al. (2005)	Calier et al. (2005)	Calier et al. (2005)
Classification	Kersantite (Oroschocha enclaves)	Leucitite	Leucite tephrite	Leucite tephrite	Diopside theralite	Diopside theralite	Leucite phonotephrite
SampleID	Kersantite	1	2	3	4	5	6
SiO2 (wt%)	49.38	45.78	45.46	46.72	47.31	49.00	47.32
TiO_2	1.56	0.97	1.06	0.93	1.14	1.37	0.96
Al_2O_3	14.63	11.78	11.57	11.80	13.38	14.86	13.18
FeO*	4.11	*10.48*	*11.34*	*9.44*	*10.51*	*10.80*	*9.89*
Fe_2O_3*	3.89	11.65	12.60	10.49	11.68	12.00	10.99
MnO	0.13	0.18	0.20	0.17	0.18	0.17	0.17
MgO	8.2	7.91	7.25	7.58	5.80	4.88	6.05
CaO	7.24	11.29	11.08	11.07	10.76	6.77	9.44
Na_2O	2.75	3.65	4.16	3.97	1.64	3.39	4.62
K_2O	4.52	1.46	1.43	1.97	5.18	4.41	2.16
P_2O_5	1.38	0.86	0.86	0.76	0.68	0.97	0.81
LOI %	0.48	4.42	3.80	3.72	1.95	0.94	3.67
Mg#	78	57.00	53.00	59.00	50.00	45.00	52.00
Sc (ppm)		24.00	35.00	33.00	22.00	23.00	28.00
V	174.00	301.00	335.00	270.00	260.00	311.00	291.00
Cr	347	140	139	264	69	29	114
Co	29.00						
Ni	89.00	44.00	48.00	75.00	30.00	26.00	42.00
Cu							
Zn							
Rb	128.00	43.00	37.00	67.00	149.00	113.00	37.00
Sr	2153.00	1468.00	1273.00	2336.00	1317.00	1240.00	1939.00
Y	2.86	19.00	22.00	20.00	23.00	27.00	22.00
Zr	415.00	99.00	95.00	108.00	135.00	157.00	110.00
Nb	36.00	6.70	6.00	7.00	8.90	9.80	8.00
Cs	3.13	2.90					
Ba	4880.00	1734.00	1132.00	1871.00	1405.00	1157.00	1622.00
La	114.00	25.00	22.00	24.00	23.00	29.00	26.00
Ce	229.00	48.00	41.00	47.00	48.00	61.00	49.00
Pr	24.00	6.30			6.00	7.80	
Nd	98.00	26.00	25.00	27.00	26.00	34.00	28.00
Sm	16.00	5.90	6.40	6.60	6.10	7.90	6.70
Eu	4.25	2.08	1.75	1.75	1.93	2.22	1.81
Gd	10.00	5.20	5.50	5.40	5.20	6.20	5.70
Tb	1.30	0.66			0.73	0.98	
Dy	6.23	3.64	4.04	3.74	4.38	5.20	4.03
Ho	1.00	0.64			0.94	1.05	
Er	2.53	1.65	1.71	1.58	2.12	2.55	1.76
Tm	0.33	0.24			0.29	0.37	
Yb	2.13	1.45	1.54	1.42	1.89	2.35	1.64
Lu	0.31	0.22	0.21	0.21	0.31	0.39	0.24
Hf	9.00	2.40					
Ta	2.12	0.52					
Pb		14.00					
Th	19.00	6.00	6.00	8.00			8.00
U	4.09	1.07					
La/Yb		17.24	14.29	16.90	12.17	12.34	15.85
Sr/Y		77.26	57.86	116.80	57.26	45.93	88.14

Table C.4 continued.

Volcanic Suite	Weatern Altiplano (K-UK mafic)	Weatern Altiplano (K-UK mafic)	Weatern Altiplano (K-UK mafic)	Weatern Altiplano (K-UK mafic)	Weatern Altiplano (K-UK mafic)	Eastern Altiplano (K-UK mafic)	Eastern Altiplano (K-UK mafic)
Data Source	Calier et al. (2005)	Calier et al. (2005)	Calier et al. (2005)	Calier et al. (2005)	Calier et al. (2005)	Calier et al. (2005)	Calier et al. (2005)
Classification	Diopside trachybasalt	Diopside trachybasalt	Diopside trachybasalt	Olivine trachybasalt	Olivine trachybasalt	sanadine phlogopite lamproite	sanadine phlogopite lamproite
SampleID	7	8	9	10	11	12	13
SiO2 (wt%)	46.39	46.48	47.65	47.37	52.53	56.28	59.20
TiO_2	1.47	1.47	1.25	1.36	2.29	1.51	1.56
Al_2O_3	15.66	15.74	16.02	13.02	15.07	12.88	13.33
FeO*	*9.63*	*9.51*	*9.77*	*7.70*	*8.41*	*5.53*	*4.68*
Fe_2O_3*	10.70	10.57	10.86	8.56	9.35	6.15	5.20
MnO	0.17	0.18	0.18	0.13	0.12	0.08	0.03
MgO	6.49	6.08	7.41	10.30	3.90	7.58	5.50
CaO	10.10	10.49	10.20	8.54	6.79	3.43	2.09
Na_2O	2.96	3.22	2.50	1.77	4.30	1.48	0.83
K_2O	2.63	2.47	2.12	4.28	3.36	7.94	8.00
P_2O_5	0.66	0.65	0.42	0.87	1.08	1.16	1.34
LOI %	2.28	2.26	1.34	3.39	1.14	1.97	1.97
Mg#	55.00	53.00	57.00	70.00	45.00	71.00	68.00
Sc (ppm)			25.00		13.00		11.00
V	265.00	265.00	313.00	189.00	183.00	113.00	125.00
Cr	55	52	204	610	162	449	567
Co							
Ni	32.00	32.00	57.00	247.00	90.00	209.00	141.00
Cu							
Zn							
Rb	72.00	70.00	64.00	78.00	56.00	658.00	709.00
Sr	1177.00	1041.00	625.00	1527.00	1513.00	928.00	602.00
Y	21.00	22.00	26.00	30.00	29.00	32.00	34.00
Zr	113.00	119.00	106.00	287.00	434.00	755.00	779.00
Nb	7.10	7.30	5.60	23.00	30.00	34.00	38.00
Cs	2.10	12.70	2.30	6.30	0.40	32.00	
Ba	819.00	848.00	533.00	1922.00	1854.00	5180.00	4126.00
La	17.00	18.00	24.00	107.00	112.00	88.00	95.00
Ce	38.00	39.00	52.00	205.00	219.00	223.00	237.00
Pr	4.80	5.00	6.70	24.00	26.00	31.00	35.00
Nd	22.00	23.00	29.00	92.00	97.00	130.00	160.00
Sm	5.10	5.20	5.90	16.00	16.00	26.00	33.00
Eu	1.73	1.81	1.66	3.97	4.12	4.67	5.40
Gd	4.50	4.80	5.20	10.00	11.00	15.00	18.00
Tb	0.67	0.69	0.75	1.39	1.37	1.79	2.01
Dy	3.71	3.80	4.33	6.30	6.60	7.60	8.80
Ho	0.84	0.84	0.89	0.90	1.03	1.06	1.33
Er	1.95	2.03	2.26	2.33	2.44	2.78	2.96
Tm	0.28	0.29	0.36	0.31	0.32	0.38	0.38
Yb	1.88	1.91	2.51	1.80	1.95	2.18	2.58
Lu	0.30	0.31	0.41	0.29	0.28	0.30	0.36
Hf	2.82	2.97	2.67	6.30	9.90	21.00	
Ta	0.51	0.55	0.42	1.28	1.84	2.48	
Pb	11.30	11.80	6.70	12.00	8.00	67.00	
Th	2.60	2.60	4.00	11.00	10.00	104.00	
U	1.19	1.32	0.83	2.50	1.60	20.00	
La/Yb	9.04	9.42	9.56	59.44	57.44	40.37	36.82
Sr/Y	56.05	47.32	24.04	50.90	52.17	29.00	17.71

Table C.4 continued.

Volcanic Suite	Eastern Altiplano (K-UK mafic)	Eastern Altiplano (K-UK mafic)	Eastern Altiplano (K-UK mafic)	Eastern Altiplano (K-UK mafic)	Eastern Altiplano (K-UK mafic)	Eastern Altiplano (K-UK mafic)	Eastern Altiplano (K-UK mafic)
Data Source	Calier et al. (2005)	Calier et al. (2005)	Calier et al. (2005)	Calier et al. (2005)	Calier et al. (2005)	Calier et al. (2005)	Calier et al. (2005)
Classification	sanadine phlogopite lamproite	sanadine phlogopite lamproite	sanadine phlogopite lamproite	sanadine phlogopite lamproite	Orthopyroxene phlogopite lamproite	Orthopyroxene phlogopite lamproite	Olivine minette
SampleID	14	15	16	17	18	19	20
SiO2 (wt%)	58.02	58.51	55.27	58.08	56.41	57.59	46.42
TiO_2	1.57	1.35	0.93	1.36	0.91	0.91	1.77
Al_2O_3	12.76	13.58	11.94	13.67	13.88	14.26	11.45
FeO*	*4.86*	*4.57*	*6.58*	*4.57*	*6.12*	*5.93*	*7.51*
Fe_2O_3*	5.40	5.08	7.31	5.08	6.80	6.59	8.35
MnO	0.04	0.04	0.06	0.04	0.09	0.06	0.12
MgO	7.11	7.06	9.26	7.07	4.77	4.39	10.42
CaO	1.90	1.78	2.91	1.88	3.98	3.74	5.52
Na_2O	1.01	0.49	0.08	0.60	2.60	2.70	3.62
K_2O	8.13	8.94	4.41	8.58	6.57	5.94	2.85
P_2O_5	0.92	1.28	1.18	1.27	0.87	0.83	1.51
LOI %	3.36	2.31	6.84	2.34	2.62	2.47	7.85
Mg#	72.00	73.00	72.00	73.00	58.00	57.00	71.00
Sc (ppm)			15.00			18.00	14.00
V	97.00	88.00	97.00	90.00	93.00	102.00	145.00
Cr	481	551	579	562	188	254	511
Co							
Ni	235.00	151.00	313.00	146.00	115.00	364.00	446.00
Cu							
Zn							
Rb	658.00	913.00	408.00	839.00	375.00	405.00	200.00
Sr	618.00	456.00	211.00	543.00	1322.00	1359.00	3020.00
Y	28.00	31.00	24.00	31.00	29.00	24.00	28.00
Zr	789.00	678.00	431.00	703.00	499.00	502.00	539.00
Nb	36.00	29.00	27.00	24.00	26.00	32.00	
Cs	9.10	12.00		12.00	11.00		
Ba	3864.00	4042.00	2629.00	3617.00	8719.00	6552.00	5996.00
La	99.00	73.00	58.00	76.00	71.00	69.00	75.00
Ce	214.00	191.00	130.00	195.00	153.00	131.00	164.00
Pr	32.00	27.00		28.00	19.00		20.00
Nd	134.00	123.00	91.00	127.00	77.00	71.00	82.00
Sm	24.00	25.00	24.00	26.00	16.00	16.00	17.00
Eu	4.30	4.62	4.33	4.49	3.95	3.48	4.64
Gd	13.00	16.00	15.00	15.00	11.00	10.00	11.00
Tb	1.74	1.75		1.90	1.41		1.42
Dy	7.60	7.70	6.20	7.60	6.80	5.70	6.70
Ho	1.10	1.13		1.11	1.04		1.00
Er	2.79	2.77	2.63	2.59	2.45	2.34	2.48
Tm	0.35	0.32		0.33	0.33		0.30
Yb	2.31	2.19	2.00	2.22	2.32	1.96	1.68
Lu	0.35	0.34	0.33	0.34	0.33	0.33	0.24
Hf	22.00	19.00		20.00	13.00		
Ta	2.46	2.19		2.25	1.73	1.62	2.00
Pb	52.00	38.00		45.00	150.00		
Th	93.00	98.00	63.00	103.00	75.00	61.00	42.00
U	14.00	17.00		18.00	17.00		
La/Yb	42.86	33.33	29.00	34.23	30.60	35.20	44.64
Sr/Y	22.07	14.71	8.79	17.52	45.59	56.63	107.86

Table C.5. Calcite δ13C and $\delta^{18}O$ and phlogopite δD

	calcite			phlogopite
Sample	$\delta^{13}C$ (VPDB)	$\delta^{18}O$ (VSMOW)	$\delta^{18}O$ (VPDB)	δD (VSMOW)
CH19RX-66	+0.8	-14.4	+16.0	-197
CH19RX-70	-0.1	-14.7	+15.8	
CH19RX-47	-1.2	-14.3	+16.1	-165
CH19RX-71	-2.5	-14.1	+16.4	

APPENDIX D

Copyright release for Chapter 2

ELSEVIER

Publishing Agreement

Elsevier B.V.

^3He evidence for fluid transfer and continental hydration above a flat slab

Corresponding author	Mr. Coleman D. Hiett
E-mail address	coleman.hiett@aggiemail.usu.edu
Journal	Earth and Planetary Science Letters
Article number	116722
Our reference	EPSL_116722
PII	S0012-821X(20)30666-X

Your Status

- I am one author signing on behalf of all co-authors of the manuscript

Assignment of Copyright

I hereby assign to Elsevier B.V. the copyright in the manuscript identified above (where Crown Copyright is asserted, authors agree to grant an exclusive publishing and distribution license) and any tables, illustrations or other material submitted for publication as part of the manuscript (the "Article"). This assignment of rights means that I have granted to Elsevier B.V., the exclusive right to publish and reproduce the Article, or any part of the Article, in print, electronic and all other media (whether now known or later developed), in any form, in all languages, throughout the world, for the full term of copyright, and the right to license others to do the same, effective when the Article is accepted for publication. This includes the right to enforce the rights granted hereunder against third parties.

Supplemental Materials

"Supplemental Materials" shall mean materials published as a supplemental part of the Article, including but not limited to graphical, illustrative, video and audio material.

With respect to any Supplemental Materials that I submit, Elsevier B.V. shall have a perpetual worldwide, non-exclusive right and license to publish, extract, reformat, adapt, build upon, index, redistribute, link to and otherwise use all or any part of the Supplemental Materials in all forms and media (whether now known or later developed), and to permit others to do so.

Research Data

"Research Data" shall mean the result of observations or experimentation that validate research findings and that are published separate to the Article, which can include but are not limited to raw data, processed data, software, algorithms, protocols, and methods.

With respect to any Research Data that I wish to make accessible on a site or through a service of Elsevier B.V., Elsevier B.V. shall have a perpetual worldwide, non-exclusive right and license to publish, extract, reformat, adapt, build upon, index, redistribute, link to and otherwise use all or any part of the Research Data in all forms and media (whether now known or later developed) and to permit others to do so. Where I have selected a specific end user license under which the Research Data is to be made available on a site or through a service, the publisher shall apply that end user license to the Research Data on that site or service.

Reversion of rights

Articles may sometimes be accepted for publication but later rejected in the publication process, even in some cases after public posting in "Articles in Press" form, in which case all rights will revert to the author (see https://www.elsevier.com/about/our-business/policies/article-withdrawal).

Revisions and Addenda

I understand that no revisions, additional terms or addenda to this Journal Publishing Agreement can be accepted without Elsevier B.V.'s express written consent. I understand that this Journal Publishing Agreement supersedes any previous agreements I have entered into with Elsevier B.V. in relation to the Article from the date hereof.

Author Rights for Scholarly Purposes

I understand that I retain or am hereby granted (without the need to obtain further permission) the Author Rights (see description below), and that no rights in patents, trademarks or other intellectual property rights are transferred to Elsevier B.V..
The Author Rights include the right to use the Preprint , Accepted Manuscript and the Published Journal Article for Personal Use and Internal Institutional Use . They also include the right to use these different versions of the Article for Scholarly Sharing purposes, which include sharing:

- the Preprint on any website or repository at any time;
- the Accepted Manuscript on certain websites and usually after an embargo period;
- the Published Journal Article only privately on certain websites, unless otherwise agreed by Elsevier B.V..

In the case of the Accepted Manuscript and the Published Journal Article the Author Rights exclude Commercial Use (unless expressly agreed in writing by Elsevier B.V.), other than use by the author in a subsequent compilation of the author's works or to extend the Article to book length form or re-use by the author of portions or excerpts in other works (with full acknowledgment of the original publication of the Article).

Author Representations / Ethics and Disclosure / Sanctions

I affirm the Author Representations noted below, and confirm that I have reviewed and complied with the relevant Instructions to Authors, Ethics in Publishing policy, Declarations of Interest disclosure and information for authors from countries affected by sanctions (Iran, Cuba, Sudan, Burma, Syria, or Crimea). Please note that some journals may require that all co-authors sign and submit Declarations of Interest disclosure forms. I am also aware of the publisher's policies with respect to retractions and withdrawal (https://www.elsevier.com/about/our-business/policies/article-withdrawal).

For further information see the publishing ethics page at https://www.elsevier.com/about/our-business/policies/publishing-ethics and the journal home page. For further information on sanctions, see https://www.elsevier.com/about/our-business/policies/trade-sanctions

Author representations

- The Article I have submitted to the journal for review is original, has been written by the stated authors and has not been previously published.
- The Article was not submitted for review to another journal while under review by this journal and will not be submitted to any other journal.
- The Article and the Supplemental Materials do not infringe any copyright, violate any other intellectual property, privacy or other rights of any person or entity, or contain any libellous or other unlawful matter.
- I have obtained written permission from copyright owners for any excerpts from copyrighted works that are included and have credited the sources in the Article or the Supplemental Materials.
- Except as expressly set out in this Journal Publishing Agreement, the Article is not subject to any prior rights or licenses and, if my or any of my co-authors' institution has a policy that might restrict my ability to grant the rights required by this

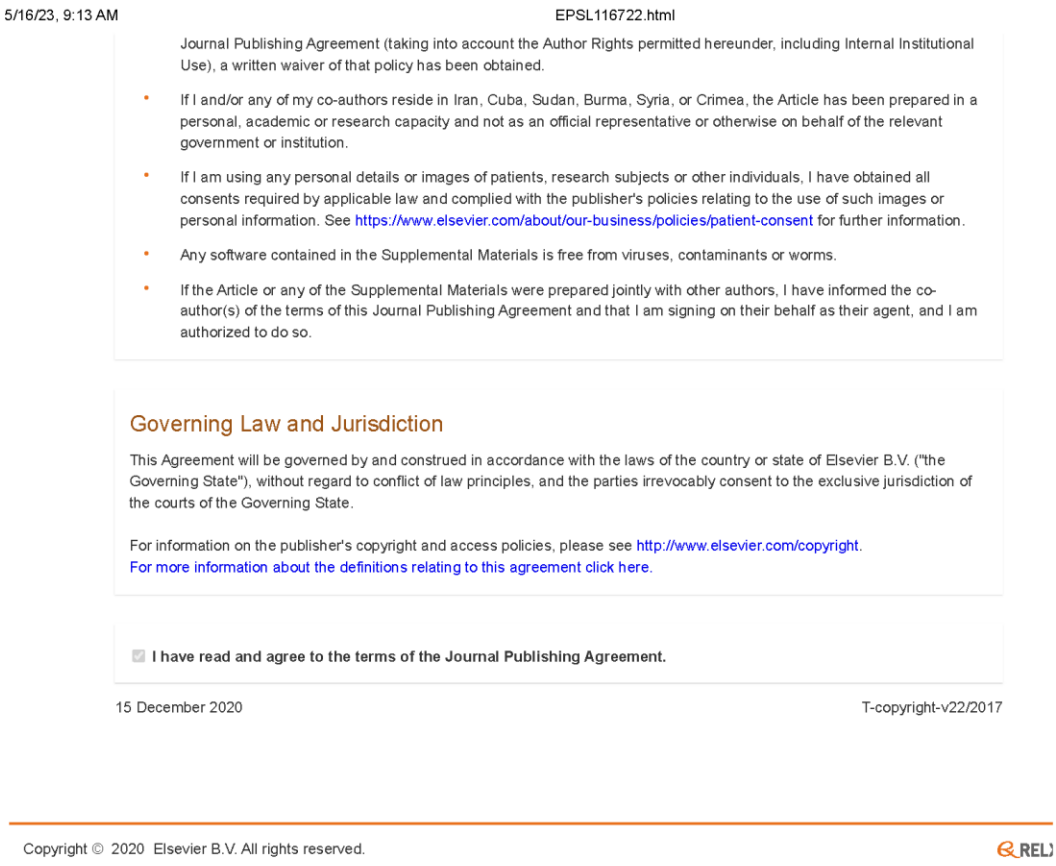

5/16/23, 9:13 AM EPSL116722.html

Journal Publishing Agreement (taking into account the Author Rights permitted hereunder, including Internal Institutional Use), a written waiver of that policy has been obtained.

- If I and/or any of my co-authors reside in Iran, Cuba, Sudan, Burma, Syria, or Crimea, the Article has been prepared in a personal, academic or research capacity and not as an official representative or otherwise on behalf of the relevant government or institution.
- If I am using any personal details or images of patients, research subjects or other individuals, I have obtained all consents required by applicable law and complied with the publisher's policies relating to the use of such images or personal information. See https://www.elsevier.com/about/our-business/policies/patient-consent for further information.
- Any software contained in the Supplemental Materials is free from viruses, contaminants or worms.
- If the Article or any of the Supplemental Materials were prepared jointly with other authors, I have informed the co-author(s) of the terms of this Journal Publishing Agreement and that I am signing on their behalf as their agent, and I am authorized to do so.

Governing Law and Jurisdiction

This Agreement will be governed by and construed in accordance with the laws of the country or state of Elsevier B.V. ("the Governing State"), without regard to conflict of law principles, and the parties irrevocably consent to the exclusive jurisdiction of the courts of the Governing State.

For information on the publisher's copyright and access policies, please see http://www.elsevier.com/copyright.
For more information about the definitions relating to this agreement click here.

I have read and agree to the terms of the Journal Publishing Agreement.

15 December 2020 T-copyright-v22/2017

*Elsevier defines “Personal use” as including “inclusion in a thesis or dissertation”. (https://authors.elsevier.com/authorform/staticpage/definitions.do?lang=en#personalUse)

Copyright release for Chapter 3

Elsevier Logo

Publishing Agreement

Elsevier B.V.

Deep CO2 and N2 emissions from Peruvian hot springs: Stable isotopic constraints on volatile cycling in a flat-slab subduction zone

Corresponding author	Mr. Coleman D. Hiett
E-mail address	coleman.hiett@usu.edu
Journal	Chemical Geology
Article number	120787
Our reference	CHEMGE_120787
PII	S0009-2541(22)00081-X
DOI	10.1016/j.chemgeo.2022.120787

Your Status

I am one author signing on behalf of all co-authors of the manuscript

Assignment of Copyright

I hereby assign to Elsevier B.V. the copyright in the manuscript identified above (where Crown Copyright is asserted, authors agree to grant an exclusive publishing and distribution license) and any tables, illustrations or other material submitted for publication as part of the manuscript (the "Article"). This assignment of rights means that I have granted to Elsevier B.V., the exclusive right to publish and reproduce the Article, or any part of the Article, in print, electronic and all other media (whether now known or later developed), in any form, in all languages, throughout the world, for the full term of copyright, and the right to license others to do the same, effective when the Article is accepted for publication. This includes the right to enforce the rights granted hereunder against third parties.

Supplemental Materials

"Supplemental Materials" shall mean materials published as a supplemental part of the Article, including but not limited to graphical, illustrative, video and audio material.

With respect to any Supplemental Materials that I submit, Elsevier B.V. shall have a perpetual worldwide, non-exclusive right and license to publish, extract, reformat, adapt, build upon, index, redistribute, link to and otherwise use all or any part of the Supplemental Materials in all forms and media (whether now known or later developed), and to permit others to do so.

Research Data

"Research Data" shall mean the result of observations or experimentation that validate research findings and that are published separate to the Article, which can include but are not limited to raw data, processed data, software, algorithms, protocols, and methods.

With respect to any Research Data that I wish to make accessible on a site or through a service of Elsevier B.V., Elsevier B.V. shall have a perpetual worldwide, non-exclusive right and license to publish, extract, reformat, adapt, build upon, index, redistribute, link to and otherwise use all or any part of the Research Data in all forms and media (whether now known or later developed) and to permit others to do so. Where I have selected a specific end user license under which the Research Data is to be made available on a site or through a service, the publisher shall apply that end user license to the Research Data on that site or service.

Reversion of rights

Articles may sometimes be accepted for publication but later rejected in the publication process, even in some cases after public posting in "Articles in Press" form, in which case all rights will revert to the author (see https://www.elsevier.com/about/our-business/policies/article-withdrawal).

Revisions and Addenda

I understand that no revisions, additional terms or addenda to this Journal Publishing Agreement can be accepted without Elsevier B.V.'s express written consent. I understand that this Journal Publishing Agreement supersedes any previous agreements I have entered into with Elsevier B.V. in relation to the Article from the date hereof.

Author Rights for Scholarly Purposes

I understand that I retain or am hereby granted (without the need to obtain further permission) the Author Rights (see description below), and that no rights in patents, trademarks or other intellectual property rights are transferred to Elsevier B.V..
The Author Rights include the right to use the Preprint , Accepted Manuscript and the Published Journal Article for Personal Use and Internal Institutional Use . They also include the right to use these different versions of the Article for Scholarly Sharing purposes, which include sharing:

- the Preprint on any website or repository at any time;
- the Accepted Manuscript on certain websites and usually after an embargo period;
- the Published Journal Article only privately on certain websites, unless otherwise agreed by Elsevier B.V..

In the case of the Accepted Manuscript and the Published Journal Article the Author Rights exclude Commercial Use (unless expressly agreed in writing by Elsevier B.V.), other than use by the author in a subsequent compilation of the author's works or to extend the Article to book length form or re-use by the author of portions or excerpts in other works (with full acknowledgment of the original publication of the Article).

Author Representations / Ethics and Disclosure / Sanctions

I affirm the Author Representations noted below, and confirm that I have reviewed and complied with the relevant Instructions to Authors, Ethics in Publishing policy, Declarations of Interest disclosure and information for authors from countries affected by sanctions (Iran, Cuba, or Syria). Please note that some journals may require that all co-authors sign and submit Declarations of Interest disclosure forms. I am also aware of the publisher's policies with respect to retractions and withdrawal (https://www.elsevier.com/about/our-business/policies/article-withdrawal).

For further information see the publishing ethics page at https://www.elsevier.com/about/our-business/policies/publishing-ethics and the journal home page. For further information on sanctions, see https://www.elsevier.com/about/our-business/policies/trade-sanctions

Author representations

- The Article I have submitted to the journal for review is original, has been written by the stated authors and has not been previously published.
- The Article was not submitted for review to another journal while under review by this journal and will not be submitted to any other journal.
- The Article and the Supplemental Materials do not infringe any copyright, violate any other intellectual property, privacy or other rights of any person or entity, or contain any libellous or other unlawful matter.
- I have obtained written permission from copyright owners for any excerpts from copyrighted works that are included and have credited the sources in the Article or the Supplemental Materials.
- Except as expressly set out in this Journal Publishing Agreement, the Article is not subject to any prior rights or licenses.

*Elsevier defines “Personal use” as including “inclusion in a thesis or dissertation”. (https://authors.elsevier.com/authorform/staticpage/definitions.do?lang=en#personalUse)

APPENDIX E

Curriculum Vitae

Coleman Hiett

Department of Geosciences, Utah State University
4505 Old Main Hill, Logan, UT 84322

coleman.hiett@usu.edu | coleman.hiett@gmail.com
(720) 271-6187

EDUCATION

2018 – **Ph.D. Candidate, Geology – Utah State University**
Advisor: Dr. Dennis Newell
Research Focus: Mantle and crustal fluid geochemistry and interactions with the continental lithosphere in flat-slab subduction zones, observations from geothermal systems, xenoliths, and volcanism

2013 – 2017 **B.A., Geological Sciences – University of Colorado Boulder**
summa cum laude

APPOINTMENTS

Spring 2022 Instructor of Record – Utah State University, Geosciences

2019 – NSF Graduate Research Fellow – Utah State University, Geosciences

2018 – 2019 Presidential Doctoral Research Fellow – Utah State University, Geosciences

2018 Physical Science Intern – Science and Resource Management, Grand Canyon National Park, AZ

2015 – 2016 Research & Laboratory Assistant – University of Colorado Thermochronology Research and Instrumentation Lab; Boulder, CO

PUBLICATIONS

Newell, D.L., Benowitz, J.A., Regan, S., and **Hiett, C.D**., 2023. Roadblocks and speed limits: mantle-to-surface volatile flux through the lithospheric-scale Denali fault, Alaska: Geology, v. 51 (6) p.576, doi.org/10.1130/G51068.1

Hiett, C.D., Newell, D.L., Jessup, M.J., Grambling, T.A., Scott, B.E., and Upin, H., 2022. Deep CO_2 and N_2 emissions from Peruvian hot springs: Stable isotopic constraints on volatile cycling in a flat-slab subduction zone: Chemical Geology, v. 595, p. 120787, doi.org/10.1016/j.chemgeo.2022.120787

Hiett, C.D., Newell, D.L., and Jessup, M.J., 2021. ^{3}He evidence for fluid transfer and continental hydration above a flat slab: Earth and Planetary Science Letters, v. 556, p. 116722, doi:10.1016/j.epsl.2020.116722.

manuscripts submitted, in-review, or in-preparation

Grambling T.A., Jessup M.J., Newell D.L., Grambling N.L., and **Hiett, C.D.**, Protracted magmatism and rapid intrusion in the high Andes: Contrasting magmatic conditions preceding synconvergent extension above the Peruvian flat slab: (in prep)

Hiett C.D., Newell D. L., and Shervais, J.W., Metasomatism and melting of cordilleran lithosphere resulting from sediment relamination during shallow subduction: (in-prep)

Hiett C.D., Newell D. L., and Shervais, J.W., Shallow subduction-derived metasomatism at the root of alkaline backarc magmatism in the northern altiplano: (in-prep)

non peer-reviewed

Hiett, C. D., 2017. Constraining the Timing of River Incision in the Upper Colorado Drainage Basin Using Apatite (U-Th)/He Thermochronology in the Elk Mountains, Western Colorado. *University of Colorado Undergraduate Honors Theses*. 1367. https://scholar.colorado.edu/honr_theses/1367

GRANTS & FELLOWSHIPS

2022 ($175)	Geological Society of America - Rocky Mountain Division Student Travel Grant
	USU School of Graduate Studies Travel Grant ($200)
2021	USU School of Graduate Studies Travel Grant ($200)
2019	**National Science Foundation Graduate Research Fellowship** ($138,000 – includes research funding, tuition, and stipend; support from 08/20 to 8/23)
	Geological Society of America / MGPV Division Lipman Research Award ($2,500)
	USU School of Graduate Studies Travel Grant ($200)
2018	**Presidential Doctoral Research Fellowship - Utah State University**
	Undergraduate Research Opportunity Grant - University of Colorado ($2,090)
	Tim Wawrzyniec Fellowship in Support of Geological Research at the Rocky Mtn. Bio Lab (named undergraduate researcher, Lead PI: Lon Abbott, $5,810)
2016	T. Keith Marks Scholarship for Outstanding Geology Majors - University of Colorado ($3,500)

AWARDS & RECOGNITION

2022	Geology PhD Researcher of the Year - Utah State University Geosciences
2020	Geology PhD Researcher of the Year - Utah State University Geosciences
2017	Neal J. Harr Outstanding Student Award - Rocky Mountain Association of Geologists
2015 – 2017	University of Colorado Dean’s List

TEACHING & MENTORSHIP

Instructor of Record
GEO2800 – Minerals and Rocks

- Redesigned and created new course material utilizing a new online open-access course textbook.
- Lead a two-day field trip to Topaz Mountain and Eureka Mining Distract, UT
- Supervised a graduate student TA who oversaw two lab sections.
- Feedback includes formal course evaluation by students and formal teaching evaluation by tenured faculty member

Graduate Mentor for Undergraduate Researchers

- Jacob Ladner – Igneous Petrology of lava flows in the Peruvian Altiplano. USU Undergraduate Creative Opportunities Research Grant (URCO) awarded Fall 2022 ($2,000).
- Alyssa Shiwal – Isotopic Analysis of Hydrous Phenocrysts in Lava Flows of the Peruvian Altiplano Plateau: Testing for a Subduction Signature. Presented at USU's Student Research Symposium in Spring 2022.

Mentor for NSF GRFP Grant Writing Workshop - Fall 2019, 2020, 2021, 2022
Served as fellowship awardee mentor for applicants writing grant proposals for NSF Graduate Research Program. Workshop held by USU Science Writing Center. Eight applicants mentored to date. One mentee was offered the award (AJ Walters, 2022) and two received honorable mentions (Valerie Martin, 2021; Maria Stahl 2022).

PROFESSIONAL INVOLVEMENT & SERVICE

External

2022 *Reviewer*, Journal of Applied Volcanology
Reviewer, Geophysical Research Letters
Proposal Reviewer, Graduate Woman in Science National Fellowship Program

Utah State University

2022 *Working group member*, Unlearning Racism in Geosciences (URGE), USU Geo Pod
2021 *Proposal Reviewer*, Undergraduate Research and Creative Opportunities Grant Program
2020 *Graduate representative*, College of Science Graduate Student Council
Graduate representative, Geoscience Department
Proposal Reviewer, Undergraduate Research and Creative Opportunities Grant Program
2019 *Student Committee Member,* Department of Geosciences Faculty Search Committee
Proposal Reviewer, Undergraduate Research and Creative Opportunities Grant proposals
2019 *Student judge*, Student Research Symposium
Panelist, Undergraduate Research Fellows (URF) Mentor Relationships Workshop

2018 *Volunteer,* Science Unwrapped, Presentation by Dr. Carol Dehler

Universidad del San Antonia Abad – Cusco, Peru

2019 *Guest Lecturer,* "Thermal springs of the Peruvian Andes - evidence for mantle-to-crust fluid connections in a flat-slab subduction setting" (co-presented with Dr. Dennis Newell)

Community

2019 – 2021 *Volunteer,* Department of Geoscience's Annual Rock and Fossil Day
2019 *Guest judge*, Cache Valley, UT K-12 Homeschool Science Fair

Grand Canyon National Park

2017 *Associate Naturalist* – Interpretation Division, delivered geology talks on the rim and volunteered at park visitor's center

University of Colorado – Boulder

2016 – 2017 *Student Mentor,* Undergraduate Research Seminar

CONFERENCE PRESENTATIONS (* indicates student mentee)

Hiett, C.D., Newell, D.L., and *Schiwal, A., Metasomatic enrichment of the northern Altiplano lithosphere constrained by isotopic and trace element characteristics of biotite monzogabbro and pyroxenite xenoliths: Geological Society of America *Abstracts with Programs,* 2022 (oral presentation)

*Schiwal, A., **Hiett, C.D.**, and Newell, D.L., Isotopic analysis of hydrous phenocrysts in lava flows of the Peruvian Altiplano Plateau: Testing for a subduction signature: Utah State University Student Research Symposium, Spring 2022

Hiett, C.D., Newell, D.L., Jessup, M.J., Grambling, T.A., Scott, B.E., and Upin, H., From Mantle to Surface in the Absence of Magmatism: Mantle Gases in Peruvian Hot Springs and Implications for Volatile Cycling in Flat-Slab Subduction Zones: AGU Fall Meeting Abstracts, 2021 (oral presentation)

Abbott, L.D., Flowers, R.M., Metcalf, J.R., **Hiett, C.D.**, Kelleher, R., Camm, H., Ramba, M., McCorkel, N., and Riccio, E., The Gothic Dome: Kilometer-scale Miocene Exhumation in Colorado's Elk and West Elk Mountains: AGU Fall Meeting Abstracts, 2021 https://doi.org/10.1002/essoar.10508533.1

Grambling, T.A., Jessup M.J., Dygert, N., Newell, D.L., Grambling, N.L., and **Hiett C.D.**, Over dispersion of zircon crystallization ages in the Cordillera Blanca batholith, Central Peru: Lead loss or prolonged magmatism and protracted crystallization?: AGU Fall Meeting Abstracts, 2021

Hiett, C.D., Newell, D.L., Upin, H., Jessup, M. J., Scott, B. E., Grambling, T. A., Hughes, C.A. and Shaw, C.A., 2020, Mantle-to-Surface Fluid Transit Times Estimated from Helium Isotopes in Thermal Springs above the Peruvian Flat Slab: Implications for Tectonic Controls during Flat Slab-to-Lithosphere Fluid Transfer. In AGU Fall Meeting Abstracts (Vol. 2020, pp. V046-06). (oral presentation)

Hiett, C.D., Newell, D.L., Upin, H., Jessup, M.J., Scott, B.E., Grambling, T.A., Hughes, C.A. and Shaw, C.A., 2019, September. Mantle-to-Crust Fluid Transfer above the Peruvian Flat Slab: Insight from Helium Isotopes in Thermal Springs of the Peruvian Andes: Geological Society of

America *Abstracts with Programs.* Vol. 51, No. 5. doi: 10.1130/abs/2019AM-336838 (oral presentation)

Newell, D.L., Jessup, M.J., Upin, H., Scott, B.E., Grambling, T.A., **Hiett, C.**, Shaw, C.A. and Hughes, C.A., 2019, September. He and CO2 Flux from the Peruvian Flat Slab Estimated from Hot Spring Geochemistry: Geological Society of America *Abstracts with Programs.* Vol. 51, No. 5 doi:10.1130/abs/2019AM-336538

Abbott, L. D., Flowers, R. M., Metcalf, J. R., **Hiett, C.**, McCorkel, N., Schanock, E., and Gonzalez, N., 2018 Investigating a bull's-eye of late Miocene exhumation in Colorado's Elk and West Elk Mountains using (U-Th)/He thermochronology: Geological Society of America *Abstracts with Programs*. Vol. 50, No. 6.

LABORATORY EXPERIENCE

Includes instruments that I have routinely used and/or have been trained to operate, unless otherwise stated

Utah State University, Geosciences Department, various labs

- Thermo Scientific Delta V Advantage Isotope Ratio MS (continuous flow) with TC/EA and GasBench II interfaces
    - Primary instrument utilized for PhD research, including method development, maintenance, and troubleshooting
- Agilent 8900 Triple-Quadrupole ICP-MS
- Horiba LabRAM HR Evolution Micro Raman
- Bruker Tracer III Handheld XRF
- Panalytical X'Pert Pro X-ray Diffraction Spectrometer

Utah State University Core Microscopy Facility

- FEI Quanta FEG 650 SEM with Oxford EDS detector

University of Colorado Boulder TIMS Laboratory – PI Lang Farmer

Three-week visit (2022)

- Sample digestion and column chromatography in preparation for Sr and Nd isotope analysis
- In situ micro-sampling of thin and thick rock sections with New Wave Micromilling device

USGS Noble Gas Laboratory – PI Andrew Hunt

One-week visit (2019)

- Ultrahigh vacuum gas extraction line connected to gas-source, magnetic sector noble gas mass spectrometer (Thermo Scientific Helix MC Plus)

University of New Mexico Volatiles Laboratory – PI Tobias Fischer

One-week visit (2019)

- High vacuum gas extraction line connected to GOW-MAC Gas Chromatograph and Pfeiffer Quadrupole MS

WORKSHOPS & SEMINARS ATTENDED

Aug 2021 Empowering Teaching Excellence (USU) - Pedagogies of Care: Community, Research, and Mentorship Virtual Conference

Jun 2021 Council on Undergraduate Research - Centering DE&I in Undergraduate Research and Creative Activity Conference

Spring 2021	Community Engagement in Research - PDRF coffee workshop series, Utah State University
Jan 2021	Cultivating Leadership for Change and Justice in the Geosciences - Sponsored by Geoscientists of Color and Allies
Spring 2019	Prepping for Post-Grad Career - PDRF coffee workshop series, Utah State University
Sep 2018	Graduate Student Grant Writing Seminar - Utah State University

PROFESSIONAL AFFILIATIONS

- Council on Undergraduate Research, *Graduate Student Member since 2021*
- American Geophysical Union, *Student* Member since 2020
- Sigma Xi Scientific Research Honor Society, *Associate M*ember 2019
- Geological Society of America, *Student Membe*r since 2018